Extending Density-Functional Theory to Molecules in Magnetic Fields

James W. Furness

December, 2016

Contents

Introduction v

1 Theoretical Foundations 1
- 1.1 The electronic structure problem . . . 1
  - 1.1.1 The Born–Oppenheimer approximation . . . 2
  - 1.1.2 The variational principle . . . 2
- 1.2 Hartree–Fock theory . . . 2
  - 1.2.1 The Slater determinant . . . 3
  - 1.2.2 Restricted and unrestricted formalisms . . . 4
- 1.3 The finite basis set expansion . . . 5
  - 1.3.1 The Roothaan–Hall equations . . . 5
  - 1.3.2 The self consistent field procedure . . . 8
- 1.4 Beyond Hartree–Fock theory . . . 8
  - 1.4.1 Configuration interaction . . . 9
  - 1.4.2 Coupled-cluster methods . . . 10
- 1.5 Density-functional theory . . . 11
  - 1.5.1 The Rayleigh–Ritz variational principle . . . 12
  - 1.5.2 Gauge transformations of the potential . . . 12
  - 1.5.3 The first Hohenberg–Kohn theorem . . . 13
  - 1.5.4 The second Hohenberg–Kohn theorem . . . 14
  - 1.5.5 Levy–Lieb constrained search scheme . . . 15
  - 1.5.6 The Lieb functional . . . 20
- 1.6 Kohn–Sham DFT . . . 23
  - 1.6.1 The Kohn–Sham kinetic energy functional . . . 23
  - 1.6.2 The effective local potential . . . 24
- 1.7 Density-functional approximations . . . 25
  - 1.7.1 The local density approximation . . . 25
  - 1.7.2 The gradient expansion and generalised gradient approximation . . . 26
  - 1.7.3 The meta-generalised gradient approximation . . . 27
  - 1.7.4 Hybrid exchange-correlation functionals . . . 28

2 Functionals in Current-Density-Functional Theory 29
- 2.1 The quantum mechanics of electrons in magnetic fields . . . 29
  - 2.1.1 Classical electromagnetism . . . 29
  - 2.1.2 The magnetic hamiltonian . . . 30
  - 2.1.3 Gauge transformations . . . 33
  - 2.1.4 Basis sets for strong magnetic fields - London atomic orbitals . . . 33
  - 2.1.5 The Born–Oppenheimer approximation in strong magnetic fields . . . 35
- 2.2 Current-density-functional theory . . . 36
  - 2.2.1 The current-density . . . 36
  - 2.2.2 CDFT by constrained search . . . 37
  - 2.2.3 CDFT by convex conjugation . . . 38
  - 2.2.4 The choice of basic variables . . . 39
  - 2.2.5 Kohn–Sham current density functional theory . . . 39
  - 2.2.6 Gauge invariance of the exchange-correlation functional . . . 40
- 2.3 Vorticity dependent exchange correlation functionals . . . 41

2.3.1 The VRG functional . . . 42
2.3.2 Parametrisations of g(ρ) in vorticity functionals . . . 43
2.4 mGGA functionals in CDFT . . . 45
2.4.1 The current modified kinetic energy density . . . 46
2.4.2 Current generalised kinetic energy densities . . . 47
2.4.3 The current modified B98 functional . . . 48
2.4.4 The current modified TPSS functional . . . 49
2.5 Computational methods . . . 50
2.5.1 Computational evaluation of CDFT quantities . . . 50

3 The Calculation of Magnetic Response Properties 53
3.1 Energy expansion in a field . . . 54
3.2 Perturbative evaluation of molecular properties . . . 54
3.3 Finite field calculation of magnetic properties . . . 55
3.3.1 Isotropic molecular magnetizability and hyper-magnetizability . . . 55
3.3.2 Isotropic nuclear magnetic shielding constants . . . 56
3.3.3 Computational details . . . 56
3.3.4 Sensitivity of vorticity dependent functionals to vorticity regularisation . . . 57
3.4 CDFT estimates of magnetic response properties . . . 57
3.4.1 Molecular magnetizabilities . . . 59
3.4.2 Nuclear shielding constants . . . 62
3.4.3 Comparative summary . . . 62
3.4.4 Molecular hyper-magnetizabilities . . . 65
3.5 CDFT beyond the perturbative regime . . . 68
3.5.1 Perpendicular paramagnetic bonding . . . 69
3.5.2 Standard DFT and vorticity dependent functionals . . . 69
3.5.3 Current modified meta-GGA functionals . . . 71
3.6 Concluding remarks . . . 76

4 Properties From Current-Density-Functional Theory 77
4.1 Understanding the mechanism of perpendicular paramagnetic bonding . . . 77
4.1.1 Kohn–Sham orbital analysis . . . 78
4.1.2 Interaction electron densities . . . 79
4.2 The current modified electron localisation function . . . 80
4.2.1 The field free electron localisation function . . . 81
4.2.2 ELF in Kohn–Sham theory . . . 81
4.2.3 Generalisation to magnetic systems . . . 82
4.3 Field induced changes in electron localisation . . . 83
4.3.1 The topology of cELF . . . 87
4.3.2 Structural similarities in cELF and the physical current density . . . 87
4.3.3 The importance of self interaction correction within a magnetic field . . . 87
4.3.4 Concluding remarks . . . 89

5 Excited States in Magnetic Fields 91
5.1 The maximum overlap method . . . 92
5.2 The electronic states of H_2 within a strong magnetic field . . . 93
5.2.1 Potential energy curves . . . 93
5.2.2 Spin Zeeman induced state re-ordering . . . 96
5.2.3 Vertical excitation energies . . . 97
5.2.4 Equilibrium bond distances . . . 98
5.3 Concluding remarks . . . 100

6 Potential Based Density Functional Theory 101
6.1 Limitations of the generalised gradient expansion . . . 101
6.1.1 Anions and the lack of Rydberg states . . . 101
6.1.2 Dispersion forces . . . 102
6.2 The optimised effective potential . . . 103
6.2.1 The exact exchange functional . . . 104
6.2.2 Numerical solution for the exact exchange potential . . . 104

6.3 The finite basis OEP problem . . . 105
6.3.1 The Yang–Wu optimised effective potential scheme . . . 105
6.4 Computational methods . . . 106
6.4.1 Orbital dependent exchange-correlation functionals . . . 107
6.4.2 The Lieb maximisation . . . 107
6.4.3 The Gidopolous variational principle . . . 110
6.4.4 Numerical equivalence . . . 111
6.5 Concluding remarks . . . 111

7 Regularisation of The Optimised Effective Potential 115
7.1 The ill-posed nature of finite basis OEP . . . 115
7.2 The regularisation of ill-posed problems . . . 116
7.3 Classical regularisation techniques for the OEP problem . . . 117
7.3.1 Truncated singular value decomposition . . . 118
7.3.2 Tikhonov regularisation . . . 119
7.4 Relationship with the trust-region sub-problem . . . 120
7.4.1 Trust-region sub-problem regularisation . . . 122
7.5 Automatic regularisation . . . 124
7.5.1 The L-Curve . . . 124
7.5.2 The RPTRS algorithm . . . 126
7.6 RPTRS for the OEP problem . . . 126
7.6.1 Regularisation of the full potential . . . 126
7.6.2 Optimisation termination criteria . . . 127
7.6.3 Global L-Curve scan . . . 128
7.6.4 The absence of an elbow . . . 128
7.7 Atomic exchange potentials . . . 129
7.8 Targeted regularisation methods . . . 131
7.8.1 Generalised Tikhonov regularisation . . . 131
7.8.2 The choice of penalty matrix . . . 132
7.8.3 The generalised Tikhonov L-Curve . . . 132
7.8.4 The Yang smoothing norm . . . 133
7.8.5 Improvement of the near nucleus region . . . 134
7.9 Exact constraints for multiplicative potentials . . . 134
7.9.1 Hartree–Fock energy bound . . . 134
7.9.2 The HOMO condition . . . 136
7.9.3 The virial conditions . . . 136
7.10 Evaluation using exact constraints . . . 136
7.10.1 The orbital and potential basis limit . . . 137
7.10.2 Analysis through exact relations . . . 139
7.10.3 Future developments . . . 142
7.11 The regularisation of spin polarised systems . . . 142
7.11.1 Independent spin potential regularisation . . . 143
7.12 Concluding remarks . . . 143

8 Concluding Remarks 145

Acknowledgments 147

Introduction

The density-functional theory (DFT) of Hohenberg and Kohn [1] has become the Swiss army knife of the quantum chemist, able to tackle nearly all electronic structure problems with impressive accuracy and efficiency, and it is common to see DFT calculations reported alongside experimental observations in the wider chemical literature. Some systems remain problematic for DFT however and, as DFT was constructed to simulate the systems commonly encountered in the chemistry lab, magnetic fields and the electron currents they induce are completely absent from the theory. Instead, DFT must be generalised for use in a magnetic field by including these currents directly, becoming current-density-functional theory (CDFT) [2]. By making this generalisation it is hoped that the practical utility of standard DFT can be leveraged to investigate molecules in both weak and strong magnetic fields.

Whilst the study of molecular systems in strong magnetic fields is clearly of astrochemical and academic interest [3–7], it is reasonable to ask what place such calculations have with regards to laboratory problems, and what the eventual goal of CDFT is. To answer this one should look, for example, to the laboratory field semi-conductor systems that have been shown to be good analogues of molecules in strong fields [8, 9]. Empirical studies of such systems show that a proper description of the magnetic effects is likely to be essential for their accurate simulation and, with the large size of these systems, the low cost correlated description of CDFT is likely to be instrumental in understanding their electronic structure.

The theoretical framework for CDFT has long been established, only very recently however has a computer code, LONDON , been available to actually perform self-consistent molecular CDFT calculations in strong magnetic fields [10, 11]. As a result of this absence, the functionals and approximations that comprise CDFT remain relatively untested. This thesis aims to utilise the LONDON code to address this absence, first establishing the accuracy of existing CDFT functionals before developing the ideas to investigate the effect of a strong magnetic field on various aspects of electronic structure.

The thesis begins by establishing the necessary theoretical foundations of DFT in Chapter 1 and its extension to CDFT in Chapter 2. The accuracy of a number of CDFT functionals is tested in Chapter 3 for predicting both the weak field magnetic phenomena encountered on earth, and the more exotic physics found in strong fields. The course of this study reveals a modified implementation of the meta-generalised gradient approximation (mGGA) class of functionals to be particularly well suited to strong field CDFT, providing a promising route to high accuracy descriptions of strong field phenomena.

Using the modified mGGA functionals, Chapter 4 makes use of the interpretive powers of CDFT and the Kohn–Sham orbitals in order to develop a qualitative understanding of strong field electronic structure, and the origins of a new bonding mechanism, termed perpendicular paramagnetic bonding. This exploration of strong field phenomena provides a rationalisation for the the successes of the mGGA functionals, highlighting the importance of self-interaction error in strong magnetic fields.

The presence of a strong magnetic field has a complicated effect on the excited electronic states, with important consequences for molecular structure in a field. The maximum overlap method (MOM) of Gilbert *et al.* [12] is employed in Chapter 5 in the context of strong field Hartree–Fock theory to facilitate the study of excited states in magnetic fields. The MOM method is shown to give an excellent agreement with high accuracy calculations and paves the way for a MOM-CDFT program capable of giving an accurate, correlated description of excited states in a field.

The rest of the thesis moves away from directly dealing with the complications of a magnetic field, and instead considers the optimised effective potential (OEP) method in DFT as a means to fully orbital dependent functionals. This investigation is made with an eye to the future extension of CDFT to incorporate the OEP method, enabling the use of orbital dependent functionals in the CDFT description of molecules in magnetic fields. Such functionals are expected to be an effective route to higher accuracy calculations, as the currents induced by the magnetic field are inherently orbital dependent quantities themselves. The core framework of magnetic field free OEP is explored in Chapter 6 and a previously unrecognised connection between the recently proposed variational principle of Gidopolous [13] and the Lieb functional [14] is established.

The optimised effective potential problem is notoriously ill behaved in a finite basis representation and the problem of regularising its equations to give physical potentials remains unsolved, despite considerable effort. Previous regularisation schemes are severely limited by their requirement for a user defined regularisation strength parameter, with no *a priori* guide towards the correct choice. This requirement prevents the OEP method from being used as a black box method and restricts the basis set combinations that can be considered. Chapter 7 addresses the absence of a satisfactory regularisation solution by first thoroughly studying the general ill-posed problem and the classical techniques employed in its regularisation. From this base, a fully automatic regularisation scheme is constructed to automatically tune regularisation strength from measures that are internal to the OEP. In doing so, an optimal regularisation is applied throughout the calculation, removing the need for a manually set parameter. The automatic scheme is then augmented with information from the potential basis set and shown to produce a physically meaningful potential from a single OEP calculation, regardless of the basis sets chosen.

Finally, Chapter 8 summarises the work and discusses future directions for the continued development of the field.

Chapter 1

Theoretical Foundations

The most precise description of matter to date is that of quantum mechanics, captured concisely by the well known Schrödinger equation, the non-relativistic limit of the more complicated Dirac equations. As the relativistic effects are small for the atoms of the first two periods which are the focus of this work the Dirac equations will not be considered beyond the introduction of electron spin in Section 2.1.2.

The time-independent Schrödinger equation can be written as,

$$\hat{H}\Psi_i(\{\mathbf{x}_n\},\{\mathbf{X}_K\}) = E_i\Psi_i(\{\mathbf{x}_n\},\{\mathbf{X}_K\}), \tag{1.1}$$

where $\mathbf{x}_n$ and $\mathbf{X}_K$ denote the combined space and spin coordinates of electron n and nucleus K respectively. The system is in state i described by the wave function Ψ_i and does not vary with time. The wave function is an eigenfunction of the system specific Hamiltonian operator $\hat{H}$ with eigenvalue E_i, the expectation value of the total energy. It is convenient to express the quantities of quantum mechanics in a system of atomic units (a.u.) for which $m_e = |e| = \hbar = 4\pi\epsilon_0 = 1$ allowing these constants to be omitted from equations, and this system is adopted throughout this thesis (unless otherwise stated). For a molecule comprising of N electrons and M nuclei the Hamiltonian operator can be written in the position representation as,

$$\hat{H} = -\frac{1}{2}\sum_{i=1}^{N}\nabla_i^2 - \frac{1}{2}\sum_{K=1}^{M}\frac{1}{M_K}\nabla_K^2 - \sum_{i=1}^{N}\sum_{K=1}^{M}\frac{Z_K}{|\mathbf{r}_i-\mathbf{R}_K|} + \sum_{i=1}^{N}\sum_{j>i}^{N}\frac{1}{|\mathbf{r}_i-\mathbf{r}_j|} + \sum_{K=1}^{M}\sum_{L>K}^{M}\frac{Z_K Z_L}{|\mathbf{R}_K-\mathbf{R}_L|}, \tag{1.2}$$

where M_K, Z_K and R_K are the nuclear mass, charge and spatial coordinate of nucleus K respectively, $\mathbf{r}_i$ is the spatial coordinate of electron i.

Regrettably, a coupling in the motions of the electrons and nuclei renders the solution of Eq. (1.1) with the Hamiltonian of Eq. (1.2) completely intractable for all but the simplest of systems. The goal for quantum chemistry development must turn instead to producing approximate models of the molecular Schrödinger equation that are both accurate and amenable to calculation.

This chapter details the theoretical foundations upon which the developments of the later work are grounded. First the core techniques and approximations common to most quantum chemical methods are established before the wave function methods that have been used in this work are described. The second half of the chapter is devoted to a derivation and description of the theoretical framework of density-functional theory, developments to which will form the body of this thesis.

1.1 The electronic structure problem

The following section details the approximate methods that allow the calculation of the energy and properties of molecular systems without requiring a solution to the Schrödinger equation of Eq. (1.1). The section begins by considering the powerful simplification of the Born–Oppenheimer approximation before detailing the variational principle and how it can guide approximate models towards increasing accuracy.

1.1.1 The Born–Oppenheimer approximation

The Born–Oppenheimer approximation exploits the disparity in nuclear and electron masses in order to decouple their motions and separate Eq. (1.1) into an electronic Scrödinger equation, in which the nuclear positions enter parametrically,

$$\hat{H}_{\mathrm{elec}}\Psi_{\mathrm{elec}}(\{\mathbf{x}_i;\mathbf{X}_K\}) = E_{\mathrm{elec}}\Psi_{\mathrm{elec}}(\{\mathbf{x}_i;\mathbf{X}_K\}), \tag{1.3}$$

and a nuclear Schrödinger equation,

$$\hat{H}_{\mathrm{nuc}}\Psi_{\mathrm{nuc}}(\{\mathbf{X}_K\}) = E_{\mathrm{nuc}}\Psi_{\mathrm{nuc}}(\{\mathbf{X}_K\}). \tag{1.4}$$

Following this separation the electronic Hamiltonian becomes,

$$\begin{aligned}\hat{H}_{\mathrm{elec}} &= -\frac{1}{2}\sum_{i=1}^{N}\nabla_i^2 - \sum_{i=1}^{N}\sum_{K=1}^{M}\frac{Z_K}{|\mathbf{r}_i-\mathbf{R}_K|} + \sum_{i=1}^{N}\sum_{j>i}^{N}\frac{1}{|\mathbf{r}_i-\mathbf{r}_j|} + \sum_{K=1}^{M}\sum_{L>K}^{M}\frac{Z_K Z_L}{|\mathbf{R}_K-\mathbf{R}_L|}\\ &= \hat{T}+\hat{V}_{\mathrm{Ne}}+\hat{V}_{\mathrm{ee}}+\hat{V}_{\mathrm{NN}},\end{aligned} \tag{1.5}$$

with the corresponding nuclear Hamiltonian,

$$\begin{aligned}\hat{H}_{\mathrm{nuc}} &= -\sum_{K=1}^{M}\frac{M_K}{2}\nabla_K^2 + \sum_{K}^{M}U_{\mathrm{elec}}(\mathbf{R}_K;\{\mathbf{R}_L\})\\ &= \hat{T}+U(\{\mathbf{R}_K\}),\end{aligned} \tag{1.6}$$

in which $U(\{\mathbf{R}_K\})$ is the potential energy resulting from the solution of the electronic Schrödinger equation with nuclei at positions $\{\mathbf{R}_K\}$.

The Born–Oppenheimer approximation justifies this separation through the argument that the electrons are so light in comparison to the nuclei that they adapt instantaneously to any change in nuclear positions, allowing the nuclei to appear fixed in the electronic equations. The Born–Oppenheimer separation is common to all the quantum chemical methods considered in this work and allows attention to be shifted entirely onto the electronic problem, greatly reducing the complexity of the equations. In some exceptionally simple cases, such as the Hydrogen atom, it is possible to solve the electronic Schrödinger equation analytically, though all systems of chemical interest require further approximations.

1.1.2 The variational principle

When constructing approximate electronic structure models it is important to identify what constitutes a good solution and how such a solution may be systematically improved. The variational principle is invaluable in this regard, ensuring that the expectation value of the electronic Hamiltonian of Eq. (1.5) with a trial wave function Ψ_{trial} is an upper bound to the electronic energy of the real ground state wave function Ψ_0. This identifies the lower energy wave function as the more correct wave function, and allows a systematic search to the most accurate solution as that which gives the lowest energy.

Assuming all wave functions are normalised the variational principle can be written as,

$$\left\langle \Psi_{\mathrm{trial}}\middle|\hat{H}\middle|\Psi_{\mathrm{trial}}\right\rangle = E_{\mathrm{trial}} \geq E_0 = \left\langle \Psi_0\middle|\hat{H}\middle|\Psi_0\right\rangle, \tag{1.7}$$

a proof of which is straightforward and can be found in any undergraduate physics textbook.

1.2 Hartree–Fock theory

The many electron wave function has so far been left undefined and an explicit definition is required if the energy of a molecule is to be evaluated. In Hartree–Fock (HF) theory it is chosen as a single

Slater determinant of one-electron spin orbitals. Constructing the many electron wave function in this way is the simplest approximate wave function that is still able to produce useful results and careful analysis of the omissions and deficiencies in HF theory can give important insight into more refined approximation schemes.

1.2.1 The Slater determinant

The Slater determinant at the core of HF theory is constructed as an anti-symmetrised product of one electron spin orbitals,

$$\Phi = \frac{1}{\sqrt{N!}} \det\left\{\chi_1(\mathbf{x}_1), \chi_2(\mathbf{x}_2), \ldots, \chi_N(\mathbf{x}_N)\right\}, \tag{1.8}$$

where $\chi_i(\mathbf{x})$ is a spin orbital,

$$\chi_i(\mathbf{x}) = \begin{cases} \varphi_i^{\alpha}(\mathbf{r})\alpha(\omega) \\ \varphi_i^{\beta}(\mathbf{r})\beta(\omega) \end{cases}, \tag{1.9}$$

and $\mathbf{x}$ is a combined space, $\mathbf{r}$, and spin, ω, coordinate, $(\mathbf{r}, \omega)$. The determinantal composition of the wave function is an important aspect of Hartree–Fock theory, producing a wave function that is correctly anti-symmetric under the exchange of any two electrons. By contrast, the simple Hartree product of spin orbitals is inadequate for a fermionic wave function as a product of one electron functions is not anti-symmetric under the exchange of two electrons.

The expectation value for the electronic Hamiltonian of Eq. (1.5) acting on the normalised Slater determinant wave function is,

$$E_{\mathrm{HF}} = \left\langle \Phi \middle| \hat{H} \middle| \Phi \right\rangle = \sum_{i}^{N} \left\langle i \middle| \hat{h} \middle| i \right\rangle + \sum_{i}^{N} \sum_{j=i}^{N} [ii|jj] - [ij|ji], \tag{1.10}$$

where the Hamiltonian has been partitioned into $\langle i| \hat{h} |i\rangle$, an integral over all space of spin orbital χ_i with the one electron operator $\hat{h}$,

$$\left\langle i \middle| \hat{h} \middle| i \right\rangle = \int \chi_i^*(\mathbf{x}_1) \left(\frac{1}{2}\nabla^2 - \sum_{K}^{M} \frac{Z_K}{|\mathbf{r}_i - \mathbf{R}_K|} \right) \chi_i(\mathbf{x}_1) \mathrm{d}\mathbf{x}_1. \tag{1.11}$$

The remaining $[ii|jj]$ and $[ij|ji]$ terms of Eq. (1.10) are the Coulomb and exchange integrals respectively with the Coulomb integral arising from the application of the two electron r_{ij}^{-1} operator, the 3rd term of Eq. (1.5), and the exchange integral resulting from the anti-symmetry of the determinantal wave function. The Coulomb and exchange integrals can be written as,

$$[ii|jj] = \iint \frac{\chi_i^*(\mathbf{x}_1)\chi_i(\mathbf{x}_1)\chi_j^*(\mathbf{x}_2)\chi_j(\mathbf{x}_2)}{|\mathbf{r}_1 - \mathbf{r}_2|} \mathrm{d}\mathbf{x}_1 \mathrm{d}\mathbf{x}_2, \tag{1.12}$$

$$[ij|ji] = \iint \frac{\chi_i^*(\mathbf{x}_1)\chi_j(\mathbf{x}_1)\chi_j^*(\mathbf{x}_2)\chi_i(\mathbf{x}_2)}{|\mathbf{r}_1 - \mathbf{r}_2|} \mathrm{d}\mathbf{x}_1 \mathrm{d}\mathbf{x}_2, \tag{1.13}$$

respectively.

By exploiting the variational principle of Section 1.1.2 the ground state Hartree–Fock energy for a given molecular system can be found through a variational search in the spin orbitals that comprise the Slater determinant under the constraint that they remain orthonormal,

$$\int \chi_i(\mathbf{x})\chi_j^*(\mathbf{x}) \mathrm{d}\mathbf{x} = \delta_{ij}, \tag{1.14}$$

where δ_{ij} is the Kronecker delta,

$$\delta_{ij} = \begin{cases} 0 & \text{if } i \neq j \\ 1 & \text{if } i = j \end{cases}. \tag{1.15}$$

The constrained optimisation is achieved through the method of Lagrange multipliers, producing a system of one electron equations,

$$\left\langle \chi_i \middle| \hat{f} \middle| \chi_i \right\rangle = \epsilon_i \left\langle \chi_i | \chi_j \right\rangle , \quad i = 1, 2, \ldots, N, \tag{1.16}$$

with multipliers ϵ_i that are determined to give the set of spin-orbitals that minimise E_{HF}. The matrix of Lagrange multipliers ϵ_i is diagonal, defining the *canonical* HF orbitals and orbital energies. In Eq. (1.16) the one electron Fock operator $\hat{f}_i$ was introduced as,

$$\hat{f}_i = -\frac{1}{2}\nabla^2 - \sum_K^M \frac{Z_K}{|\mathbf{r}_i - \mathbf{R}_K|} + v_{\mathrm{HF}}(\mathbf{r}_i), \tag{1.17}$$

where the first and second terms are the kinetic and nuclear attraction energies respectively of electron i moving in the potential v_{HF},

$$v_{\mathrm{HF}}(\mathbf{r}_1) = \sum_j^N (\hat{J}_j(\mathbf{r}_1) - \hat{K}_j(\mathbf{r}_1)). \tag{1.18}$$

The Coulomb operator,

$$\hat{J}_j(\mathbf{x}_1) = \int \frac{|\chi_j(\mathbf{x}_2)|^2}{|\mathbf{r}_1 - \mathbf{r}_2|} \mathrm{d}\mathbf{x}_2 \tag{1.19}$$

gives the repulsion felt by an electron at $\mathbf{r}_1$ as a result of the average charge distribution of another electron in orbital χ_j. The Coulomb repulsion is integrated over all space and spin, $\mathbf{x}_2$, such that operation of $\hat{J}_j(\mathbf{r}_1)$ on $\chi_i(\mathbf{x}_1)$ depends only on the value of χ_i at $\mathbf{r}_1$, revealing $\hat{J}$ as a local operator with a local potential.

The exchange operator corresponding to $[ij|ji]$ in Eq. (1.13) is defined by the effect of its operation on a spin orbital,

$$\hat{K}_j(\mathbf{x}_1)\chi_i(\mathbf{x}_1) = \int \frac{\chi_j^*(\mathbf{x}_2)\chi_i(\mathbf{x}_2)}{|\mathbf{r}_1 - \mathbf{r}_2|} \mathrm{d}\mathbf{x}_2 \, \chi_j(\mathbf{x}_1), \tag{1.20}$$

resulting in an exchange of variables between two spin orbitals. In contrast to the Coulomb operator of Eq. (1.19) the exchange operator depends on χ_i at all points in space and hence is a non-local potential. As a result of the orthonormality of the spin orbitals, Eq. (1.14), the integral over spin contained in Eq. (1.20) is non-zero only for electrons of like spin, giving the expected result that the exchange interaction only exists between fermions with the same spin.

None of the operators in the HF equations are spin dependent and consequently the spin component of the orbitals can be integrated out by application of the orthogonality of the spin functions $\sigma(\omega) \in \{\alpha(\omega), \beta(\omega)\}$,

$$\langle \sigma | \sigma' \rangle = \delta_{\sigma\sigma'}, \tag{1.21}$$

allowing a reduction of the spin orbitals to just the spatial components, $\varphi_i(\mathbf{r})$, in the following equations.

Careful examination of Eq. (1.10) reveals that the term $i = j$ is explicitly included within the two electron summation, having the physical interpretation of an electron interacting with itself. Clearly an electron does not repel itself, but as a result of the summation in Eq. (1.10) the Coulomb repulsion energy in a one electron system is non-zero. The paradox of self interaction is resolved by an exact cancellation of the Coulomb term by the exchange term, removing the self interaction. This elegant cancellation of self interaction terms is important to the success of the HF scheme and should be regarded as an interesting lesson for the construction of approximate local exchange functionals, discussed later in this work.

1.2.2 Restricted and unrestricted formalisms

When forming the spin orbitals $\{\chi_i\}$ a choice is presented, can electrons in the same spin orbital with different spin have different spatial orbitals? In the restricted Hartree–Fock (RHF) scheme the answer

is no and electrons in the same spin orbital are required to have the same spatial component,

$$\chi_i(\mathbf{x}) = \begin{cases} \varphi_i(\mathbf{r})\alpha(\omega) \\ \varphi_i(\mathbf{r})\beta(\omega) \end{cases} . \tag{1.22}$$

The opposite choice is made in the unrestricted Hartree–Fock (UHF) scheme, and the spatial orbitals are allowed to differ.

The RHF formalism is a good model for closed shell singlet state molecules, and reduces the computational cost of a calculation significantly by halving the number of spatial integrals required. The RHF scheme is not always the best choice however and causes a significant inaccuracy in the dissociation of closed shell molecules into open shell fragments, with electrons on separated fragments being forced to share a spatial orbital. The dissociation of H_2 is the canonical example of this failure, with RHF giving a pronounced overestimation of the dissociation energy through an overemphasis of the ionic dissociation state, $H^+ + H^-$ caused by the shared spatial function. Additionally, the RHF formalism cannot handle open shell systems at all, as each spin orbital is required to be doubly occupied. Instead the theory must be generalised to restricted open-shell Hartree–Fock theory (ROHF) [15] to account for unpaired electrons. The ROHF method is not used in this work and will not be considered further.

The more flexible UHF formalism facilitates the treatment of open shell molecules by relaxing the restriction of double occupation and allowing electrons in the same spin orbital to have different spatial functions,

$$\chi_i(\mathbf{r},\omega) = \begin{cases} \varphi_i^{\alpha}(\mathbf{r})\alpha(\omega) \\ \varphi_i^{\beta}(\mathbf{r})\beta(\omega) \end{cases} . \tag{1.23}$$

By allowing electrons in the same spin orbital to have different spatial components the UHF theory can properly describe open shell molecules and lower the energy of bond dissociation. Whilst both RHF and UHF give the same energy for H_2 when the internuclear distance is shorter than the Coulson–Fischer point [16] of $R \approx 2.3\ a_0$ at longer separations the energies split, with the UHF wave function having a lower energy than RHF. This energetic difference is exaggerated at longer ranges and only the UHF scheme attains the correct dissociation limit.

The UHF formalism achieves a lower energy dissociation curve by introducing a *spin contamination* from the lowest energy triplet configuration into the ground state wave function. This contamination by the triplet state, and consequent loss of spin purity, prevents the UHF wave function being an eigenfunction of the spin operator, $\hat{S}^2$. In contrast, the RHF method always gives a pure singlet state solution and remains an eigenfunction of $\hat{S}^2$ for all separations, at the price of an incorrect dissociation limit.

1.3 The finite basis set expansion

Evaluating the restricted Hartree–Fock equations for a given molecule requires solving the system of spatial integro-differential equations,

$$\hat{f}_i(\mathbf{r})\varphi_i(\mathbf{r}) = \epsilon_i\varphi_i(\mathbf{r}). \tag{1.24}$$

Such problems can be tackled with numerical grid methods [17,18] but doing so is too computationally demanding for all but the simplest systems. Instead it is common to discretise the problem space by using a basis set representation of the spin orbitals, giving the Roothaan–Hall equations.

1.3.1 The Roothaan–Hall equations

In the absence of a computationally tractable numerical solver for Eq. (1.24) an approximate solution can be found instead by representing the orbitals $\{\varphi_i\}$ as a combination of K basis functions, $\{\phi_\mu\}$, producing a set of algebraic equations amenable to solution by standard matrix techniques. In this

way the unknown molecular orbitals are expressed linear combinations of the basis functions in terms of a matrix of expansion coefficients $\mathbf{C}$,

$$\varphi_i = \sum_{\nu=1}^{K} C_{\nu i}\phi_\nu \quad i = 1, 2, \ldots, K. \tag{1.25}$$

Using this finite basis representation, multiplying Eq. (1.24) on the left by ϕ_μ and integrating over all space reduces the complicated integro-differential equations of Eq. (1.24) to the set of matrix equations,

$$\sum_\nu C_{\nu i} \int \phi_\mu^*(\mathbf{r})\hat{f}\phi_\nu(\mathbf{r})\mathrm{d}\mathbf{r} = \epsilon_i \sum_\nu C_{\nu i} \int \phi_\mu^*(\mathbf{r})\phi_\nu(\mathbf{r})\mathrm{d}\mathbf{r}. \tag{1.26}$$

These equations are simplified by the introduction of the overlap matrix $\mathbf{S}$,

$$S_{\mu\nu} = \int \phi_\mu^*(\mathbf{r})\phi_\nu(\mathbf{r})\mathrm{d}\mathbf{r} \tag{1.27}$$

and the Fock matrix $\mathbf{F}$,

$$F_{\mu\nu} = \int \phi_\mu^*(\mathbf{r})\hat{f}\phi_\nu(\mathbf{r})\mathrm{d}\mathbf{r}. \tag{1.28}$$

giving the matrix expression of Eq. (1.24) in a finite basis as,

$$\mathbf{FC} = \mathbf{SC}\boldsymbol{\epsilon}, \tag{1.29}$$

where $\boldsymbol{\epsilon}$ is the diagonal matrix of orbital energies ϵ_i for the canonical HF orbitals.

The solution of Eq. (1.29) requires an expression for the Fock matrix $\mathbf{F}$ from the Fock operator, Eq. (1.17), in terms of the basis functions $\{\phi_\mu\}$ and coefficient matrix $\mathbf{C}$. To this end we introduce the electron density function,

$$\rho(\mathbf{r}) = 2\sum_a^{N/2} |\varphi_a(\mathbf{r})|^2, \tag{1.30}$$

determined in the finite basis representation from the density matrix $\mathbf{P}$,

$$P_{\mu\nu} = 2\sum_a^{N/2} C_{\mu a}C_{\nu a}^*, \tag{1.31}$$

as,

$$\rho(\mathbf{r}) = \sum_{\mu\nu} P_{\mu\nu}\phi_\mu(\mathbf{r})\phi_\nu^*(\mathbf{r}). \tag{1.32}$$

Using the density matrix $\mathbf{P}$ the Fock matrix of Eq. (1.28) can be expressed as

$$F_{\mu\nu} = H_{\mu\nu}^{\mathrm{core}} + \sum_i^{N/2} 2(\mu\nu|ii) - (\mu i|i\nu), \tag{1.33}$$

where the Fock matrix has been partitioned by identifying the first two terms of Eq. (1.17) as the *core Hamiltonian* matrix,

$$H_{\mu\nu}^{\mathrm{core}} = T_{\mu\nu} + V_{\mu\nu}^{\mathrm{nuc}}, \tag{1.34}$$

comprised of the kinetic and nuclear attraction matrices, $\mathbf{T}$ and $\mathbf{V}^{\mathrm{nuc}}$, respectively,

$$T_{\mu\nu} = -\frac{1}{2}\int \phi_\mu^*(\mathbf{r})\nabla^2\phi_\nu(\mathbf{r})\mathrm{d}\mathbf{r}, \tag{1.35}$$

$$V_{\mu\nu}^{\mathrm{nuc}} = \int \phi_\mu^*(\mathbf{r})\left[-\sum_K \frac{Z_K}{|\mathbf{r}-\mathbf{R}_K|}\right]\phi_\nu(\mathbf{r})\mathrm{d}\mathbf{r}. \tag{1.36}$$

The remaining term is identified as the two electron integral matrix, $\mathbf{G}$, that is implicitly dependent on $\mathbf{C}$ through $\mathbf{P}$,

$$G_{\mu\nu} = \sum_{\lambda\sigma} P_{\lambda\sigma}[(\mu\nu|\sigma\lambda) - \frac{1}{2}(\mu\lambda|\sigma\nu)]. \tag{1.37}$$

Close inspection of Eq. (1.37) shows that constructing the two electron integral matrix requires (with correct use of permutational symmetry) $K^4/8$ two electron integral evaluations,

$$(\mu\nu|\lambda\sigma) = \iint \frac{\phi_\mu^*(\mathbf{r}_1)\phi_\nu(\mathbf{r}_1)\phi_\lambda^*(\mathbf{r}_2)\phi_\sigma(\mathbf{r}_2)}{r_{12}} \mathrm{d}\mathbf{r}_1\mathbf{r}_2. \tag{1.38}$$

The quartic scaling in the number of two electron integrals renders this evaluation the most computationally expensive step in a finite basis HF calculation. Fortunately, Eq. (1.38) does not depend on $\mathbf{P}$ and hence it cannot change throughout the course of the calculation.

The fact that the two electron integrals do not change during a calculation introduces an operation-memory trade-off when optimising of an implementation of the HF scheme. Either the two electron integrals are calculated at the start of the calculation and stored in memory, saving on operations at the expense of memory, or they can be re-evaluated as needed, reducing the memory requirements at the expense of repeating integral evaluation work. The evaluation and storage of the two electron integrals can be optimised further in large systems by noting the negligible overlap integral of spatially separated orbitals and exploiting the resulting sparsity of $\mathbf{G}$. Naturally the choice between integral storage and direct calculation is system and hardware dependent, though a direct approach is usually required for larger systems.

Expansion of the molecular orbitals in a set of basis functions is not an approximation if the basis set $\{\phi_\mu\}$ is complete and the molecular orbitals are represented exactly. For all but the simplest molecular cases however this is not possible and an incomplete set must be employed to obtain an approximation of the molecular orbitals that is as accurate as possible whilst remaining computationally tractable. It is theoretically pleasing to use atom centred Slater type orbitals (STO) as the basis functions in molecular calculations as these orbitals are the exact orbitals for the hydrogen atom and have correct nuclear cusp and decay behaviours. An STO function can be written as,

$$\phi^{\mathrm{STO}}(\mathbf{r};\mathbf{R}) = (R_x - r_x)^l \cdot (R_y - r_y)^m \cdot (R_z - r_z)^n \cdot e^{-\alpha|\mathbf{R}-\mathbf{r}|}, \tag{1.39}$$

with the exponent α controlling how diffuse the function is, and $l+m+n$ giving the orbital angular momentum. In practice however, evaluation of Eq. (1.38) with STO functions is difficult and requires numerical techniques, preventing the widespread practical use of STO basis sets. Instead it is common to use a larger basis set of Gaussian type orbitals (GTO) chosen to approximate an STO,

$$\phi^{\mathrm{GTO}}(\mathbf{r};\mathbf{R}) = (R_x - r_x)^l \cdot (R_y - r_y)^m \cdot (R_z - r_z)^n \cdot e^{-\alpha|\mathbf{R}-\mathbf{r}|^2}. \tag{1.40}$$

The use of GTO functions allows the analytical evaluation of Eq. (1.38) by application of the Gaussian product rule, drastically reducing the computational cost of constructing the two electron integrals. The faster integral evaluation for GTO functions is a trade-off however as the incorrect cusp and decay properties of GTO functions mean many more GTO than STO basis functions are required to give the same quality basis. In general the faster evaluation of GTO two electron integrals more than compensates for the greater number, and in this work all calculations have been carried out with atom centred GTO basis sets.

Many GTO basis sets have been suggested over the years with the values of α optimised on a per atom basis to give the best possible performance using the minimal number of functions. A number of basis set series have been proposed that allow for a systematic increase in accuracy through an expansion in overall size and the addition of higher angular momentum functions [19,20]. In particular the basis sets of Dunning [20] are used extensively throughout this work.

The computational cost associated with a GTO basis set can be further reduced by forming a *contracted set* of GTOs in which a number of *primitive* GTO functions are collected together as a fixed linear combination. Forming contractions reduces computational cost once the integrals of Eqs. (1.35-1.38) have been evaluated as all subsequent steps in the calculation scale with the number of basis functions, rather than primitives. Clearly the contracted set of GTOs is less flexible than handling the primitives separately, but the contracted set of GTOs allows for a higher quality basis set than simple GTO functions at a similar computational cost.

The preceding discussion of the finite basis representation has only considered the RHF formalism, and a modification to the UHF case is straightforward, resulting in the Pople–Nesbet equations. The UHF generalisation is not discussed here and the reader is referred to [21] for a full derivation.

1.3.2 The self consistent field procedure

The Roothaan–Hall equations of Eq. (1.29) can be solved within a suitably orthogonalised basis set representation[1] to find the molecular orbitals that minimise the Hartree–Fock equations for the given basis. A simple evaluation of Eq. (1.29) is not possible as the left and right sides are coupled through the dependence of $\mathbf{F}$ on $\mathbf{P}$ and hence $\mathbf{C}$,

$$\mathbf{FC} = \mathbf{C}\boldsymbol{\epsilon}, \tag{1.41}$$

forming a highly non-linear set of equations that must instead be solved using the iterative self consistent field (SCF) method. At its core the SCF procedure consists of constructing a Fock matrix from the current density matrix and diagonalising it to produce a new set of molecular orbitals and eigenvalues. A new density matrix and Fock matrix can then be constructed from the new MOs, and the process repeated until the density matrix no longer changes between iterations and the equations are self consistent.

In a practical SCF calculation the system of interest is specified as a set of nuclear co-ordinates $\{\mathbf{R}_K\}$, nuclear charges $\{Z_K\}$, number of electrons N and a basis set $\{\phi_\mu\}$. The required integrals, $S_{\mu\nu}$, $H_{\mu\nu}^{\text{core}}$ and $(\mu\nu|\lambda\sigma)$ are evaluated and (if requested) stored for future use. A suitable guess density is constructed and the initial Fock matrix is built from $\mathbf{P}^{\text{guess}}$ and the two electron integrals $(\mu\nu|\lambda\sigma)$ and then diagonalised to produce a new set of molecular orbital coefficients $\mathbf{C}'$, eigenvalues $\boldsymbol{\epsilon}$ and density matrix $\mathbf{P}'$. A new Fock matrix, $\mathbf{F}'$ is built from $\mathbf{P}'$ by occupying the $N/2$ orbitals with lowest eigenvalues (orbital energies), a choice known as the aufbau principle. The process is then repeated until a convergence criteria is met. The aufbau principle occupation criteria usually gives convergence to the ground state, but is not the only occupation scheme possible. Alternative occupation schemes are necessary for calculations of excited state configurations, and are discussed in the context of molecules in magnetic fields in Chapter 5.

It is common practice to form the initial guess density matrix by evaluating an uncoupled version of Eq. (1.41) with $\mathbf{F} = \mathbf{H}^{\text{core}}$ to give the molecular orbitals for an equivalent system with no electron-electron interactions. The core Hamiltonian guess density matrix is usually a suitable starting point and generally allows a smooth convergence of the SCF cycle, though many alternative guess density schemes are available that may require fewer iterations to converge and give smoother convergence for difficult systems [22, 23].

In most cases the procedure outlined above is sufficient to converge the density matrix and solve the Roothaan–Hall equations. As with any self consistent procedure however, there is no guarantee of convergence, and even if convergence is possible it may take an unacceptably large number of iterations. A number of schemes have been proposed to accelerate the convergence of the SCF procedure, the most popular of which is the direct inversion of the iterative subspace (DIIS) scheme of Pulay [24, 25] which has been used throughout this work.

1.4 Beyond Hartree–Fock theory

If the Hartree–Fock scheme of Section 1.3 is iterated to self consistency then the converged orbitals and eigenvalues produced will be exact (to within the basis set) for any system where the real electronic wave function is a single Slater determinant. This is only the case for one electron systems and in general a single determinant wave function is an approximation to the real wave function. Therefore, as a consequence of the variational principle, the Hartree–Fock scheme can only ever give an upper bound to the true electronic energy, giving a definition of the correlation energy as the difference between the Hartree–Fock solution and the exact ground state electronic energy,

$$E_c = E_0 - E_0^{\text{HF}}, \tag{1.42}$$

the Löwdin definition of correlation energy [26].

Despite completely neglecting the multi-determinantal character of the exact many electron wave, function Hartree–Fock theory gives surprisingly good accuracy, qualitatively reproducing many chemically interesting phenomena. The neglect of correlation energy remains a limitation however and

[1] Such that $\mathbf{S} = \mathbf{I}$, see for example Szabo and Ostlund [21] for details of appropriate orthogonalisation schemes.

prevents the method giving a useful accuracy for the majority of systems of chemical interest. The remainder of this section details methods for systematically recovering increasing portions of the correlation energy by expanding a multi-determinantal wave function from a Hartree–Fock reference.

1.4.1 Configuration interaction

The configuration interaction (CI) method recovers the correlation energy of a molecular system by forming a linear combination of N-electron Slater determinants as excitations from a Hartree–Fock reference, producing the exact many electron wave function for a basis set when all excitations are considered. The CI method gives a conceptually simple, but computationally demanding, means for calculating the full electronic energy and if a complete basis is employed, the full configuration interaction (FCI) expansion gives the exact electronic energy of the system. As FCI gives the exact electronic energy for the basis set the method can be used to make benchmark data against which less computationally expensive schemes can be compared, and is especially useful in situations where a comparison against experiment is difficult or impossible.

Consider a set of $2K$ molecular orbitals, $\{\varphi_i\}$, obtained by solving the Roothaan–Hall equations and the Slater determinant constructed from the N lowest orbitals, the Hartree–Fock ground state wave function $|\Psi_0\rangle$. The next set of determinants in the CI series can be constructed as the Slater determinants corresponding to all possible excitations of a single electron into a higher energy orbital. This corresponds to replacing $\{\varphi_i\}$ with $\{\varphi_a\}$, to form $\{|\Psi_i^a\rangle\}$, where the indices $\{i, j, k, \ldots\}$ denote occupied HF orbitals and $\{a, b, c, \ldots\}$ denote the virtual orbitals. This process is repeated for double excitations, $\{\left|\Psi_{ij}^{ab}\right\rangle\}$, and the series is continued up to the N-tuply excited determinants. The FCI ground state wave function, $|\Phi_0\rangle$, is then constructed as a linear combination of these determinantal wave functions with the expansion coefficients optimised using the variation principle. Thus, the FCI wave function can be written as,

$$|\Phi_0\rangle = c_0 |\Psi_0\rangle + \sum_{ia} c_i^a |\Psi_i^a\rangle + \sum_{ijab} c_{ij}^{ab} \left|\Psi_{ij}^{ab}\right\rangle + \cdots , \tag{1.43}$$

with permutational symmetry factors included into the expansion coefficients. It is often more convenient to express Eq. (1.43) in the symbolic form,

$$|\Phi_0\rangle = c_0 |\Psi_0\rangle + c_S |S\rangle + c_D |D\rangle + \cdots , \tag{1.44}$$

with $|S\rangle$ denoting the singly excited determinants, $|D\rangle$ denoting the doubly excited and so on throughout the expansion.

The FCI matrix is constructed from the expansion of Eq. (1.44) by application of the electronic Hamiltonian operator to the FCI wave function, $\langle\Phi_0| \hat{H} |\Phi_0\rangle$, and can be diagonalised to find the FCI eigenvalues and natural orbitals. The lowest eigenvalue of the FCI matrix is the ground state electronic energy and the higher eigenvalues correspond to the excited states of the system. In this way the difference between the lowest FCI eigenvalue and the Hartree–Fock energy defines the correlation energy in the basis set. The remaining difference between the FCI energy and the real electronic energy can only be retrieved by increasing the basis set span.

With an exact solution to the finite basis molecular Schrödinger equation provided by the FCI expansion it is tempting to think that quantum chemistry is solved. However the extreme increase in computational complexity associated with increasing system size prevents the use of FCI for all but the simplest of systems. A common strategy to reduce the computational complexity is to limit the number of determinants that must be considered by truncating the CI expansion at a certain level, singles and doubles only for example, drastically reducing the number of excitations that must be considered at the cost of recovering less of the correlation energy. An alternative approach is to restrict the active space of the configuration interaction by considering some orbitals as frozen or to remove the very high energy virtual orbitals from the reference set, in both cases reducing the number of excitations.

Within this work the FCI method is used to provide exact benchmark energies against which new approximate methods can be compared. In Section 3.5 an implementation of FCI generalised for the

presence of external magnetic fields [27] is used to provide benchmark interaction energy profiles for H_2 and He_2 and is used again in Section 5 to benchmark excited states in a magnetic field calculated using the maximum overlap method.

1.4.2 Coupled-cluster methods

In practice it is necessary to truncate the CI expansion, even for small systems, typically considering only the single and double excitations (CISD). A truncation of the CI expansion breaks *size consistency* however, meaning truncated CI calculations are not equally accurate for two sub-systems that are far apart as the same sub-systems calculated separately. In addition to breaking size consistency, truncated CI methods are not *size extensive*, with the errors caused by the truncation becoming worse as system size increases. Such size dependent errors are apparent at any level of truncation and are only completely avoided when the full CI expansion is considered, presenting a major flaw for general chemical applications. A detailed discussion of the origin of the size dependent behaviour of truncated CI methods can be found in Ref. [28].

The size consistency and extensivity problems seen in truncated CI methods are solved in an alternate multi-determinant approach termed coupled-cluster (CC) theory. Coupled-cluster methods allow for a similar systematic approach to the finite basis limit whilst retaining size consistent and extensive behaviour when truncated. The price paid for correct size dependency is a loss of strict variational behaviour in the truncated CC series, allowing calculated energies to fall below the real ground state value. The full CC expansion is exactly equivalent to FCI however, and similarly gives the exact electronic energy for the chosen basis set.

The CC method determines the correlation energy by considering electronic excitations, but differs from CI by generating the excitations through application of the exponential cluster operator,

$$\exp[\hat{T}] = 1 + \hat{T} + \frac{1}{2!}\hat{T}^2 + \frac{1}{3!}\hat{T}^3 + \ldots = \sum_{\lambda=0}^{N} \frac{1}{\lambda!}\hat{T}^{\lambda}, \tag{1.45}$$

where $\hat{T}$ is the excitation operator. The excitation operator produces the excited states from a Hartree–Fock reference determinant as,

$$\begin{aligned}\hat{T}\Psi_0 &= (\hat{T}_1 + \hat{T}_2 + \ldots)\Psi_0 \\ &= \sum_{ia} t_i^a \Psi_i^a + \sum_{\substack{i>j \\ a>b}} t_{ij}^{ab} \Psi_{ij}^{ab} + \ldots,\end{aligned}$$

where $i, j, \ldots$ and $a, b, \ldots$ sum over the occupied and virtual states respectively and the weights $t_{i\ldots}^{a\ldots}$ are termed the cluster amplitudes. The ground state energy is then found by varying the cluster amplitudes to minimise the electronic energy.

The key advantage of the cluster operator over the simple CI excitations is that the correct size consistent and size extensive behaviour is maintained when the excitation series is truncated. The origin of the size consistency in CC is most clearly seen by considering a CC series truncated at the singles and doubles level, CCSD, giving the excitation operator $\hat{T}_{\text{SD}} = \hat{T}_1 + \hat{T}_2$. Application of the CCSD cluster operator to the Hartree–Fock reference determinant Ψ_0 leads to,

$$\begin{aligned}\Phi_{\text{CCSD}} &= \exp[\hat{T}_1 + \hat{T}_2]\Psi_0 \\ &= \left(1 + \hat{T}_1 + \hat{T}_2 + \frac{1}{2}\hat{T}_1^2 + \hat{T}_1\hat{T}_2 + \frac{1}{2}\hat{T}_2^2\right)\Psi_0 \\ &= \Psi_0 + \sum_{ia} t_i^a \Psi_i^a + \sum_{ij}^{ab} t_{ij}^{ab} \Psi_{ij}^{ab} + \frac{1}{2}\sum_{i}^{a} t_i^a \sum_{j}^{b} t_j^b \Psi_{ij}^{ab} + \\ &\quad \sum_{i}^{a} t_i^a \sum_{jk}^{bc} t_{jk}^{bc} \Psi_{ijk}^{abc} + \frac{1}{2}\sum_{ij}^{ab} t_{ij}^{ab} \sum_{kl}^{cd} t_{kl}^{cd} \Psi_{ijkl}^{abcd}\end{aligned} \tag{1.46}$$

The terms of $\hat{T}$ are collected into two categories, the connected clusters, $\hat{T}_n^{\lambda}$, that are similar to the excitations of CI theory, and the disconnected clusters which appear as the product terms, $\hat{T}_m\hat{T}_n$,

which are absent in CI and enforce the size consistency of the truncated CC series. Although a truncated CC expansion is not strictly variational practical application has established the reliable accuracy of truncated CC methods.

In practical calculations the CC expansion is typically truncated at the singles and doubles level, giving CCSD, which scales in computational complexity as $O(N^6)$ and is applicable to moderately sized systems. The next level of truncation is achieved by including the triple excitations to give CCSDT with an associated scaling of $O(N^8)$, quickly becoming too computationally demanding for most applications. Instead it is common to treat the energetic contributions of the triple excitations via perturbation theory, termed CCSD(T) theory which scales as $O(N^7)$. The CCSD(T) approach has become the workhorse of high accuracy quantum chemistry calculations and is frequently employed to generate high accuracy of benchmark data for systems that are too large for FCI.

Within this work CCSD(T) has been used to generate benchmark magnetic response properties and strong field interaction curves against which CDFT functionals could be compared.

1.5 Density-functional theory

The methods discussed in Section 1.4 give a systematic route to a complete description of non-relativistic Born–Oppenheimer systems through increasingly sophisticated many electron wave functions. The application of such methods to the larger molecules found in nature is made difficult however by the enormous computational effort required for their operation, though much advancement has been made in reducing these costs. With the prohibitive scaling in cost associated with more precise wave functions it is natural to search for an alternative foundation upon which quantum chemical models may be built.

Work to this effect began in the 1920s when Thomas and Fermi independently presented a quantum mechanical theory for the electronic structure of many-electron systems using the electron density as the basic variable, rather than a wave function. The theory was grossly limited and unable to even qualitatively account for basic features like electron shell structure or molecular bonding. Despite these shortcomings the Thomas–Fermi model stands as the precursor to the more developed density functional theory that has been built upon a rigorous definition of the electronic density function, $\rho(\mathbf{r})$, as its basic variable.

The electron density, $\rho(\mathbf{r})$, is constructed from the many electron wave function as

$$\rho(\mathbf{r}) = N \int \cdots \int |\Psi(\mathbf{r}_1, \ldots, \mathbf{x}_N)|^2 \mathrm{d}\sigma_1, \mathrm{d}\mathbf{x}_2, \ldots, \mathrm{d}\mathbf{x}_N, \tag{1.47}$$

where σ_i is the spin coordinate for electron i.

The electron density function is a scalar field of three dimensional space and a quantised measure of spin, α or β. Therefore a complete description of any system through the electron density requires only 4 variables, an enormous improvement over the $4N$ coordinates required by the many electron wave function. With electron density based methods suggesting pronounced computational advantages there was a clear incentive for a density-functional quantum theory and the foundations for such a therory were laid down in the seminal 1964 work of Hohenberg and Kohn [1] outlining key connections and showing the validity of the electron density model. This publication established the core of density-functional theory (DFT) from which Kohn and Sham [29] developed a system of DFT equations amenable to practical calculation. Since this beginning Levy [30] and Lieb [14] have refined the Hohenberg–Kohn arguments to carefully describe the densities and potentials that can be studied, and presented the constrained search formulation and convex analysis to place DFT on solid mathematical ground. The remainder of this chapter reviews these foundations to provide the appropriate background for the extensions to DFT discussed later in the thesis.

1.5.1 The Rayleigh–Ritz variational principle

Consider the non-relativistic spin-free Hamiltonian outlined in Section 1.1.1 for N electrons in the external potential $v(\mathbf{r})$,

$$\hat{H}_N[v] = \hat{T}_N + \hat{W}_N + \sum_{i=1}^{N} v(\mathbf{r}_i). \tag{1.48}$$

It is immediately apparent from Eq. (1.48) that the only element of the molecular Hamiltonian that distinguishes one N electron system from any other is the functional dependence upon an external potential, $v(\mathbf{r})$. The kinetic, $\hat{T}_N$, and two electron repulsion, $\hat{W}_N$, operators are universal to all N electron systems, a universality that is key to the arguments of the following section.

We shall require that $v(\mathbf{r})$ enter Eq. (1.48) as a multiplicative potential that belongs to the set of *ρ-representable* potentials defined as

$$\mathcal{V}_N : \left\{ v \,\middle|\, \hat{H}_N[v] \text{ has an } N \text{ electron ground state } \Psi_v \right\}, \tag{1.49}$$

By restricting attention to potentials in $\mathcal{V}_N$ the existence of a ground state energy is guaranteed such that,

$$\hat{H}_N[v]\,\Psi_v = E_0[v]\,\Psi_v, \;\; \forall v \in \mathcal{V}_N \tag{1.50}$$

which defines the ground state energy E_0 as a mapping of the ρ-representable potentials to the real numbers as ground state electronic energies,

$$E_0 : \mathcal{V}_N \mapsto \mathbb{R}. \tag{1.51}$$

Similarly, let $\mathcal{W}_N$ be the set of all normalised anti-symmetric N electron wave functions for which $\hat{H}_N[v]$ has a finite expectation value. In order to form a variation principle in Ψ_v and prove a ground state mapping we will make use of the Rayleigh–Ritz variation principle,

Theorem 1.5.1 (The Rayleigh–Ritz variation principle)**.** *For all pairs,* $(v, \Psi) \in \mathcal{V}_N \times \mathcal{W}_N$*,*

$$E_0 \leq \left\langle \Psi \middle| \hat{H}_N[v] \middle| \Psi \right\rangle. \tag{1.52}$$

For each $v \in \mathcal{V}_N$ *one or more ground states* $\Psi_v \in \mathcal{W}_N$ *exists as the global minimiser with ground state energy* E_0*,*

$$E_0[v] = \left\langle \Psi_v \middle| \hat{H}_N[v] \middle| \Psi_v \right\rangle, \;\; \Psi_v \in \underset{\Psi \in \mathcal{W}_N}{\operatorname{argmin}} \left\langle \Psi \middle| \hat{H}_N[v] \middle| \Psi \right\rangle. \tag{1.53}$$

The proof of Theorem 1.5.1 can be found in, for example, Ref. [31], and makes no assumptions about degeneracy. As such, Theorem 1.5.1 holds for any case in which Ψ_v can be chosen as a linear combination of N-fold degenerate ground state eigenfunctions.

As we shall see, the density functional theory of Hohenberg–Kohn requires the existence of the Rayleigh–Ritz variational principle in its construction and thus requires that all potentials be elements of $\mathcal{V}_N$. This restriction is lifted by the work of Levy and Lieb and is discussed in Section 1.5.5.

1.5.2 Gauge transformations of the potential

Consider the effect of introducing a constant shift to the potential v_0 in the form of the simple gauge transformation: the addition of a scalar c,

$$v_0 \to v' = v_0 + c, \;\; v \in \mathcal{V}_N, \;\; c \in \mathbb{R}. \tag{1.54}$$

Under this transformation the corresponding ground state energy changes by,

$$E_0[v_0 + c] = E_0[v_0] + Nc, \quad \forall c \in \mathbb{R}. \tag{1.55}$$

The appearance of $E_0[v_0]$ on the right hand side shows, through Theorem 1.5.1, that the ground state wave function is unaffected by the transformation and hence v' remains in $\mathcal{V}_N$.

The next obvious step is to ask what other interesting transformations can be made in the potential and how are the wave functions and ground state energies changed as a result? By exploring these transformations a striking relationship is proved: two external potentials that differ by more than an additive constant cannot share a common ground state wave function and cannot have the same ground state density. The first Hohenberg–Kohn theorem is a formal statement of this, and is derived in Section 1.5.3.

To understand how $E_0[v]$ changes when v is transformed by more than a constant addition we must understand how the wave function changes. To this effect, consider two N-electron systems with potentials v_1, $v_2 \in \mathcal{V}_N$ that have a common normalised ground state wave function

$$\Psi_0 = \Psi_{v_1} = \Psi_{v_2} \tag{1.56}$$

As in Theorem 1.5.1 no assumptions have been made about the degeneracy of these wave functions, and they may be comprised of a linear combination of degenerate ground states. The equation describing the energy difference between these systems is,

$$(\hat{H}_N[v_1] - \hat{H}_N[v_2])\Psi_0 = \sum_i [v_1(\mathbf{r}_i) - v_2(\mathbf{r}_i)]\Psi_0 = (E_0[v_1] - E_0[v_2])\Psi_0, \tag{1.57}$$

and dividing through by Ψ_0 gives, [2]

$$\sum_i [v_1(\mathbf{r}_i) - v_2(\mathbf{r}_i)] = E_0[v_1] - E_0[v_2], \tag{1.58}$$

showing that v_1 and v_2 can only differ by a constant. Consequently, it has been shown that any potentials that differ by more than the addition of a constant must give linearly independent wave functions.

Theorem 1.5.2. *Any pair of potentials $v_1, v_2 \in \mathcal{V}_N$ that differ by more than a constant shift must give rise to linearly independent wave functions,*

$$v_1 \neq v_2 + c \Rightarrow \Psi_{v_1} \neq \Psi_{v_2},\ v_1, v_2 \in \mathcal{V}_N. \tag{1.59}$$

1.5.3 The first Hohenberg–Kohn theorem

As a consequence of Theorem 1.5.2 all energies, and hence properties, of a system are uniquely determined by the external potential v through the Hamiltonian operator of Eq. (1.48).

Consider $v_0 \in \mathcal{V}_N$ with ground state wave function Ψ_0 and ground state density ρ_0, and another potential $v \in \{v \,|\, v \in \mathcal{V}_N,\, v \neq v_0 + c,\, c \in \mathbb{R}\}$, with Hamiltonian $\hat{H}_N[v]$ and ground state wave function Ψ_v. Then, by Theorem 1.5.2, Ψ_0 is linearly independent from Ψ_v.

Invoking the Rayleigh-Ritz variation principle of Theorem 1.5.1 shows that

$$\left\langle \Psi_v \middle| \hat{H}_N[v] \middle| \Psi_v \right\rangle \leq \left\langle \Psi_0 \middle| \hat{H}_N[v] \middle| \Psi_0 \right\rangle \tag{1.60}$$

and using the linearity of the Hamiltonian, $\hat{H}_N[v_0] - \hat{H}_N[v] = \sum_i [v_0(\mathbf{r}_i) - v(\mathbf{r}_i)]$, it is shown that,

$$E_0[v] \leq \left\langle \Psi_0 \middle| \hat{H}_N[v_0] \middle| \Psi_0 \right\rangle + \int (v - v_0)\rho_0(\mathbf{r})\mathrm{d}\mathbf{r} \tag{1.61}$$

$$\leq E_0[v_0] + \int (v - v_0)\rho_0(\mathbf{r})\mathrm{d}\mathbf{r}, \tag{1.62}$$

proving the ground state is strictly concave in the external potential. Such concavity ensures that the change in ground state energy accompanying a change in external potential is strictly less than the linear change that results from the same change with a fixed wave function.

[2] Clearly this division is problematic in regions where $\Psi_0 = 0$. As the ground state wave functions of the Coulomb systems encountered in quantum chemistry are only 0 in infinitesimal regions the problem is avoided.

From the above relations it follows that if ρ_0 is a ground state density associated with $v_0 \in \mathcal{V}_N$ then,

$$E_0[v] = E_0[v_0] + \int (v - v_0)\rho_0(\mathbf{r})\mathrm{d}\mathbf{r}, \quad \text{for all } v = v_0 + c, v \in \mathcal{V}_N, c \in \mathbb{R}, \tag{1.63}$$

$$E_0[v] < E_0[v_0] + \int (v - v_0)\rho_0(\mathbf{r})\mathrm{d}\mathbf{r}, \quad \text{for all } v \neq v_0 + c, v \in \mathcal{V}_N, c \in \mathbb{R}, \tag{1.64}$$

showing that two external potentials that differ by more than a constant cannot have a common ground state density and that the ground state energy is concave with respect to a non-constant change in the external potential. No assumptions have been made about the degeneracy of the ground state so Eq. (1.63) and Eq. (1.64) hold for all pairs of potentials in $\mathcal{V}_N$.

A further interpretation of the Hohenberg–Kohn theorem is reached by applying the relationship in Eq. (1.64) to two densities, ρ_1, ρ_2 corresponding to potentials $v_1, v_2 \in \mathcal{V}_N$ where $v_1 \neq v_2 + c$ yielding,

$$E_0[v_1] < E_0[v_2] + \int (v_1 - v_2)\rho_2(\mathbf{r})\mathrm{d}\mathbf{r} \tag{1.65}$$

$$E_0[v_2] < E_0[v_1] - \int (v_1 - v_2)\rho_1(\mathbf{r})\mathrm{d}\mathbf{r}, \tag{1.66}$$

which can be rearranged to,

$$\int (v_1 - v_2)(\rho_1(\mathbf{r}) - \rho_2(\mathbf{r}))\mathrm{d}\mathbf{r} < 0. \tag{1.67}$$

The two densities have been obtained from the ground state wave functions of $\hat{H}_N[v_1]$ and $\hat{H}_N[v_2]$ with $v_1, v_2 \in \mathcal{V}_N$ and as such belong to the set of *v-representable densities*. Defined as

$$\mathcal{A}_N = \{\rho \mid \rho \text{ from } N \text{ electron ground state of } \hat{H}_N[v],\ v \in \mathcal{V}_N\} \tag{1.68}$$

Using this definition the first Hohenberg-Kohn theorem is,

Theorem 1.5.3 (The First Hohenberg-Kohn theorem)**.** *A ground state density, degenerate or otherwise, $\rho_0 \in \mathcal{A}_N$ determines the external potential $v \in \mathcal{V}_N$ uniquely up to a constant.*

$$\rho_0 \to v \to \hat{H}_N \to \Psi_0 \to E_0 \tag{1.69}$$

A closer inspection of Eq. (1.67) reveals that a stronger interpretation of the first Hohenberg-Kohn theory can be made showing a correlation between changes in v and ρ: if one increases, the other must decrease.

$$\int \nabla v \nabla \rho \, \mathrm{d}\mathbf{r} < 0 \tag{1.70}$$

1.5.4 The second Hohenberg–Kohn theorem

Theorem 1.5.3 set out in Section 1.5.3 was the first major achievement of the seminal paper of 1964. Within the same publication Hohenberg and Kohn also proved a variation principle for density-functional theory, analogous to the variation principle of Section 1.1.2.

The variational principle argument begins by setting $\rho_0 = \rho$ and $v_0 = v_\rho$ in Eq. (1.63) and Eq. (1.64) to give the non-strict inequality,

$$E_0[v] \leq E_0[v_\rho] - (v_\rho|\rho) + (v|\rho), \tag{1.71}$$

where $(v|\rho)$ denotes $\int v(\mathbf{r}) \cdot \rho(\mathbf{r})\mathrm{d}\mathbf{r}$. The Hohenberg-Kohn universal density functional is then defined as the mapping of a v-representable density to a real number,

$$\begin{aligned} E_0[v] &\leq \mathrm{F}_{\mathrm{HK}}[\rho] + (v|\rho) \\ \mathrm{F}_{\mathrm{HK}}[\rho] &= E_0[v_\rho] - (v_\rho|\rho) \end{aligned} \tag{1.72}$$

where the potential $v_\rho \in \mathcal{V}_N$ is associated with the density $\rho \in \mathcal{A}_N$. The universal functional is possible because (as guaranteed by the first Hohenberg–Kohn theorem) ρ uniquely defines v_ρ to within a scalar and the term $E_0[v_\rho] - (v_\rho|\rho)$ is invariant to such an addition.

Introducing Eq. (1.72) into Eq. (1.71) results in two inequalities that are valid for all pairs $(\rho, v) \in \mathcal{V}_N \times \mathcal{A}_N$,

$$E_0[v] \leq \mathrm{F}_{\mathrm{HK}}[\rho] + (v|\rho) \tag{1.73}$$

$$\mathrm{F}_{\mathrm{HK}}[\rho] \geq E_0[v] - (v|\rho). \tag{1.74}$$

By the definition of $\mathcal{V}_N$ each ρ-representable potential has at least one conjugate density and likewise, each v-representable density has an associated conjugate potential. As a result the inequalities of Eq. (1.73) and Eq. (1.74) can be sharpened to an equality by minimising or maximising the right hand side with respect to the appropriate arguments. Doing so produces two variational principles, the Hohenberg-Kohn variational principle for $E_0[v]$, and a variational principle for $F[\rho]$, termed the Lieb variational principle (for reasons that will become apparent in Section 1.5.6).

Theorem 1.5.4 (The Hohenberg-Kohn and Lieb Variational Principles.)**.** *The ground-state energy* $E_0 : \mathcal{V}_N \mapsto \mathbb{R}$ *and universal density functional* $\mathrm{F}_{\mathrm{HK}} : \mathcal{A}_N \mapsto \mathbb{R}$ *are related as*

$$E_0[v] = \min_{\rho \in \mathcal{A}_N} [\, \mathrm{F}_{\mathrm{HK}}[\rho] + (v|\rho)] \qquad [\textit{HK variational principle}] \tag{1.75}$$

$$\mathrm{F}_{\mathrm{HK}}[\rho] = \max_{v \in \mathcal{V}_N} [\, E_0[v] - (v|\rho)] \qquad [\textit{Lieb variational principle}] \tag{1.76}$$

It is apparent from Eq. (1.76) that a related method can be developed for generating the potential associated with a given ground state density, and vice versa, from the rearrangements

$$\mathcal{A}_v = \operatorname*{argmin}_{\rho \in \mathcal{A}_N} [\, \mathrm{F}_{\mathrm{HK}}[\rho] + (v|\rho)] \subset \mathcal{A}_N \tag{1.77}$$

$$\mathcal{V}_\rho = \operatorname*{argmin}_{v \in \mathcal{V}_N} [\, E_0[v] - (v|\rho)] \subset \mathcal{V}_N \tag{1.78}$$

By Eq. (1.77) $\mathcal{A}_v$ contains all the densities associated with v and by Eq. (1.78) $\mathcal{V}_\rho$ contains all the potentials able to support a ground state density ρ,

$$\mathcal{V}_\rho = \{v_\rho + c \mid v_\rho \in \mathcal{V}_N \text{ that has ground state density } \rho,\ c \in \mathbb{R}\}. \tag{1.79}$$

Through the remarkable power of the first and second Hohenberg–Kohn principles it is shown that the ground state energy of N electrons in a given external potential can be calculated using only $\rho(\mathbf{r})$ without requiring the complicated many electron wave function. No additional approximations have been made during the derivation of the Hohenberg-Kohn theorems and if an exact form for the universal density-functional was known, along with its associated domains ($\mathcal{V}_N$ and $\mathcal{A}_N$), an exact solution could be obtained. Unfortunately the exact form of the universal functional is unknown, and density-functional theory development must turn to deriving accurate and inexpensive approximations to the universal functional that are amenable to computation.

1.5.5 Levy–Lieb constrained search scheme

The Hohenberg–Kohn theorems outlined previously stand as great achievements, opening the way for what has become the most widely used method in theoretical chemistry, density-functional theory. The requirement of the Hohenberg–Kohn theorems that $v \in \mathcal{V}_N$ and $\rho \in \mathcal{A}_N$ remains a severe difficulty however, as the sets $\mathcal{V}_N$ and $\mathcal{A}_N$ are unknown. This leaves Hohenberg–Kohn DFT on uncertain mathematical foundations as it is unknown if the potential and density of a given system are indeed members of $\mathcal{V}_N$ and $\mathcal{A}_N$. The limitation to $\mathcal{V}_N$ and $\mathcal{A}_N$ is lifted in the more general formulation of DFT of Levy [30] and Lieb [14], the Levy–Lieb constrained search theory.

Before the set of allowed densities and potentials is characterised a brief outline the mathematics of vector spaces and inner products is given to provide the necessary background.

Vector Spaces

A mathematical field is defined as a set of elements that satisfy the field axioms for additive and multiplicative operations,

Axiom	Additive Operations	Multiplicative Operations
Associativity	$(a+b)+c = a+(b+c)$	$(ab)c = a(bc)$
Commutativity	$a+b = b+a$	$ab = ba$
Distributivity	$a(b+c) = ab+ac$	$(a+b)c = ac+ab$
Identity	$a+0 = 0+a = a$	$a \cdot 1 = 1 \cdot a = a$
Inverses	$a+(-a) = (-a)+a = 0$	$aa^{-1} = a^{-1}a = 1, \;\; (a \neq 0)$

The real numbers, $\mathbb{R}$, and the natural numbers $\mathbb{N}$ are examples of fields.

A vector space $\mathcal{V}$ can be constructed over a field $\mathbb{K}$ as a set that satisfies the vector addition and scalar multiplication operations. The vectors $\mathbf{x}, \mathbf{y}, \mathbf{z} \in \mathcal{V}$ and scalars $\alpha, \beta \in \mathbb{K}$ must satisfy the vector space axioms,

- Associativity of Addition $\mathbf{x} + (\mathbf{y} + \mathbf{z}) = (\mathbf{x} + \mathbf{y}) + \mathbf{z}$
- Commutativity of Addition $\mathbf{x} + \mathbf{y} = \mathbf{y} + \mathbf{x}$
- Zero Vector $\exists \mathbf{0} \in \mathcal{V}$ where $\mathbf{x} + \mathbf{0} = \mathbf{x}, \; \forall \mathbf{x} \in \mathcal{V}$
- Additive Inverse $\forall \mathbf{x} \in \mathcal{V}, \exists \mathbf{y} \in \mathcal{V}$ where $\mathbf{x} + \mathbf{y} = \mathbf{0}$
- Associativity of Multiplication $\alpha(\beta\mathbf{x}) = (\alpha\beta)\mathbf{x}$
- Distributivity $\alpha(\mathbf{x} + \mathbf{y}) = \alpha\mathbf{x} + \alpha\mathbf{y}$
- Multiplicative Identity $\exists 1 \in \mathbb{K}$ where $1 \cdot \mathbf{x} = \mathbf{x}, \; \forall \mathbf{x} \in \mathcal{V}$

A norm can be defined on the vector space $\mathcal{V}$ as a function $||\cdot|| : \mathcal{V} \mapsto \mathbb{R}$ if and only if $\forall \mathbf{x}, \mathbf{y} \in \mathcal{V}$ and $\alpha \in \mathbb{R}$:

- $||\mathbf{x}|| \geq 0$ and $||\mathbf{x}|| = 0$ if and only if $\mathbf{x} = \mathbf{0}$
- $||\mathbf{x} + \mathbf{y}|| \leq ||\mathbf{x}|| + ||\mathbf{y}||$
- $||\alpha\mathbf{x}|| = |\alpha| \, ||\mathbf{x}||$

A vector space with a defined norm is termed a normed vector space, and is complete if and only if every Cauchy sequence[3] in $\mathcal{V}$ converges to an element of $\mathcal{V}$. A vector space that is complete and normed is termed a Banach space.

Within a Banach space a p-norm can be defined as,

$$||\mathbf{x}||_p = \left(\sum_i |x_i|^p \right)^{\frac{1}{p}}. \tag{1.80}$$

An important subset of the Banach spaces are the Lebesgue spaces, identified as a Banach space consisting only of functions whose p-norm is Lebesgue integrable. The notation for a specific Lebesgue space is then $L^p(S)$, denoting the space of measurable functions f over the field S which obey the identity,

$$||f||_p = \left(\int_S |f(\mathbf{r})|^p \mathrm{d}\mathbf{r} \right)^{\frac{1}{p}} < +\infty. \tag{1.81}$$

An inner product can be defined on the vector space $\mathcal{V}$ as a function $(\cdot, \cdot) : \mathcal{V} \times \mathcal{V} \mapsto \mathbb{R}$ such that $\forall \mathbf{x}, \mathbf{y}, \mathbf{z} \in \mathcal{V}$ and $\forall \alpha \in \mathbb{R}$:

- $(\mathbf{x}, \mathbf{x}) \geq 0$ and $(\mathbf{x}, \mathbf{x}) = 0$ if and only if $\mathbf{x} = \mathbf{0}$
- $(\mathbf{x} + \mathbf{y}, \mathbf{z}) = (\mathbf{x}, \mathbf{z}) + (\mathbf{y}, \mathbf{z})$
- $(\alpha\mathbf{x}, \mathbf{y}) = \alpha(\mathbf{x}, \mathbf{y})$

[3] A Cauchy sequence is a sequence $\{x_i\}$ for which $\forall \epsilon > 0$ there is an $N \in \mathbb{N}$ such that $|x_i - x_j| \leq \epsilon$ when $i, j \geq N$, the sequence is said to converge to ϵ.

- $(\mathbf{x}, \mathbf{y}) = \overline{(\mathbf{y}, \mathbf{x})}$, where $\overline{(\cdot, \cdot)}$ is the complex conjugate of $(\cdot, \cdot)$

A vector space with a defined inner product is an inner product space and a Banach space with a defined inner product is a Hilbert space. The Lebesgue space $L^2(a, b)$ is an example of a Hilbert space with an inner product defined as,

$$(f, g) = \int_a^b f(x)\overline{g}(x)\mathrm{d}x \tag{1.82}$$

and the norm,

$$\begin{aligned} ||x||_2 &= \left(\int_a^b |f(x)|^2 \mathrm{d}x \right)^{\frac{1}{2}} \\ &= \sqrt{(f, f)} \end{aligned} \tag{1.83}$$

With this framework for the classification of vector spaces in place explicit definitions of admissible densities and potentials can be made in terms of L^p spaces, allowing a precise definition and characterisation.

The generalised Rayleigh–Ritz variation principle

The requirement that $v \in \mathcal{V}_N$ was made in the Hohenberg–Kohn theory to ensure that an N-electron ground state Ψ_0 with eigenvalue $E_0[v]$ exists in the Rayleigh–Ritz variation principle, Theorem 1.5.1. To lift this restriction we define the N-electron ground state energy as the infimum of the Hamiltonian expectation value,

$$E_0[v] = \inf_{\Psi \in \mathcal{W}_N} \langle \Psi | H_N[v] | \Psi \rangle \,, \quad \forall v \in \mathcal{U}, \tag{1.84}$$

in which the set of all potentials $\mathcal{U}$ (to be determined later) and normalised N-electron wave functions $\mathcal{W}_N$ are defined by,

$$| \langle \Psi | H_N[v] | \Psi \rangle | < \infty, \quad \forall \Psi \in \mathcal{W}_N, \; v \in \mathcal{U}, \tag{1.85}$$

removing the requirement of $v \in \mathcal{V}_N$.

For a subset of $\mathcal{U}$ there exists a ground state wave function $\Psi_0(\mathbf{r})$ of $H_N[v]$ and $v \in \mathcal{V}_N$, giving a minimum $E_0[v]$ for the Rayleigh–Ritz variation principle. When this is not the case and $v \notin \mathcal{V}_N$ then by definition no minimising wave function can exist and $E_0[v]$ is instead the infimum over all expectation values for all $\Psi \in \mathcal{W}_N$, giving Eq. (1.84) as the generalised Rayleigh–Ritz variation principle.

Permissible potentials and N-electron wave functions

The set of allowed N-electron wave functions that comprise $\mathcal{W}_N$ are restricted to the set of normalised N-electron antisymmetric wave functions with a finite value for $H_N[v]$,

$$\mathcal{W}_N = \left\{ \Psi \;\middle|\; ||\Psi||_2 = 1, \; \left| \left\langle \Psi \middle| \hat{H}_N[v] \middle| \Psi \right\rangle \right| < \infty, \; v \in \mathcal{V}_C, \text{ N-electron, antisymmetric } \Psi \right\} \tag{1.86}$$

where $\mathcal{V}_C$ is the set of all point charge Coulomb potentials, defined as,

$$\mathcal{V}_C = \left\{ v \;\middle|\; v(\mathbf{r}) = -\sum_A^{N_{\text{nuc.}}} \frac{Z_A}{|\mathbf{r} - \mathbf{R}_A|}, \; N_{\text{nuc.}} \in \mathbb{N}, \; Z_A \in \mathbb{R} \right\}. \tag{1.87}$$

The set $\mathcal{W}_N$ of Eq. (1.86) does not preclude systems with no nuclear charges $Z_A = 0$ for which the Coulomb potential, v, is zero. As the wave functions for these systems must obey the constraints of Eq. (1.86), an additional constraint is revealed: the wave functions of $\mathcal{W}_N$ must also have a finite expectation value for the system independent Hamiltonian $\hat{H} = \hat{T} + \hat{W}_N$,

$$\left| \left\langle \Psi \middle| \hat{T} + \hat{W}_N \middle| \Psi \right\rangle \right| < \infty. \tag{1.88}$$

Separation of Eq. (1.88) reveals that the kinetic energy and Coulombic interactions must be independently finite and a further analysis reveals that a finite expectation value for the universal Hamiltonian is obtained if and only if $\Psi \in \mathcal{H}_N^1$, the first-order Sobolev space, as proved in Ref. [14]. The first order Sobolev space contains the functions for which the inner product $(\Psi, \Psi) = \langle \Psi | \Psi \rangle + \sum_i^N \langle \nabla_i \Psi | \nabla_i \Psi \rangle$ is finite,

$$\mathcal{H}_N^1 = \left\{ \Psi \;\middle|\; | \langle \Psi | \Psi \rangle + \sum_i^N \langle \nabla_i \Psi | \nabla_i \Psi \rangle | < \infty \right\}, \tag{1.89}$$

which identifies an arbitrary wave function as permissible or otherwise using only information from the first derivative.

Requiring that $\Psi \in \mathcal{H}_N^1$ guarantees the existence of the following theorem,

Theorem 1.5.5. *The condition $\Psi \in \mathcal{H}_N^1$ is both necessary and sufficient to guarantee finite kinetic and Coulomb energies,*

$$0 < \left\langle \Psi \middle| \hat{T}_N \middle| \Psi \right\rangle < \infty, \quad 0 < \left\langle \Psi \middle| \hat{W}_N \middle| \Psi \right\rangle < \infty, \tag{1.90}$$

and a finite expectation value for the full Hamiltonian $H_N[v]$ for all $v \in \mathcal{V}_C$,

$$\left| \left\langle \Psi \middle| \hat{H}_N[v] \middle| \Psi \right\rangle \right| < \infty, \tag{1.91}$$

that is bounded from below, showing that the infimum $E_0[v]$ is finite for all $v \in \mathcal{V}_C$.

Permissible electron densities

With the set of permissible wave functions described the task for a density functional theory becomes identifying which density functions, $\rho(\mathbf{r})$, correspond to an antisymmetric wave function, without requiring $\Psi \in \mathcal{W}_N$. We begin by requiring that the N-electron density function satisfies the conditions of non-negativity and normalisation,

$$\rho(\mathbf{r}) \geq 0, \; \forall \mathbf{r} \in \mathbb{R}^3 \tag{1.92}$$

$$\int \rho(\mathbf{r}) \mathrm{d}\mathbf{r} = N. \tag{1.93}$$

The functions obeying Eqs. (1.92) and (1.93) must belong to the subset of functions in the $L^1(\mathbb{R}^3)$ Lebesgue space that are everywhere non-negative and integrate to N, denoted L_N^1,

$$L_N^1 = \{ \rho \in L_N^1(\mathbb{R}^3) \mid \rho \geq 0, \int \rho(\mathbf{r}) \mathrm{d}\mathbf{r} = N \}. \tag{1.94}$$

It can be shown [14] that any electronic density that is a member of L_N^1 can be constructed as the density arising from a set of N orthonormal complex orbitals $\{\phi_k\}$,

$$\phi_k(\mathbf{r}) = N^{-1/2} \rho^{1/2}(\mathbf{r}) \exp[2\pi \mathrm{i}(k-1)q(x)], \quad k = 1, 2, \ldots, N, \tag{1.95}$$

where the real, non-negative function q is defined from the density ρ as,

$$q(x) = N^{-1} \int_{-\infty}^{x} \iint_{-\infty}^{\infty} \rho(t, y, z) \mathrm{d}t \mathrm{d}y \mathrm{d}z. \tag{1.96}$$

A Slater determinant to give any electron density $\rho \in L_1^N$ can be constructed from $\{\phi_k\}$ and the arbitrary spin functions σ_α and σ_β,

$$\rho_{\mathrm{SD}}(\mathbf{r}) = \sum_k^N |\phi_k(\mathbf{r})|^2 = \sum_k^N N^{-1} \rho(\mathbf{r}) = \rho(\mathbf{r}), \tag{1.97}$$

which guarantees the existence of the following theorem,

Theorem 1.5.6. *Each $\rho \in L_N^1$ is the density of some N-electron antisymmetric wave function, which may be taken to be a Slater determinant.*

The density is invariant to a unitary rotation of the orbitals in the Slater determinant and as such, infinitely many Slater determinants and linear combinations thereof can yield the same density ρ.

N-representable densities

Having identified the set of electron densities that can be constructed from an antisymmetric wave function, $\rho \in L_N^1$, and the set of N-electron wave functions for which the electronic energy is finite, $\Psi \in \mathcal{H}_N^1$, attention is turned to the set that is of central importance to DFT, the N-representable densities,

$$\mathcal{I}_N = \{\rho \mid \rho \text{ can be obtained from } \Psi \in \mathcal{H}_N^1\}. \tag{1.98}$$

An efficient test is required to identify whether the conditions $\rho \in L_N^1$ and $\rho \in \mathcal{I}_N$ are true for a given density ρ, without resorting to evaluating the wave function $\Psi \in \mathcal{H}_N^1$ that gives ρ. This is achieved by application of the von Weizsäcker kinetic energy functional that maps a functional from L_N^1 to the half open interval $(0, +\infty]$,

$$T^{\mathrm{vW}} : L_N^1 \mapsto (0, +\infty], \tag{1.99}$$

$$T^{\mathrm{vW}}[\rho] = \frac{1}{8} \int \frac{|\nabla \rho(\mathbf{r})|^2}{\rho(\mathbf{r})} \mathrm{d}\mathbf{r}. \tag{1.100}$$

The von Weizsäcker kinetic energy can be interpreted as the kinetic energy of a system of bosons with density $\rho(\mathbf{r})$, and gives the exact kinetic energy for a one electron, or spin paired (one orbital) two electron, system. Importantly, the von Weisäcker kinetic energy functional gives rise to the following theorem,

Theorem 1.5.7. *The von Weizsäcker kinetic energy of $\rho \in \mathcal{I}_N$ is a lower bound to the kinetic energy of all N-electron wave functions with the same density,*

$$T^{\mathrm{vW}}[\rho] \leq \inf_{\Psi \mapsto \rho} \left\langle \Psi \middle| \hat{T}_N \middle| \Psi \right\rangle < \infty, \quad \rho \in \mathcal{I}_N \tag{1.101}$$

Consider some density $\rho \in L_N^1$ for which $T^{\mathrm{vW}}[\rho] < \infty$. From Theorem 1.5.6 this density can be obtained from the Slater determinant Ψ_ρ^{SD} and it can be shown [31] that the kinetic energy of this Slater determinant obeys the inequality,

$$\left\langle \Psi_\rho^{\mathrm{SD}} \middle| \hat{T}_N \middle| \Psi_\rho^{\mathrm{SD}} \right\rangle \leq \frac{16\pi^2 N^2}{3} T^{\mathrm{vW}}[\rho] \tag{1.102}$$

As a result, if $T^{\mathrm{vW}}[\rho] < \infty$ then $\Psi_\rho^{\mathrm{SD}} \in \mathcal{W}_N$ and $\rho \in \mathcal{I}_N$. Thus, a finite von Weiszäcker kinetic energy is necessary and sufficient to ensure a given density is N-representable. This is summarised in Theorem 1.5.8,

Theorem 1.5.8. *A function $\rho \in L_N^1(\mathbb{R}^3)$ is N-representable if and only if $T^{\mathrm{vW}}[\rho] < \infty$,*

$$\mathcal{I}_N = \{\rho \in L_N^1(\mathbb{R}^3) \mid \rho \geq 0, \int \rho(\mathbf{r}) \mathrm{d}\mathbf{r} = N, \; T^{\mathrm{vW}}[\rho] < \infty\} \tag{1.103}$$

The Levy–Lieb constrained-search functional

With the set of N-representable densities characterised the identification of the density corresponding to the ground state of a system can be achieved by the Levy–Lieb constrained search, a two step minimisation,

$$E_0[v] = \inf_{\Psi \in \mathcal{W}_N} \langle \Psi | H_N[v] | \Psi \rangle = \inf_{\rho \in \mathcal{I}_N} \inf_{\Psi \mapsto \rho} \left\langle \Psi \middle| \hat{T}_N + \hat{W}_N + \sum_i v(\mathbf{r}_i) \middle| \Psi \right\rangle \tag{1.104}$$

$$= \inf_{\rho \in \mathcal{I}_N} \left[\inf_{\Psi \mapsto \rho} \left\langle \Psi \middle| \hat{T}_N + \hat{W}_N \middle| \Psi \right\rangle + (v|\rho) \right], \qquad \forall v \in \mathcal{V}_C. \tag{1.105}$$

In Eq. (1.105) the interaction of the density with the external potential has been removed from the minimisation over the wave functions, as it is necessarily the same for all $\Psi \mapsto \rho$. With this separation

the Levy–Lieb constrained search functional can be identified from Eq. (1.105) as,

$$F_{\mathrm{LL}} : \mathcal{I}_N \mapsto \mathbb{R},$$
$$F_{\mathrm{LL}} = \inf_{\Psi \mapsto \rho} \left\langle \Psi \middle| \hat{T}_N + \hat{W}_N \middle| \Psi \right\rangle, \quad \forall \rho \in \mathcal{I}_N, \tag{1.106}$$

showing the functional to give the minimum kinetic and Coulomb repulsion energies for a given electron density. It can be shown that for every $\rho \in \mathcal{I}_N$ there exists a minimising wave function allowing infimum in Eq. (1.106) to be sharpened to a minimum,

Theorem 1.5.9. *A minimising density exists for the Levy–Lieb constrained-search functional,*

$$F_{\mathrm{LL}} : \mathcal{I}_N \mapsto \mathbb{R},$$

which is finite and positive for all $\rho \in \mathcal{I}_N$,

$$F_{\mathrm{LL}}(\rho) = \min_{\Psi \mapsto \rho} \left\langle \Psi \middle| \hat{T}_N + \hat{W}_N \middle| \Psi \right\rangle, \quad \rho \in \mathcal{I}_N. \tag{1.107}$$

This can be combined with the Hohenberg–Kohn theorem (1.5.4) to express the Hohenberg–Kohn theorem for all N-representable densities,

Theorem 1.5.10 (The Hohenberg–Kohn variation principle with the Levy–Lieb functional)**.**

$$E_0(v) = \inf_{\rho \in \mathcal{I}_N} [F_{\mathrm{LL}}(\rho) + (v|\rho)], \forall v \in \mathcal{V}_C. \tag{1.108}$$

Theorem 1.5.10 improves upon the second Hohenberg–Kohn theorem of Theorem 1.5.4 by resolving the representability problems of the original formulation. The search for the ground state energy is now an infimum rather than a minimum, requiring only that the potential originate from a Coulomb system, $v \in \mathcal{V}_C$, rather than requiring that it supports a ground state wave function, $v \in \mathcal{V}_N$, as in the original. Additionally, the search is now performed over all N-representable densities, $\rho \in \mathcal{I}_N$, as opposed to the subset of the these densities, the v-representable densities $\rho \in \mathcal{A}_N \subset \mathcal{I}_N$. In this way it is clear that,

Theorem 1.5.11. *The Hohenberg–Kohn functional is the restriction of F_{LL} to $\mathcal{A}_N$:*

$$F_{\mathrm{LL}}\Big|_{\mathcal{A}_N} = F_{\mathrm{HK}} \tag{1.109}$$

As opposed to $\mathcal{V}_N$ and $\mathcal{A}_N$, the sets $\mathcal{V}_C$ and $\mathcal{I}_N$ have been explicitly characterised, solving the representability problem of the original Hohenberg–Kohn formulation.

1.5.6 The Lieb functional

Before discussing the contribution of Lieb in reformulating the constrained search DFT to ensure a unique solution it is necessary to briefly describe some of the mathematical framework required.

Convex functions and the Legendre–Fenchel transform

A function is described as convex[4] when it has the property that any point on a linear interpolation between two points $f(x_1)$ and $f(x_2)$ is greater than the value of the function at that point,

$$f(\lambda x_1 + (1-\lambda)x_2) \leq \lambda f(x_1) + (1-\lambda) f(x_2) \quad 0 \leq \lambda \leq 1. \tag{1.110}$$

A function is strictly convex if Eq. (1.110) can be sharpened to a strict inequality for the entire interpolation range, $0 < \lambda < 1$.

[4] Similarly, a function f is concave when $-f$ is convex.

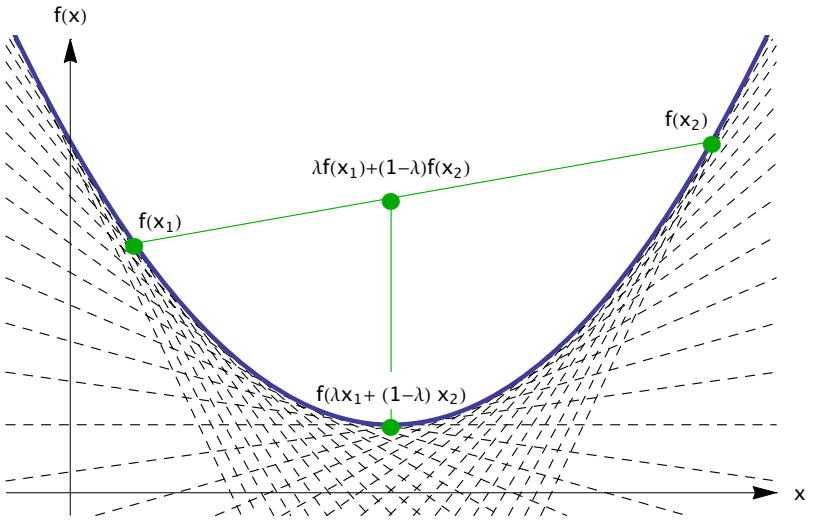


Figure 1.1: A subset of the supporting lines of a convex function $f(x)$. The linear interpolation between point $f(x_1)$ and $f(x_2)$ is shown in green, demonstrating that at any point along this interpolation is greater than the true function value.

A convex function can be defined in terms of its *supporting lines*, a continuum of lines defined at each point of the function such that each line intersects the function only at one point and does not exceed the value of f anywhere. The slope of the supporting line that intersects f at point $(x, f(x))$ is defined as the subgradient of f at x, giving a definition for the supporting line with slope y as,

$$l_y(x) = xy - g(y), \tag{1.111}$$

where $-g(y)$ is is the intersection of the supporting line with the function axis, as illustrated in Figure 1.1.

As the value of the convex function f at x is exactly given by the largest value of any of its supporting lines at the same point, any convex function can be expressed as the pointwise supremum of its supporting lines,

$$f(x) = \sup_y [xy - g(y)]. \tag{1.112}$$

From this it is clear that the convex function $f(x)$ is completely described by the function $g(y)$, the function that defines the point at which the supporting line with slope y crosses the function axis. The representation of the convex function f by g is known as the Legendre–Fenchel transform of f,

Theorem 1.5.12 (The Legendre–Fenchel Transform)**.** *For any convex function $f : \mathbb{R} \mapsto \mathbb{R}$, there is a function f^* such that,*

$$f(x) = \sup_{y \in \mathbb{R}} [xy - f^*(y)] \tag{1.113}$$

$$f^*(y) = \sup_{x \in \mathbb{R}} [xy - f(x)] \tag{1.114}$$

defining f^* as the Legendre–Fenchel transform of f.

An important consequence of the Legendre–Fenchel transform is that the function f^* is always a convex function, even if the original function f was not convex. A further Legendre–Fenchel transform can be applied to f^* to give f^{**}, the biconjugate function of f, having the following identities,

$$\begin{aligned} f^{**} &\leq f \\ f^{**} &= f \text{ if } f \text{ is convex.} \end{aligned} \tag{1.115}$$

For the cases where f is not convex the biconjugate function gives the largest convex lower bound to f, termed the *convex envelope*, illustrated in Figure 1.2. It is clear from the definitions in Eq. (1.115) that applying the Legendre–Fenchel transform to a convex function entails no loss of information and

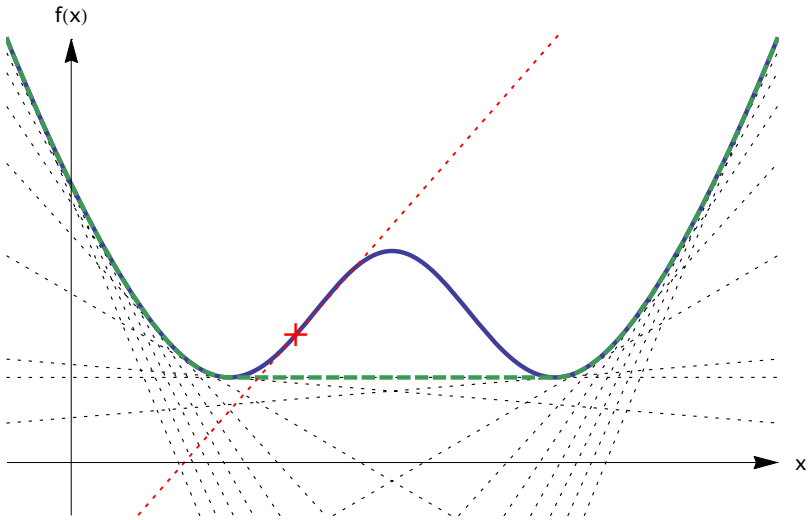


Figure 1.2: A non-convex function $f(x)$ (solid blue), its convex envelope $f^{**}(x)$ (dashed green) and a subset of the supporting lines of f (dotted gray). Note: the line $l_y(x)$ (dotted red) defined from f and its subderivative y at point x (red cross) by Eq. (1.111) is *not* a supporting line of f as $l_y(x) \leq f(x)$ is not true for all values of x.

is completely reversible. The same is not true when f is not a convex function as only the convex envelope to f can be recovered from f^*, though this property is often beneficial, allowing a convex function to be defined from a non-convex function as the biconjugate. When $f^{**} = f$, f^* is said to be the dual of f.

The Lieb functional

A link can be made back to the second Hohenberg–Kohn theorem and Eqs. (1.73) and (1.74), rewriting them as an infimum and supremum respectively,

$$E_0[v] = \inf_{\rho}[F[\rho] + (v|\rho)] \tag{1.116}$$

$$F[\rho] = \sup_{v}[E_0[\rho] - (v|\rho)]. \tag{1.117}$$

As $E_0[v]$ was derived from the variational principle it is simple to show that $E_0[v]$ is a concave functional of v,

$$\begin{aligned} E_0[\lambda v_1 + (1-\lambda)v_2] &= \inf_{\Psi}[\lambda \left\langle \Psi \middle| \hat{H}[v_1] \middle| \Psi \right\rangle + (1-\lambda) \left\langle \Psi \middle| \hat{H}[v_2] \middle| \Psi \right\rangle] \\ &\geq \lambda \inf_{\Psi}[\left\langle \Psi \middle| \hat{H}[v_1] \middle| \Psi \right\rangle] + (1-\lambda) \inf_{\Psi}[\left\langle \Psi \middle| \hat{H}[v_2] \middle| \Psi \right\rangle] \\ &= \lambda E_0[v_1] + (1-\lambda)E_0[v_2], \quad 0 < \lambda < 1. \end{aligned} \tag{1.118}$$

The concavity of $E_0[v]$ proves $-E_0[v]$ to be convex and reveals $F[\rho]$ as its convex conjugate, showing that $F[\rho]$ is an exact description of $E_0[v]$. This in turn reveals that v and ρ are conjugate variables, belonging to dual vector spaces.

The vector space of admissible densities can then be identified from the criteria set in Section 1.5.5,

- The density must be normalised and everywhere integrable, $\int \rho(\mathbf{r})\mathrm{d}\mathbf{r} = N$.
  - Identified as $\rho \in L^1$.
- The kinetic energy must be finite, $\int |\nabla \rho^{\frac{1}{2}}(\mathbf{r})|^2 \mathrm{d}\mathbf{r} < +\infty$.
  - Identified as $\nabla \rho^{\frac{1}{2}} \in L^2$.

These conditions are shown in Ref. [14] to be satisfied when,

$$\rho \in L^3 \cap L^1 \quad \text{defined as } \mathcal{X} \tag{1.119}$$

The constrained search formulation of Levy and Lieb allows this restriction to be lifted, requiring only that the potential have a finite interaction with the density. From the characterisation of the density in Eq. (1.119) it was shown by Lieb in Ref. [14] that a finite interaction can only occur when

$$v \in L^{\frac{3}{2}} + L^{\infty} \quad \text{defined as } \mathcal{X}^*. \tag{1.120}$$

In this way the spaces $\mathcal{X}$ and $\mathcal{X}^*$ are dual vector spaces, as expected.

With the spaces of ρ and v identified the Lieb functional can be identified as,

Theorem 1.5.13 (The Lieb Functional)**.** *The Lieb functional is given by,*

$$F[\rho] = \sup_{v \in \mathcal{X}^*} [E_0[v] - (v|\rho)] \quad \rho \in \mathcal{X} \tag{1.121}$$

with the dual energy functional,

$$E[v] = \inf_{\rho \in \mathcal{X}} [F[\rho] + (\rho|v)] \quad v \in \mathcal{X}^* \tag{1.122}$$

In the cases where ρ is a non-degenerate ground state density the Lieb functional is identical to the Hohenberg–Kohn universal functional (Theorem 1.5.4) and the constrained search functional (Theorem 1.5.10), but only the constrained search and Lieb functionals are defined when ρ is not a ground state density. The Lieb functional is identified as the convex envelope of the constrained search functional, this guarantees that the Lieb functional has a unique optimiser, where no such guarantee can be made for the constrained search functional.

1.6 Kohn–Sham DFT

The density-functional theory described in Section 1.5 determines the energy of a fully interacting many electron system through the minimisation of Eq. (1.122). The universal functional $F[\rho]$ is identified from the electronic Hamiltonian as,

$$F[\rho] = T[\rho] + J[\rho] + E_{\text{ee}}[\rho], \tag{1.123}$$

in which $T[\rho]$ is the fully interacting kinetic energy, $J[\rho]$ is the classical Coulomb energy and $E_{\text{ee}}[\rho]$ is the non-classical part of the two electron operator. As previously stated, if exact expressions for all the terms in the universal functional were known, then Eq. (1.122) would yield an exact energy. Only the classical Coulomb repulsion $J[\rho]$ is known exactly however, and approximate forms are required for $T[\rho]$ and $E_{\text{ee}}[\rho]$.

1.6.1 The Kohn–Sham kinetic energy functional

The Thomas–Fermi [32, 33] scheme was historically the first attempt to solve this problem[5] by constructing a kinetic energy functional for the uniform electron gas model and neglecting all non-classical electron interactions. As noted before this approximate universal functional is highly inaccurate in nearly all cases, the exception being solid first period metallic systems. Only mild improvements are observed when the exchange interaction for the uniform electron gas is included as $E_{\text{ee}}[\rho]$, the Thomas–Fermi–Dirac universal functional [34].

When contrasted with solutions from Hartree–Fock theory, which show a reasonable quantitative accuracy, it becomes clear that the biggest source of error in the Thomas–Fermi–Dirac functional lies in the kinetic energy contribution, the largest single term in the expansion of Eq. (1.123). For density functional theory to be useful to chemistry a more accurate approximation of $T[\rho]$ is needed and the derivation of improved approximate kinetic energy functionals remains the most active field in orbital free density functional development.

[5] Though Thomas–Fermi theory pre-dates the Hohenberg–Kohn theorems it presents the first explicit expression for $F[\rho]$.

In lieu of an explicit kinetic energy density functional Kohn and Sham (KS) derived a different, though formally still exact, construction for the universal functional by considering an auxiliary system of non-interacting electrons constrained to have the same density as the interacting system. The Hamiltonian operator for this non-interacting system can be written as,

$$\hat{H}_{\mathrm{S}} = -\frac{1}{2}\sum_{i}^{N}\nabla_i^2 + \sum_{i}^{N} v_{\mathrm{S}}(\mathbf{r}), \tag{1.124}$$

and is minimised by the Slater determinant wave function of spin orbitals, φ_i, that are the solutions to the KS eigenvalue equation,

$$\left[-\frac{1}{2}\nabla^2 + v_{\mathrm{S}}\right]\varphi_p = \epsilon_p\varphi_p, \tag{1.125}$$

constrained to give the correct density,

$$\rho(\mathbf{r}) = \sum_{i}^{N}|\varphi_i(\mathbf{r})|^2 \tag{1.126}$$

Eq. (1.124) introduces the effective local potential, $v_{\mathrm{S}}(\mathbf{r})$ that acts to constrain the non-interacting electrons to have the density of the real system.

The genius of the Kohn–Sham theory is to use this model non-interacting system of electrons to account for as much of the kinetic energy as possible by rewriting the universal functional of Eq. (1.123) as,

$$F[\rho] = T_{\mathrm{S}}[\rho] + J[\rho] + E_{\mathrm{xc}}[\rho] \tag{1.127}$$

where the non-interacting kinetic energy functional $T_{\mathrm{S}}[\rho]$ is defined from the auxiliary non-interacting wave function as,

$$T_{\mathrm{S}}[\rho] = -\frac{1}{2}\sum_{i}^{N}\left\langle\varphi_i\middle|\nabla^2\middle|\varphi_i\right\rangle. \tag{1.128}$$

The total KS energy is then,

$$\mathrm{E}[\rho] = T_{\mathrm{S}}[\rho] + J[\rho] + E_{\mathrm{xc}}[\rho] + E_{\mathrm{ext}}[\rho], \tag{1.129}$$

where $E_{\mathrm{ext}}[\rho]$ gives the interaction of the density with the external potential.

The non interacting kinetic energy, $T_{\mathrm{S}}[\rho]$ is of course an approximation to the fully interacting kinetic energy, which will always be greater than the non-interacting approximation, $T[\rho] \geq T_{\mathrm{S}}[\rho]$. The theory remains exact by accounting for all the energetic contributions missed by T_{S} and J within the *exchange-correlation* functional,

$$E_{\mathrm{xc}}[\rho] \equiv (T[\rho] - T_{\mathrm{S}}[\rho]) + E_{\mathrm{ee}}[\rho] = T_{\mathrm{c}}[\rho] + E_{\mathrm{ncl}}[\rho], \tag{1.130}$$

where $E_{\mathrm{ncl}}[\rho]$ are the non-classical electron interactions.

This can be viewed as partitioning the kinetic energy into a majority that is captured exactly by the expectation value of the kinetic energy operator acting on the Slater determinant wave function of the non-interacting auxiliary system, $T_{\mathrm{S}}[\rho]$, and the smaller kinetic energy resulting from the correlated movements of the electrons, T_{c}. This partitioning is highly successful as T_{S} is far greater in magnitude than T_{c}, allowing for the majority of the kinetic energy, and hence total electronic energy, to be calculated exactly.

1.6.2 The effective local potential

With the Kohn–Sham universal functional defined, a set of orbital dependent equations can be determined from Eq. (1.129) as,

$$E[\rho] = T_S[\rho] + J[\rho] + E_{\mathrm{xc}}[\rho] + E_{\mathrm{ext}}[\rho(\mathbf{r})] \tag{1.131}$$

$$= -\frac{1}{2}\sum_{i}^{N}\left\langle\varphi_i\middle|\nabla^2\middle|\varphi_i\right\rangle + \frac{1}{2}\sum_{ij}^{N}\iint\frac{|\varphi_i(\mathbf{r})|^2\cdot|\varphi_j(\mathbf{r}')|^2}{|\mathbf{r}-\mathbf{r}'|}\mathrm{d}\mathbf{r}\mathrm{d}\mathbf{r}'$$

$$+ E_{\mathrm{xc}}[\rho] - \sum_{i}^{N}\int\sum_{A}^{M}\frac{Z_A|\varphi_i(\mathbf{r})|^2}{|\mathbf{r}-\mathbf{R}_A|}\mathrm{d}\mathbf{r} \tag{1.132}$$

where only $E_{\mathrm{xc}}[\rho(\mathbf{r})]$ remains unknown.

We allow the N non-interacting electron spin orbitals to vary, under the usual constraint that the orbitals remain orthonormal (Eq. (1.14)), such that we can perform a variational search for the minimum of $E[\rho]$ through the orbitals $\{\varphi_i\}$.

A system of Lagrange multipliers is constructed from Eq. (1.132) with the constraint of orthonormality,

$$\Omega[\{\varphi_i\}] = E[\rho] - \sum_{ij}^{N} \epsilon_{ij} \int \varphi_i^*(\mathbf{r})\varphi_j(\mathbf{r})\mathrm{d}\mathbf{r}. \tag{1.133}$$

$E[\rho]$ is at a minimum when the condition,

$$\delta\Omega[\{\varphi_i\}] = 0, \tag{1.134}$$

is reached, leading to the set of equations,

$$\hat{h}\varphi_i = \left[-\frac{1}{2}\nabla^2 + v_{\mathrm{eff}}\right]\varphi_i = \sum_{i}^{N} \epsilon_{ij}\varphi_i, \tag{1.135}$$

with the Hermitian matrix ϵ_{ij} which can be diagonalised to give the canonical Kohn–Sham equations,

$$\left[-\frac{1}{2}\nabla^2 + v_{\mathrm{eff}}\right]\varphi_i = \epsilon_i\varphi_i. \tag{1.136}$$

Comparison of Eq. (1.136) with Eq. (1.125) shows that the effective potential required is the non-interacting potential v_{s},

$$v_{\mathrm{s}}(\mathbf{r}) = v_{\mathrm{ext}}(\mathbf{r}) + v_{\mathrm{J}}(\mathbf{r}) + v_{\mathrm{xc}}(\mathbf{r}), \tag{1.137}$$

where,

$$v_{\mathrm{ext}}(\mathbf{r}) = -\sum_{A}^{M} \frac{Z_A}{|\mathbf{r} - \mathbf{R}_A|} \tag{1.138}$$

$$v_{\mathrm{J}}(\mathbf{r}) = \int \frac{\rho(\mathbf{r}')}{|\mathbf{r} - \mathbf{r}'|}\mathrm{d}\mathbf{r}' \tag{1.139}$$

$$v_{\mathrm{xc}}(\mathbf{r}) \equiv \frac{\delta E_{\mathrm{xc}}[\rho]}{\delta\rho(\mathbf{r})}. \tag{1.140}$$

The exchange-correlation potential of Eq. (1.140) is defined by the approximate form used for the unknown exchange correlation functional through its functional derivative with respect to the electron density.

1.7 Density-functional approximations

The utility of the density-functional theory derived in Section 1.5 is entirely determined by the availability of low cost approximations to the universal density-functional of Eq. (1.74). The Kohn–Sham scheme simplifies this problem by capturing the majority of the energy contributions through the introduction of a non-interacting system with the same density as the physical system, allowing the energy to be expressed as Eq. (1.127) in which only the final term, $E_{\mathrm{xc}}[\rho]$, remains to be approximated. Many approximate models of the exchange-correlation functional have been proposed over the years incorporating many different philosophies and design goals and despite the large number of functionals available, the majority can be identified as a member of one of a few classes.

1.7.1 The local density approximation

The first exchange-correlation (XC) functionals were based on the local density approximation (LDA). These functionals depend only on the electron density at a point and are built with the uniform

electron gas as a model system. The uniform electron gas is an infinite system of homogeneous electron density in a uniform positive background charge, giving a neutral net charge. The exchange-correlation energy for the uniform electron gas can be expressed simply as,

$$E_{\mathrm{xc}}^{\mathrm{LDA}}[\rho] = \int \rho(\mathbf{r})\epsilon_{\mathrm{xc}}(\rho(\mathbf{r}))\mathrm{d}\mathbf{r}, \tag{1.141}$$

with ϵ_{xc} the LDA exchange-correlation energy density. This energy density can be split further to separate exchange and correlation contributions,

$$\epsilon_{\mathrm{xc}}(\rho(\mathbf{r})) = \epsilon_{\mathrm{x}}(\rho(\mathbf{r})) + \epsilon_{\mathrm{c}}(\rho(\mathbf{r})). \tag{1.142}$$

An exact form for the exchange energy of a uniform electron gas was derived by Bloch and Dirac through the spherical exchange hole,

$$\epsilon_{\mathrm{x}} = -\frac{3}{4}\sqrt[3]{\frac{3\rho(\mathbf{r})}{\pi}}, \tag{1.143}$$

but no exact expression for the correlation energy of the uniform electron gas is known. Instead, highly accurate interpolations have been derived from numerical quantum Monte-Carlo simulations to construct accurate approximations of the uniform electron gas correlation energy density [35]. The most widely adopted of these approximations is that of Vosko, Wilk and Nusair (VWN) [36] and is commonly used as a component in more complicated functional forms.

Despite the apparent crudeness of the underlying assumption that the XC energy density at a point is that of the equivalent uniform electron gas, the performance of these functionals is surprisingly good, giving reasonable accuracy for many electronic properties, often comparable or better than the Hartree–Fock approximation. The LDA functionals are not completely successful however and often fall far short of the 1.5 $\mathrm{mE_h}$ required for chemical accuracy. In order to increase the accuracy, the XC functional must be expanded to include information about the surrounding density and become less local.

1.7.2 The gradient expansion and generalised gradient approximation

A logical route for improving the accuracy of density functionals is to consider the LDA as the first term in a Taylor expansion of the energy with respect to the electron density, and proceed by including a dependence on the gradient of the density. In doing so, one hopes to capture some of the inhomogeneity present in the real system and improve accuracy. Naively adopting this approach gives the gradient expansion approximation (GEA), the XC functionals defined around a slowly varying electron density.

Counter-intuitively, GEA functionals are frequently less accurate than the LDA functional. The root of the poor GEA accuracy lies in a failure to reproduce many of the features that are known in the exact exchange-correlation functional, notably that the exchange hole is everywhere negative and represents a deficit of one electron [37]. The LDA exchange hole construction obeys these conditions, rationalising the unexpected success of the LDA functional form. A solution to the poor performance of the GEA functionals is achieved through the generalised gradient approximation (GGA), in which the XC functional is directly restricted to obey many of the exact features missing from GEA functionals [38],

$$E_{\mathrm{xc}}^{\mathrm{GGA}}[\rho_\alpha, \rho_\beta] = \int f(\rho_\alpha, \rho_\beta, \nabla\rho_\alpha, \nabla\rho_\beta)\mathrm{d}\mathbf{r}. \tag{1.144}$$

Many constructions and parametrisations for GGA functionals have been presented throughout the years and the class remains the core driving force behind the success of practical DFT, providing impressive accuracy for a variety of systems. Whilst the increased information present in GGA functionals through the density gradient gives some information of the surrounding electronic environment, GGA functionals remain only a semi-local density functional. In order to increase accuracy further, and capture more features of the exact XC functional, a non-local form must be considered.

1.7.3 The meta-generalised gradient approximation

Given the success of GGA functionals it is tempting include the further derivatives of the density or molecular orbitals, such as the Laplacian of the density or the non-interacting kinetic density,

$$\tau_\sigma(\mathbf{r}) = \frac{1}{2}\sum_i^{\text{occ.}} |\nabla\varphi_{i\sigma}|^2. \tag{1.145}$$

Functionals of this type are termed meta-GGA (mGGA) functionals and are a fertile ground for the continued development of XC functionals.

The enhanced accuracy shown by mGGA functionals arises from an ability to correctly obey more of the known exact constraints through a recognition of one-electron and one-orbital regions of space. This identification is made by the comparison of τ_σ with the von Weizsäcker kinetic energy density,

$$\tau_\sigma^{\text{vW}}(\mathbf{r}) = \frac{|\nabla\rho_\sigma|^2}{8\rho_\sigma}. \tag{1.146}$$

For a system comprised of a single orbital occupied by up to two electrons of different spin $\tau_\sigma = \tau_\sigma^{\text{vW}}$, allowing for the construction of an *iso-orbital indicator* function,

$$z_\sigma(\mathbf{r}) = \frac{\tau_\sigma^{\text{vW}}(\mathbf{r})}{\tau_\sigma(\mathbf{r})}. \tag{1.147}$$

The iso-orbital indicator function has the value of 1 in a region dominated by a single orbital, and approaches 0 where the density becomes electron gas like, allowing the identification of one electron regions where the correlation energy can be forced to become zero, preventing self correlation error. The lack of an iso-orbital indicator makes this identification impossible in LDA and GGA functionals, making mGGA functionals better able to obey more of the exact constraints.

By including a dependence on τ, mGGA functionals become functionals of the KS orbitals and implicit functionals of the electronic density.[6] The mGGA dependence on the KS orbitals produces an increased difficulty in finding the one-electron XC potential, v_{xc}, required by Eq. (1.137). For LDA and GGA functionals v_{xc} is given by the functional derivative of E_{xc} with respect to the density, but for an implicit density functional this is less straightforward. An optimised effective potential (OEP) method must be used to construct the formally correct multiplicative XC potential for the orbital dependent mGGA functionals. The OEP method, and the machinery for its calculation are discussed in detail in Chapters 6 and 7.

The implementation of the OEP scheme and correct handling of the numerical difficulties associated with finite basis sets discourages the use of an OEP in existing DFT codes. Instead, it is common for a more pragmatic approach to be taken to determine the XC potential for a mGGA functional in the KS equations, the XC potential is allowed to be different for each orbital and formed as the XC functional derivative with respect to the variation of the orbital in question [39, 40].

$$\begin{aligned}\frac{\delta E_{\text{xc}}^{\text{mGGA}}}{\delta\varphi_i(\mathbf{r})} = &-\left(\nabla\frac{\delta f}{\delta\tau(\mathbf{r})}\right)\nabla\varphi_i(\mathbf{r}) - \frac{\delta f}{\delta\tau(\mathbf{r})}\nabla^2\varphi_i(\mathbf{r}) \\ &-\left(\nabla\frac{\delta f}{\delta\nabla\rho(\mathbf{r})}\right)\varphi_i(\mathbf{r}) + \frac{\delta f}{\delta\rho(\mathbf{r})}\varphi_i(\mathbf{r})\end{aligned} \tag{1.148}$$

The third and fourth terms of Eq. (1.148) are the only terms arising in the standard XC potential Eq. (1.140), with the first and second terms containing the gradient and Laplacian of the orbitals multiplied by the local operators. This use of orbital specific potentials is commonly adopted and though computationally convenient, it is a minor deviation from pure Kohn–Sham theory. Despite this deviation the orbital specific potential method has been found to be a close approximation to the exact KS proceedure for most applications [41–43].

[6] As opposed to LDA and GGA functionals, which are explicit density functionals

1.7.4 Hybrid exchange-correlation functionals

The exchange energy for a Slater determinant wave function, such as the auxiliary system used in Kohn–Sham DFT, can be calculated exactly by application of the exchange operator of Eq. (1.20). A natural progression for more accurate exchange energies in XC functionals is to use Eq. (1.20) to calculate the majority of the exchange energy exactly from the auxiliary system, similarly to the kinetic energy. A naive inclusion of exact exchange in calculations for molecular systems however results in a mismatch of the fully non-local exchange with the (semi-)local correlation functional, causing a sharp decrease accuracy.

A more refined method for utilising exact exchange with semi-local functionals is achieved by mixing a portion of exact exchange with approximate local exchange functionals to form a hybrid functional. The most widely adopted of the hybrid functionals is the 3 parameter form of Becke [44] in which exact exchange is balanced with the LDA exchange functional of Eq. (1.143) and the B88 gradient dependent correction [45], with the weighting parameters optimised to minimise errors relative to the G2 benchmark dataset,

$$E_{\mathrm{xc}}^{\mathrm{B3LYP}} = E_{\mathrm{xc}}^{\mathrm{LDA}} + a(E_{\mathrm{x}}^{\mathrm{EXX}} - E_{\mathrm{x}}^{\mathrm{LDA}}) + bE_{\mathrm{x}}^{\mathrm{B88}} + c(E_{\mathrm{c}}^{\mathrm{LYP}} - E_{\mathrm{c}}^{\mathrm{VWN-LDA}}). \tag{1.149}$$

The success of this approach is evidenced by its position as the most commonly used of all quantum chemical methods, though the extensive use has revealed its deficiencies in predicting the properties and reactions of large chemical systems.

Using perturbation theory arguments Perdew [46] and Burke [47] derived a general expression for a hybrid functional constructed from any semi-local exchange-correlation functional as,

$$E_{\mathrm{xc}}^{\mathrm{hybrid}} = E_{\mathrm{xc}}^{\mathrm{(m)GGA}} + 0.25(E_{\mathrm{x}}^{\mathrm{HF}} - E_{\mathrm{x}}^{(m)GGA}), \tag{1.150}$$

and functionals such as PBE0 [48] have utilised this model to produce accurate hybrid functionals, without resorting to an empirical fitting.

In a similar manner to the mGGA functionals of Section 1.7.3, the orbital dependence of the exact exchange term requires the exchange-correlation potential of a hybrid functional to be different for each orbital, unless the more sophisticated OEP formalism of Chapter 7 is used to construct the proper multiplicative potential.

Chapter 2

Functionals in Current-Density-Functional Theory

The density-functional theory discussed in Chapter 1 is a complete description of the electronic structure of molecules in the absence of external fields but is fundamentally incomplete in the presence of a magnetic field. The presence of an electromagnetic field imposes additional challenges in practical calculations through gauge freedoms and basis set issues, these are discussed in Section 2.1.3 and Section 2.1.4 respectively. Additionally, the presence of an external magnetic field induces orbital currents in the electron density that must be accounted for within a density-functional theory. The formal inclusion of current density is discussed in Section 2.2 and the correct description of the current-density energy within the exchange-correlation functional is described in the remaining sections.

2.1 The quantum mechanics of electrons in magnetic fields

The purpose of this section is to derive a generalised density-functional theory suitable for the description of systems within a magnetic field, incorporating the electron current-density that arises. To this end we shall begin by reviewing the classical description of charged particles in external electromagnetic fields before adapting this classical model to a system of quantum particles.

A full quantum mechanical description of electromagnetic fields requires the theory of quantum electrodynamics and is beyond the scope of this work. Instead the electromagnetic fields will be treated using classical electrodynamics, giving a semi-classical treatment of molecules in electromagnetic fields. The difference in calculated molecular properties between a full quantum mechanical description of electromagnetic fields and a semi-classical description is expected to be small [49]. An exploration of the important gauge freedoms and their consequences follows, setting the stage for the formal derivation of a current-density-functional theory in Section 2.2.

2.1.1 Classical electromagnetism

The classical description of a charged particle in an electromagnetic field begins with the Lorentz law in combination with Maxwell's equations of electromagnetism in a vacuum. The Lorentz law, describes the force imparted on a particle with charge q by an external electromagnetic field,

$$\mathbf{F}(\mathbf{r},t) = q[\mathbf{E}(\mathbf{r},t) + \mathbf{v} \times \mathbf{B}(\mathbf{r},t)], \tag{2.1}$$

where $\mathbf{v}$ is the velocity of the particle, $\mathbf{E}$ and $\mathbf{B}$ are the vectors describing the electric and magnetic fields respectively, also known as the flux density and magnetic induction. Maxwell's equations of

electromagnetism in a vacuum are expressed in terms of these fields as,

$$\boldsymbol{\nabla} \cdot \mathbf{E}(\mathbf{r}, t) = 0, \tag{2.2}$$

$$\boldsymbol{\nabla} \cdot \mathbf{B}(\mathbf{r}, t) = 0, \tag{2.3}$$

$$\boldsymbol{\nabla} \times \mathbf{E}(\mathbf{r}, t) = -\frac{\partial \mathbf{B}(\mathbf{r}, t)}{\partial t}, \tag{2.4}$$

$$\boldsymbol{\nabla} \times \mathbf{B}(\mathbf{r}, t) = \frac{\partial \mathbf{E}(\mathbf{r}, t)}{\partial t}. \tag{2.5}$$

It is more convenient to express $\mathbf{E}$ and $\mathbf{B}$ in terms of scalar and vector potentials, ϕ and $\mathbf{A}$ respectively, chosen to satisfy the Maxwell equations,

$$\mathbf{E}(\mathbf{r}, t) = -\boldsymbol{\nabla}\phi(\mathbf{r}, t) - \frac{\partial \mathbf{A}(\mathbf{r}, t)}{\partial t}, \tag{2.6}$$

$$\mathbf{B}(\mathbf{r}, t) = \boldsymbol{\nabla} \times \mathbf{A}(\mathbf{r}, t). \tag{2.7}$$

The present work is concerned only with electromagnetic fields that are static and uniform across all space. Consequently ϕ and $\mathbf{A}$ satisfying Eq. (2.6) and Eq. (2.7) can be chosen as homogeneous in space and time giving,

$$\phi(\mathbf{r}) = -\mathbf{r} \cdot \mathbf{E}, \tag{2.8}$$

$$\mathbf{A}(\mathbf{r}) = \frac{1}{2}\mathbf{B} \times \mathbf{r}. \tag{2.9}$$

It is immediately apparent from the properties of the curl operator that ϕ and $\mathbf{A}$ are not uniquely defined by Eq. (2.8) and Eq. (2.9) and addition of the gradient of a time independent scalar gauge function $\chi(\mathbf{r})$ leaves the physical fields $\mathbf{E}$ and $\mathbf{B}$ unchanged,[1]

$$\mathbf{A}(\mathbf{r}) \rightarrow \mathbf{A}' = \mathbf{A}(\mathbf{r}) + \boldsymbol{\nabla} \cdot \chi(\mathbf{r}). \tag{2.10}$$

The observable electromagnetic field is represented equally well by $\mathbf{A}$ and $\mathbf{A}'$ and consequently all observable properties calculated from $\mathbf{A}$ and ϕ must be invariant to transformations that leave the observed field unchanged. This property means there is some freedom in the in choosing the potentials to represent an electromagnetic field. This freedom is referred to as choosing a gauge and must be handled with care in all aspects of calculations within a magnetic field. Gauge transformations are discussed in detail in Section 2.1.3.

With the scalar and vector potentials defined in Eq. (2.8) and Eq. (2.9) we may rewrite the Lorentz force arising from the electromagnetic field, Eq. (2.1), in terms of the vector and scalar fields,

$$\mathbf{F} = q\left\{-\boldsymbol{\nabla}\phi(\mathbf{r}) + \mathbf{v} \times \left[\boldsymbol{\nabla} \times \mathbf{A}(\mathbf{r})\right]\right\}. \tag{2.11}$$

2.1.2 The magnetic hamiltonian

In the real molecular system (and that defined by quantum electrodynamics) the internal fields intrinsic to the molecule dynamically enhance, resist and respond to the external fields. In the semi-classical approximation adopted at the beginning of this chapter however, the fields and nuclear magnetic moments are treated as external to the molecule and not part of the system, i.e. they do not respond to the presence of the molecule. This allows the fields and moments to enter the electronic Hamiltonian as external perturbations, similar to the Coulomb charges of the nuclei. Regarding the electromagnetic fields as external in this way is termed the *minimal coupling approximation*.

In order to derive the electronic Hamiltonian operator for a molecule in the presence of a magnetic field, we will first derive a classical Hamiltonian for a system of classical electrons in an external electromagnetic field that is a function of the electron positions and canonical momenta. When a classical Hamiltonian is known the quantum Hamiltonian operator may be constructed by substitution of the position and momentum variables with the corresponding operators.

[1] This follows from the properties of the gradient of a scalar field function, $\nabla \times (\nabla \cdot \chi(\mathbf{r})) = \mathbf{0}$.

The derivation of the classical Hamiltonian begins by considering the classical Lagrangian,

$$\mathcal{L}(\mathbf{r}, \mathbf{v}, t) = T(\mathbf{r}, \mathbf{v}, t) - U(\mathbf{r}, \mathbf{v}, t), \tag{2.12}$$

where T is the kinetic energy of the particles in positions $\mathbf{r}$ with velocities $\mathbf{v}$ at time t. The generalised potential, $U(\mathbf{r}, \mathbf{v}, t)$, is chosen such that when the Euler-Lagrange equations,

$$\frac{\mathrm{d}}{\mathrm{d}t}\left[\frac{\mathrm{d}\mathcal{L}}{\mathrm{d}\mathbf{v}}\right] - \frac{\mathrm{d}\mathcal{L}}{\mathrm{d}\mathbf{r}} = 0, \tag{2.13}$$

are applied to the Lagrangian of Eq. (2.12) Newton's second law is recovered,

$$\mathbf{F} = m\frac{\mathrm{d}\mathbf{v}}{\mathrm{d}t}. \tag{2.14}$$

An electron moving in an external magnetic field experiences the Lorentz force given by Eq. (2.11) which can be equated with Eq. (2.14),

$$\mathbf{F} = \nabla\phi(\mathbf{r}, t) + \frac{\partial \mathbf{A}(\mathbf{r}, t)}{\partial t} - \mathbf{v} \times [\nabla \times \mathbf{A}(\mathbf{r}, t)] = m_e\frac{\mathrm{d}\mathbf{v}}{\mathrm{d}t}, \tag{2.15}$$

where the electron mass $m_e = 1$ a.u. has been included for familiarity with Newton's second law, but is omitted henceforth. Eqs. (2.12) and (2.15) can be satisfied if the generalised potential is chosen as,

$$U(\mathbf{r}, \mathbf{v}, t) = -\phi(\mathbf{r}, t) + \mathbf{v} \cdot \mathbf{A}(\mathbf{r}, t), \tag{2.16}$$

giving the classical Lagrangian,

$$\mathcal{L}(\mathbf{r}, \mathbf{v}, t) = \frac{1}{2}\mathbf{v}^2 + \phi(\mathbf{r}, t) - \mathbf{v} \cdot \mathbf{A}(\mathbf{r}, t). \tag{2.17}$$

A classical Hamiltonian can be related to its corresponding Lagrangian through the Legendre transformation,[2]

$$H(\mathbf{r}, \mathbf{p}, t) = \mathbf{p} \cdot \mathbf{v} - \mathcal{L}(\mathbf{r}, \mathbf{v}, t). \tag{2.18}$$

A generalised momentum vector $\mathbf{p}$ can be identified from Eq. (2.17) through the application of

$$\mathbf{p} = \frac{\partial \mathcal{L}(\mathbf{r}, \mathbf{v}, t)}{\partial \mathbf{v}}, \tag{2.19}$$

to produce the canonical electron momentum $\mathbf{p}$,

$$\mathbf{p} = \mathbf{v} - \mathbf{A}(\mathbf{r}, t). \tag{2.20}$$

In the presence of electromagnetic fields the canonical momentum $\mathbf{p}$ is no longer equal to the product of mass and velocity and, as the kinetic energy for a classical particle is,

$$T = \frac{\mathbf{p}^2}{2m}, \tag{2.21}$$

it is convenient to define a physical momentum[3] $\boldsymbol{\pi}$ as,

$$\boldsymbol{\pi} \equiv m\mathbf{v} = \mathbf{p} + q\mathbf{A}(\mathbf{r}, t), \tag{2.22}$$

where m and q are the particle's mass and charge respectively such that in a field,

$$T = \frac{\pi^2}{2m}. \tag{2.23}$$

The physical momentum of Eq. (2.22) is utilised in Section 2.4.2 in the formation of a gauge invariant physical kinetic energy density, τ_{MS}.

[2] The Legendre transformation is a less general form of the Legendre–Fenchel transform discussed in Section 1.5.6. This identifies the Lagrangian and the Hamiltonian as convex conjugates with the velocities and conjugated momenta related as conjugate variables.

[3] Also known as *kinematical*, *mechanical* or *gauge invariant* momentum.

Inserting Eq. (2.20) into Eq. (2.18) gives the classical Hamiltonian for a system of electrons in an electromagnetic field in terms of the canonical momentum as,

$$\mathcal{H} = \frac{1}{2}[\mathbf{p} + \mathbf{A}(\mathbf{r}, t)]^2 - \phi(\mathbf{r}, t). \tag{2.24}$$

A Hamiltonian operator for a quantum system of electrons can be constructed from Eq. (2.24) by substitution of the classical variables with the appropriate operators,

$$\mathbf{p} \to \hat{\mathbf{p}} = -i\hat{\nabla}, \tag{2.25}$$

to give

$$\hat{H} = \frac{1}{2}[\hat{\mathbf{p}} + \hat{\mathbf{A}}(\mathbf{r}, t)]^2 - \hat{\phi}(\mathbf{r}, t), \tag{2.26}$$

where the potentials have been substituted for multiplicative operators. The Coulomb gauge is defined by imposing that the vector potential be divergence free,

$$\boldsymbol{\nabla} \cdot \mathbf{A} = \mathbf{0}, \tag{2.27}$$

which can be imposed without effecting the magnetic induction. The Hamiltonian operator for a single electron in an external electromagnetic field can be expanded in the Coulomb gauge as,

$$\hat{H} = \frac{1}{2}\hat{\mathbf{p}}^2 + \hat{\mathbf{A}}(\mathbf{r}, t) \cdot \hat{\mathbf{p}} + \frac{1}{2}\hat{\mathbf{A}}(\mathbf{r}, t)^2 - \hat{\phi}(\mathbf{r}, t) \tag{2.28}$$

The electron spin does not appear within the Schrödinger description of quantum mechanics and in order to account for the important interaction of the electron spin with the external field we must consider the non-relativistic limit of the Dirac equation. The reader is referred to Ref. [50] for a full derivation. Here we utilise the result as an additional additive term within the one electron Hamiltonian, the spin Zeeman term,

$$\hat{H}^{\text{Zeeman}} = \frac{g_e}{2}\hat{\mathbf{s}} \cdot \left[\hat{\nabla} \times \hat{\mathbf{A}}(\mathbf{r}, t)\right], \tag{2.29}$$

where $\hat{\mathbf{s}} = (1/2)\boldsymbol{\sigma}$ is the electron spin operator, $\boldsymbol{\sigma}$ are the Pauli spin matrices and g_e is the electron *g-factor* calculated from quantum electrodynamics as $g_e \approx 2.0023$.

The full spin-Zeeman term including one-electron Hamiltonian is therefore,

$$\hat{H} = \frac{1}{2}[\hat{\mathbf{p}} + \hat{\mathbf{A}}(\mathbf{r}, t)]^2 - \hat{\phi}(\mathbf{r}, t) + \frac{g_e}{2}\hat{\mathbf{s}} \cdot \left[\hat{\nabla} \times \hat{\mathbf{A}}(\mathbf{r}, t)\right]. \tag{2.30}$$

By comparison with the electronic Hamiltonian of Eq. (1.5) a many electron spin-including Hamiltonian can be produced through the addition of the electron-electron Coulomb repulsion operator,

$$\hat{H} = \sum_i \frac{1}{2}[\hat{\mathbf{p}}_i + \hat{\mathbf{A}}(\mathbf{r}_i, t)]^2 + \sum_{i<j} \frac{1}{|\mathbf{r}_i - \mathbf{r}_j|} - \sum_i \hat{\phi}(\mathbf{r}_i, t) + \sum_i \frac{g_e}{2}\hat{\mathbf{s}} \cdot \left[\hat{\nabla} \times \hat{\mathbf{A}}(\mathbf{r}_i, t)\right]. \tag{2.31}$$

It is instructive to decompose the Hamiltonian of Eq. (2.31) into unperturbed and perturbed Hamiltonians,

$$\hat{H} = \hat{H}^{(0)} + \hat{H}^{(1)} + \hat{H}^{(2)} \tag{2.32}$$

$$= \sum_i^N \hat{h}^{(0)} + \sum_{i<j} \hat{g}(i, j) + \sum_i^N \hat{h}^{(1)} + \sum_i^N \hat{h}^{(2)} \tag{2.33}$$

with $\hat{h}$ and $\hat{g}$ denoting one and two electron operators respectively.

The unperturbed operators are identified as the one and two electron operators in the absence of an electromagnetic field,

$$\hat{h}^{(0)} = -\frac{1}{2}\hat{\mathbf{p}}_i^2 - \sum_K^M \frac{Z_K}{|\mathbf{r}_i - \mathbf{R}_k|},$$

$$\hat{g}^{(0)} = \frac{1}{|\mathbf{r}_i - \mathbf{r}_j|}.$$

The linear field perturbations are collected into $\hat{h}^{(1)}$,

$$\hat{h}^{(1)} = \hat{\mathbf{A}}(\mathbf{r}_i) \cdot \hat{\mathbf{p}}_i + \frac{g_e}{2} \hat{\mathbf{s}}_i \cdot \left[\boldsymbol{\nabla} \times \hat{\mathbf{A}}(\mathbf{r}_i) \right] - \hat{\phi}(\mathbf{r}_i), \tag{2.34}$$

and the quadratic perturbations are collected into $\hat{h}^{(2)}$,

$$\hat{h}^{(2)} = \frac{1}{2} \hat{\mathbf{A}}^2(\mathbf{r}_i). \tag{2.35}$$

2.1.3 Gauge transformations

With the many electron Hamiltonian of Eq. (2.31) in place the approximate schemes of Sections 1.2, 1.4.1 and 1.4.2 can be modified according to the field dependent Hamiltonian of Eq. (2.31) and used to carry out practical calculations within a magnetic field. However, as noted in Section 2.1.1 the potentials ϕ and $\mathbf{A}$ are not uniquely defined by Eqs. (2.8) and (2.9) and a gauge transformation can be made that changes the potentials whilst leaving the observable electromagnetic field unchanged. For example,

$$\mathbf{A}(\mathbf{r}, t) \rightarrow \mathbf{A}(\mathbf{r}, t)' = \mathbf{A}(\mathbf{r}, t) + \nabla \chi(\mathbf{r}, t) \tag{2.36}$$

$$\phi(\mathbf{r}, t) \rightarrow \phi(\mathbf{r}, t)' = \phi(\mathbf{r}, t) - \frac{\mathrm{d}\chi(\mathbf{r}, t)}{\mathrm{d}t} \tag{2.37}$$

produces the potentials $\mathbf{A}(\mathbf{r}, t)'$ and $\phi(\mathbf{r}, t)'$ that also satisfy Eqs. (2.6) and (2.7) for any choice of scalar function $\chi(\mathbf{r}, t)$. Understanding how internal quantities respond to this gauge transformation reveals important restrictions on how approximations to Eq. (2.31) may be constructed.

All fields considered in this work are homogeneous in space and time and as a result the only gauge transformation that must be explicitly considered is a transformation of the vector potential,

$$\mathbf{A}(\mathbf{r})' = \mathbf{A}(\mathbf{r}) + \nabla \chi(\mathbf{r}). \tag{2.38}$$

The vector potential $\mathbf{A}$ directly enters the molecular Hamiltonian of Eq. (2.31) and its gauge transformation must leave the physical observables, such as the energy, unaltered. Upon a gauge transformation of the vector potential by Eq. (2.38) the electronic Hamiltonian operator transforms as,

$$\hat{H} \rightarrow \hat{H}' = \exp\left[-\mathrm{i} \sum_i \chi(\mathbf{r}_i) \right] \hat{H} \exp\left[\mathrm{i} \sum_i \chi(\mathbf{r}_i) \right]. \tag{2.39}$$

In order for the energy expectation value to remain constant the Hamiltonian transformation must be accompanied by a simultaneous transformation of the electronic wave function,

$$|\Psi\rangle \rightarrow |\Psi'\rangle = \exp\left[-\mathrm{i} \sum_i \chi(\mathbf{r}_i) \right] \cdot |\Psi\rangle, \tag{2.40}$$

and we must take care that any approximate wave functions also have this freedom.

Note that it is not required that all operators have a gauge invariant expectation value, only those that correspond to a physically observable property. For example, the canonical momentum, $\hat{\mathbf{p}}_i$, changes under gauge transformation, whereas the physically observable mechanical momentum $\hat{\boldsymbol{\pi}}_i$ of Eq. (2.22) does not.

2.1.4 Basis sets for strong magnetic fields - London atomic orbitals

The most important gauge transformation for the computational implementations in this work is the movement of an arbitrary gauge origin $\mathbf{R}_G$ relative to the coordinate origin, described by the function,

$$\chi(\mathbf{r}_i) = -\frac{1}{2} \mathbf{B} \times \mathbf{R}_G \cdot \mathbf{r}_i. \tag{2.41}$$

Transformation of $\mathbf{A}$ with this gauge function through Eq. (2.38) gives the transformed potential as,

$$\mathbf{A}(\mathbf{r}_i) = \frac{1}{2}\mathbf{B} \times (\mathbf{r}_i - \mathbf{R}_G). \tag{2.42}$$

The corresponding wave function transformation is given by application of Eq. (2.40) as,

$$\Psi_{\mathbf{R}_G} = \exp\left[\mathrm{i}\mathbf{A}(\mathbf{R}_G) \cdot \mathbf{r}\right] \cdot \Psi_{\mathbf{0}}. \tag{2.43}$$

Whilst a wave function represented by a *complete* basis set of Gaussian (GTO) or Slater functions (STO) can capture this transformation, the convergence of a finite GTO basis set to the gauge-origin invariant limit is too slow to be practically obtainable in even the simplest molecules. A new finite basis expansion is required.

Convergence to the basis set limit is accelerated by modifying the basis functions to account for the gauge-origin freedom directly. A suitable modification to standard GTO functions was proposed by Fritz London in 1937 as a multiplicative complex phase factor derived from the wave function gauge origin transformation,

$$\omega(\mathbf{r}_K, \mathbf{B}, \mathbf{R}_G) = \exp\left[-\mathrm{i}\frac{1}{2}\mathbf{B} \times (\mathbf{R}_G - \mathbf{R}_K) \cdot \mathbf{r}\right] \cdot \phi(\mathbf{r}_K), \tag{2.44}$$

where $\phi(\mathbf{r}_K)$ is a standard GTO function. The modified basis functions, termed London atomic orbitals (LAO) or gauge-origin including atomic orbitals (GIAO)[4] directly accommodate the gauge origin transformation of the wave function to first order within the basis functions giving a rapid convergence to gauge origin invariance at modest basis set sizes.

Calculations performed with an inflexible basis set, and hence a gauge-origin variant wave function, will always produce physically meaningless results. This is illustrated in Figure 2.1 in which the dissociation energy curves for the H_2 molecule have been calculated using FCI theory with LAO and standard GTO basis sets. In the absence of a magnetic field the complex phase factor of the LAO functions have a value of one and the calculations are equivalent, as should be expected. In the presence of a field the size consistency of FCI is broken for the GTO basis sets and a considerable inaccuracy is seen at equilibrium bond lengths. The equivalent calculations performed using a basis of LAOs do not show these artefacts, giving a correctly size consistent dissociation and proper accuracy in all regions.

The inclusion of the complex phase factor into LAO functions requires additional computational machinery to evaluate the now complex integrals. As such, implementing a self consistent scheme for LAOs into standard computational packages requires a considerable degree of implementation work and has not previously been undertaken. To address this deficiency the LONDON program was purpose built to carry out self consistent field calculations of molecules in finite magnetic fields, utilising LAO basis sets [11, 51]. The work described in Chapters 2, 4 and 5 uses and extends the LONDON program to investigate the performance of current-density functionals in both strong and weak magnetic fields. All calculations in magnetic fields were carried out using LAO basis sets within the LONDON program to ensure correctly gauge-origin invariant results.

On a practical note, very strong magnetic fields, $||\mathbf{B}|| \gg 1$ a.u. $= 2.35 \times 10^5$ T result in a substantial deformation and compression of atomic orbitals [52–55]. In such fields, the standard isotropic GTOs of Eq. (1.40) are ill suited for the expansion of the electron wave function and an anisotropic basis set must be employed to account for the deformations. Without direct comparison between isotropic and anisotropic basis sets it is difficult to directly assess the effects of using anisotropic basis functions. Instead calculations are restricted to a relatively modest range of fields in the range $||\mathbf{B}|| \leq 1$ a.u. in which the distortion is expected to be sufficiently small and well represented by large, un-contracted isotropic LAO basis sets augmented with additional polarisation functions. The implementation of anisotropic basis functions within the LONDON program would offer a unique opportunity to define a more accurate confidence limit for the use of isotropic LAO basis sets and is suggested for future investigation.

[4] It is common to see GIAOs erroneously referred to as gauge *invariant* atomic orbitals. This is a misnomer. The basis functions themselves vary significantly under gauge transformation in order that the calculated observables remain invariant. The term gauge-origin *including* atomic orbitals is to be preferred.

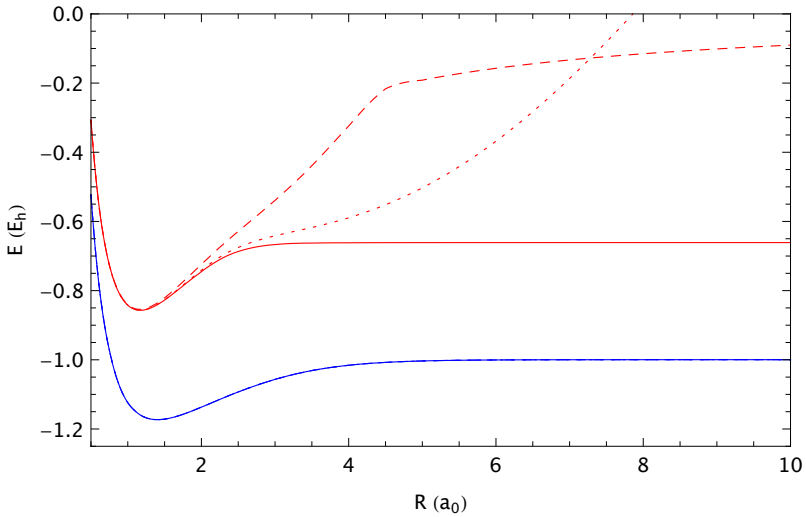


Figure 2.1: The energy of the H_2 molecule as a function of inter-nuclear separation, R, calculated using FCI / aug-cc-pCVTZ basis set. The interaction curves for $\mathbf{B} = 0.0$ (blue) and 1.0 a.u. (red) are calculated using an LAO basis set (solid) and standard GTO basis sets with the gauge origin $\mathbf{R}_G$ chosen at the center of the bond (dotted) and at the position of one nucleus (dashed).

2.1.5 The Born–Oppenheimer approximation in strong magnetic fields

In the absence of a perturbing electromagnetic field the Born–Oppenheimer approximation has proven very reliable when the electronic energy levels are well separated, with errors on the order of the ratio of electron and nuclear masses [56]. In the presence of an external electromagnetic field however it is not so simple. The origin of the Born–Oppenheimer approximation lies in setting the internal nuclear velocities to zero, in direct conflict with the velocity dependent forces imposed on the nuclei through the vector potential through Eq. (2.11). Furthermore, a Born–Oppenheimer treatment of the nuclei does not allow the screening of the nuclear magnetic fields by the electrons, treating them instead as 'naked charges', as well as omitting the magnetic field dependent non-adiabatic coupling between electronic and nuclear motions that becomes increasingly important as the magnetic field strength grows. These deficiencies give reason to question the validity of the Born–Oppenheimer approximation in a magnetic field, especially as the field grows stronger and the non-adiabatic effects become more pronounced.

The validity of the Born–Oppenheimer approximation in the presence of strong magnetic fields is summarised by Schmelcher *et al.* in Ref. [57] and discussed in detail in Ref. [58]. Care is advised at higher field strengths in light of their analysis of the increasing significance of non-adiabatic effects. Unfortunately the field strength at which the non-adiabatic effects become significant is highly system dependent and can only be assessed by their direct calculation. Due to the prohibitive cost associated with such calculations a full analysis for molecular systems is beyond the scope of the current work.

In practice, the uncertainty in non-Born–Oppenheimer effects will never be encountered when isotropic London GTO type basis are employed as the inflexibility of the basis set (discussed in Section 2.1.4) becomes an issue far before non-adiabatic difficulties are encountered. As a result of both uncertainties a conservative rule of thumb has been employed: all calculations are restricted to field strengths $||\mathbf{B}|| \leq 1$ atomic units, encompassing the majority of naturally occuring field strengths found for all but the strongest magnetars [3, 4].

2.2 Current-density-functional theory

The generalisation of wave function methods to account for strong external magnetic fields simply requires the addition of vector potential terms and a generalisation of operators.[5] One may hope that the equivalent generalisation of DFT will be as simple, however an additional complexity is required to account for the electronic current-density induced within the molecule by the external field. A non-zero current-density requires the basic variables of DFT to be expanded to include an additional dependency on the paramagnetic current density, giving current-density-functional theory (CDFT). The following discussion on the derivation of CDFT follows the work of Tellgren *et al.* [59] in which CDFT is derived through the convex analysis techniques of Section 1.5.6, building on the initial derivation of a Hohenberg–Kohn like CDFT by Vignale *et al.* in Ref. [2].

2.2.1 The current-density

The derivation of CDFT begins by considering the Hamiltonian for molecular systems in the presence of an external magnetic field, derived in the preceding section,

$$\hat{H} = \sum_i \frac{1}{2}[\hat{\mathbf{p}}_i + \hat{\mathbf{A}}(\mathbf{r}_i, t)]^2 + \sum_{i<j} \frac{1}{|\mathbf{r}_i - \mathbf{r}_j|} - \sum_i \hat{\phi}(\mathbf{r}_i, t), \tag{2.45}$$

where the spin Zeeman term has been omitted as its inclusion does not significantly alter the subsequent analysis. The Raylegh–Ritz variation principle of Section 1.5.1 in the presence of a vector potential can be expressed as,

$$E[v, \mathbf{A}] = \inf_{\Psi} \left[\left\langle \Psi \middle| \hat{H} \middle| \Psi \right\rangle \right] \tag{2.46}$$

where the infimum ensures that the energy is well defined when $\hat{H}[v, \mathbf{A}]$ has no bound ground state. As in Eq. (1.78) the set of potentials that support a ground state are the members of the set,

$$\mathcal{V}_N = \{(v, \mathbf{A}) \,|\, \hat{H}[v, \mathbf{A}] \text{ has a ground state } \Psi\}. \tag{2.47}$$

The non-zero vector potential arising from the external magnetic field[6] induces currents in the electron density that have a non-negligible energetic contribution and increase in magnitude with increasing field strength. The observable *physical current-density* is defined from the orbitals of Ψ as,

$$\mathbf{j}(\mathbf{r}) = \mathrm{Re}\left[\sum_{ij}^{\text{occ.}} \left(\int \varphi_i^* \hat{\mathbf{p}}_j \varphi_i + \rho \mathbf{A} \, \mathrm{d}\omega \mathrm{d}\mathbf{x}_2, \ldots . \mathbf{x}_N \right) \right], \tag{2.48}$$

where the integral is over all N spin and spatial coordinates except $\mathbf{r}_1$. The physical current density can be decomposed into two terms, identified as: a *paramagnetic current-density*,

$$\mathbf{j}_p(\mathbf{r}) = -\frac{\mathrm{i}}{2} \sum_i^{\text{occ.}} \left[\varphi_i^*(\mathbf{r}) \nabla \varphi_i(\mathbf{r}) - \varphi_i(\mathbf{r}) \nabla \varphi_i^*(\mathbf{r}) \right]. \tag{2.49}$$

and a *diamagnetic current-density*,

$$\mathbf{j}_d(\mathbf{r}) = \rho(\mathbf{r}) \mathbf{A}(\mathbf{r}). \tag{2.50}$$

The physical current-density is an observable quantity and hence must be gauge invariant, its components however, the dia- and para-magnetic current-densities, are not observable and vary (in an equal and opposite amount) with gauge transformation.

A set of v-representable physical and paramagnetic current-densities can be identified as,

$$\mathcal{B}_N = \{(\rho, \mathbf{j}) \mid (\rho, \mathbf{j}) \text{ is a ground state density of some } \hat{H}[v, \mathbf{A}]\}, \tag{2.51}$$

$$\mathcal{B}_N^p = \{(\rho, \mathbf{j}_p) \mid (\rho, \mathbf{j}_p) \text{ is a ground state density of some } \hat{H}[v, \mathbf{A}]\}. \tag{2.52}$$

[5] An easy generalisation on paper, but considerable work to implement for practical calculations.

[6] A non-zero current-density is also found in some open-shell systems, such as the carbon atom. A rigorous treatment of such systems must also follow a CDFT formalism.

The absence of a Hohenberg–Kohn theorem

The first Hohenberg–Kohn theorem (Theorem 1.5.3) states that the ground state electron density ρ determines the potential v to within a constant, giving a bijective mapping of the ground-state densities to potentials. Using a similar approach, the 1988 paper of Vignale and Rasolt [2] showed that two different scalar-vector potential pairs with different ground state wave functions cannot give the same ground state paramagnetic current-densities,

$$(v_1, \mathbf{A}_1) \neq (v_2, \mathbf{A}_2), \text{ and } \Psi_1 \neq \Psi_2 \;\Rightarrow\; (\rho_1, \mathbf{j}_{p,1}) \neq (\rho_2, \mathbf{j}_{p,2}). \tag{2.53}$$

The proof given by Vignale and Rasolt is insufficient to form a full Hohenberg–Kohn like theorem for CDFT however, as it does not consider the situation in which two different potential pairs have the same ground state wave functions. When the wave functions are the same the paramagnetic ground state densities are the same and the bijective mapping between potentials and current-densities is prevented.

This failure was noted in Ref. [60] and is illustrated with a simple example. Consider an atom with nuclear charge Z subject to a uniform magnetic field of strength B aligned with the z axis, the Hamiltonian for this system is,

$$\hat{H} = \sum_i \left(\frac{\hat{\mathbf{p}}_i^2}{2} - \frac{Z}{\mathbf{r}_i} + \frac{\mathbf{B}^2 r_{\perp,i}^2}{8} \right) + \sum_{i \neq j} \frac{1}{2r_{ij}} + \frac{\hat{L}_z + 2\hat{S}_z}{2} B, \tag{2.54}$$

where $r_{\perp,i}^2 \equiv r_{x,i}^2 + r_{y,i}^2$ and $\hat{L}_z$ and $\hat{S}_z$ are the z components of the orbital and spin angular-momentum operators $\hat{\mathbf{L}}$ and $\hat{\mathbf{S}}$. Both $\hat{L}_z$ and $\hat{S}_z$ are constants of motion so a non-degenerate ground state of $\hat{H}$ is also an eigenstate of $\hat{L}_z$ and $\hat{S}_z$ with eigenvalues m_L and m_S.

Consider now the same atom in a different uniform magnetic field along z with strength B' and the external scalar potential,

$$v'(\mathbf{r}) = -\frac{Z}{r} - \frac{1}{8}(B'^2 - B^2) r_\perp^2. \tag{2.55}$$

The Hamiltonian for this system can be written in terms of $\hat{H}$ for the original atomic system as,

$$\hat{H}' = \hat{H} + \frac{1}{2}(\hat{L}_z + 2\hat{S}_z)(B' - B). \tag{2.56}$$

As the Hamiltonian of the modified system can be written in terms of the original plus a constant any ground state of $\hat{H}$ must also be a ground state of $\hat{H}'$ with the eigenvalue,

$$E' = E_0 + \frac{1}{2}(m_L + 2m_S)(B' - B). \tag{2.57}$$

If the difference $B' - B$ is not too large then this eigenstate will be the ground state for both $\hat{H}$ and $\hat{H}'$.

As the two different Hamiltonians have been shown to have the same ground state wave functions and eigenvalues we have shown that two different potentials $(v, \mathbf{A} = \mathbf{B} \times \mathbf{r})/2$ and $(v', \mathbf{A}' = \mathbf{B} \times \mathbf{r})/2$ can yield the same ground state wave functions and hence paramagnetic densities.

No bijective mapping from ground state densities to potentials can be made, so it is not possible to derive a full Hohenberg–Kohn like theorem for CDFT. This is not fatal however as the rigorous definition of standard DFT through the Lieb functional does not require such a bijective mapping. The definition of CDFT will therefore continue through the convex conjugation technique of the Legendre–Fenchel transform.

2.2.2 CDFT by constrained search

The field free energy functional of Eq. (1.116) has the important property of being concave with respect to a change in v, allowing a duality with the universal functional $F[\rho]$. In the presence of a non-zero vector potential however $E[v, \mathbf{A}]$ is not concave. The absence of concavity prevents the

representation of $E[v, \mathbf{A}]$ through a convex conjugate function but does not prevent a constrained search formulation of CDFT entirely. A constrained search type variation principle is constructed by analogy with the Levy–Lieb constrained search of Eq. (1.105) to give,

$$E[v, \mathbf{A}] = \inf_{(\rho, \mathbf{j}_p)} \left[F_{\mathrm{VR}}[\rho, \mathbf{j}_p] + \left(\rho \middle| v + \frac{1}{2} A^2 \right) + (\mathbf{j}_p | \mathbf{A}) \right] \tag{2.58}$$

in which,

$$(\mathbf{j}_p | \mathbf{A}) = \int \mathbf{j}_p(\mathbf{r}) \cdot \mathbf{A}(\mathbf{r}) \mathrm{d}\mathbf{r}, \tag{2.59}$$

is the pairing between paramagnetic current density and vector potential.

The Vignale–Rasolt constrained search functional is defined in Eq. (2.58) as,

$$F_{\mathrm{VR}}[\rho, \mathbf{j}_p] = \inf_{\Psi \mapsto (\rho, \mathbf{j}_p)} \left\langle \Psi \middle| \frac{1}{2} \hat{\mathbf{p}}^2 + \hat{W} \middle| \Psi \right\rangle, \tag{2.60}$$

in which F_{VR} is a universal functional, depending only on the paramagnetic density $(\rho, \mathbf{j}_p)$.

To establish the convexity of F_{VR} let $(\rho_1, \mathbf{j}_{p,1})$ and $(\rho_2, \mathbf{j}_{p,2})$ be arbitrary Lebesgue integrable functions and $(\lambda\rho_1 + (1-\lambda)\rho_2,\, \lambda\mathbf{j}_{p,1} + (1-\lambda)\mathbf{j}_{p,2})$ be a linear interpolation between them with $0 < \lambda < 1$. The convexity is then shown by,

$$\begin{aligned} &F_{\mathrm{VR}}[\lambda\rho_1 + (1-\lambda)\rho_2, \lambda\mathbf{j}_{p,1} + (1-\lambda)\mathbf{j}_{p,2}] \\ &\quad \leq \inf_{\substack{\Psi_1 \mapsto (\rho_1, \mathbf{j}_{p,1}) \\ \Psi_2 \mapsto (\rho_2, \mathbf{j}_{p,2})}} \left\langle \lambda\Psi_1 + (1-\lambda)\Psi_2 \middle| \frac{1}{2} \hat{\mathbf{p}}^2 + \hat{W} \middle| \lambda\Psi_1 + (1-\lambda)\Psi_2 \right\rangle \\ &\quad = \lambda F_{\mathrm{VR}}[\rho_1, \mathbf{j}_{p,1}] + (1-\lambda) F_{\mathrm{VR}}[\rho_2, \mathbf{j}_{p,2}]. \end{aligned} \tag{2.61}$$

The convexity follows as the infimum over the wavefunctions $\Psi_1 \mapsto (\rho_1, \mathbf{j}_{p,1})$ and $\Psi_2 \mapsto (\rho_2, \mathbf{j}_{p,2})$ is restricted, where an infimum over $\Psi \mapsto (\lambda\rho_1 + (1-\lambda)\rho_2,\, \lambda\mathbf{j}_{p,1} + (1-\lambda)\mathbf{j}_{p,2})$ is able to relax to a lower energy.

As $F_{\mathrm{VR}}[\rho, \mathbf{j}_p]$ is convex it can be exactly represented by a convex conjugate through the Legendre–Fenchel transform, in the case of standard DFT this relationship is between $F[\rho]$ and $E_0[v]$. It has already been shown that $E[v, \mathbf{A}]$ is not convex, so $E[v, \mathbf{A}]$ cannot be the convex conjugate to the Vignale–Rasolt universal functional $F_{\mathrm{VR}}[\rho, \mathbf{j}_p]$. An appropriate energy conjugate must be identified.

2.2.3 CDFT by convex conjugation

In order to build an energy functional through the Legendre–Fenchel transform a change of variables must be made, modifying the basic scalar potential to introduce a dependence on the vector potential,

$$u = v + \frac{1}{2} A^2, \tag{2.62}$$

showing u as the members of the set defined as,

$$\mathcal{U}_N = \{ (v + \frac{1}{2} A^2, \mathbf{A}) \mid \hat{H}[v, \mathbf{A}] \text{ has a ground state } \Psi \}. \tag{2.63}$$

The modified scalar potential u allows a Hohenberg–Kohn variation principle to be constructed from a Legendre–Fenchel transform of the CDFT universal functional with a linear pairing $(\rho|u) + (\mathbf{j}_p|\mathbf{A})$ of the densities and potentials,

$$\begin{aligned} E[u - \frac{1}{2} A^2, \mathbf{A}] &= \inf_{\Psi} \left\langle \Psi \middle| \hat{H}[u - \frac{1}{2} A^2, \mathbf{A}] \middle| \Psi \right\rangle \\ &= \inf_{\rho, \mathbf{j}_p} [F_{\mathrm{VR}}[\rho, \mathbf{j}_p] + (\rho|u) + (\mathbf{j}_p|\mathbf{A})] \end{aligned} \tag{2.64}$$

The energy of $E[u - \frac{1}{2}A^2, \mathbf{A}]$ is concave by construction and gives $F_{\mathrm{VR}}[\rho, \mathbf{j}_p]$ under a further Legendre–Fenchel transformation, as required,

$$E[u - \frac{1}{2}A^2, \mathbf{A}]^* = F_{\mathrm{VR}}[\rho, \mathbf{j}_p] = \sup_{u,\mathbf{A}} \left[E[u - \frac{1}{2}A^2] - (\rho|u) - (\mathbf{j}_p|\mathbf{A}) \right]. \tag{2.65}$$

The corresponding vector space of densities, $\mathcal{X}_p$, and its dual space of potentials, $\mathcal{X}^*$, are yet to be determined and the authors of Ref. [59] note that some difficulty may be encountered as a result of the gauge freedoms of the vector potential $\mathbf{A} + \nabla\chi$. The gauge function χ may be any scalar function and can therefore be arbitrarily ill-behaved, introducing a difficulty for defining the space of allowed potentials. Tellgeren *et al.* propose that some gauge restrictions should be imposed in order to define the domains of $F[\rho, \mathbf{j}_p]$ and $E[u - \frac{1}{2}A^2, \mathbf{A}]$.[7]

2.2.4 The choice of basic variables

It is intuitively pleasing that the basic variable of standard DFT is an observable quantity, the electron density. The same cannot be said for a formulation of CDFT built upon the paramagnetic current density, $\mathbf{j}_p$. The paramagnetic current density is *not* an observable quantity, though the physical current density $\mathbf{j}$ *is* observable. A natural question arises: can a CDFT be built with the physical densities $(\rho, \mathbf{j})$ as its basic variables? Whilst it has not been conclusively shown that a CDFT cannot be constructed around the physical densities, mathematical intuition suggests it unlikely that a theory dealing with gauge dependent vector potentials and wave functions can be formed from gauge independent variables.

A number of attempts have been made by various groups to formulate CDFT around the physical current-density [61–63], but to date none have been successful. Most notably Pan and Sahni attempted to derive a Hohenberg–Kohn style theorem, arguing that potentials $(v, \mathbf{A}) \nsim (v', \mathbf{A}')$ that differ by more than a gauge transformation cannot yield the same density $(\rho_0, \mathbf{j}_0) = (\rho_0', \mathbf{j}_0')$ [61, 62]. The proof was shown to be in error however [59, 64]. The core difficulty with constructing CDFT around the physical current-density is that given a wave function, it is impossible to determine the physical current-density without knowledge of the vector potential. The undetermined physical current-density becomes a problem when the energy functional is constructed,

$$E_{v,\mathbf{A}}[\rho, \mathbf{j}] = F_{\mathrm{PS}}[\rho, \mathbf{j}] + \int \mathbf{j}(\mathbf{r}) \cdot \mathbf{A}(\mathbf{r}) \mathrm{d}\mathbf{r} - \frac{1}{2} \int \rho(\mathbf{r}) A^2(\mathbf{r}) \mathrm{d}\mathbf{r} + \int \rho(\mathbf{r}) v(\mathbf{r}) \mathrm{d}\mathbf{r}, \tag{2.66}$$

in which the Pan–Sahni universal functional is the expectation of the many body Hamiltonian with the ground state wave function defined by $(\rho, \mathbf{j})$. It is impossible to form $F_{\mathrm{PS}}[\rho, \mathbf{j}]$ as the minimisation of $\langle \Psi | \hat{T} + \hat{W} | \Psi \rangle$ over the set of wave functions that yield ρ and $\mathbf{j}$ as, this set of densities cannot be defined without first defining a fixed $\mathbf{A}$.

If the vector potential $\mathbf{A}$ is fixed then one returns to the Vignale–Rasolt universal functional [2] $F_{\mathrm{VR}}[\rho, \mathbf{j}_p]$ of Eq. (2.60), as the paramagnetic current and the physical current have become essentially the same variable, $\mathbf{j} = \mathbf{j}_p + \rho\mathbf{A}$. Consequently a minimisation with respect to $\mathbf{j}$ and ρ at constant $\mathbf{A}$ is equivalent to a minimisation with respect to $\mathbf{j}_p$ and ρ.

2.2.5 Kohn–Sham current density functional theory

The construction of a CDFT scheme amenable for practical calculations of molecules in magnetic fields proceeds similarly to standard DFT through a Kohn–Sham like decomposition of the universal functional [2],

$$F[\rho, \mathbf{j}_p] = T_s[\rho, \mathbf{j}_p] + \iint \frac{\rho(\mathbf{r})\rho(\mathbf{r}')}{|\mathbf{r} - \mathbf{r}'|} \mathrm{d}\mathbf{r}\mathrm{d}\mathbf{r}' + E_{\mathrm{xc}}[\rho, \mathbf{j}_p]. \tag{2.67}$$

The non-interacting kinetic energy functional $T_s[\rho, \mathbf{j}_p]$ is the expectation value of the usual kinetic energy operator, Eq. (1.128), operating on an auxiliary system of N non-interacting electrons with the same paramagnetic density $(\rho, \mathbf{j}_p)$ as the interacting system. As in Section 1.6 this non-interacting

[7] Though the gauge restrictions would not have any physical interpretation.

auxiliary system is constructed as a Slater determinant of complex valued orbitals, related to the physical system as,

$$\rho(\mathbf{r}) = \sum_{i=1}^{N} |\varphi_i(\mathbf{r})|^2, \tag{2.68}$$

$$\mathbf{j}_p(\mathbf{r}) = -\frac{\mathrm{i}}{2} \sum_{i=1}^{N} \left[\varphi_i^*(\mathbf{r}) \nabla \varphi_i(\mathbf{r}) - \nabla \varphi_i^*(\mathbf{r}) \varphi_i(\mathbf{r})\right]. \tag{2.69}$$

The second term of Eq. (2.67) is the classical Coulomb interaction of the density with itself and $E_{\mathrm{xc}}[\rho, \mathbf{j}_p]$ is the XC energy functional, the form of which is the focus of this chapter.

By construction the non-interacting Slater determinant wave function $\Psi[\rho, \mathbf{j}_p]$ is comprised of the N lowest lying one electron solutions of the one electron Schrödinger equation,

$$\left[\frac{1}{2}\hat{\mathbf{p}}^2 + \hat{\mathbf{p}} \cdot \mathbf{A}_{\mathrm{s}}(\mathbf{r}) + u_{\mathrm{s}}(\mathbf{r})\right] \varphi_i(\mathbf{r}) = \epsilon_i \varphi_i(\mathbf{r}), \tag{2.70}$$

The effective scalar $u_{\mathrm{s}}(\mathbf{r})$ and vector $\mathbf{A}_{\mathrm{s}}(\mathbf{r})$ potentials play a similar role to the effective potential in standard Kohn–Sham DFT,

$$u_{\mathrm{s}}(\mathbf{r}) = v_{\mathrm{ext}}(\mathbf{r}) + v_{\mathrm{J}}(\mathbf{r}) + v_{\mathrm{xc}}(\mathbf{r}) + \frac{1}{2}\mathbf{A}_{\mathrm{s}}^2(\mathbf{r}) \tag{2.71}$$

$$\mathbf{A}_{\mathrm{s}}(\mathbf{r}) = \mathbf{A}_{\mathrm{ext}}(\mathbf{r}) + \mathbf{A}_{\mathrm{xc}}(\mathbf{r}), \tag{2.72}$$

in which $v_{\mathrm{ext}}(\mathbf{r})$ and $v_{\mathrm{J}}(\mathbf{r})$ are defined as in standard DFT as Eq. (1.138) and Eq. (1.139) respectively. The exchange-correlation scalar and vector potentials are defined as,

$$v_{\mathrm{xc}}(\mathbf{r}) = \frac{\delta E_{\mathrm{xc}}[\rho, \mathbf{j}_p]}{\delta \rho(\mathbf{r})} \tag{2.73}$$

$$\mathbf{A}_{\mathrm{xc}}(\mathbf{r}) = \frac{\delta E_{\mathrm{xc}}[\rho, \mathbf{j}_p]}{\delta \mathbf{j}_p(\mathbf{r})}. \tag{2.74}$$

With suitable constructions for the XC functional the Kohn–Sham CDFT scheme can be solved to self consistency by iterative update of the orbitals $\{\varphi_i\}$ and potentials, u_{s} and $\mathbf{A}_{\mathrm{s}}$. Existing SCF acceleration schemes derived for standard DFT, such as DIIS, function as in standard DFT with a simple generalisation to complex orbitals.

2.2.6 Gauge invariance of the exchange-correlation functional

It can be shown that $E_{\mathrm{xc}}[\rho, \mathbf{j}_p]$ must be independently gauge invariant [65]. This poses constraints on the forms a $\mathbf{j}_p$ dependent XC functional can take, and how $\mathbf{j}_p$ can enter the XC functional. To understand this restriction, consider the universal current-density functional defined in Section 2.2.5 with the electron-electron interactions scaled by the parameter $0 \leq \lambda \leq 1$,

$$F_\lambda[\rho, \mathbf{j}_p] = \min_{\Psi \mapsto (\rho(\mathbf{r}), \mathbf{j}_p(\mathbf{r}))} \left\langle \Psi \middle| \hat{T} + \lambda \hat{W} \middle| \Psi \right\rangle. \tag{2.75}$$

The CDFT energy expression for the fully interacting $\lambda = 1$ case is then,

$$E[\rho, \mathbf{j}_p(\mathbf{r})] = F_{\lambda=1}[\rho, \mathbf{j}_p] + \int \mathbf{j}_p(\mathbf{r}) \cdot \mathbf{A}(\mathbf{r}) \mathrm{d}\mathbf{r} + \int \rho(\mathbf{r}) v(\mathbf{r}) \mathrm{d}\mathbf{r} + \frac{1}{2} \int \rho(\mathbf{r}) \mathbf{A}^2(\mathbf{r}) \mathrm{d}\mathbf{r}, \tag{2.76}$$

the minimum of which defines the ground state densities ρ_0 and $\mathbf{j}_p$. The electronic density ρ_0 is invariant under the gauge transformation of Eq. (2.38) whereas $\mathbf{j}_{p,0}$ transforms as,

$$\mathbf{j}_{p,0}(\mathbf{r}) \to \mathbf{j}_{p,0}(\mathbf{r}) - \rho_0(\mathbf{r}) \nabla \chi(\mathbf{r}). \tag{2.77}$$

The universal current density functional must therefore transform with $\mathbf{j}_p$ as,

$$F_\lambda[\rho, \mathbf{j}_p - \rho \nabla \chi] = F_\lambda[\rho, \mathbf{j}_p] - \int \mathbf{j}_p \cdot \nabla \chi(\mathbf{r}) \mathrm{d}\mathbf{r} + \frac{1}{2} \int \rho(\mathbf{r}) \left|\nabla \chi(\mathbf{r})\right|^2 \mathrm{d}\mathbf{r}. \tag{2.78}$$

and must do so equally for all values of λ. In the non-interacting limit of $\lambda = 0$ the functional becomes $F_{\lambda=0}[\rho, \mathbf{j}_p] = T_\mathrm{s}[\rho, \mathbf{j}_p]$. Showing that T_s must transform as

$$T_\mathrm{S}[\rho, \mathbf{j}_p - \rho\nabla\chi] = T_\mathrm{S}[\rho, \mathbf{j}_p] + \int \mathbf{j}_p \cdot \nabla\chi(\mathbf{r})\mathrm{d}\mathbf{r} - \frac{1}{2}\int \rho(\mathbf{r})|\nabla\chi(\mathbf{r})|^2\mathrm{d}\mathbf{r}. \tag{2.79}$$

Examining the individual components of the two electron operator $\hat{W}$ we note that the Coulomb energy is a functional only of the electronic density and is therefore constant under gauge transformation. The remaining contributions to $\hat{W}$ are contained within the XC functional and, given the gauge transformation properties of T_s, must be independently gauge invariant to match the total gauge invariance of $F[\rho, \mathbf{j}_p]$ in Eq. (2.78). Hence, we have shown that $E_\mathrm{xc}[\rho, \mathbf{j}_p]$ must be independently gauge invariant,

$$E_\mathrm{xc}[\rho, \mathbf{j}_p - \rho\nabla\chi] = E_\mathrm{xc}[\rho, \mathbf{j}_p]. \tag{2.80}$$

The requirement for a gauge invariant XC functional imposes a severe restriction on how approximate XC functionals can be constructed for use in magnetic fields, mandating great care in how $\mathbf{j}_p$ dependence is introduced. Two promising approaches for CDFT XC functional construction are explored thoroughly in this work, Section 2.3 describes the functionals in which $\mathbf{j}_p$ enters as the electronic vorticity $\boldsymbol{\nu}$ whilst Section 2.4 describes the introduction of $\mathbf{j}_p$ through a modified kinetic energy density $\tilde{\tau}$.

2.3 Vorticity dependent exchange correlation functionals

The Vignale–Rasolt constrained search formulation of current-density-functional theory, described in Section 2.2, expresses the energy of N electrons in an external scalar and vector potential through,

$$\begin{aligned} E[v, \mathbf{A}] &= \inf_\Psi \left\langle \Psi \middle| \hat{H}[v, \mathbf{A}] \middle| \Psi \right\rangle \\ &= \inf_{\rho, \mathbf{j}_p} \left(F[\rho, \mathbf{j}_p] + \int (\rho v + \frac{1}{2}\rho A^2 + \mathbf{j}_p \cdot \mathbf{A})\, \mathrm{d}\mathbf{r} \right), \end{aligned} \tag{2.81}$$

with the Vignale–Rasolt constrained search functional,

$$F[\rho, \mathbf{j}_p] = \inf_{\Psi \mapsto \rho, \mathbf{j}_p} \left\langle \Psi \middle| \hat{H}[0, 0] \middle| \Psi \right\rangle. \tag{2.82}$$

In the Kohn–Sham theory of Section 2.2.5, the universal functional is decomposed into a non-interacting kinetic-energy term $T_\mathrm{s}[\rho, \mathbf{j}_p]$, a Hartree term $J[\rho]$, and an exchange–correlation term $E_\mathrm{xc}[\rho, \mathbf{j}_p]$,

$$F[\rho, \mathbf{j}_p] = T_\mathrm{s}[\rho, \mathbf{j}_p] + J[\rho] + E_\mathrm{xc}[\rho, \mathbf{j}_p]. \tag{2.83}$$

As a result of the required gauge invariance of the XC functional, Vignale and Rasolt argued that the exchange–correlation energy should depend on $\mathbf{j}_p$ through the gauge-invariant vorticity,

$$\begin{aligned} \boldsymbol{\nu}(\mathbf{r}) &= \boldsymbol{\nabla} \times \frac{\mathbf{j}_p(\mathbf{r})}{\rho(\mathbf{r})} \\ &= \frac{\rho(\mathbf{r})\boldsymbol{\nabla} \times \mathbf{j}_p(\mathbf{r}) - \boldsymbol{\nabla}\rho(\mathbf{r}) \times \mathbf{j}_p(\mathbf{r})}{\rho(\mathbf{r})^2}. \end{aligned} \tag{2.84}$$

In the expressions given above, the spin degrees of freedom and the spin-Zeeman term have been neglected. The literature contains slightly different formalisms for taking these into account and in particular, a spin resolved F and E_xc have been considered functionals of the following variables:

1. the total density ρ, the spin density $\mathbf{m}$, and the total paramagnetic current-density $\mathbf{j}_p$,
2. the total density ρ and the total paramagnetic current-spin-density $\mathbf{j}_m = \mathbf{j}_p + \boldsymbol{\nabla} \times \mathbf{m}$ [66],

3. the fully spin-resolved densities $\rho_\uparrow$ and $\rho_\downarrow$ and the paramagnetic current-densities $\mathbf{j}_{p;\uparrow}$ and $\mathbf{j}_{p;\downarrow}$ [2].

The choice between spin-resolved or total densities matters in particular for the vorticity, which is not additive with respect to spins, $\boldsymbol{\nu}_{\text{tot}} \neq \boldsymbol{\nu}_\uparrow + \boldsymbol{\nu}_\downarrow$ and which vanishes identically for densities arising from a single natural orbital (or Kohn–Sham orbital). Hence, it is possible for $\boldsymbol{\nu}_{\text{tot}} \neq 0$, yet $\boldsymbol{\nu}_\uparrow \equiv \boldsymbol{\nu}_\downarrow \equiv 0$ (e.g., for a two-electron system in a triplet spin state). In the present work the existing vorticity functionals are only applied to closed-shell systems, for which these distinctions do not matter. The spin indices have therefore been suppressed in the following.

The fact that vorticities arising from a single orbital vanish identically raises the question as to which paramagnetic densities $(\rho, \mathbf{j}_p)$ can be represented by a Kohn–Sham ground-state wave function. Clearly, a closed-shell two-electron system with a nonzero total vorticity is neither non-interacting v-representable nor N-representable by a Kohn–Sham system. Moreover, an open-shell two-electron system may feature nonvanishing spin vorticities, which also cannot be represented by a Kohn–Sham system; see also Taut *et al.* for a discussion of non-interacting v-representability in two-electron systems [67]. For $N \geq 4$ electrons, a recent result shows that all paramagnetic densities satisfying mild regularity conditions are non-interacting N-representable. [68] Depending on how the question of non-interacting N-representability is resolved for few-particle systems and how non-interacting v-representability is resolved for $N \geq 3$, a rigorous approach to CDFT may require extended (ensemble) Kohn–Sham theory and the use of methods for determining fractional occupation numbers [69–72]. It has recently been proven that essentially any density and paramagnetic current-density (subject only to the minimal regularity condition that a von Weizäcker-like bound on the kinetic energy is locally integrable) are N-representable in extended Kohn–Sham CDFT. [73]

The exchange-correlation vector potential for vorticity dependent CDFT functionals can be expressed directly in terms of the electronic vorticity,

$$\mathbf{A}_{\text{xc}} = \frac{\delta E_{\text{xc}}[\rho, \mathbf{j}_p]}{\delta \mathbf{j}_p} = \frac{1}{\rho(\mathbf{r})} \boldsymbol{\nabla} \times \frac{\delta E_{\text{xc}}[\rho, \boldsymbol{\nu}]}{\delta \boldsymbol{\nu}}. \tag{2.85}$$

The scalar exchange-correlation potential takes the usual form for $u(\mathbf{r})$ given in Eq. (2.71).

2.3.1 The VRG functional

Compared with the very large number of DFT exchange–correlation functionals, there exist only a handful of specific CDFT functionals. Some of these are based on the vorticity expansion and take the general form

$$E_{\text{xc}}^{\text{VRG}}[\rho, \boldsymbol{\nu}] = \int g(\rho(\mathbf{r}))\ |\boldsymbol{\nu}(\mathbf{r})|^2 \, \mathrm{d}\mathbf{r}, \tag{2.86}$$

where approximations to $g(\rho)$ have been established from models of the uniform electron gas. Indeed, such a functional form was considered by Vignale and Rasolt already in Ref. [65] and subsequently fitted to reference values computed with the random-phase approximation (RPA) by Vignale, Rasolt, and Geldart (VRG) in Ref. [74].

This original parametrisation has been revisited several times—specifically, reparametrisations have been proposed by Lee, Handy, and Colwell (LHC) [75, 76], by Orestes, Marcasso, and Capelle (OMC) [77], by Tao and Perdew (TP) [78], and by Tao and Vignale (TV) [79]. Additionally, Higuchi and Higuchi (HH) [80, 81] have constructed an approximate exchange–correlation functional designed to satisfy exact conditions derived from scaling relations for the CDFT exchange and correlation energies.

For molecules, it is essential that the parametrisation of the VRG functional has a sensible low-density limit. However, in the above parametrisations, reference data for fitting $g(\rho)$ were available only for Wigner–Seitz radii in the range $0 < r_{\text{s}} \leq 10$ (VRG, LHC, OMC, TP) and in the range $0 < r_{\text{s}} \leq 20$ (TV). The low-density limit is consequently under-determined by the reference data.

The low-density behaviour of the different parametrizations is shown in Figure 2.2. Importantly, the original VRG form and the OMC re-parametrisation do not tend to zero in the low-density

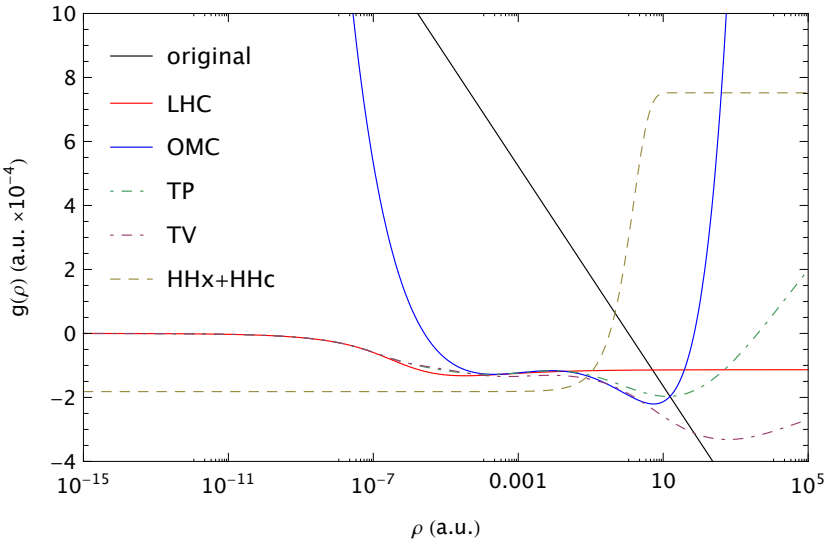


Figure 2.2: Different model functions $g(\rho)$ used in the VRG functional.

limit, making them ill-suited for molecular applications. By contrast, the LHC, TP, and TV re-parametrisations do tend to zero, albeit slowly, for sufficiently small ρ, we find that

$$g_{\mathrm{LHC}}(\rho) \approx g_{\mathrm{TP}}(\rho) \approx g_{\mathrm{TV}}(\rho) \sim -\rho^{1/3}. \tag{2.87}$$

For the LHC and TV re-parametrisations, which result in everywhere negative functions $g_{\mathrm{LHC}}(\rho)$ and $g_{\mathrm{TV}}(\rho)$, respectively, this decay behaviour is readily visualized in a log–log plot; see Figure 2.3.

Higuchi and Higuchi's exchange functional HHx is constant: $g_{\mathrm{HHx}}(\rho) = 2 \times 3.76 \times 10^{-4}$ a.u. By adjusting this constant (i.e., setting $\bar{D}_x = -\bar{C}_0$ in the notation of Ref. [80]), it is possible to make their total $g_{\mathrm{HH}}(\rho)$ almost vanish for small densities; giving a modified Higuchi–Higuchi functional denoted HHmod, see Figure 2.3. However, the Higuchi–Higuchi correlation functional HHc has a singularity at $\rho = 10^{-30}$ a.u., so the approach to the low-density limit is interrupted by an infinite discontinuity.

Finally, it is noted that Zhu and Trickey [82] compared vorticity-dependent functionals with an exactly solvable model for a Hooke's atom in a magnetic field, reporting that the vorticity is a difficult quantity to work with.

2.3.2 Parametrisations of g(ρ) in vorticity functionals

The parametrisations of $g(\rho)$ plotted in Figure 2.2 are collected here and given explicit form. For consistency of presentation, the notation has been modified from the original papers.

Introducing the Fermi momentum $k_{\mathrm{F}} = (3\pi^2\rho)^{1/3}$ and the Wigner–Seitz radius $r_{\mathrm{s}} = (4\pi\rho/3)^{-1/3}$, the original VRG parametrization of Refs. [65, 74] is given by

$$g_{\mathrm{orig}}(\rho) = \frac{1}{24\pi^2} k_{\mathrm{F}} (0.02764 r_{\mathrm{s}} \ln r_{\mathrm{s}} + 0.01407 r_{\mathrm{s}}), \tag{2.88}$$

where the first constant comes from an analytical expression: $(9\pi/4)^{-1/3}/(6\pi) \approx 0.02764$.

The Lee–Handy–Colwell parametrisation

The Lee–Handy–Colwell (LHC) parametrisation of the VRG functional is given by

$$g_{\mathrm{LHC}}(\rho) = -\frac{1}{24\pi^2} k_{\mathrm{F}} \left[1 - \mathrm{e}^{-a_0 r_{\mathrm{s}}}(a_1 + a_2 r_{\mathrm{s}})\right], \tag{2.89}$$

with $a_0 = 0.042$, $a_1 = 1$, and $a_2 = 0.028$. [76]

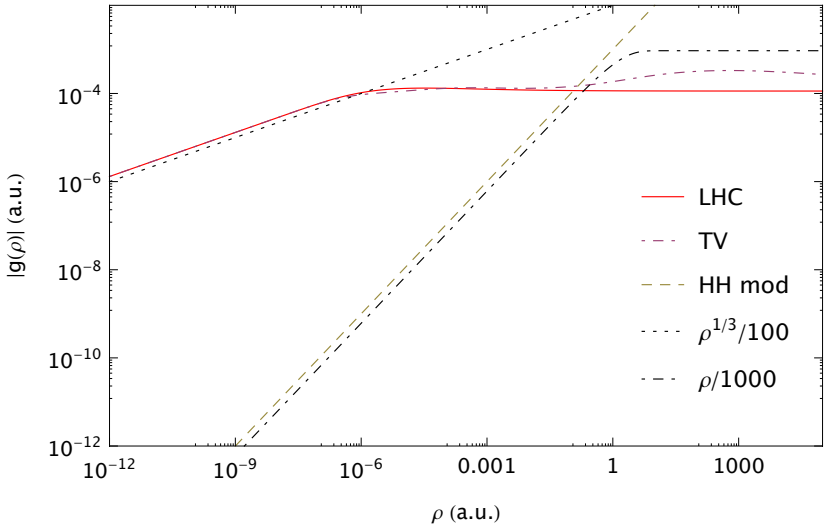


Figure 2.3: The low-density behavior of three model functions $g(\rho)$ used in the VRG functional. The Higuchi–Higuchi exchange functional HHx has been re-parametrised so that the total exchange–correlation functional approaches zero for small densities; however, the correlation functional HHc goes through a singularity and a sign shift at $\rho = 10^{-30}$ a.u.. The indicated asymptotic HHx+HHc behavior therefore does not extend to this region.

The Orestes–Marcasso–Capelle parametrisation

Orestes, Marcasso, and Capelle [77] presented a three-term fit and a five-term fit of the VRG integrand, the latter OMC fit being given by

$$g_{\mathrm{OMC}}(\rho) = -\frac{1}{24\pi^2} k_{\mathrm{F}} \left[1 - C^{\mathrm{OMC}}(\rho)\right], \tag{2.90}$$

with

$$\begin{aligned} C^{\mathrm{OMC}}(\rho) = 1.1038 - 0.4990 r_{\mathrm{s}}^{1/3} + 0.4423\sqrt{r_{\mathrm{s}}} \\ - 0.06696 r_{\mathrm{s}} + 0.0008432 r_{\mathrm{s}}^2. \end{aligned} \tag{2.91}$$

The Tao–Perdew parametrisation

The Tao–Perdew (TP) parametrisation is defined by [78]

$$g_{\mathrm{TP}}(\rho) = -\frac{1}{24\pi^2} k_{\mathrm{F}} \left[1 - \bar{C}^{\mathrm{TP}}(\rho)\right]. \tag{2.92}$$

The Tao–Perdew fit, $\bar{C}^{\mathrm{TP}}(\rho)$, is constructed as

$$\bar{C}^{\mathrm{TP}}(\rho) = \left[C_1^{\mathrm{TP}} e^{-2.8 r_{\mathrm{s}}} + (1 - \mathrm{e}^{-2.8 r_{\mathrm{s}}}) C_2^{\mathrm{TP}}\right] \mathrm{e}^{-0.05 r_{\mathrm{s}}} + (1 - \mathrm{e}^{-0.05 r_{\mathrm{s}}}) C_3^{\mathrm{TP}},$$

with

$$C_1^{\mathrm{TP}}(\rho) = 1 + 0.027643 r_{\mathrm{s}} \log r_{\mathrm{s}}, \tag{2.93}$$

capturing the the high-density limit expansion [74],

$$C_2^{\mathrm{TP}}(\rho) = C^{\mathrm{OMC}}(\rho) = 1.1038 - 0.4990 r_{\mathrm{s}}^{1/3} + 0.4423\sqrt{r_{\mathrm{s}}} - 0.06696 r_{\mathrm{s}} + 0.0008432 r_{\mathrm{s}}^2,$$

containing the OMC fit for the intermediate region, and,

$$C_3^{\mathrm{TP}}(\rho) = (1 + 0.027 r_{\mathrm{s}}) e^{-0.041 r_{\mathrm{s}}}, \tag{2.94}$$

as a slightly modified version of the LHC parametrisation included for the correct low density behaviour.

The Tao–Vignale parametrisation

The Tao–Vignale (TV) parametrisation of the VRG functional is defined by [79] as the Tao–Perdew parametrisation modified to fit data for the greater range of $r_s \leq 20$,

$$g_{\mathrm{TV}}(\rho) = -\frac{1}{24\pi^2} k_{\mathrm{F}} \left[1 - \bar{C}^{\mathrm{TV}}(\rho)\right], \tag{2.95}$$

with

$$C_1^{\mathrm{TV}}(\rho) = 1 + b_1 r_{\mathrm{s}} \log r_{\mathrm{s}}, \tag{2.96}$$

$$C_2^{\mathrm{TV}}(\rho) = b_3 + b_4 r_{\mathrm{s}}^{1/3} + b_5 \sqrt{r_{\mathrm{s}}} + b_6 r_{\mathrm{s}} + b_7 r_{\mathrm{s}}^2, \tag{2.97}$$

$$C_3^{\mathrm{TV}}(\rho) = (1 + b_9 r_{\mathrm{s}}) \mathrm{e}^{-b_{10} r_{\mathrm{s}}}, \tag{2.98}$$

$$\begin{aligned} \bar{C}^{\mathrm{TV}}(\rho) = &\left[C_1^{\mathrm{TV}} \mathrm{e}^{-b_2 r_{\mathrm{s}}} + C_2^{\mathrm{TV}} (1 - \mathrm{e}^{-b_2 r_{\mathrm{s}}})\right] \mathrm{e}^{-b_8 r_{\mathrm{s}}} \\ &+ (1 - \mathrm{e}^{-b_8 r_{\mathrm{s}}}) C_3^{\mathrm{TV}}, \end{aligned} \tag{2.99}$$

where $b_1 = (9\pi/4)^{-1/3}/(6\pi)$, $b_2 = 2.5$, $b_3 = 1.1$, $b_4 = -0.49$, $b_5 = 0.438$, $b_6 = -0.07$, $b_7 = 0.00182$, $b_8 = 0.054$, $b_9 = 0.02$, and $b_{10} = 0.05$.

The Higuchi–Higuchi parametrisation

The Higuchi–Higuchi parametrisation is given by [80, 81]

$$g_{\mathrm{HHx}}(\rho) = 2D_x, \tag{2.100}$$

$$g_{\mathrm{HHc}}(\rho) = 2C_0 \mathrm{e}^{-\alpha\rho} \frac{\rho^3}{(\rho - \delta)^3}, \tag{2.101}$$

$$g_{\mathrm{HH}}(\rho) = g_{\mathrm{HHx}}(\rho) + g_{\mathrm{HHc}}(\rho), \tag{2.102}$$

where $\alpha = 0.653$, $D_x = 3.76 \times 10^{-4}$, $C_0 = -4.669 \times 10^{-4}$, and $\delta = 10^{-30}$. In the modified functional, HHmod, the value of D_x was changed to $D_x = -C_0 = 4.669 \times 10^{-4}$ to ensure a useful low-density limit. The parameter δ was also set to $\delta = 0$, since this makes no difference, to within normal numerical precision, in regions where $\rho \gg 10^{-30}$ and inclusion of regions where $\rho \approx 10^{-30}$ would make the original exchange-correlation energy ill-defined.

Implementation

All of the above parametrisations to the VRG vorticity dependent XC functional were implemented into the XCFUN library. As previously mentioned, the low density limit is critical for molecular systems, precluding the use of the original VRG and OMC parametrisation. The HHmod parametrisation does give the correct low density behaviour, but application is made difficult by the singularity at $\rho \approx 10^{-30}$.

2.4 mGGA functionals in CDFT

The electronic vorticity is a theoretically convenient choice of current dependent XC variable, ensuring the gauge-origin invariance of the exchange-correlation energy. It has been observed in this work (Chapter 3) and elsewhere [10, 83] however, that the electronic vorticity brings significant numerical stability issues to self-consistent calculations. How severe these issues are depends on the exact parametrisation of the functional form but in all cases some degree of numerical regularisation is required to ensure that a self-consistent solution of the Kohn–Sham equations can be obtained. Furthermore, molecular properties computed by such calculations display an un-acceptably strong dependence on the regularisation parameters — with no obvious convergence towards a single value (Section 3.3.4).

An alternative approach has been proposed by Becke [84], while a more elaborate version (relying on currents from individual Kohn–Sham orbitals) was proposed by Pittalis *et al.* [85]. These functionals are based on the observation that a gauge-invariant density can be formed from a combination of the Kohn–Sham canonical-kinetic-energy density and the paramagnetic current-density. The paramagnetic current can therefore be incorporated in an exchange-correlation functional via $\tilde{\tau}$ and this approach to CDFT XC functional construction will be explored in this section.

2.4.1 The current modified kinetic energy density

Most practical mGGAs make use of the spin resolved kinetic energy density,

$$\tau_\sigma = \sum_i^{\text{occ.}} \nabla\varphi_{i\sigma}^* \cdot \nabla\varphi_{i\sigma}, \tag{2.103}$$

in their construction, where φ_i are the occupied KS orbitals and σ is the electron spin index.[8] The kinetic energy density of Eq. (2.103) is gauge-origin dependent and as a result an XC functional depending on τ is also gauge-origin variant, contradicting the conclusion of Section 2.2.6. As a result of this gauge-origin variance the unmodified kinetic energy density is unsuitable for use in mGGAs in the presence of a magnetic field. In order to develop mGGA functionals for CDFT the gauge-origin independence of the exchange-correlation functional must be restored. A natural modification, which can be applied to any mGGA dependent on the kinetic energy density, was derived by Dobson [86,87] through a generalisation of the exchange-hole expansion to include the case of non-zero current densities.

The spherically averaged exchange hole at zero field can be modelled with a Taylor expansion [88] and is commonly considered [84, 89, 90] up to the quadratic term,

$$Q_\sigma = \frac{1}{6}\left[\nabla^2\rho_\sigma - 2\tau_\sigma + \frac{|\nabla\rho_\sigma|^2}{2\rho_\sigma}\right]. \tag{2.104}$$

This expansion can be generalised to a non-zero field and the curvature term becomes [84, 86, 87]

$$Q_\sigma = \frac{1}{6}\left[\nabla^2\rho_\sigma - 2\tau_\sigma + \frac{|\nabla\rho_\sigma|^2}{2\rho_\sigma} + \frac{2\,|\mathbf{j}_{p\sigma}|^2}{\rho_\sigma}\right], \tag{2.105}$$

where $\mathbf{j}_{p\sigma}$ is the spin resolved paramagnetic current density of Eq. (2.49).

Comparing Eq. (2.104) and Eq. (2.105) it is possible to identify a correction to the conventional $\tau_\sigma(\mathbf{r})$ such that a modified gauge-origin invariant kinetic energy density is formed that may be utilised in mGGA functionals,

$$\tau_\sigma \to \tilde{\tau}_\sigma = \tau_\sigma - \frac{|\mathbf{j}_{p\sigma}|^2}{\rho_\sigma}, \tag{2.106}$$

with the associated KS vector potential contribution,

$$\mathbf{A}_{\text{xc}} = -\frac{\delta E_{\text{xc}}[\rho,\tilde{\tau}]}{\delta\tilde{\tau}}\frac{\mathbf{j}_p}{\rho}. \tag{2.107}$$

It is noted that this generalisation of the kinetic energy density is not unique and is discussed further in Section 2.4.2.

The use of Eq. (2.106) has been put forward many times in the literature. Becke suggested its use in the Becke–Roussel model [84] to generate a current dependent analogue of this functional. He also suggested that this quantity could be used to define a current dependent inhomogeneity parameter in the more empirical B98 functional [90]. The current generalised kinetic energy density has also been suggested for use in the TPSS functional [91] by Tao [92]. Recently Bates and Furche [93] considered the application of the resulting cTPSS functional in the calculation of excitation energies via response theory. The present work considers the application of mGGA functionals with this modification to calculate magnetic properties in the weak and strong field regimes in a non-perturbative manner.

[8] Note the omission of the factor of $1/2$ commonly employed, such that $T_{\text{s}} = \frac{1}{2}\int\tau(\mathbf{r})\mathrm{d}\mathbf{r}$.

In particular we consider three functional forms, cB98, cTPSS and cTPSS(h), where the prefix 'c' denotes the use of the modified $\tilde{\tau}_\sigma$ of Eq. (2.106). Section 2.4.3 and Section 2.4.4 give a full account of the B98 and TPSS functionals respectively, showing explicitly how the modifications enter into the functional forms.

The Kohn-Sham eigenvalue problem with current dependent mGGA functionals then has the form (disregarding spin dependence),

$$\left[\frac{1}{2}\mathbf{p}\cdot(1+\eta_{\mathrm{xc}})\mathbf{p}+\frac{1}{2}\{\mathbf{p},\mathbf{A}_{\mathrm{ext}}+\mathbf{A}_{\mathrm{xc}}\}+u_{\mathrm{s}}\right]\varphi_p=\varepsilon_p\varphi_p, \tag{2.108}$$

with

$$\eta_{\mathrm{xc}}=\frac{\partial f_{\mathrm{xc}}}{\partial\tau}=\frac{\partial g_{\mathrm{xc}}}{\partial\tilde{\tau}}, \tag{2.109}$$

$$\mathbf{A}_{\mathrm{xc}}=\frac{\partial f_{\mathrm{xc}}}{\partial\mathbf{j}_p}=-2\eta_{\mathrm{xc}}\frac{\mathbf{j}_p}{\rho}, \tag{2.110}$$

$$u_{\mathrm{s}}=v_{\mathrm{s}}+\frac{1}{2}A^2_{\mathrm{ext.}}, \tag{2.111}$$

and $\{A,B\}$ denoting the anti-commutator of A and B, $AB+BA$.

Unlike for the VRG functional, the vector potential $\mathbf{A}_{\mathrm{xc}}$ is now gauge dependent. However, the gauge dependence of $\mathbf{A}_{\mathrm{xc}}$ cancels against the gauge dependence of the η_{xc}-dependent modification to the canonical kinetic energy, giving a gauge invariant total. The generalisation to spin-resolved densities is straightforward.

2.4.2 Current generalised kinetic energy densities

The choice of how τ is modified to form a current generalised kinetic energy density is not unique. As this quantity is of central importance to current dependent mGGA functional construction and the electron localisation analysis of Section 4.2 a discussion of gauge invariant τ choice is given here. The reader is referred to Ref. [94] for a full analysis of kinetic energy densities in the presence of a magnetic field.

The kinetic energy density is commonly used to enhance the accuracy of exchange-correlation functionals through the iso-orbital indicator z, allowing the functional to distinguish between regions that are electron gas like and regions dominated by a single orbital. In the absence of a magnetic field the iso-orbital indicator has the form,

$$z_\sigma(\mathbf{r})=\frac{\tau^{\mathrm{vW}}_\sigma(\mathbf{r})}{\tau_\sigma(\mathbf{r})}, \tag{2.112}$$

where $\tau^{\mathrm{vW}}=|\nabla\rho_\sigma|^2/8\rho_\sigma$ is the von-Weizsäcker kinetic energy. The iso-orbital indicator z approaches 0 in free-electron gas like regions and approaches 1 in regions dominated by a single orbital.

As derived in Section 2.1.3, under gauge transformation with the gauge function $\nabla\chi(\mathbf{r})$ the Kohn-Sham orbitals transform as Eq. (2.40) and the kinetic energy density, τ, correspondingly transforms as,

$$\tau(\mathbf{r})\rightarrow\tau'(\mathbf{r})=\tau(\mathbf{r})+\mathbf{j}_p(\mathbf{r})\cdot\nabla\chi(\mathbf{r})+\frac{1}{2}|\nabla\chi(\mathbf{r})|^2\rho(\mathbf{r}). \tag{2.113}$$

The von-Weisäcker kinetic energy is an explicit functional of the observable electron density however, and is consequently gauge invariant. An iso-orbital indicator built from the unmodified kinetic energy density is therefore gauge variant, contradicting the requirement of XC functional gauge invariance (Section 2.2.6).

Three different gauge independent kinetic energies have been proposed that can be used in a gauge invariant iso-orbital indicator suitable for use in current-dependent mGGA functionals. The first was suggested by Maximoff and Scuseria [95] as the physical kinetic energy density, constructed from the physical momentum operator,

$$\tilde{\tau}_{\mathrm{MS}}(\mathbf{r})=\tau^{\mathrm{phys}}[\rho,\mathbf{A}]=\tau(\mathbf{r})+\mathbf{j}_p(\mathbf{r})\cdot\mathbf{A}(\mathbf{r})+\frac{1}{2}\rho(\mathbf{r})A^2(\mathbf{r}), \tag{2.114}$$

which is naturally gauge invariant but does not produce the correct bounded interval of [0, 1] in the standard iso-orbital indicator of Eq. (2.112). A modified iso-orbital indicator for use with τ_{MS} is suggested in Ref. [94] that recovers these bounds, but introduces a dependence on $\mathbf{A}$ in the exchange-correlation functional. Incorporating the vector potential into XC functional design directly is undesirable however as the universal functional $F_{\mathrm{VR}}[\rho, \mathbf{j}_p]$ ceases to be system independent, deviating from the theoretical framework for CDFT derived in Section 2.2.

Tao and Perdew seek to eliminate the field dependence entirely from $E_{\mathrm{xc}}^{\mathrm{mGGA}}$ and produce a current independent kinetic energy density,

$$\tilde{\tau}_{\mathrm{TP}}(\rho, \mathbf{j}_p = \mathbf{0}) = \tau^{\mathrm{phys}}[\rho, \mathbf{B}] + \frac{1}{2}\chi_L^0(\rho)B^2(\mathbf{r}), \tag{2.115}$$

$$= \tau(\mathbf{r}) - |\mathbf{j}_p(\mathbf{r})|^2/(2\rho(\mathbf{r})) - (k_{\mathrm{F}}(\rho)|\boldsymbol{\nu}|^2)/(24\pi^2) \tag{2.116}$$

in which χ_L^0 is the diamagnetic susceptibility of the non-interacting electron gas. This expression gives the exact $\tau(\rho, \mathbf{j}_p = 0)$ for a uniform electron gas, and makes the implicit assumption that electron density of the molecule can be regarded as only slightly perturbed.

Using τ_{TP} produces a gauge invariant but current insensitive mGGA XC functional suitable for use with the VRG vorticity correction described in Section 2.3. Given the severe numerical limitations of vorticity dependent functionals however (discussed in Chapter 3) this approach, and consequently the use of τ_{TP} cannot be recommended. In addition to the limitations of vorticity based constructions, the analysis of Ref. [94] show situations in which z_{TP} deviates from the [0, 1] bounds rendering it unsuitable for use as an iso-orbital indicator, calling into question the reliability of any mGGA functionals depending on τ_{TP}.

The derivation of a third generalised kinetic energy density by Dobson, Becke and Tao is detailed in Section 2.4.1, and has the form of Eq. (2.106). The Dobson–Becke generalised kinetic energy density $\tilde{\tau}_{\mathrm{DB}}$ has the desirable property that $\tilde{\tau}_{\mathrm{DB}} \geq \tau^{\mathrm{vW}}$ and as such, when provided in place to Eq. (2.112) produces a gauge invariant iso-orbital indicator z_{DB} that obeys the required [0, 1] bounds. As a result $\tilde{\tau}_{\mathrm{DB}}$ allows the correct formation of a current sensitive electron localisation function in Section 4.2 and the current dependent mGGA functionals of Section 2.4.3 and Section 2.4.4.[9]

2.4.3 The current modified B98 functional

The B98 functional [90] has a general construction that is similar to the popular B97 functional form [96], however, instead of using reduced spin-density gradients it makes use of an inhomogeneity parameter q_σ,

$$q_\sigma = \frac{(Q_\sigma - Q_\sigma^{\mathrm{UEG}})}{|Q_\sigma^{\mathrm{UEG}}|}, \tag{2.117}$$

where the exchange hole curvature for the uniform electron gas takes the simple form,

$$Q_\sigma^{\mathrm{UEG}} = -\frac{1}{5}(6\pi^2)^{2/3}\rho_\sigma^{5/3}, \tag{2.118}$$

and Q_σ is defined in Eq. (2.104). This inhomogeneity factor, q_σ, controls the enhancement or attenuation of the exchange and correlation energy over the uniform gas values.

The exchange component of the functional takes the form,

$$E_{\mathrm{x},\sigma} = \int e_{\mathrm{x},\sigma}^{\mathrm{UEG}}(\rho_\sigma) g_{\mathrm{x},\sigma}(q_\sigma) \mathrm{d}\mathbf{r}, \tag{2.119}$$

and the opposite- and same-spin components of the correlation energy take the forms,

$$E_{\mathrm{c},\sigma\sigma'} = \int e_{\mathrm{c},\alpha\beta}^{\mathrm{UEG}}(\rho_\sigma, \rho'_\sigma) g_{\mathrm{c},\alpha\beta}(q_{\mathrm{avg}}) \mathrm{d}\mathbf{r}, \tag{2.120}$$

$$E_{\mathrm{c},\sigma\sigma} = \int e_{\mathrm{c},\sigma\sigma}^{\mathrm{UEG}}(\rho_\sigma) f_\sigma^{\mathrm{SCC}} g_{\mathrm{c},\sigma\sigma}(q_\sigma) \mathrm{d}\mathbf{r}. \tag{2.121}$$

[9] The notation of Ref. [94] uses τ_{BT} to refer to τ_{DB}.

The functions $g_{\mathrm{x},\sigma}(q_\sigma)$, $g_{\mathrm{c},\sigma\sigma'}(q_{\mathrm{avg}})$ and $g_{\mathrm{c},\sigma\sigma}(q_\sigma)$ are dimensionless inhomogeneity correction factors depending on q_σ and $q_{\mathrm{avg}} = \frac{1}{2}(q_\alpha + q_\beta)$. In addition the same-spin correlation energy contains a self-correlation correction (SCC) factor

$$f_\sigma^{\mathrm{SCC}} = \left[\tau_\sigma - \frac{1}{4}\frac{(\nabla\rho_\sigma)^2}{\rho_\sigma}\right]/\tau_\sigma. \tag{2.122}$$

This factor varies between 0 and 1 and vanishes in one-orbital regions, ensuring the functional is self-correlation free. For convenience in deriving fitted forms for the inhomogeneity correction factors g, Becke proposed the following transformation to a finite interval,

$$w = \frac{\gamma q}{\sqrt{1+\gamma^2 q^2}} \tag{2.123}$$

where γ is a parameter to be determined and separate transformations are carried out for the exchange, opposite-spin correlation and like-spin correlation respectively using the appropriate definitions of q as in Eq. (2.119) and Eq. (2.120). Based on calculations of atomic exchange–correlation energies Becke proposed the values $\gamma_{\mathrm{x},\sigma} = 0.11$, $\gamma_{\mathrm{c},\alpha\beta} = 0.14$ and $\gamma_{\mathrm{c},\sigma\sigma} = 0.16$. The inhomogeneity corrections g were then determined by fitting a power series expansion of the form

$$g = \sum_{i=0}^{m} c_i w^i \tag{2.124}$$

with $m = 2$ chosen to prevent unphysical over-fitting. This fitting was carried out using the G2 thermochemical dataset and basis set free, post-LSDA, calculations. The optimal parameters can be found in Ref. [90].

Here this parametrisation is used directly but it is noted that in future the parameters could be re-optimised with self-consistent data. In addition an amount of Hartree–Fock exchange is included with weight $c_{\mathrm{x}} = 0.1985$. The resulting B98 functional therefore possesses a high degree of non-locality and may be classified as a hybrid mGGA functional with dependence not only on τ but also on the laplacian of the density $\nabla^2\rho$.

The original definition of B98 utilised the zero-field exchange hole curvature of Eq. (2.104) in its definition. However, it was noted [90] that this form can be readily extended to include current effects via Eq. (2.105) and it is this avenue that is explored in the present work. Unless otherwise stated this modified form is employed throughout and denoted as cB98.

2.4.4 The current modified TPSS functional

One of the most widely used meta-GGA functionals is due to Tao, Perdew, Staroverov and Scuseria (TPSS) [91]. This functional is designed to satisfy exact constraints without empirical parameters and as such is an interesting candidate to study in the context of generalisation to finite magnetic field strengths where much less is known about the performance of approximate functionals. In this functional the ratio

$$z = 2\tau^{\mathrm{vW}}/\tau, \qquad \tau = \sum_\sigma \tau_\sigma, \qquad \tau^{\mathrm{vW}} = \frac{1}{8}\frac{|\nabla\rho|^2}{\rho} \tag{2.125}$$

plays a key role as a dimensionless inhomogeneity parameter, along with

$$p = \frac{|\nabla\rho|^2}{4(3\pi^2)^{2/3}\rho^{8/3}} = s^2 \tag{2.126}$$

Note that throughout this work the definition of τ in Eq. (2.103) is used, which does not include the factor of $1/2$ commonly employed. The exchange functional then takes the form

$$E_{\mathrm{x}}[\rho] = \int \rho\varepsilon_{\mathrm{x}}^{\mathrm{UEG}}(\rho)F_{\mathrm{x}}(p,z) \tag{2.127}$$

where the precise details of the form chosen for the enhancement factor $F_{\mathrm{x}}(p,z)$ can be found in Ref. [91]. The correlation energy takes the form

$$\begin{aligned} E_{\mathrm{c}}[\rho_\alpha,\rho_\beta,\nabla\rho_\alpha,\nabla\rho_\beta,\tau] = \\ \int \rho\varepsilon_{\mathrm{c}}^{\mathrm{revPKZB}}(\rho_\alpha,\rho_\beta,\nabla\rho_\alpha,\nabla\rho_\beta,\tau) \\ \times \left[1+d\varepsilon_{\mathrm{c}}^{\mathrm{revPKZB}}(\rho_\alpha,\rho_\beta,\nabla\rho_\alpha,\nabla\rho_\beta,\tau)(\tau^{\mathrm{vW}}/\tau)^3\right]\mathrm{d}\mathbf{r} \end{aligned} \tag{2.128}$$

where $d = 2.8\ \mathsf{E}_{\mathsf{h}}^{-1}$.

Using the replacement in Eq. (2.106) leads to modifications in the exchange contribution via z in Eq. (2.125) and in the correlation energy as shown in Eq. (2.128). This modified form is noted cTPSS and is consistent with that used in the response implementation of Ref. [93].

2.5 Computational methods

It is a non-trivial endevour to implement the one and two electron integrals required for the self consistent field equations when LAO basis sets are employed in strong magnetic fields. As a result, standard computational packages lack the ability to compute such integrals. The LONDON program was created to address this absence and, initially, to perform HF and FCI calculations in finite magnetic fields. [27] Much of the computational framework required for HF is the same as that required for KS-CDFT. This commonality was exploited to add CDFT capabilities to the LONDON program and the work of Chapter 3 stands as the first documented molecular self consistent KS-CDFT calculations, published in Ref. [10].

The LONDON program makes extensive use of the XCFUN library [97] to evaluate XC functionals and obtain XC potentials. The XCFUN library utilises automatic differentiation techniques to generate arbitrary order derivatives of XC functionals with no additional programmer input beyond the initial definition of the functional. The XCFUN library was extended to include the derivatives with respect to paramagnetic current density required for the Kohn–Sham CDFT XC potentials. The XCFUN framework allowed rapid implementation of CDFT XC functionals into LONDON greatly aiding the implementation and testing of CDFT functional forms. The library calling structure within LONDON was extended as part of this work to allow generalised kinetic energy densities to be passed into XC functionals in XCFUN, facilitating current-dependent mGGA functionals in LONDON 's CDFT module. With this framework in place the LONDON program is capable of performing CDFT using both vorticity dependent and mGGA CDFT functionals.

The gauge invariant SCF CDFT framework of LONDON was used to explore and develop the CDFT functionals described in this chapter with the evaluation of magnetic response properties and small molecule potential energy surfaces [10, 98], detailed in Chapter 3. The implementation was then used to investigate electron localisation effects in magnetic fields [99] and analyse the origin of the perpendicular paramagnetic bonding mechanism in Chapter 4. An implementation of the maximum overlap method (MOM) within the finite magnetic field HF implementation was made to facilitate exploring excited states in strong magnetic fields, detailed in Chapter 5.

2.5.1 Computational evaluation of CDFT quantities

The main modification to the existing LONDON Hartree–Fock code [51] in order to enable CDFT calculations was the implementation of a numerical integration scheme, the evaluation of quantities such as $\rho(\mathbf{r})$, $\boldsymbol{\nabla}\rho(\mathbf{r})$, $\mathbf{j}_p(\mathbf{r})$, and $\boldsymbol{\nu}(\mathbf{r})$ on the numerical grid and the assembly of these components in the expressions of the exchange–correlation energies and the functional derivatives required for their corresponding potentials.

For the molecular numerical integration, a set of grid points and weights was constructed using Becke's space partitioning scheme with atomic size corrections [100], decomposing the molecular integral into a sum of one-centre atom-like integrations. To eliminate crowding of points close to nuclei, grid pruning is implemented using the approach outlined by Murray, Handy and Laming.

[101] For the radial part of these integrations, the scheme proposed by Lindh, Malmqvist, and Gagliardi was employed; [102] for the angular part, Lebedev quadrature was used. [103–108] The C++ implementation for standard density functionals was tested by comparison with the DALTON quantum chemistry program, [109] in which similar Fortran 77 angular and radial implementations are available. Because of the slow decay of the vorticity-dependent integrand in the present VRG parametrisations, very conservative screening criteria were used when eliminating negligible points on the integration grid.

The evaluation of $\rho(\mathbf{r})$, $\boldsymbol{\nabla}\rho(\mathbf{r})$, $\mathbf{j}_p(\mathbf{r})$, and $\boldsymbol{\nu}(\mathbf{r})$ at the grid points is straightforward, given the elements of the one-particle reduced density matrix $D_{\gamma\zeta}$, the values of basis functions $\omega_\gamma(\mathbf{r})$ and their gradients $\boldsymbol{\nabla}\omega_\gamma(\mathbf{r})$ at the grid points,

$$\rho(\mathbf{r}) = \sum_{\gamma\zeta} \omega_\gamma(\mathbf{r})\ D_{\gamma\zeta}\ \omega^*_\zeta(\mathbf{r}), \tag{2.129}$$

$$\boldsymbol{\nabla}\rho(\mathbf{r}) = \sum_{\gamma\zeta} \omega_\gamma(\mathbf{r})\ D_{\gamma\zeta}\ \boldsymbol{\nabla}\omega^*_\zeta(\mathbf{r}) + \text{c.c.}, \tag{2.130}$$

$$\mathbf{j}_p(\mathbf{r}) = \frac{\mathrm{i}}{2} \sum_{\gamma\zeta} \omega_\gamma(\mathbf{r})\ D_{\gamma\zeta}\ \boldsymbol{\nabla}\omega^*_\zeta(\mathbf{r}) + \text{c.c.}, \tag{2.131}$$

where "c.c." denotes the complex conjugate of the preceding expression. (Note that the *number* density and *number* current are used, rather than the *charge* density and *charge* current, the difference being a factor of $-\mathrm{e}$ in general, or -1 in atomic units.) Notably, the curl of $\mathbf{j}_p$ can be computed from the first-order functional derivatives of basis functions since the second-order derivatives cancel:

$$\boldsymbol{\nabla} \times \mathbf{j}_p(\mathbf{r}) = \mathrm{i} \sum_{\gamma\zeta} D_{\gamma\zeta}\, \boldsymbol{\nabla}\omega_\gamma(\mathbf{r}) \times \boldsymbol{\nabla}\omega^*_\zeta(\mathbf{r}). \tag{2.132}$$

At first glance, the right-hand side looks like an imaginary quantity; however, for a complex vector $\mathbf{w}$, the cross-product $\mathrm{i}\mathbf{w} \times \mathbf{w}^*$ is real.

The vorticity may be assembled from the above densities using the right-hand side of Eq. (2.84). In practice, to guard against division by near-zero and the resulting loss of precision, the regularized vorticity was preferred

$$\boldsymbol{\nu}_\epsilon(\mathbf{r}) = \frac{\rho(\mathbf{r})\boldsymbol{\nabla} \times \mathbf{j}_p(\mathbf{r}) - \boldsymbol{\nabla}\rho(\mathbf{r}) \times \mathbf{j}_p(\mathbf{r})}{\sqrt{\epsilon^4 + \rho(\mathbf{r})^4}}, \tag{2.133}$$

where ϵ plays the role of a soft density cut-off. This regularization results in an underestimate of the magnitude of the true vorticity.

Once the required CDFT quantities have been assembled at the grid points, the exchange–correlation energies and the derivatives required for construction of their associated Kohn–Sham matrix contributions can be calculated. For the standard DFT contributions, the afforementioned flexible XCFUN package was used [97], which utilises automatic differentiation to provide derivatives of the exchange–correlation energies from specified energy expressions. Once these contributions have been evaluated, LONDON constructs the associated Kohn–Sham matrix elements.

For the vorticity dependent CDFT contributions (which were added as corrections to standard functionals), the exchange–correlation energy and Kohn–Sham matrix element constructions were implemented in the LONDON code. For $F_{\mathrm{VRG(LHC)}}$ and $F_{\mathrm{VRG(TV)}}$, which have everywhere negative integrands, the regularization of Eq. (2.133) was used and the corresponding vorticity correction was therefore underestimated—at least when applied non-self-consistently. For VRG parametrisations that decay as $\rho^{1/3}$ in the low-density limit, the regularization in Eq. (2.133) yields a VRG integrand of the form

$$g(\rho)\nu_\epsilon^2 \sim -\rho^{1/3}\, \frac{\left|\rho\boldsymbol{\nabla} \times \mathbf{j}_p - \boldsymbol{\nabla}\rho \times \mathbf{j}_p\right|^2}{\epsilon^4 + \rho^4}. \tag{2.134}$$

Without regularization (i.e., with $\epsilon = 0$), this decay may be numerically problematic—in regions where the vorticity vanishes or is very small, numerical noise in the squared factor would be amplified by a factor $\rho^{-11/3}$. The need for appropriate regularization of the vorticity has been noted in Ref. [110]. The sensitivity of calculated properties to the choice of the regularization parameters is investigated in Section 3.3.4.

Chapter 3

The Calculation of Magnetic Response Properties

Chapter 2 details a current-density-functional theory suitable for the self consistent gauge-origin-invariant calculation of molecular energies in finite magnetic fields. CDFT offers a simple and convenient way to estimate static magnetic response quantities, as well as enabling the study of molecules in very strong magnetic fields, for which a perturbation expansion converges very slowly, if at all [27, 51, 111, 112]. In both perturbative and non-perturbative approaches, LAOs (Section 2.1.4) provide an efficient means of accelerating basis-set convergence by building gauge-origin freedom into the basis functions and thus are used throughout the following work.

A magnetic response property describes the response of a molecule to a perturbing electromagnetic field through the changes in ground state energy induced by an external field. In particular this work is concerned with static response properties; those that do not vary with time. Whilst high accuracy estimates can be obtained from perturbative wave function approaches these methods are prohibitively expensive and are restricted to lower order properties, becoming cumbersome when higher order derivatives are required. The current-density-functional theory derived in Chapter 2 and implemented in the LONDON program as described in Section 2.5 presents a computationally efficient correlated evaluation of magnetic response properties using finite difference techniques, accounting for induced current effects through the vorticity correction functionals of Section 2.3 and the current modified mGGA functionals of Section 2.4.

The following chapter evaluates the performance of CDFT functionals in two key domains. The weak field accuracy is established by calculating the purely magnetic response properties amenable to finite difference calculation, the molecular magnetizability and nuclear shielding constants. These properties are calculated for the set of benchmark molecules given in Table 3.1 and compared against accurate benchmark data from Refs. [113] and [114]. The strong field accuracy is established through the calculation of the interaction energy surfaces of rare gas diatomics bound by a perpendicular paramagnetic bonding mechanism [27], benchmarked against the field generalised CCSD(T) implementation of Ref. [115].

Table 3.1: The set of benchmark molecules for which accurate NMR shielding and magnetisability data was available [113, 114]. All molecules are considered at the CCSD(T) cc-pVTZ optimised geometries of Ref. [113]

HF	CO	N_2	H_2O	HCN	HOF	LiH
NH_3	H_2CO	CH_4	C_2H_4	AlF	CH_3F	C_3H_4
FCCH	FCN	H_2S	HCP	HFCO	H_2C_2O	LiF
	N_2O	OCS	H_4C_2O	PN	SO_2	

3.1 Energy expansion in a field

A rigid, non-rotating molecule in a singlet electronic state with nuclear magnetic moments, $\{\mathbf{M}_K\}$, exposed to the homogeneous static magnetic field, $\mathbf{B}$, responds to the perturbing field, changing the ground state energy. The perturbed energy can be defined as a Taylor expansion of the energy in terms of the perturbing field and molecular magnetic moments,

$$\begin{aligned} E(\mathbf{B},\{\mathbf{M}_k\}) = E_0 & && \text{(unperturbed energy)} \\ + & \underbrace{\mathbf{B}^{\mathrm{T}}\mathbf{E}^{(10)}}_{\text{perm. mag. mom.}} + \underbrace{\sum_K \mathbf{M}_K^{\mathrm{T}}\mathbf{E}_K^{(01)}}_{\text{hyperfine coupling}} && \text{(1st order terms)} \\ + & \underbrace{\frac{1}{2}\mathbf{B}^{\mathrm{T}}\mathbf{E}^{(20)}\mathbf{B}}_{-\text{magnetizability}} + \underbrace{\frac{1}{2}\sum_K \mathbf{B}^{\mathrm{T}}\mathbf{E}_K^{(11)}\mathbf{M}_K}_{\text{NMR shieldings + 1}} + \underbrace{\frac{1}{2}\sum_{KL}\mathbf{M}_K^{\mathrm{T}}\mathbf{E}_{KL}^{(02)}\mathbf{M}_L}_{\text{spin-spin couplings}} + \ldots && \text{(2nd order terms)} \end{aligned} \tag{3.1}$$

The individual intrinsic molecular properties can be identified from the relevant derivatives in Eq. (3.1) with respect to the external field or nuclear magnetic moment in the limit of vanishing field. Since both $\mathbf{B}$ and $\mathbf{M}_k$ are vector fields the static responses are tensor properties. The molecules of Table 3.1 have been aligned with their principle symmetry axis oriented along the z axis. Whilst this uniquely defines the z component of a response tensor the x and y components cannot be easily defined and are left ambiguous, preventing the straightforward comparison of individual tensor elements between calculations or with experiment. As a result attention was restricted to isotropic quantities defined as,

$$\zeta^{\mathrm{iso}} = \frac{1}{3}\operatorname{Tr}\boldsymbol{\zeta}, \tag{3.2}$$

avoiding the ambiguity of molecular orientation.

For the closed shell singlet molecules in Table 3.1 the odd order terms in Eq. (3.1) disappear and the isotropic molecular magnetizability can be identified as,

$$\zeta^{\mathrm{iso}} = \frac{1}{3}\operatorname{Tr}\left[-\frac{\mathrm{d}^2 E}{\mathrm{d}\mathbf{B}\mathrm{d}\mathbf{B}}\Big|_{\mathbf{B}=\mathbf{0}} \right], \tag{3.3}$$

with the isotropic NMR shielding constant for nucleus k,

$$\sigma_k^{\mathrm{iso}} = \frac{1}{3}\operatorname{Tr}\left[-\frac{\mathrm{d}^2 E}{\mathrm{d}\mathbf{B}\mathrm{d}\mathbf{M}_k}\Big|_{\mathbf{B}=\mathbf{M}_k=\mathbf{0}} + \mathbf{1} \right]. \tag{3.4}$$

3.2 Perturbative evaluation of molecular properties

The difficulties associated with carrying out *ab initio* calculations in a finite magnetic field preclude the direct analytical evaluation of derivatives with respect to magnetic field. Instead it is common for Eq. (3.1) to be calculated from a zero field reference using perturbation theory. A response property expressed as the general combination of energy derivatives with respect to external magnetic field and nuclear magnetic moments, $\mathbf{F} = \{\mathbf{B}, \mathbf{M}_k\}$, can be determined using perturbation theory as,

$$\frac{\mathrm{d}^2 E}{\mathrm{d}\mathbf{F}\mathrm{d}\mathbf{F}} = \left\langle 0 \middle| \frac{\mathrm{d}^2 H}{\mathrm{d}\mathbf{F}\mathrm{d}\mathbf{F}} \middle| 0 \right\rangle - 2\sum_{\mathrm{n}\neq 0} \frac{\left\langle 0 \middle| \frac{\mathrm{d}H}{\mathrm{d}\mathbf{F}} \middle| n \right\rangle \left\langle n \middle| \left(\frac{\mathrm{d}H}{\mathrm{d}\mathbf{F}}\right)^{\mathrm{T}} \middle| 0 \right\rangle}{E_n - E_0} \tag{3.5}$$

where the summation runs over all singly excited states $|n\rangle$. The first term of Eq. (3.5) is the diamagnetic contribution from the ground state, and the second sum-over-states term contains the paramagnetic contributions.

The sum-over-states required for the paramagnetic contribution is computationally impractical, requiring an accurate description of the full set of singly excited states. Instead the linear response of

the unperturbed wave function is determined from the Hellman–Feynman theorem. A full derivation of response theory for magnetic properties is not presented here, instead the reader is referred to Ref. [116] for a comprehensive review.

The benchmark NMR shielding and molecular magnetizabilities of Ref. [113] and Ref. [114] were calculated from CCSD(T) wave functions using a linear response analysis. The uncontracted aug-cc-pCV[TQ]Z basis sets were used and the extrapolation technique of Ref. [117] was used to estimate the basis set limit to give a benchmark data set against which the new CDFT implementation could be compared. See the respective references for full computational details of the benchmarking calculations.

3.3 Finite field calculation of magnetic properties

When fully self consistent calculations are available at arbitrary field strengths it is conceptually simpler to evaluate the derivatives of Eq. (3.1) numerically using finite difference techniques than to evaluate the derivatives analytically. Evaluation by finite difference has two main advantages over the perturbative approaches. Firstly, the response equations become unwieldy for higher order properties but are simple to obtain numerically given sufficient SCF data points. Secondly, the perturbative response of a zero field wave function is only strictly valid for infinitesimal fields, becoming less reliable and requiring higher order perturbation theory for stronger fields. In contrast a fully self consistent calculation can be made at any field strength allowing the evaluation of molecules in strong magnetic fields, such as are found around some stellar objects [5, 7, 118].

It should be noted however that calculation of properties by finite field is not without limitation. In order to assure the accuracy of the numerical derivatives upon which properties are based a careful convergence study must be made in the range, spacing and in the order of fitting polynomial to establish confidence in calculated results. This is especially true of the higher order hyper-magnetizability considered in this work for which no benchmark data was available. An additional limitation for finite field evaluation is the considerable computational effort that must be expended to produce the energy values required for numerical fitting.

A further difficulty with a finite field evaluation of magnetic properties arrises from the extra theoretical challenges associated with carrying out calculations within an explicit magnetic field. Until the implementation of CDFT detailed in this work, finite field calculations have only been possible at the uncorrelated Hartree-Fock and the impractically expensive FCI levels of theory [27]. As a result the properties calculated using CDFT detailed here are the first correlated estimates of magnetic properties evaluated by finite field techniques.

3.3.1 Isotropic molecular magnetizability and hyper-magnetizability

Consider a uniform magnetic field $\mathbf{B}$ with a corresponding vector potential given by Eq. (2.38). Expanding the energy in orders of $\mathbf{B}$, we obtain for a closed-shell system,

$$\begin{aligned} E(\mathbf{B}) =& E(\mathbf{0}) - \frac{1}{2}\sum_{\alpha\beta}\chi_{\alpha\beta}B_\alpha B_\beta \\ & - \frac{1}{4!}\sum_{\alpha\beta\gamma\zeta}X_{\alpha\beta\gamma\zeta}B_\alpha B_\beta B_\gamma B_\zeta + \mathcal{O}(B^6), \end{aligned} \tag{3.6}$$

where odd-order terms vanish. The magnetizability tensor $\chi_{\alpha\beta}$ and fourth-rank hyper-magnetizability tensor $X_{\alpha\beta\gamma\zeta}$ can be obtained by least-squares fitting of a polynomial to energies $E(\mathbf{B}_{\alpha\ell})$ for a suitable discrete grid of a sample fields $\mathbf{B}_{\alpha\ell}$. The diagonal tensor elements (which require less fitting data) are sufficient to evaluate the isotropic property defined by Eq. (3.2), using $\mathbf{B}_{\alpha\ell} = \ell\mathbf{e}_\alpha$. It was found that $\ell = 0.00, 0.01, \ldots, 0.03$ a.u. in each Cartesian direction, $\alpha \in \{x, y, z\}$ provided sufficient data to accurately determine molecular magnetizabilities; the results reproducing those of the perturbative DALTON [109] implementation to better than 0.1 JT^{-4} for standard density functionals. Careful study of the convergence of hyper-magnetizabilities, detailed in Section 3.4.4, revealed that higher field strengths were required to obtain robust results requiring grids supplemented with the points

$\ell = 0.03, 0.04, \ldots, 0.1$ a.u. in each Cartesian direction, making the calculations considerably more expensive. The tensor elements were calculated by fitting 6th-order polynomials in each Cartesian direction.

3.3.2 Isotropic nuclear magnetic shielding constants

The NMR shielding constants were calculated non-perturbatively by considering the dependence of the molecular electronic energy $E(\mathbf{B}, \mathbf{M}_k)$ on the external magnetic field $\mathbf{B}$ and the nuclear magnetic moment $\mathbf{M}_k$ of nucleus k represented by the vector potential,

$$\mathbf{A}_k(\mathbf{r}) = \frac{\mu_0}{4\pi} \frac{\mathbf{M}_k \times (\mathbf{r} - \mathbf{R}_k)}{|\mathbf{r} - \mathbf{R}_k|^3} = \frac{\mu_0}{4\pi} \mathbf{M}_k \times \frac{1}{\partial \mathbf{R}_k} \frac{1}{|\mathbf{r} - \mathbf{R}_k|}, \tag{3.7}$$

to obtain the Taylor expansion,

$$E(\mathbf{B}, \mathbf{M}_k) = E(\mathbf{0}, \mathbf{0}) + \sum_{\alpha\beta} \sigma_{k;\alpha\beta} B_\alpha M_{k;\beta} + \cdots, \tag{3.8}$$

where the nuclear shielding tensor is the leading-order mixed term in the expansion of the energy,

$$\sigma_{k;\alpha\beta} = \frac{\partial^2 E(\mathbf{B}, \mathbf{M}_k)}{\partial B_\alpha \partial M_{k;\beta}}\Big|_{\mathbf{B}=\mathbf{M}_k=\mathbf{0}}. \tag{3.9}$$

The kinetic-energy operator in the molecular Hamiltonian now becomes $\hat{\pi}^2/2 = (\hat{\mathbf{p}} + \mathbf{A}(\mathbf{r}) + \mathbf{A}_k(\mathbf{r}))^2/2$. By exploiting the Hellmann–Feynman theorem the derivative with respect to $\mathbf{M}_k$ is computed analytically,

$$\begin{aligned} \Xi_{k;\beta}(\mathbf{B}) &= \frac{\partial E(\mathbf{B}, \mathbf{M}_k)}{\partial M_{k;\beta}}\Big|_{\mathbf{M}_k=\mathbf{0}} \\ &= \frac{e\mu_0}{4\pi m} \epsilon_{\alpha\beta\gamma} \frac{\partial}{\partial k_\gamma} \left\langle \psi \right| \left\{ \hat{p}_\alpha + eA_\alpha, |\mathbf{r} - \mathbf{R}_k|^{-1} \right\} \left| \psi \right\rangle, \end{aligned} \tag{3.10}$$

the braces denote the anti-commutator. The expectation value is similar to a nuclear attraction integral, and may be evaluated using the McMurchie–Davidson scheme described in Ref. [51]. The remaining differentiation may be performed directly by numerical differentiation,

$$\sigma_{k;\alpha\beta} \approx \frac{\Xi_{k;\beta}(\epsilon \mathbf{e}_\alpha) - \Xi_{k;\beta}(-\epsilon \mathbf{e}_\alpha)}{2\epsilon} = \frac{\Xi_{k;\beta}(\epsilon \mathbf{e}_\alpha)}{\epsilon}, \tag{3.11}$$

or indirectly by polynomial fitting to computed $\Xi_{k;\beta}(\mathbf{B})$ values as a function of $\mathbf{B}$. The fitting is simplified by the fact that only odd-orders of $\mathbf{B}$ enter in the expansion of $\Xi_{k;\beta}(\mathbf{B})$.

The NMR shielding constants showed similar convergece to the molecular magnetizabilities (Section 3.3.1), showing that $\ell = 0.00, 0.01, \ldots, 0.03$ a.u. in each Cartesian direction, $\alpha \in \{x, y, z\}$ provided sufficient data to accurately determine shielding constants with a 6$^{\text{th}}$ order polynomial fitting; the results reproducing those of the perturbative DALTON [109] implementation to better than 0.1 ppm for standard density functionals.

3.3.3 Computational details

The current dependent functionals discussed in Sections 2.3 and 2.4 were implemented within the LONDON and XCFUN software packages and used to calculate the shielding constants and molecular magnetizabilities by the finite field methods detailed above for the 26 molecules of Table 3.1. Calculations were performed using molecular geometries taken from Ref. [114], which were optimised at the all-electron CCSD(T)/cc-pVTZ level.

Benchmark response properties were calculated in a perturbative manner using the ACESII (MAB version) quantum chemistry package and were originally published in Ref. [113, 114] using CCSD(T) theory with the aug-cc-pCV[TQ]Z basis set extrapolated to the basis set limit using the extrapolation technique of Ref. [117]. Previous work shows this data to be highly accurate, comparing well

with experimental values. All errors quoted in Section 3.4 are given relative to these benchmark data.

In all cases the aug-cc-pCVTZ London atomic orbital basis set has been employed. The CDFT vorticity dependent functionals were regularised with a hard cutoff on the Wigner–Seitz radius, r_s, of 9.1055 a.u. and a soft cutoff $\epsilon = 10^{-14}$ a.u., see Eq. (2.133). Experimentation revealed that results were not particularly sensitive to the angular or radial grid parameters, the default parameters were therefore used. For the Lebedev grid, the angular integration was specified to be exact for spherical harmonics up to order 35; in the LMG radial integration, the accuracy parameter specifying the upper limit of the error in the case of an atomic integration was set to 10^{-13} a.u.

Even when employing the regularisation of Eq. (2.133) issues with SCF convergence were encountered for the VRG(LHC) parametrised CDFT corrections at some field strengths when using the standard DIIS SCF acceleration approach. Interestingly, no such issues were encountered with the VRG(TP) parametrisation, for which calculations on the full set of 26 molecules could be routinely performed at a range of field strengths up to 1 a.u. This may reflect differences in the function $g(\rho)$ examined in Figure 2.2 and Figure 2.3. In particular, the 8 molecules CH_3F, HCN, HCP, H_4C_2O, CH_2O, OCS, and SO_2 could not be reliably converged using the VRG(LHC) parametrisation. To account for this all plots and error analyses of VRG corrected functionals refer to the remaining subset of 19 molecules. The full data set may be found in the Table 3.3 and Table 3.4, including full VRG(TP) results for all 26 molecules.

3.3.4 Sensitivity of vorticity dependent functionals to vorticity regularisation

Before considering the benchmark calculations, the VRG corrections to the oxygen shielding constant in H_2O were plotted against the integration cut-off parameter $\rho_{\text{cut-off}}$ (with hard and soft cut-offs) for the LHC, TP, and HHmod parametrisations of $g(\rho)$, shown in Figure 3.1. Substantial variations in the corrections were observed and no convergence was achieved with reasonable cut-offs—in particular, for the LHC parametrisation (with variations over 60 ppm in the plot). The LDA- and BLYP-based VRG corrections are similar to each other for cut-offs larger than about 10^{-5}; for smaller cut-offs, the LDA-based corrections tend to be larger than the BLYP-based corrections. Moreover, the differences between the corrections obtained with hard and soft cut-offs are small compared with the differences observed for different cut-off parameters.

The TP correction is much better behaved, with variations on the order of 3.5 ppm and a consistent sign for the correction term. However, this variation and a lack of convergence with respect to varying the cutoff parameters mean that it cannot be recommended for general practical use. The HHmod parametrisation shows a large variation with regularisation parameters and so also cannot be recommended for practical use. However, it is interesting that for the large cutoff values HHmod leads to a negative correction, which is opposite in sign to the high cutoff value LHC and TP corrections. This difference may reflect the qualitative difference in the functions $g(\rho)$ in Figure 2.2 and Figure 2.3, in particular for large densities $g_{\mathrm{HHmod}}(\rho)$ is positive, whilst $g_{\mathrm{LHC}}(\rho)$ and $g_{\mathrm{TP}}(\rho)$ are negative. This further re-enforces the need for an improved parametrisation of $g(\rho)$ as the stability of the functional obtained and hence the quality of the results is strongly influenced by this parametrisation.

3.4 CDFT estimates of magnetic response properties

To quantify the accuracy of the current modified mGGA CDFT functionals for the calculation of molecular magnetisability and NMR shielding constants calculated results were compared against the same CCSD(T) benchmark values of Ref. [114] and Ref. [113] as the VRG functionals.

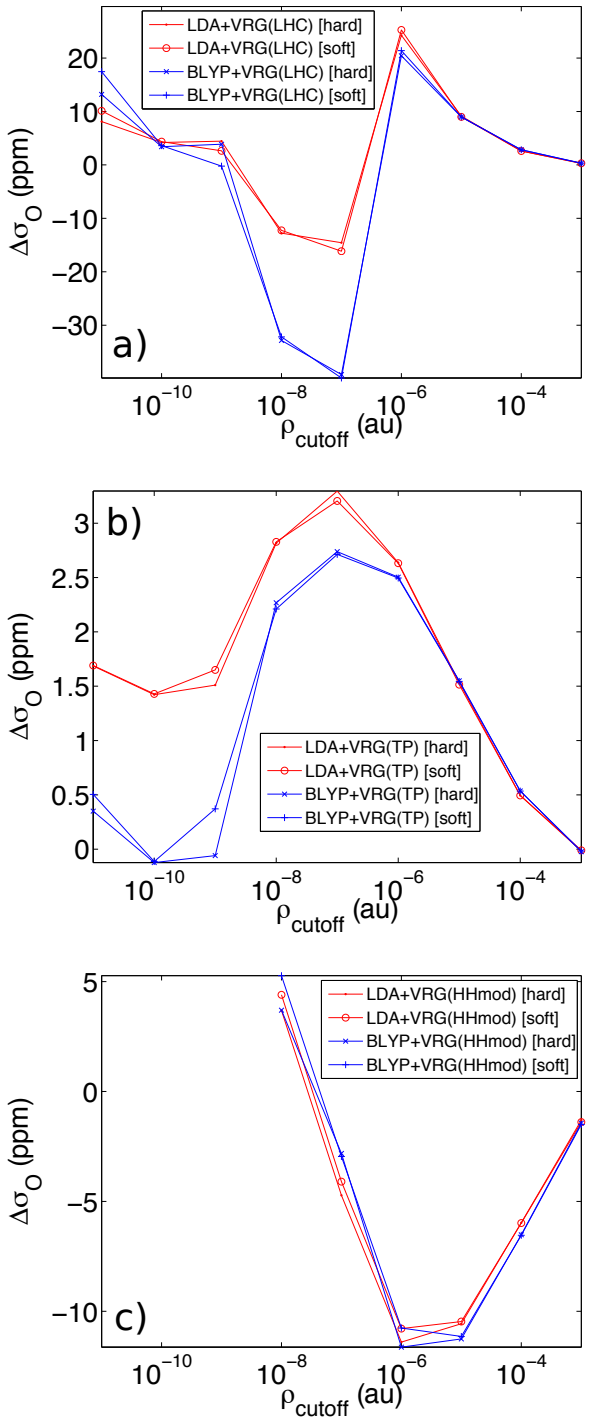


Figure 3.1: The VRG correction to the oxygen shielding constant in the water molecule plotted against the integration regularisation cut-off parameter $\rho_{\text{cut-off}}$ for the a) LHC, b) TP, and c) HHmod parametrisations of $g(\rho)$ in Eq. (2.86). Both hard and soft cut-offs are illustrated in the plots. The Huz-II basis, with London gauge factors, was used in all cases.

3.4.1 Molecular magnetizabilities

Standard DFT functionals and vorticity corrections

In a previous benchmark study of magnetizabilities and g tensors calculated from standard DFT functionals, Lutnæs *et al.* found that the standard DFT functionals (which neglect the current dependence) in general give poorer results than the Hartree–Fock model [113]. Moreover, whereas the Hartree–Fock model (like the coupled-cluster models) on average underestimates magnetizabilities, the LDA and GGA functionals overestimate the magnetizabilities. The magnetizabilities obtained using the conventional LDA, PBE, and KT3 functionals without current correction and with the VRG(LHC) and VRG(TP) corrections are plotted in Figure 3.2;[1] the Hartree–Fock results for the same systems are included for comparison. The same trends as observed in Ref. [113] are seen, with the LDA, PBE, and KT3 functionals overestimating the magnetizabilities and giving less systematic errors than the Hartree–Fock model.

Unfortunately, addition of the VRG functional (with the LHC and TP parameterisations) does not improve the situation. For all three DFT functionals, the VRG(LHC) correction increases the error in the magnetizabilities, increasing both mean errors and the spread. The results are slightly better for the VRG(TP) functional but still poorer than those obtained without the VRG correction. Clearly, the VRG-corrected functionals cannot be recommended for the calculation of magnetizabilities. It is noted that Lee, Collwell and Handy [75] studied magnetizabilities for a few small systems in the context of CDFT using a perturbative implementation. Many of the systems they considered are included in the present work, however, a direct comparison is difficult because of the use of different basis sets and the fact that the results of Ref. [75] are not gauge-origin invariant. The results of this work may therefore be considered a more extensive benchmark addressing some of the issues associated with these earlier calculations.

Current modified meta-GGA functionals

A similar set of calculations were performed for the modified meta-GGA functionals to provide a comparable set of isotropic molecular magnetizabilities for the same benchmark molecules and the errors in the calculated magnetizabilities are presented graphically in Figure 3.3.

It is clear from Figure 3.3 that none of the functionals offer high accuracy for the molecular magnetizabilities. For comparison the PBE+VRG(TP) and KT3+VRG(TP) results are included along with the equivalent non-corrected standard DFT functionals to show the effect of including the current correction. At the mGGA level this comparison is not possible as inclusion of current through the modified kinetic energy density is mandatory to ensure the exchange–correlation energy is gauge origin independent; as such it is not possible to directly quantify the current contribution.

The cTPSS and cTPSS(h) functionals give similar performance to PBE, offering marginal improvements on some error measures with cTPSS(h) performing slightly better than cTPSS. The cB98 form gives the best performance of all the functionals considered. It is noteworthy that in the mGGA class the mean errors reduce as more HF exchange is included in the functional – with cTPSS, cTPSS(h) and cB98 containing 0%, 10% and 19.85% HF exchange respectively. This suggests that the treatment of exchange may be the dominant factor in the errors. Since the treatment of long-range exchange is not rectified in the transition from GGA to mGGA type functionals (and only partially corrected by a global admixture), then it may be that this factor far out weighs any improvements due to the inclusion of current effects.

It is worth emphasising that throughout the course of the investigation the implementation of the mGGA functionals including a current generalised kinetic energy density was straightforward. In particular no special care was required with respect to numerics compared with standard functionals, and in practical use the functionals were robust and self-consistent calculations converged without significant difficulty. This sharply contrasts the behaviour for the VRG functionals as investigated in Ref. [10] and Ref. [83] and discussed in Section 3.3.4.

[1] The values that failed to converge for VRG(LHC) have been removed as per Section 3.3.3

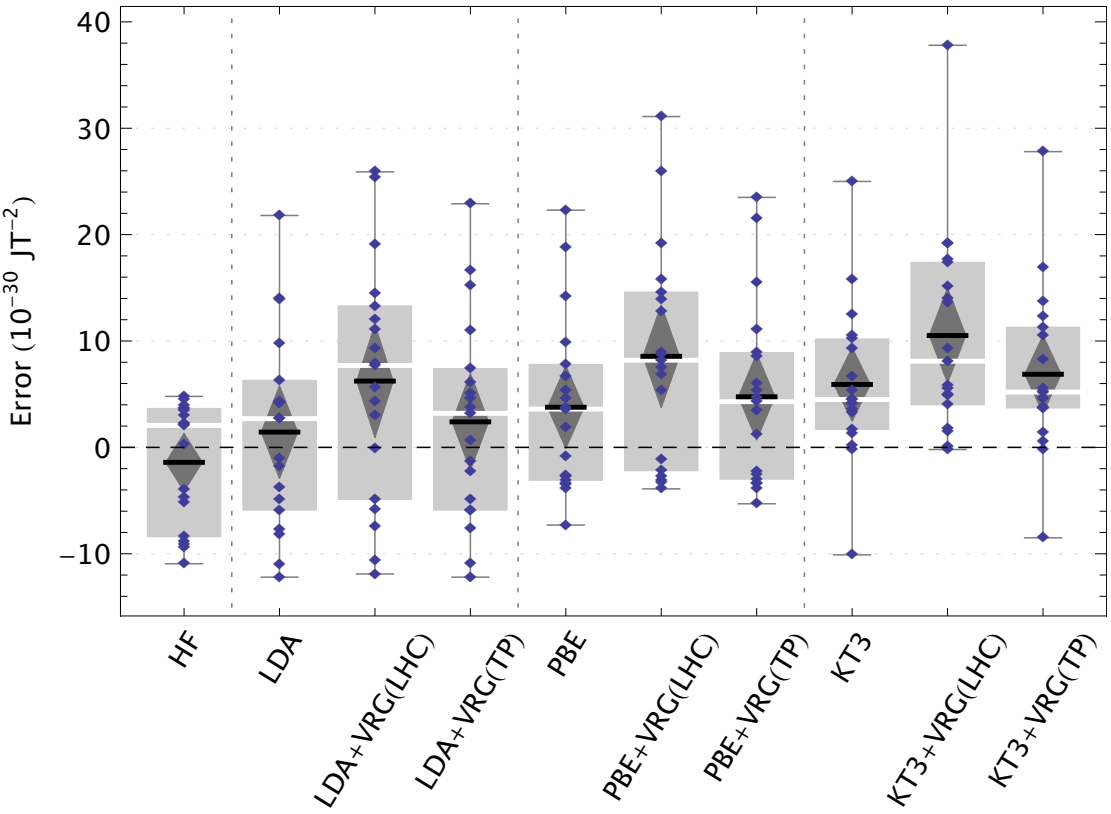


Figure 3.2: Box-whisker plot of errors in standard and vorticity corrected DFT molecular magnetizabilities relative to the basis set extrapolated CCSD(T) values of Ref. [113]. All calculations use the aug-cc-pCVTZ basis set. The upper and lower fences of the whiskers denote the maximum positive and negative errors respectively and the light gray boxes enclose errors between the 25% and 75% quantiles. Mean and median errors are marked in the plots by horizontal black and white lines respectively and grey diamonds are used to represent the confidence intervals.

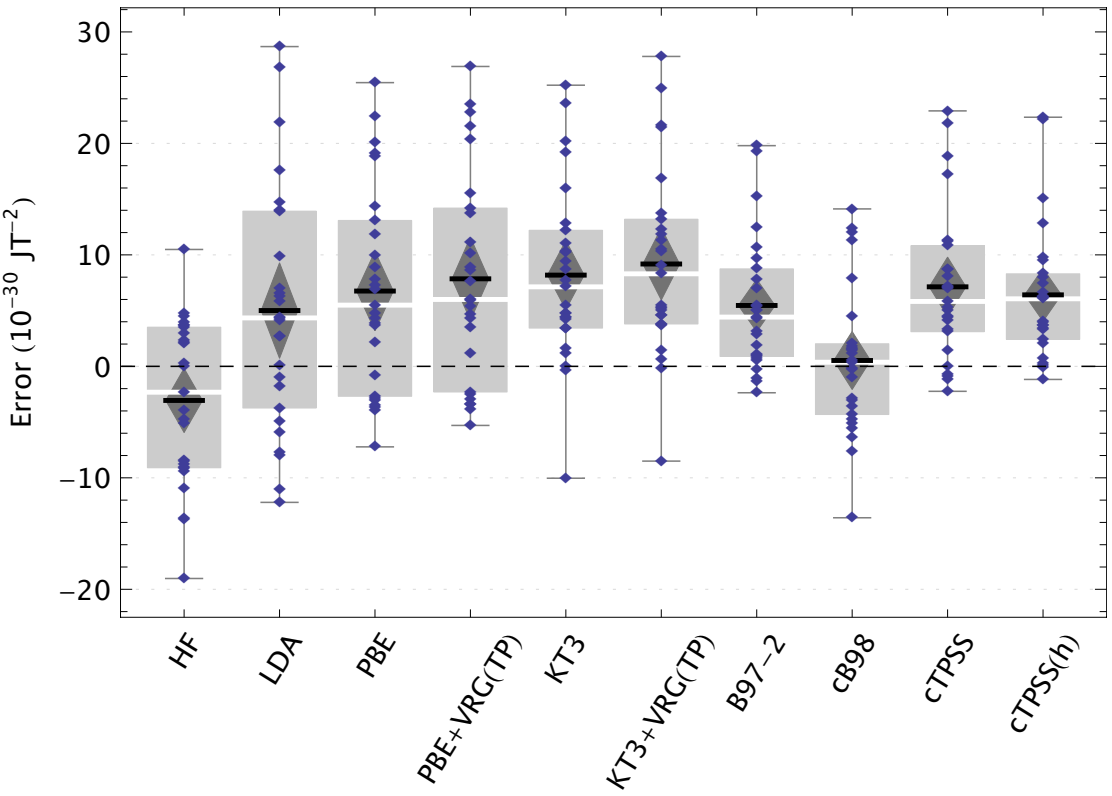


Figure 3.3: Box-whisker plot of errors in modified mGGA CDFT molecular magnetizabilities relative to the basis set extrapolated CCSD(T) values of Ref. [113]. All calculations use the aug-cc-pCVTZ basis set. The upper and lower fences of the whiskers denote the maximum positive and negative errors respectively and the light gray boxes enclose errors between the 25% and 75% quantiles. Mean and median errors are marked in the plots by horizontal black and white lines respectively and grey diamonds are used to represent the confidence intervals.

3.4.2 Nuclear shielding constants

In a recent benchmark study of NMR shielding constants and spin–rotation constants, [114] the accuracy achieved by Kohn–Sham calculations was found to be rather low. Although the various DFT approximations improve slightly upon Hartree–Fock theory, none of the DFT functionals provide an accuracy similar to that of CCSD or CCSD(T) theory; moreover, the inclusion of vibrational corrections worsened the agreement with experimental values. Regarding the different exchange–correlation functionals, a general improvement was observed when going from LDA to GGA functionals, with further improvements observed for hybrid functionals—in particular, in combination with an optimised effective potential (OEP) approach. Interestingly, KS[CCSD] and KS[CCSD(T)] calculations, where the Kohn–Sham system reproduces the CCSD and CCSD(T) densities, respectively, gave errors similar to those of the OEP calculations. This suggested that the neglect of current dependence may be a significant factor in determining the accuracy of these calculations.

Standard DFT functionals and vorticity corrections

The nuclear shieldings were calculated for the 19 molecules in the (reduced) benchmark set at the same levels of theory and same parameterizations (with a hard cut-off $\rho_{\text{cut-off}} = 3.1 \times 10^{-4} \equiv r_s = 9.1055$) as for the magnetizabilities in Section 3.4.1. Figure 3.4 presents the data for chemically unique nuclei in the subset of molecules (a total of 48 data points), all values are available in Table 3.3. It is noted that that the Kohn–Sham DFT shieldings constitute a slight improvement on the Hartree–Fock shieldings, with a smaller spread and more negative mean values. The general, though modest, improvement in the order HF, LDA, PBE, KT3 is clear, as was observed in Ref. [114]. However, as for the magnetizabilities in Figure 3.2, the addition of the VRG correction does not improve the calculated shieldings — in fact their quality tends to deteriorate with the application of VRG correction to the functional, especially for the LHC parameterisation. These results are in line with the early observations of Lee, Handy, and Colwell (LHC) [76] and indicate that (at least at the GGA level) improvement of the underlying functional to describe NMR properties, as is the case for KT3, does not lead to any significant difference in the associated VRG correction. The interplay between the choice of functional and the quality of VRG-type corrections beyond the GGA level could be investigated in future work, though given the poor performance of all vorticity based corrections there may be more successful approaches to higher accuracy CDFT XC functionals.

Current modified meta-GGA functionals

The mGGA results for NMR shielding constants are presented in Figure 3.5. The results for cB98, cTPSS and cTPSS(h) are intermediate between PBE and KT3 — offering small systematic improvements over PBE. Similar to the molecular magnetizabilities, cB98 produced the best results of the mGGA functionals. Overall however, the current including mGGA functionals do not offer any significant improvement over the standard DFT functionals for the prediction of NMR shielding values, but do not perform any worse. This represents an improvement over the VRG vorticity correction, though it is perhaps disappointing that the inclusion of current does not strengthen results significantly given the analysis of Ref. [114].

3.4.3 Comparative summary

Table 3.2 collects the mean error, mean absolute error and standard deviation of errors for molecular magnetizabilities and NMR shielding constants for all of the functional combinations considered. It is somewhat disheartening that none of the current dependent functionals offer the improvement that may be expected from the considerations of Refs. [113] and [114] for a correct handling of current effects. Further investigation in the strong field regime (Section 3.5) suggests that inclusion of current information through the current modified meta-GGA form is better able to capture the strong field limit and it is therefore suggested that the dominating errors in response property calculation lie in deficiencies in the underlying zero-field functional approximations.

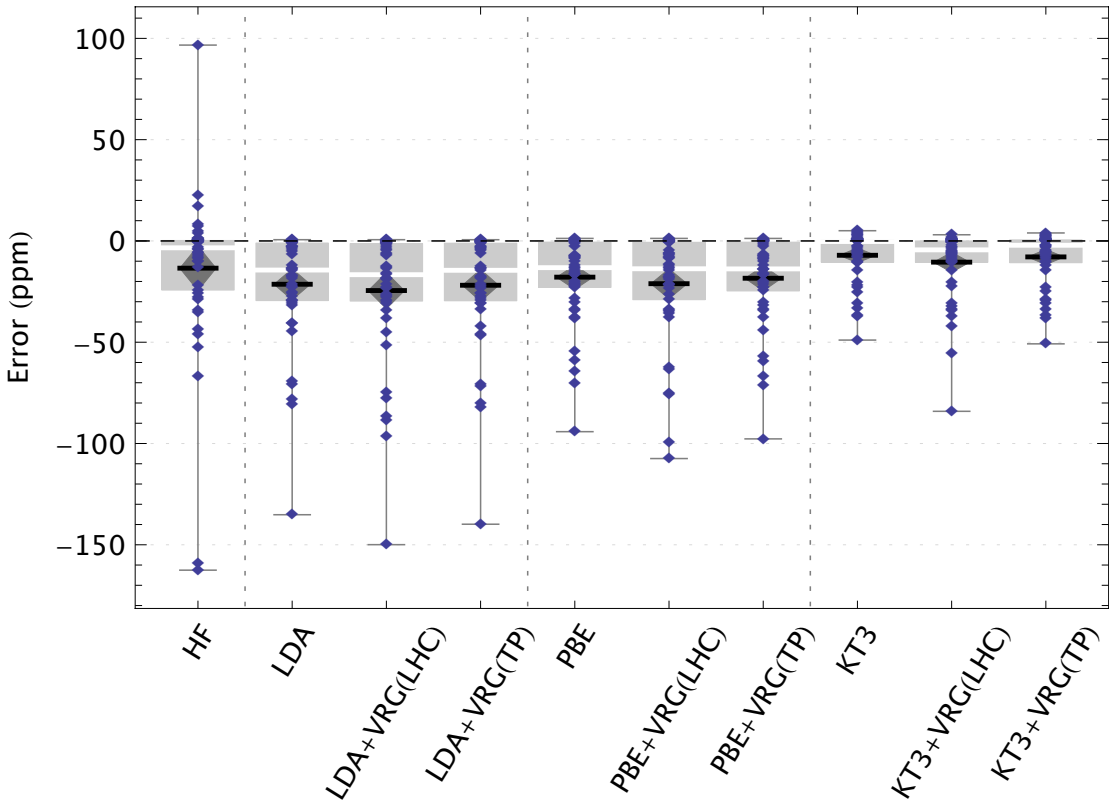


Figure 3.4: Errors in isotropic shielding constants (ppm) calculated using DFT functionals with and without the VRG(LHC) and VRG(TP) corrections in the aug-cc-pCVTZ basis set. Results that failed to converge during the SCF optimization with the VRG(LHC) correction have been omitted. The upper and lower fences of the whiskers denote the maximum positive and negative errors respectively and the light gray boxes enclose errors between the 25% and 75% quantiles. Mean and median errors are marked in the plots by horizontal black and white lines, respectively and grey diamonds are used to represent the confidence intervals. The plot markers show the individual errors for each chemically unique nuclei in the 26 molecules in the full data set of Section 3.1 (a total of 68 data points).

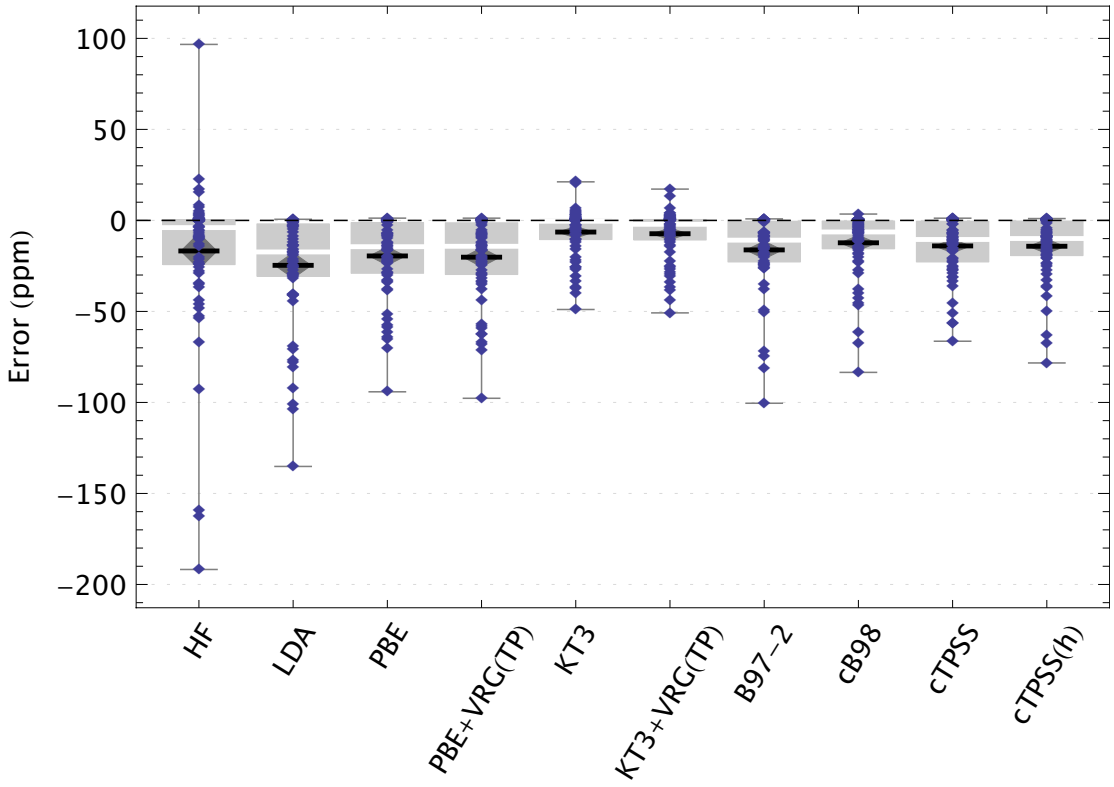


Figure 3.5: Errors in isotropic shielding constants (ppm) calculated using mGGA CDFT functionals as well as standard DFT functionals with and without the VRG(TP) voticity correction, all calculations used the aug-cc-pCVTZ basis set. The upper and lower fences of the whiskers denote the maximum positive and negative errors respectively and the light gray boxes enclose errors between the 25% and 75% quantiles. Mean and median errors are marked in the plots by horizontal black and white lines, respectively and grey diamonds are used to represent the confidence intervals. The plot markers show the individual errors for each chemically unique nuclei in the 19 molecules in the reduced data set of Section 3.1 (a total of 48 data points).

Table 3.2: The mean error (ME), mean absolute error (MAE), and standard deviation (SD) of magnetic properties relative to the CCSD(T) benchmark data of Refs. [113, 114]. The VRG(LHC) functional was unable to converge for 9 systems, this data has been omitted in this analysis and is indicated with a *. All other functionals present data for the full test set of Table 3.1. See also Figs. 3.2—3.5, and Tables 3.3 and 3.4.

	Magnetizability ($10^{-30}\mathrm{JT}^{-2}$)			NMR Shielding (ppm)		
	ME	MAE	SD	ME	MAE	SD
HF	-3.06	6.35	7.29	-16.78	22.45	41.39
LDA	5.01	9.18	10.86	-24.68	24.72	29.62
LDA+VRG(LHC)*	6.23	10.52	11.13	-24.49	24.54	31.53
LDA+VRG(TP)	6.11	9.89	11.30	-25.32	25.36	30.70
PBE	6.75	8.81	9.03	-19.52	19.65	21.20
PBE+VRG(LHC)*	8.56	10.27	10.11	-21.10	21.27	26.06
PBE+VRG(TP)	7.85	9.61	9.44	-20.20	20.33	22.15
KT3	8.18	8.95	7.83	-6.40	9.07	13.35
KT3+VRG(LHC)*	10.52	10.54	9.36	-10.47	10.94	17.43
KT3+VRG(TP)	9.18	9.83	8.19	-7.32	9.31	13.53
B97-2	5.46	5.84	5.96	-16.21	16.35	20.45
cB98	0.52	4.84	6.58	-7.48	7.86	11.91
cTPSS	7.13	7.51	6.76	-14.01	14.22	15.60
cTPSS(h)	6.41	6.51	6.00	-14.20	14.39	16.62

On the whole the quality of the mGGA results at modest field strengths may be regarded as disappointing. The overall errors suggest that mGGAs may offer modest improvements over conventional GGA functionals such as PBE — though they cannot compete with GGAs tailored to specific properties. This is broadly consistent with findings by Bates and Furche for the calculation of excitation energies using cTPSS [93]. Since current corrections are known to be relatively small it is important that the underlying functional should be relatively accurate. For the mGGAs considered here there are known weaknesses (for example in the treatment of long-range exchange) that may obscure the effect of the current dependence. For the case of NMR shielding constants a more detailed analysis of the significance of current effects and how these interplay with errors in a range of density functionals is presented in Ref. [119].

3.4.4 Molecular hyper-magnetizabilities

Over the last two decades, perturbative calculations of second-order properties such as magnetizabilities and nuclear shielding constants have become routine in quantum chemistry. Properties that require higher-order responses such as hyper-magnetizabilities have received much less attention. Perturbative approaches applied at the coupled-perturbed Hartree–Fock level using standard (non-London) orbitals have been explored by Pagola *et al.* [120, 121], while the finite-difference approach has been explored at the Hartree–Fock level using London orbitals in Ref. [51]. However, there were no calculations of molecular hyper-magnetizabilities employing methods including a correlation treatment until the current work.

Convergence analysis

The stability of isotropic hyper-magnetizabilities calculated by finite difference was determined with regards to range and spacing of field strengths as well as the order of polynomial fitting. At least 4^{th} order fitting is required — as the hyper-magnetizability is a 4^{th} order property — whilst over fitting errors from high fitting orders must also be avoided. A 6^{th} order polynomial fitting was found as an optimal compromise. The analysis was carried out for H_2O using fields from 0 to ± 0.03 a.u. in steps of 0.0001 a.u. using the STO-3G minimal basis set to produce the $xxxx$, $yyyy$ and $zzzz$ elements of the hyper-magnetizability tensor. Convergence was assessed by taking subsets of this data as an

Table 3.3: Absolute shielding constants (ppm) calculated with DFT and CDFT functionals in the aug-cc-pCVTZ basis set.

Molecule	Nucleus					VRG(LHC)				VRG(TP)							
		LDA	KT3	PBE	PBE0	LDA	KT3	PBE	PBE0	LDA	KT3	PBE	PBE0	cB98	cTPSS	cTPSS(h)	B97-2
AlF	Al	531.79	566.52	542.22	553.94	527.78	562.74	538.25	549.91	530.59	565.41	541.04	516.45	567.94	550.11	554.10	558.14
	F	142.92	175.2	154.24	179.42	137.13	169.64	148.52	173.43	141.12	173.5	152.48	86.94	184.17	166.38	175.61	185.53
C_3H_4	C	178.52	181.8	178.03	183.28	178.85	182.14	178.37	183.71	178.51	181.8	178.02	185.44	185.68	179.14	181.06	181.83
(cyclopropene)	C	58.82	77.8	64.58	67.15	56.43	75.56	62.23	64.7	58.02	77.07	63.8	68.81	72.07	70.26	70.71	68.86
	H	23.74	24.53	24.23	24.14	23.62	24.4	24.11	24.02	23.71	24.5	24.2	23.69	24.19	24.67	24.59	24.34
	H	30.25	30.79	30.62	30.67	30.16	30.69	30.52	30.58	30.24	30.77	30.6	30.45	30.80	30.86	30.86	30.77
FCCH	C	166.8	181.97	171.59	172.36	166.29	181.63	171.15	171.86	166.54	181.77	171.35	177.98	177.87	174.30	174.31	173.24
	C	79.04	95.66	84.4	89.83	76.9	93.56	82.27	87.8	78.38	95.03	83.75	80.74	92.66	89.58	91.15	91.10
	H	30.64	31	31	30.81	30.68	31.03	31.03	30.84	30.65	31	31.01	31.15	30.91	31.08	31.00	30.94
	F	393.09	393.17	390.19	399.73	392.69	392.65	389.69	399.23	392.89	392.94	389.97	388.73	401.29	392.32	396.00	398.72
C_2H_4	C	42.95	64.76	49.99	52.77	40.59	62.71	47.74	50.48	42.14	64.05	49.21	53.39	58.49	57.06	57.43	54.90
	H	25.12	26.12	25.68	25.73	25.06	26.06	25.61	25.66	25.11	26.1	25.66	25.12	25.85	26.19	26.15	25.91
H_2C_2O	C	187.25	190.74	186.68	187.98	187.4	190.9	186.82	188.1	187.16	190.66	186.58	200.54	191.84	186.42	186.95	186.86
(ketene)	C	-19.77	-2.66	-15.42	-15	-23	-5.79	-18.63	-18.23	-20.83	-3.68	-16.48	-0.01	-9.22	-11.81	-12.05	-13.36
	O	-21.1	-0.2	-17.35	-21.57	-26.91	-5.93	-23.2	-28.13	-23.13	-2.16	-19.38	-2.31	-11.14	-12.85	-14.70	-16.22
	H	29	29.6	29.44	29.34	29	29.59	29.44	29.34	29	29.59	29.44	29.75	29.53	29.66	29.61	29.47
CH_3F	C	105.09	114.05	107.06	113.69	-	-	-	-	104.66	113.64	106.64	111.54	115.80	110.93	113.09	113.14
	F	474.21	456.23	462.43	471.17	-	-	-	-	473.95	455.78	462.06	469.94	472.26	462.27	465.75	467.09
	H	26.64	27.44	27.14	27.35	-	-	-	-	26.62	27.42	27.11	26.43	27.40	27.55	27.59	27.48
CH_4	C	194.14	193.55	191.44	193.7	194.27	193.71	191.58	193.86	194.09	193.51	191.39	200.36	196.07	190.47	191.46	191.99
	H	31.24	31.68	31.53	31.5	31.24	31.68	31.53	31.5	31.24	31.68	31.53	31.6	31.63	31.72	31.69	31.58
CO	C	-19.71	5.56	-12.62	-16.73	-24.01	1.75	-16.77	-21.16	-21.18	4.27	-14.03	4.62	-8.62	-7.14	-9.26	-12.89
	O	-86.11	-54.86	-77.23	-81.64	-93.06	-61.26	-84.02	-88.96	-88.64	-57.18	-79.7	-75.43	-73.62	-68.68	-71.01	-73.85
FCN	F	344.95	337.71	340.31	350.08	344.44	337.02	339.71	349.46	344.59	337.31	339.93	351.87	351.30	340.64	344.70	348.29
	C	65.65	83.48	70.97	72.5	63.59	81.58	68.96	70.52	64.97	82.86	70.31	71.01	76.65	75.03	75.12	73.89
	N	92.87	122.58	102.51	97.87	90.9	120.94	100.67	95.7	91.99	121.83	101.68	117.48	111.19	107.91	105.52	101.74
HCN	H	28.97	29.06	29.21	29.21	-	-	-	-	28.98	29.07	29.21	29.09	29.17	29.31	29.30	29.29
	C	66.24	86.26	72.57	71.73	-	-	-	-	65.47	85.59	71.83	78.1	76.95	76.84	76.07	73.65
	N	-54.26	-16.47	-42.04	-44.83	-	-	-	-	-56.07	-18.09	-43.79	-42.2	-34.56	-31.24	-33.40	-38.72
HCP	H	29.4	29.44	29.61	29.72	-	-	-	-	29.41	29.45	29.62	29.21	29.62	29.79	29.81	29.77
	C	7.75	32.76	15.83	14.57	-	-	-	-	6.76	31.88	14.88	18.4	23.09	21.22	20.19	18.54
	P	287.67	393.07	327.81	325.7	-	-	-	-	284.91	390.66	325.18	310.34	347.98	359.10	355.32	337.46
HF	H	29.43	30.21	30.06	29.55	29.45	30.23	30.08	29.56	29.44	30.22	30.07	30.96	29.58	30.05	29.85	29.67
	F	416.64	411.75	412.63	414.11	416.31	411.34	412.26	413.71	416.48	411.56	412.45	413.25	415.72	413.06	413.67	413.40
LiH	H	25.74	26.73	26.29	26.4	25.39	26.5	25.97	26.05	25.69	26.69	26.24	24.16	26.57	26.58	26.60	26.67
	Li	86.57	92.3	88.35	88.48	81.98	89.75	84.46	84.12	86.01	91.88	87.83	86.48	88.53	88.74	88.76	88.94
LiF	Li	85.61	90.05	86.85	88.22	82.61	85.97	83.35	85.62	85.25	89.61	86.45	82.21	87.80	87.43	87.90	88.39
	F	342.63	359.46	345.21	363.57	285.89	298.37	283.26	309.95	336.04	353.04	338.31	275.02	353.17	356.67	362.61	367.39
NH_3	N	267.71	263.35	263.34	264.27	268.64	264.42	264.34	265.04	267.82	263.47	263.45	275.35	266.81	261.23	261.82	262.13
	H	31.57	32.08	31.93	31.83	31.56	32.08	31.93	31.83	31.57	32.08	31.93	32.14	31.93	32.09	32.04	31.92
N_2	N	-89.15	-60.52	-81.35	-89.64	-94.66	-65.56	-86.72	-95.42	-91.18	-62.38	-83.33	-62.67	-78.53	-75.72	-79.42	-84.77
N_2O	N	89.4	102.63	93.45	85.98	87.72	101.02	91.79	84.06	88.58	101.86	92.64	115.21	96.51	94.60	91.54	87.78
	N	0.05	15.03	4.48	-4.03	-3.5	11.69	0.98	-7.58	-1.13	13.91	3.32	9.84	3.83	6.36	2.61	-0.99
	O	180.97	176.95	178.14	176.71	180.58	176.4	177.68	176.15	180.38	176.33	177.54	208.34	183.46	175.82	175.51	175.52
PN	N	-419.91	-365.17	-406.76	-433.54	-432.48	-376.44	-419.01	-447.25	-424.25	-369.06	-410.98	-400.99	-411.57	-400.80	-411.66	-418.41
	P	-83.93	43.4	-42.02	-67.72	-99.35	29.93	-56.84	-84.08	-89.26	38.77	-47.13	-27.68	-32.90	-15.78	-27.72	-49.85
H_4C_2O	O	338.72	337.2	334.11	345.72	-	-	-	-	338.75	337.19	334.1	354.46	351.50	337.92	342.11	342.88
(oxirane)	C	137.79	145.45	139.26	145.14	-	-	-	-	137.52	145.19	138.99	146.96	147.88	142.04	144.03	144.14
	H	28.65	29.41	29.13	29.28	-	-	-	-	28.63	29.39	29.11	28.86	29.41	29.46	29.48	29.39
HFCO	O	-137.5	-89.7	-121.9	-128.02	-145.71	-97.35	-129.97	-136.88	-140.33	-92.28	-124.65	-118.71	-110.60	-107.13	-110.62	-117.11
	C	18.15	37.11	23.8	26.45	16.1	35.23	21.81	24.38	17.4	36.42	23.07	32.04	32.27	28.34	28.90	28.16
	F	85.39	116.44	95.92	123.86	78.79	109.98	89.3	117.03	83.32	114.47	93.87	67.06	127.16	114.17	123.79	127.53
	H	22.94	23.59	23.33	23.61	22.85	23.5	23.23	23.52	22.91	23.57	23.3	22.64	23.63	23.73	23.79	23.72
CH_2O	O	-488.94	-368.25	-443.38	-449.16	-	-	-	-	-496.55	-374.49	-450.48	-504.88	-432.93	-398.70	-404.74	-422.97
	C	-38.52	-2.93	-24.73	-20.24	-	-	-	-	-39.73	-3.89	-25.82	-21.2	-13.29	-13.66	-13.00	-16.15
	H	20.17	21.54	20.84	21.27	-	-	-	-	20.1	21.48	20.77	19.28	21.24	21.63	21.72	21.48
OCS	O	72.22	84.27	73.76	74.71	-	-	-	-	70.9	82.98	72.44	77.31	81.33	75.49	75.93	77.86
	C	20.92	37.42	25.46	21.17	-	-	-	-	20.09	36.63	24.64	32.57	27.09	28.14	26.00	23.30
	S	754.2	780.01	762.4	768.67	-	-	-	-	753.55	779.38	761.76	806.96	785.63	769.28	771.46	770.36
HOF	O	-137.17	-94.8	-122.55	-119.89	-146.61	-102.92	-131.55	-129.04	-140.59	-97.69	-125.78	-73.47	-111.99	-105.00	-105.66	-118.47
	H	18.58	20.21	19.47	19.52	18.32	19.98	19.22	19.28	18.5	20.14	19.4	20.06	19.52	20.03	19.99	19.67
	F	163.94	158.72	154.64	188.95	164.27	158.03	154.42	188.95	163.83	158.28	154.34	189.45	195.70	164.50	176.92	181.36
H_2O	O	334.9	327.39	329.49	330.22	335.07	327.51	329.65	330.23	334.83	327.3	329.42	339.26	332.40	328.44	328.89	328.64
	H	30.98	31.64	31.47	31.22	30.98	31.64	31.48	31.22	30.98	31.64	31.47	31.92	31.30	31.57	31.46	31.32
H_2S	S	726.85	725.04	716.39	721.77	726.29	724.46	715.8	720.97	726.43	724.6	715.95	767.12	735.06	712.12	714.75	715.49
	H	30.43	31.03	30.87	30.7	30.43	31.03	30.87	30.7	30.43	31.03	30.87	30.8	30.79	31.06	30.98	30.82
SO_2	S	-298.27	-182.15	-257.46	-301.64	-	-	-	-	-302.77	-186.25	-261.82	-214.08	-249.89	-234.53	-253.36	-284.92
	O	-317.64	-283.26	-307.04	-321.91	-	-	-	-	-321.4	-286.81	-310.75	-279.78	-304.36	-299.38	-305.60	-314.44

Table 3.4: Molecular magnetizabilities (10^{-30} J T^{-2}) calculated using DFT and CDFT functionals in the aug-cc-pCVTZ basis set.

					VRG(LHC)				VRG(TP)							
Molecule	LDA	KT3	PBE	PBE0	LDA	KT3	PBE	PBE0	LDA	KT3	PBE	PBE0	cB98	cTPSS	cTPSS(h)	B97-2
AlF	-396.3	-394.3	-397.2	-394.7	-394.6	-392.7	-395.6	-393	-395.8	-393.9	-396.8	-443	-408.1	-395.2	-394.6	-395.9
C_3H_4	-465	-453.9	-460.1	-465.6	-453	-441.1	-447.8	-453.4	-462.3	-451.1	-457.4	-478.8	-467.6	-461.7	-463.8	-463.6
FCCH	-438.9	-437.5	-438	-440.3	-433.9	-432.3	-432.9	-435.1	-437.8	-436.4	-436.9	-466	-446.3	-438.3	-439.2	-440.6
C_2H_4	-331.6	-333.1	-331.4	-335.8	-326.5	-328.2	-326.4	-331	-330.4	-331.9	-330.1	-351.9	-341.2	-334.3	-335.8	-335.9
H_2C_2O	-427.7	-417.2	-422	-423.7	-420.9	-410.3	-415	-416.7	-426.2	-415.6	-420.4	-457.2	-429.0	-419.4	-420.5	-422.0
CH_3F	-315.5	-305.5	-311.4	-314.5	-	-	-	-	-314	-303.9	-309.8	-319.8	-314.6	-310.7	-312.0	-312.6
CH_4	-329.1	-311.5	-320	-318.2	-328.8	-311.1	-319.6	-317.7	-329.1	-311.4	-319.9	-355.2	-322.5	-312.8	-312.8	-315.8
CO	-206.8	-206.2	-205.7	-203.1	-205.2	-204.6	-204.1	-201.4	-206.3	-205.7	-205.2	-237.9	-209.0	-204.2	-203.4	-204.1
FCN	-365.8	-365.5	-365.4	-367.1	-362.1	-361.9	-361.8	-363.3	-364.9	-364.7	-364.6	-392.9	-372.9	-365.6	-366.3	-367.2
HCN	-265.3	-267.2	-264.7	-266.2	-	-	-	-	-264.9	-266.8	-264.2	-293.7	-272.0	-264.8	-265.5	-267.4
HCP	-477.9	-484.2	-479.6	-483.1	-	-	-	-	-477.4	-483.7	-479.1	-522.9	-492.4	-482.0	-483.3	-485.8
HF	-181.3	-176.6	-180.3	-177.2	-181.3	-176.6	-180.3	-177.2	-181.3	-176.6	-180.3	-199.1	-179.4	-178.6	-177.6	-177.5
LiH	-135.4	-137.3	-134.5	-128.7	-117.9	-127.1	-119.7	-110.2	-133.1	-135.7	-132.5	-166.6	-133.6	-128.4	-126.9	-129.6
LiF	-196.5	-193.8	-196.3	-194.4	-183.5	-177.8	-181.6	-182.9	-194.8	-191.7	-194.3	-209.7	-195.7	-195.5	-194.8	-194.8
NH_3	-298	-286.7	-292.9	-290.2	-297.7	-286.3	-292.5	-290	-297.9	-286.6	-292.8	-323.1	-294.6	-288.9	-288.3	-289.7
N_2	-201.1	-201.1	-199.8	-198.2	-199.6	-199.7	-198.3	-196.6	-200.6	-200.6	-199.2	-230.4	-203.6	-198.2	-197.8	-199.7
N_2O	-334.8	-328.6	-332.4	-334.6	-325.8	-319.9	-323.3	-325.3	-333	-326.8	-330.5	-349.2	-337.1	-332.0	-332.9	-334.1
PN	-286.4	-292.4	-285.9	-286.4	-282.8	-289	-282.3	-282.5	-285.3	-291.3	-284.7	-324.3	-294.1	-285.3	-285.9	-288.9
H_4C_2O	-529.2	-516	-523.3	-530.9	-292.7	-293.2	-292.6	-294.4	-527	-513.8	-521	-550.5	-533.7	-524.0	-526.9	-526.5
HFCO	-297.4	-297.9	-297.3	-299.2	-224.3	-220.3	-222.6	-228.4	-296.2	-296.7	-296.1	-322.9	-305.4	-298.5	-299.2	-299.4
CH_2O	-99	-120	-107.6	-115.2	-	-	-	-	-95.8	-117.1	-104.6	-85.8	-115.4	-119.3	-121.2	-116.7
OCS	-577.2	-572.2	-575.4	-580.1	-	-	-	-	-575.8	-570.9	-574	-610.9	-585.1	-575.4	-577.4	-579.1
HOF	-229.1	-225.2	-227.6	-232.9	-	-	-	-	-228	-224.1	-226.5	-243.4	-234.0	-229.6	-231.5	-231.1
H_2O	-241	-233.8	-238.5	-235.2	-240.9	-233.6	-238.4	-235.2	-241	-233.7	-238.5	-263.3	-238.7	-236.0	-235.0	-235.3
H_2S	-466.1	-450.6	-458.6	-456.3	-465.7	-450.1	-458.2	-455.9	-466	-450.5	-458.5	-505.7	-462.7	-452.0	-451.8	-454.2
SO_2	-296.8	-294.1	-295.2	-293	-	-	-	-	-295.5	-292.7	-293.9	-341.9	-301.9	-292.5	-292.2	-294.5

Table 3.5: Hyper-magnetizability data (JT^{-4}) for H_2O calculated using LDA/STO-3G for field strengths of 0.0 to 0.03 in steps of 0.0001 a.u. Uniformly spaced subsets of this data were selected to establish convergence with number of points.

	6th Order Polynomial			4th Order Polynomial		
Data Set	xxxx	yyyy	zzzz	xxxx	yyyy	zzzz
300	11.66	5.192	3.079	11.72	5.202	3.083
150	11.66	5.182	3.082	11.72	5.201	3.083
100	11.64	5.176	3.091	11.72	5.202	3.083
75	11.64	5.191	3.076	11.72	5.200	3.083
30	11.66	5.203	3.101	11.72	5.203	3.084

Table 3.6: Hyper-magnetizability data (JT^{-4}) for H_2O calculated using LDA/STO-3G for field strengths of 0.0 to 0.1 in steps of 0.001 a.u. Uniformly spaced points from this data have been selected to establish convergence with in the sparsity of points.

	6th Order Polynomial			4th Order Polynomial		
Data Set	xxxx	yyyy	zzzz	xxxx	yyyy	zzzz
100	11.66	5.194	3.061	11.24	5.276	3.314
50	11.66	5.194	3.061	12.35	5.275	3.316
33	11.66	5.195	3.061	12.36	5.274	3.306
25	11.66	5.194	3.061	12.38	5.277	3.300
10	11.66	5.195	3.061	11.23	5.269	3.299
5	11.66	5.195	3.060	12.41	5.255	3.254
4	11.66	5.195	3.060	12.41	5.247	3.228

even spread of points across the full range. Convergence was found to be poor, with any variation in the number of fitting points producing unacceptable variations in the tensor elements, results are presented in Table 3.5.

The range of field strengths was expanded to ± 0.1 a.u. in steps of 0.001 and the analysis repeated, results are presented in Table 3.6. The wider spread of field strengths yielded far greater stability, showing only mild variation, even when reduced to only 4 points per cardinal direction. A compromise of twenty points uniformly spread between 0 and ± 0.1 a.u. was chosen to give accurate 6th order fitting in calculations whilst minimising computational effort.

Molecular hyper-magnetizability values were calculated using DFT functionals with and without the VRG(TP) vorticity correction functional, summarised in Table 3.7 and Table 3.8. In nearly all cases, the VRG correction to the hyper-magnetizability tensor elements was negative, in the absence of accurate reference data however it is difficult to judge the quality for the CDFT hyper-magnetizability values. Bearing in mind the poor performance of the VRG correction for molecular magnetizabilities, it is a reasonable assumption that the hyper-magnetizability corrections are poor as well.

3.5 CDFT beyond the perturbative regime

The availability of accurate and stable mGGA current-density functionals facilitates the study of molecules in very strong magnetic fields such as those encountered around white dwarf stars and magnetars [122]. Such strong fields may have a dramatic impact on the physics and chemistry of small molecules. Several studies have applied quantum-chemical methods such as the Hartree–Fock and FCI methods to small atoms as well as one- and two-electron molecular systems [53,55,123–127]. Such systems have also been studied with methods constructed for very high-accuracy [128]. Larger systems have been explored using density functionals based on asymptotic estimates for energies. [129, 130]

As noted in the conclusions of Section 2.1.5, the increasing deficiency of isotropic GTOs in representing the significant deformation of the electronic orbitals that occurs in strong fields limits this

Table 3.7: Hypermagnetizability tensor elements (JT^{-4}) calculated using standard DFT functionals in the aug-cc-pCVTZ basis set. The corresponding Hartree–Fock results are included for comparison. Results are presented here for a subset of 19 of the 26 molecules described in Table 3.1.

	HF			KT3			PBE		
	xxxx	yyyy	zzzz	xxxx	yyyy	zzzz	xxxx	yyyy	zzzz
AlF	94.9	94.9	91.0	90.9	90.9	95.5	84.7	84.7	95.7
C_3H_4	-3.8	-250.0	222.0	45.0	-300.0	233.0	25.3	-297.0	223.0
FCCH	-9.6	-9.6	40.3	-19.0	-19.0	45.8	-21.6	-21.6	45.8
C_2H_4	-60.1	-41.1	-4.6	-50.4	-70.9	-45.0	-69.9	-91.7	-43.5
H_2C_2O	-1.3	-94.4	228.0	-6.8	-115.0	252.0	-10.6	-113.0	259.0
CH_4	91.0	91.1	100.0	104.0	104.0	115.0	105.0	105.0	116.0
CO	-6.4	-6.4	17.5	15.8	15.8	21.2	9.9	9.9	21.8
FCN	-10.1	-10.1	23.4	-12.6	-12.6	26.6	-16.0	-16.0	26.7
HF	7.9	7.9	5.7	11.8	11.8	8.8	11.9	11.9	9.2
LiH	75.1	75.1	67.9	160.0	160.0	94.9	157.0	157.0	97.4
LiF	4.9	4.9	12.7	41.7	41.7	26.7	35.3	35.3	26.8
NH_3	38.9	38.9	50.7	49.2	49.2	60.3	49.3	49.3	61.0
N_2	-16.7	-16.7	15.8	6.4	6.4	17.8	-1.7	-1.7	18.2
N_2O	-69.6	-69.6	19.1	-81.6	-81.6	21.8	-85.3	-85.3	22.2
PN	-230.0	-230.0	56.2	-294.0	-294.0	57.0	-381.0	-381.0	57.4
HFCO	16.4	-20.5	-65.2	22.4	-18.9	-49.3	27.1	-26.2	-66.1
HOF	29.9	26.6	15.9	6.1	-12.7	24.4	5.1	-18.7	24.9
H_2O	22.3	14.8	13.5	30.6	21.5	21.7	30.7	21.8	21.8
H_2S	197.0	81.7	117.0	206.0	90.0	124.0	209.0	90.4	125.0

work to field strengths up to $||\mathbf{B}|| \approx 1$ a.u., for which the orbital deformation may be handled by uncontracting the basis set and adding polarisation functions.

3.5.1 Perpendicular paramagnetic bonding

An interesting phenomenon that can be addressed with the new computational CDFT aparatus is the chemical bonding and molecular orientation of molecules in strong magentic fields. In strong fields $||\mathbf{B}|| \approx 1$ a.u., molecules that are otherwise unstable such as H_2 in the $b^3\Sigma_u^+$ state can become stable, with a favoured orientation in the field [27, 55, 111]. In Ref. [27], this phenomenon was explained in terms of a new chemical bonding mechanism, perpendicular paramagnetic bonding, that arises from a stabilisation of anti-bonding orbitals that lie in a perpendicular orientation relative to the magnetic field. Hartree–Fock and FCI calculations have shown that this bonding is present in triplet H_2 and singlet He_2. Moreover, calculations at the Hartree–Fock level (which gives a qualitatively but not quantitatively correct description for paramagnetic bonding) on singlet helium clusters up to size He_6 indicate this bonding mechanism is not restricted to diatomic molecules, with these clusters forming hexagonal sheets lying normal to the field direction.

As the bonding interaction in paramagnetically bound systems is a field induced effect, such systems offer a powerful model for testing the performance of CDFT functionals in the strong field regime.

3.5.2 Standard DFT and vorticity dependent functionals

Figure 3.6 and Figure 3.7 give the dissociation curves for the helium dimer subject to parallel and perpendicular fields of strength $||\mathbf{B}|| = 1$ a.u. The Hartree–Fock and FCI surfaces are presented together with results obtained with standard DFT functionals. The u-aug-cc-pVTZ basis set, where u denotes an uncontracted basis set, augmented with London gauge factors, was used. The dimer has a weak minimum for both parallel and perpendicular magnetic fields with the Hartree–Fock model under-binding and all tested DFT functionals over-binding. By symmetry, the vorticity vanishes for

Table 3.8: Hyper-magnetizability data (SI a.u.) calculated using VRG(TP) current corrected functionals in the aug-cc-pCVTZ basis set. Hartree–Fock results are included for comparison.

	HF			KT3			PBE		
	xxxx	yyyy	zzzz	xxxx	yyyy	zzzz	xxxx	yyyy	zzzz
AlF	94.9	94.9	91.0	90.7	90.7	95.5	84.5	84.5	95.7
C_3H_4	-3.8	-250.0	222.0	43.9	-353.0	226.0	23.8	-345.0	217.0
FCCH	-9.6	-9.6	40.3	-26.7	-26.7	45.8	-29.1	-29.1	45.8
C_2H_4	-60.1	-41.1	-4.6	-51.9	-72.1	-59.3	-71.5	-93.0	-58.4
H_2C_2O	-1.3	-94.4	228.0	-1.2	-135.0	253.0	-16.1	-133.0	260.0
CH_3F	-6.7	-6.7	102.0	-40.2	-40.2	131.0	-42.4	-42.5	134.0
CH_4	91.0	91.1	100.0	104.0	105.0	115.0	105.0	106.0	116.0
CO	-6.4	-6.4	17.5	15.0	15.0	21.2	8.9	8.9	21.8
FCN	-10.1	-10.1	23.4	-15.6	-15.6	26.6	-19.1	-19.1	26.7
HCN	-9.0	-9.0	25.9	-6.3	-6.3	28.3	-15.1	-15.1	28.3
HCP	-8.4	-8.4	82.6	-18.1	-18.1	81.0	-44.9	-44.9	81.5
HF	7.9	7.9	5.7	11.8	11.8	8.8	11.9	11.9	9.2
LiH	75.1	75.1	67.9	160.0	160.0	94.9	151.0	151.0	97.4
LiF	4.9	4.9	12.7	22.6	22.6	26.7	17.7	17.7	26.8
NH_3	38.9	38.9	50.7	49.2	49.2	60.5	49.3	49.4	61.3
N_2	-16.7	-16.7	15.8	5.6	5.6	17.8	-2.7	-2.7	18.2
N_2O	-69.6	-69.6	19.1	-99.6	-99.6	21.8	-104.0	-104.0	22.2
PN	-230.0	-230.0	56.2	-302.0	-302.0	57.0	-390.0	-390.0	57.4
H_4C_2O	250.0	53.5	102.0	270.0	-3.7	110.0	267.0	-7.7	115.0
HFCO	16.4	-20.5	-65.2	19.4	-20.3	-50.8	24.2	-27.6	-67.9
CH_2O	-73.7	-68.6	-619.0	-185.0	-67.2	-733.0	-193.0	-81.4	-967.0
OCS	-53.7	-53.7	55.5	-75.8	-75.8	58.4	-81.4	-81.4	59.6
OF_2	24.9	30.3	33.6	-32.2	28.0	25.3	-42.6	25.9	20.0
HOF	29.9	26.6	15.9	0.8	-19.1	24.4	-0.3	-25.6	25.0
H_2O	22.3	14.8	13.5	30.7	21.5	21.6	30.8	21.8	21.7
H_2S	197.0	81.7	117.0	207.0	90.1	124.0	210.0	90.4	125.0
SO_2	45.7	-442.0	-84.4	72.5	-280.1	-84.2	79.1	-330.0	-94.0

fields parallel to the internuclear axis and a vorticity-dependent VRG-type functional consequently vanishes too for these cases.

For perpendicular fields however, the vorticity does not vanish—see the dissociation curves for conventional and vorticity-dependent functionals in Figure 3.7 (The vorticity-dependent functionals were regularised by a soft cut-off $\epsilon = 2.3873\times10^{-4}$ a.u., which corresponds to $r_s = 10$ a.u., (Eq. (2.133)) in these calculations). While the Hartree–Fock model and conventional DFT functionals show similar under- and over-binding, respectively, the addition of the VRG(LHC) and VRG(TP) functionals only degrade the accuracy. Both the depth and location of the minima become less accurate, with spurious plateaus appearing in the dissociation curves.

This behaviour may be understood from the observation that the vorticity vanishes for perpendicular fields in the dissociation and united-atom limits. Hence, the effect of the vorticity may be expected to be largest at intermediate bond lengths perpendicular to the field. Qualitatively, this behaviour is similar to the energetic preference introduced by the perpendicular paramagnetic bonding mechanism [27]. The VRG functionals tested thus showed a spurious bias towards this bonding.

The self-consistent-field (SCF) Kohn–Sham optimisation appears to be more difficult when VRG functionals are used in strong fields, a problem observed to a lesser degree during the calculation of response properties [10]. The LONDON implementation, which relies on a standard DIIS method, often found states above the ground state when VRG functionals were used. This problem was corrected by starting the SCF optimisation from different density matrices — for example, obtained by projection from a calculation with a different functional or different geometry.

Neither the conventional functionals tested (LDA, BLYP, B3LYP, and KT3) nor the VRG functionals (LHC and TP) were constructed explicitly for use with very strong magnetic fields. Whilst Hartree–

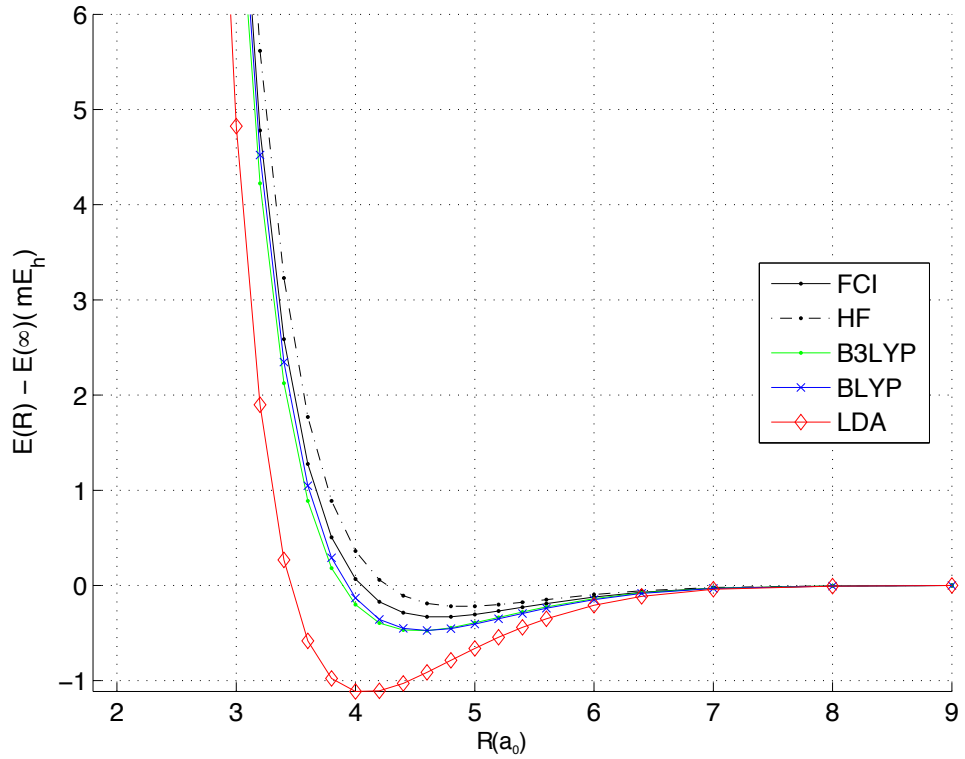


Figure 3.6: Dissociation curves for He_2 subject to a field parallel to the internuclear axis $B_{\parallel} = 1$ a.u. The u-aug-cc-pVTZ basis set was used. Note that the curves have been aligned at $R = 9\ a_0$.

Fock theory tended to lead to an under-binding, the standard LDA, BLYP and B3LYP tended to over-bind. For LDA this error was dramatic and similar to the over-binding observed in the absence of magnetic fields. The GGA functionals improved the situation but did not fully correct the error. By contrast, the VRG(LHC) and VRG(TP) corrected functionals were much less robust, and lead to an exaggeration of the over-binding effect and the introduction of spurious features on the potential energy curve. The Tao–Vignale parametrised VRG functional is expected to share this problem, since its model function $g_{\mathrm{TV}}(\rho)$ is similar to $g_{\mathrm{LHC}}(\rho)$ and $g_{\mathrm{TP}}(\rho)$.

The abject failure of the vorticity functional forms in correctly modelling strong field paramagnetic bonding reinforces the conclusions of Section 3.3.1 that the vorticity correction is fundamentally unsuitable for accurate CDFT calculations. For this reason the strong field analysis of the VRG functionals was limited to the helium dimer and the VRG funcitonals are not considered further.

3.5.3 Current modified meta-GGA functionals

To investigate the performance of current modified meta-GGA functionals at the strong field limit the potential energy profiles were calculated for H_2, He_2, NeHe and Ne_2. In particular, we consider the $b^3\Sigma_u^+(1\sigma_g 1\sigma_u^*)$ state of H_2 and the lowest $^1\Sigma_g^+$ state of He_2, NeHe and Ne_2. Each of these systems is repulsive in the absence of a magnetic field, excepting weak dispersion binding, but become more strongly bound when a field is applied. It is noted that, as a result of the spin Zeeman stabilisation energy, only the $^3\Sigma_u^+(1\sigma_g 1\sigma_u^*)$ state of H_2 is an overall ground state in the presence of the field, an effect discussed further in Section 5.2.1. Interaction curves for these systems were compared against accurate CCSD(T) interaction curves calculated using a recent non-perturbative magnetic field including implementation by Stopkowicz et al [115] available in the LONDON program. For comparison, similar profiles generated with standard LDA and GGA density functionals as well as with HF theory are also presented. The potential energy curves for H_2, He_2, NeHe and Ne_2 are shown in Figures 3.8, 3.9, 3.10 and 3.11, respectively. Equilibrium bond lengths and dissociation

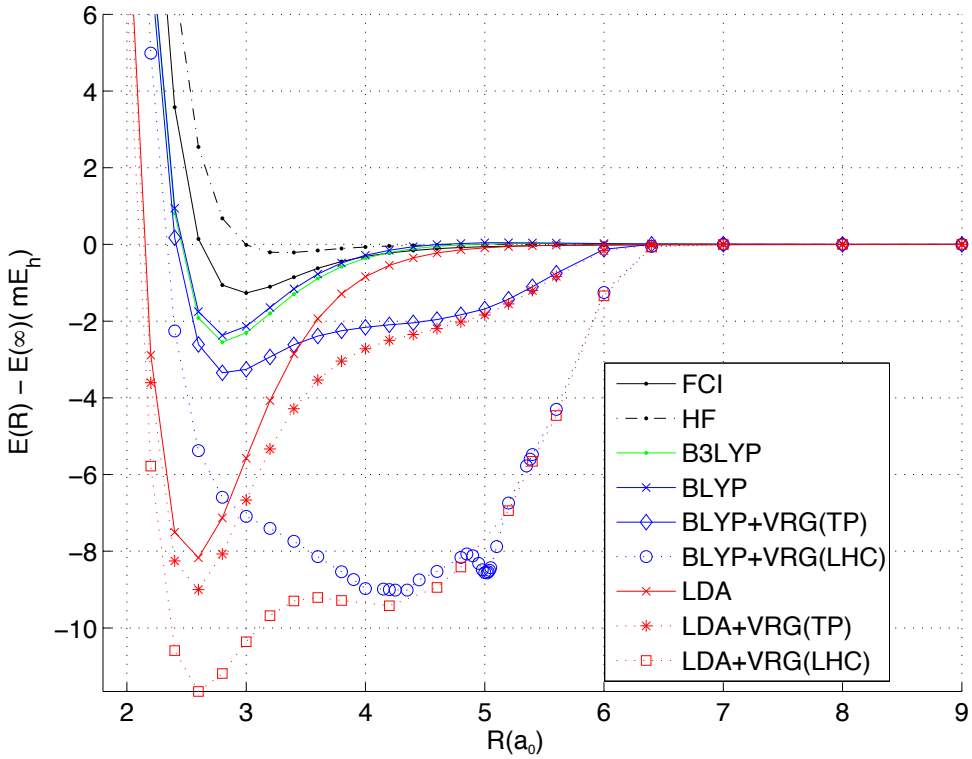


Figure 3.7: Dissociation curves for He_2 subject to a perpendicular field $B_\perp = 1$ a.u. The u-aug-cc-pVTZ basis set was used. Note that the curves have been aligned at $R = 9\ a_0$.

energies were determined numerically and are presented in Table 3.9.

The $^3\Sigma_u^+(1\sigma_g 1\sigma_u^*)$ state of the H_2 molecule in a perpendicular field was examined at the FCI level by Lange *et al.* [27] and the potential energy curves for this state are shown in Figure 3.8. HF strongly under-binds this state in comparison with the FCI data. In contrast LDA strongly over-binds, a tendency which is largely corrected by the PBE functional and significantly improved by the cTPSS and cTPSS(h) models. These trends are reflected in the equilibrium bond lengths and dissociation energies in Table 3.9. Although not highly accurate the cTPSS and cTPSS(h) models give a reasonable qualitative description of the potential energy curve. The empirically parametrised KT3 functional is interesting because it gives simultaneously a reasonable estimate of both the equilibrium bond length and dissociation energy. However, at intermediate separation an unphysical barrier is observed. For cB98 an even more pronounced barrier is present and the potential energy curve is generally even less accurate than Hartree–Fock theory. This may suggest that heavily parametrised functional forms, determined to perform well at zero field, may not be the best candidates for use in strong-field CDFT studies.

Examining the potential energy curves for He_2 in Figure 3.9 it is clear that that HF tends to under-bind, with a bond length of 3.30 a_0 compared with the CCSD(T) value of 2.98 a_0. Similarly the HF dissociation energy of 0.218 mE_h is much smaller than the corresponding CCSD(T) value of 1.259 mE_h. For this small system the CCSD(T) and FCI interaction curves can be compared, and as expected the agreement is excellent — the corresponding potential energy curves being essentially indistinguishable on the scale of Figure 3.9. For LDA a strong tendency to over-bind is seen giving much too short R_e values and much too large estimates of D_e. The GGA functionals PBE and KT3 show considerable improvement over LDA, however they still exhibit strong over-binding. The improvement for the mGGA functionals is striking, in particular cTPSS and cTPSS(h) give a good quantitative description of the potential energy curve. The corresponding R_e and D_e values indicate that there still remains a tendency towards over binding but this is greatly reduced.

The cB98 functional tends to show more significant under binding. It is noted that the arguments

Table 3.9: Dissociation energies and equilibrium bond lengths for H_2 and rare gas dimers in a 1 a.u. magnetic field perpendicular to the internuclear axis. Calculated using the u-aug-cc-pVTZ basis set.

	R_e (a_0)				D_e (mE$_h$)			
	H_2	He_2	NeHe	Ne_2	H_2	He_2	NeHe	Ne_2
HF	2.709	3.296	3.543	3.773	2.333	0.218	0.482	0.978
LDA	2.377	2.550	2.846	3.062	14.807	8.231	11.817	19.730
PBE	2.515	2.810	3.080	3.294	5.976	2.463	3.938	7.128
KT3	2.512	2.852	3.121	3.342	4.628	2.661	3.937	6.527
cB98	2.636	3.203	3.472	3.676	1.324	1.011	1.514	2.050
cTPSS	2.567	2.864	3.124	3.346	5.250	1.307	2.344	4.577
cTPSSh	2.562	2.879	3.154	3.379	5.258	1.245	2.130	3.990
CCSD(T)	2.584	2.977	3.248	3.487	4.551	1.259	2.217	4.016
FCI	2.584	2.975	-	-	4.551	1.271	-	-

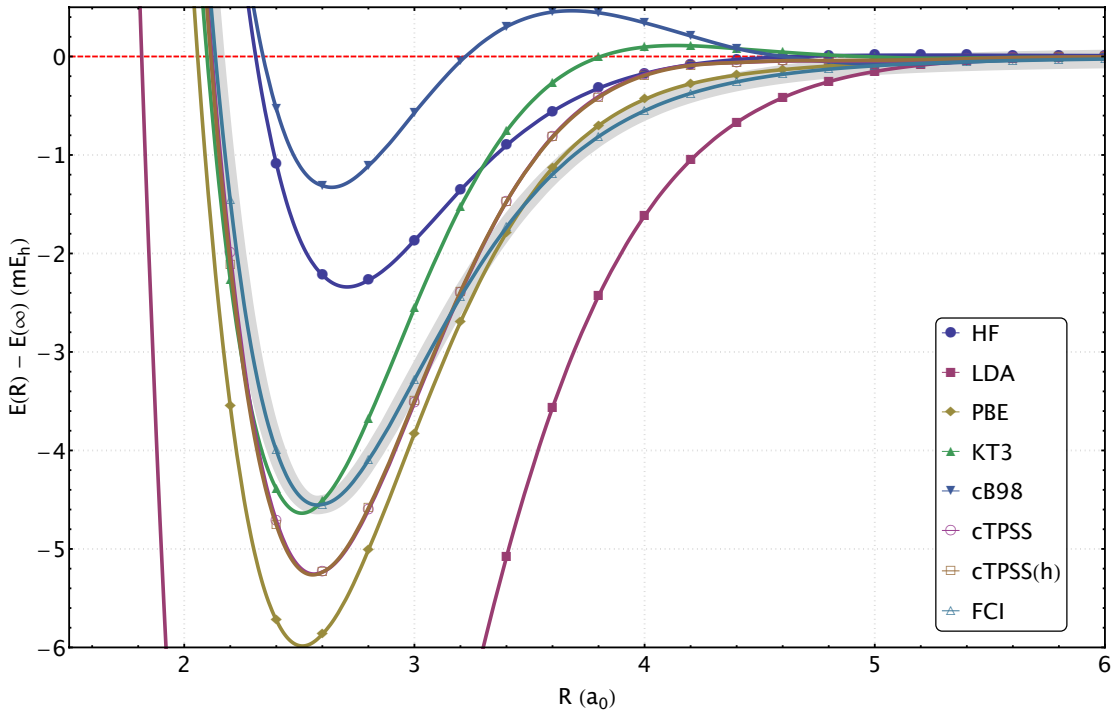


Figure 3.8: Potential energy curves for the $b^3\Sigma_u^+(1\sigma_g 1\sigma_u^*)$ state of the H_2 molecule in a magnetic field of 1 a.u. perpendicular to the bonding axis calculated using the u-aug-cc-pVTZ basis set.

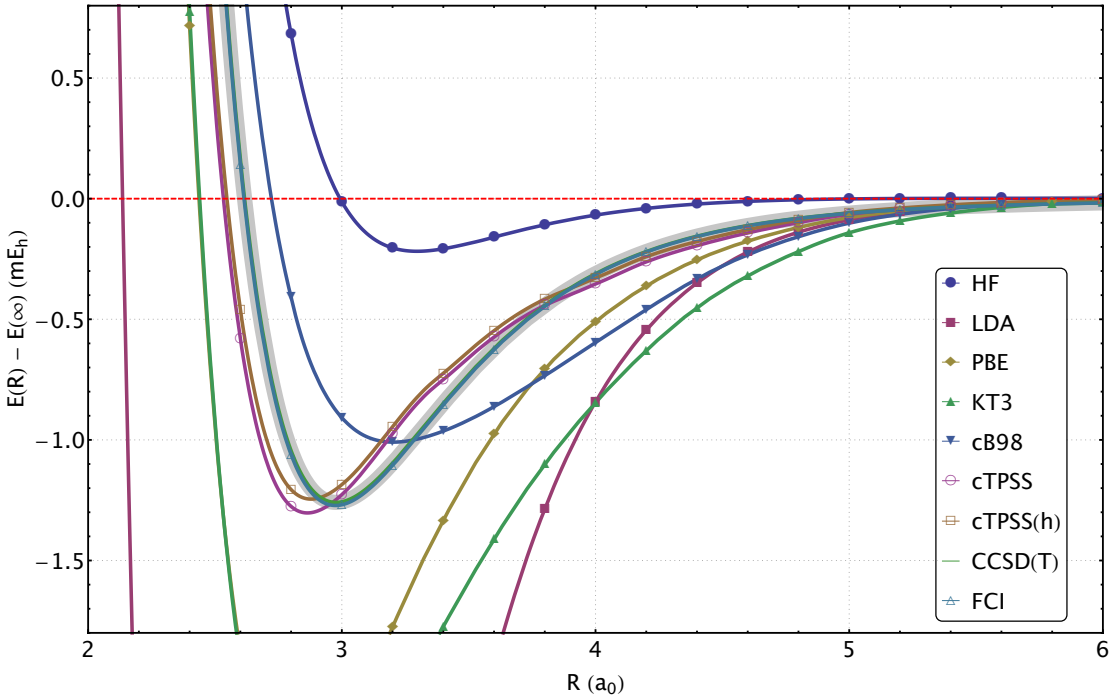


Figure 3.9: Potential energy curve for the lowest ${}^1\Sigma_g^+$ state of He_2 in a magnetic field of 1 a.u. perpendicular to the bonding axis calculated using the u-aug-cc-pVTZ basis set.

used in the construction of cB98 and cTPSS are rather different. In particular, cB98 is an empirically parametrised functional, whereas cTPSS is constructed based on the satisfaction of known exact conditions (see Sections 2.4.3 and 2.4.4). In this work the parameters determined in Ref. [90] were used to define the cB98 form. These parameters were determined at zero field and from post-LDA calculations — as a result they may not be optimal for fully self-consistent calculations in the presence of a magnetic field. On the other hand the cTPSS functional is designed to satisfy selected constraints at zero field and it could be argued that in the presence of a field both the cB98 and cTPSS functionals are open to further optimization, though this is beyond the scope of the present work. The recently derived mGGA SCAN functional of Sun, Ruszinszky and Perdew [131] presents an interesting functional for CDFT as it has been constructed to satisfy all known exact constraints for a mGGA XC functional. Similarly to cTPSS a current sensitive 'cSCAN' CDFT functional may be derived simply by supplying the Dobson–Becke $\tilde{\tau}$ in place of the standard kinetic energy density. Preliminary investigations of this functional showed a strong over-binding of the rare gas dimer systems in strong magnetic fields. This is consistent with the reported enhancement of weak binding interactions in the SCAN functional at zero field [131].

The stability of the mGGA functionals is particularly evident in the strong field regime when one compares the present results for He_2 with those for the VRG-based estimates in Figure 3.7. The VRG approaches led to very difficult SCF convergence and complex potential energy curves with a strong unphysical over binding. The mGGAs considered here are un-problematic in practical application and yield results surprisingly close to the CCSD(T) estimates.

Similar qualitative trends are observed for the NeHe and Ne_2 dimers in Figures 3.10 and 3.11. Again LDA and GGA functionals are not sufficiently accurate for practical use and the mGGA functionals provide a large improvement. The cTPSS and cTPSS(h) results remain impressive – with cTPSS(h) being consistently slightly more accurate than cTPSS. This trend is reflected in both the potential energy curves and the R_e and D_e values in Table 3.9.

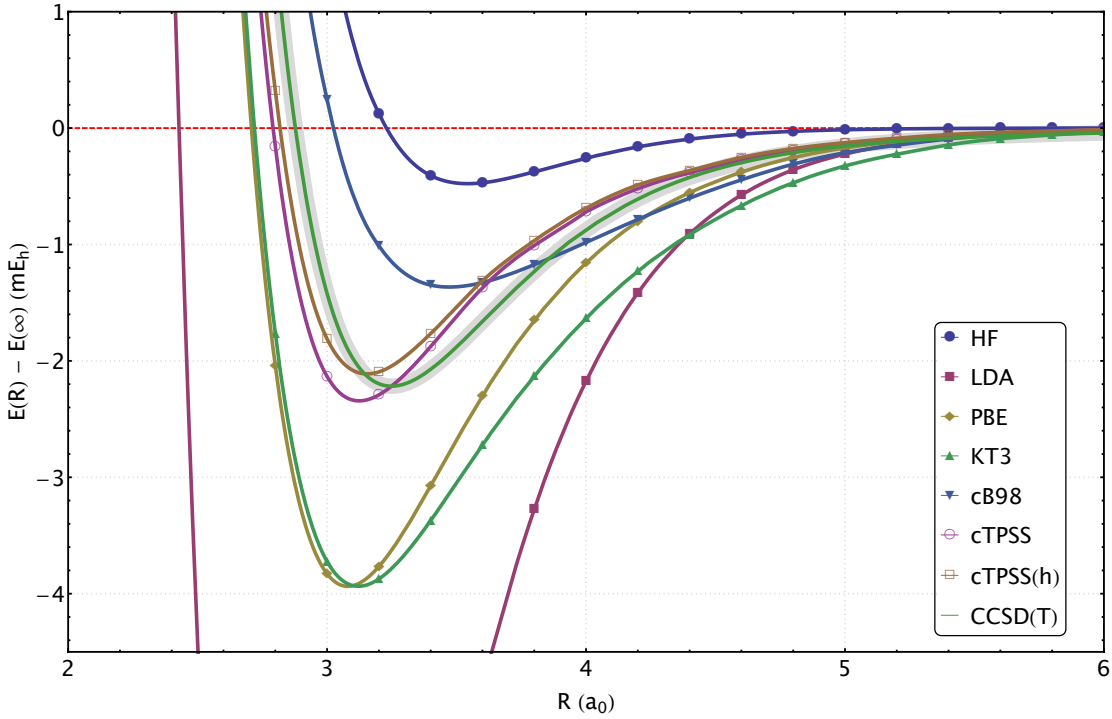


Figure 3.10: Potential energy curve for the lowest $^1\Sigma_g^+$ state of the NeHe dimer in a magnetic field of 1 a.u. perpendicular to the bonding axis calculated using the aug-cc-pCVTZ basis set.

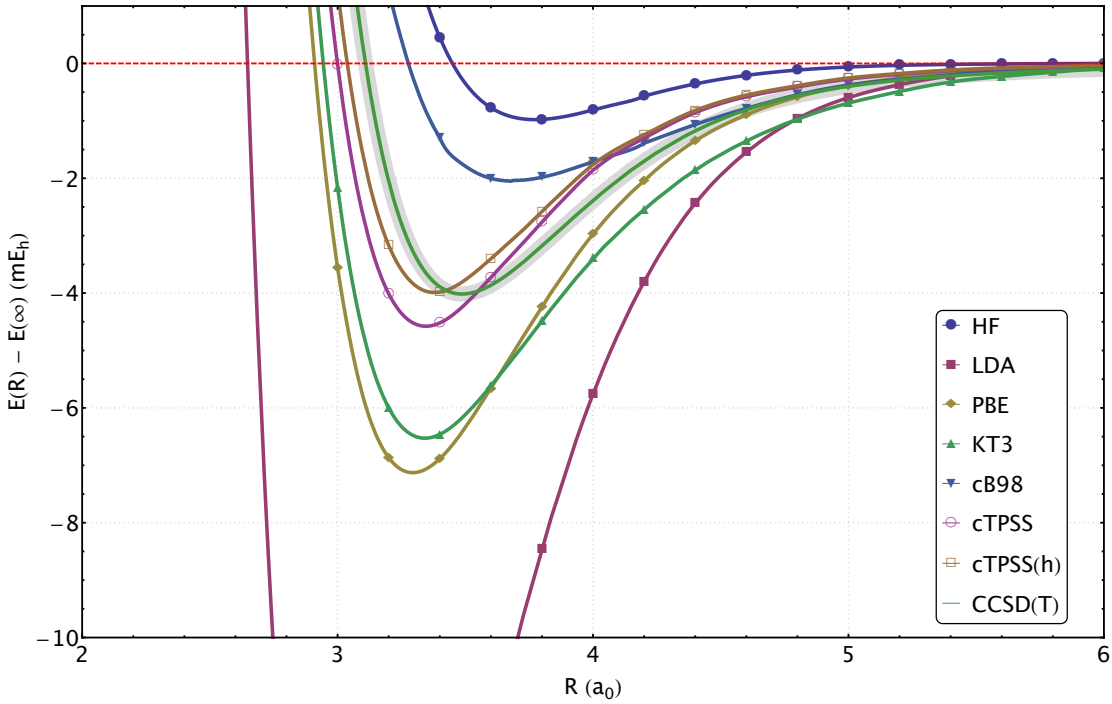


Figure 3.11: Potential energy curve for the lowest $^1\Sigma_g^+$ state of Ne_2 in a magnetic field of 1 a.u. perpendicular to the bonding axis calculated using the aug-cc-pCVTZ basis set.

3.6 Concluding remarks

For molecular magnetizabilities and nuclear shielding constants, the VRG vorticity correction functionals tend to degrade accuracy compared to conventional DFT functionals. The description of the non-perturbative phenomenon of perpendicular paramagnetic bonding also degrades when the VRG functional is added. Although these functionals were constructed to account for the effects of external magnetic fields, a common problem is that the parameter values have been selected to describe a uniform electron gas in the medium to high-density regime (i.e, $r_\mathrm{s} \leq 10$ or $r_\mathrm{s} \leq 20$). The low-density limit, which is important in molecular calculations, is thus left under-determined. The asymptotic decay of $\sim \rho^{-1/3}||\boldsymbol{\nu}||^2$ imposed in the presently available parametrisations appears to be too slow for molecular calculations, making regularisation necessary. Moreover, results obtained with the VRG functionals are too sensitive to the choice of regularisation parameter to be useful.

Interestingly, the modified version Higuchi and Higuchi's functional, [80, 132] re-parametrised so as to have a useful low-density behaviour, stands out from the other VRG functionals. It decays as $\sim \rho||\boldsymbol{\nu}||^2$, which is substantially faster, and because it has the opposite sign in the medium to high-density regime compared to the VRG(LHC) and VRG(TP) functionals, for example, it yields errors in the opposite direction. The latter point raises the tempting possibility of attempting to fit an interpolation between VRG(HHmod) and VRG(LHC) or VRG(TP) to benchmark data.

In this work the previously detailed modification to the kinetic energy density term [86, 87, 92] was implemented in mGGA functionals to perform non-perturbative CDFT calculations in a stable, gauge origin invariant manner using the LONDON program [51]. The modified mGGA functionals cB98, cTPSS and cTPSS(h) show a level of accuracy in predicting weak field magnetic properties that is competitive with existing GGA functionals, without any additional fitting. The functionals cTPSS and cTPSS(h) show excellent prediction of perpendicular paramagnetic bonding behaviour, suggesting that the modification of the kinetic energy density is a viable route for the incorporation of current effects in standard mGGA density-functionals. In contrast to the vorticity dependent forms previously studied [10,83] the functionals exhibited excellent numerical stability in the finite field setting without the need for delicate numerical regularisations.

Whilst the mGGA results show considerable promise in the high field regime, their performance in the weak field regime is perhaps disappointing — leading to only modest improvements of conventional GGA forms. To some extent this may be due to the fact that mGGAs contain many of the shortcomings associated with GGA forms. For example, the functionals still have potentials with incorrect asymptotic behaviour — particularly for the exchange contribution. Since the current effects at weak field are not dominant but rather add small corrections to the predominantly Coulombic exchange and correlation interactions, it may be necessary to further improve the underlying functional forms before the true effect of the current dependent terms can be assessed in the weak field regime.

Given the stability and strong field accuracy shown it is expected that incorporating current dependence through the Dobson–Becke modified kinetic energy density should play a central role in the future development of new CDFT functionals, and many avenues are open for development. Obvious possibilities include the generalisation of range-separated mGGA functionals [133, 134] to obtain a better balance of errors between exchange, correlation and current contributions, and the re-parameterisation of existing functionals either empirically or via the consideration of alternative exact conditions in their construction. In the latter category it is noted that the presence of a magnetic field causes compression of the electronic density in two dimensions perpendicular to the field and non-uniform coordinate scaling relations may be one example of conditions that may provide a powerful tool in further development. To this effect the SCAN functional of Ref. [131] presents an interesting case, obeying all exact conditions known for the mGGA functional. The LONDON program [51] provides a powerful platform for this work allowing CDFT approaches to be calibrated against accurate *ab initio* data for a range of field strengths where experimental data may be scarce.

Chapter 4

Properties From Current-Density-Functional Theory

The mGGA CDFT functionals developed in Chapter 2 offer a computationally inexpensive correlated description of molecules in magnetic fields, and in Chapter 3 their accuracy in the strong field regime was established. In many areas of chemistry the nature of chemical bonding, reactions, spectra, and properties are interpreted qualitatively in terms of molecular orbital interactions from the linear combination of atomic orbitals (LCAO) ansatz. The present chapter considers the extent to which information from KS-CDFT calculations can aid this picture in the simple interpretation of the changes in electronic structure that are induced by a magnetic field.

Section 4.1 examines the origins of paramagnetic bonding through an analysis of the Kohn–Sham molecular orbitals. The stabilisation of the anti-bonding orbital is revealed as the origin of the bonding mechanism, established from an analysis of the correlated set of occupied orbitals generated in KS-CDFT. The MO picture is complemented by a visualisation of the electronic density re-arrangement and induced physical currents resulting from the bonding interaction connecting areas of density increase with favourable paratropic currents.

Section 4.2 and Section 4.3 extend the analysis of chemical bonding in magnetic fields through the electron localisation function (ELF) for CDFT [135, 136]. The ELF gives a well defined visualisation of the chemical bonding in a system through the effects of the Pauli exclusion principle on the local kinetic energy density. Analysis of the ELF in strong magnetic fields shows extensive changes in localisation structure and sheds light on key aspects of CDFT functional design.

4.1 Understanding the mechanism of perpendicular paramagnetic bonding

KS-CDFT calculations provide a simple set of canonical molecular orbitals, which can be used to construct the electron density via

$$\rho(\mathbf{r}) = \sum_i \varphi_i(\mathbf{r})\varphi_i^*(\mathbf{r}) = \sum_{\gamma\zeta} \omega_\gamma(\mathbf{r}) D_{\gamma\zeta} \omega_\zeta^*(\mathbf{r}), \tag{4.1}$$

note that the occupied KS orbitals $\varphi_i(\mathbf{r})$ can be complex in the presence of a magnetic field. In the second equality the density is expressed in terms of the one-particle density matrix $D_{\gamma\zeta}$ and the basis functions $\omega_\gamma(\mathbf{r})$. Section 4.1.1 commences by considering how the molecular orbital energies associated with H_2 and rare gas diatomics change upon application of a magnetic field as the perpendicular paramagnetic bonding evolves. Since the orbitals themselves can be complex in the presence of a field the analysis proceeds in Section 4.1.2 to analyse the bonding in terms of the changes in electron density through Eq. (4.1) as a function of field, which is naturally a real observable quantity.

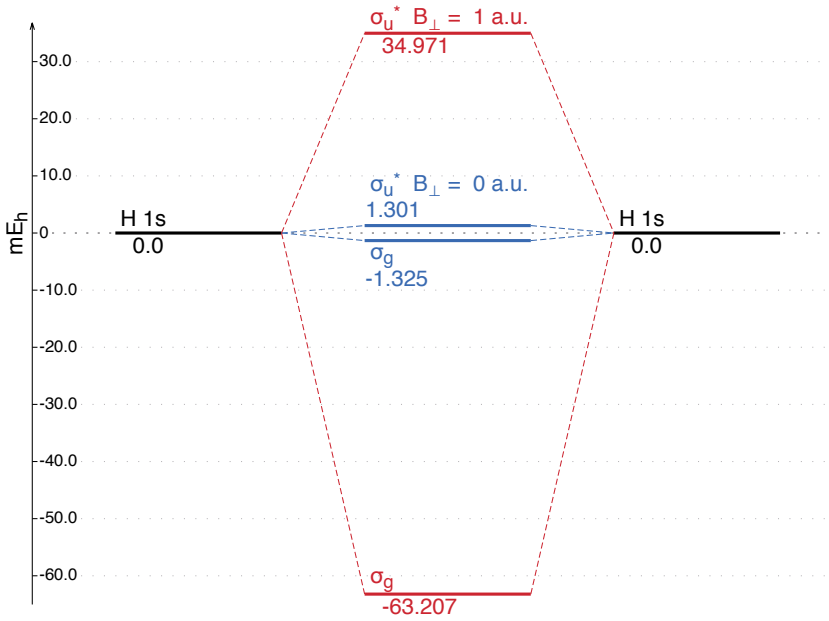


Figure 4.1: Orbital energies for the occupied σ_g and σ_u^* CDFT molecular orbitals for H_2 relative to the atomic 1s orbitals, with (red) and without (blue) a field of 1.0 a.u. perpendicular to the interatomic axis.

4.1.1 Kohn–Sham orbital analysis

KS molecular orbitals have been widely used as an interpretive aid in chemical applications throughout the literature. The KS orbitals are defined to minimise the non-interacting kinetic energy and yield the physical electron density via Eq. (4.1). They also have appealing properties; for example the highest occupied MO energy is minus the first ionization potential (IP) [137, 138] and the remaining orbital energies can be interpreted as Koopman's type approximations to higher IPs [139]. The extent to which these properties hold for general practical approximations has been a subject of debate in the literature [140, 141], as has the interpretation of KS virtual orbitals [142] owing to the role of the integer discontinuity [137], which is missing from common approximations. However, from a practical standpoint it is widely accepted that interpretations based on occupied KS orbitals (to which the following discussion is limited) are theoretically justified and their utility has been borne out in many practical applications.

We will now consider how the KS orbital energies change upon application of a perpendicular magnetic field of 1 a.u. Given that the cTPSS based models seem to be the most reliable of those studied in the present work we consider how the orbital energies from this functional change in Figure 4.1 and Figure 4.2 for H_2 and He_2, respectively.

For the H_2 molecule in the ${}^3\Sigma_u^+(1\sigma_g 1\sigma_u^*)$ state we consider how the energy of the occupied σ_g and σ_u^* orbitals change upon bonding. In particular, we plot orbital energies in the absence of a field and in a perpendicular field of 1 a.u. relative to those of the atomic orbitals in the same field. We have plotted the orbital energies at an internuclear separation $R_e = 2.564$ a.u. consistent with the cTPSS equilibrium bond length in the presence of a field.

We see that in the absence of a field the singly occupied σ_g orbital is stabilised by 1.33 mE_h, whilst the singly occupied σ_u^* is destabilised by 1.30 mE_h relative to the 1s hydrogen orbitals. This is consistent with a net bond order of zero and a repulsive profile for the corresponding potential energy curve. In the perpendicular field of 1 a.u. we see that, relative to the hydrogen 1s orbital in the same field, the σ_g orbital is shifted to 63.21 mE_h, whilst the σ_u^* orbital is shifted to 34.97 mE_h, thus there is a stabilisation of the σ_u^* orbital relative to the σ_g orbital and a net bonding interaction. This is consistent with the analysis of Ref. [27], though the present analysis makes use of higher accuracy correlated orbitals.

A similar analysis can be carried out for the lowest ${}^1\Sigma_g^+$ state of He_2 and is presented in Figure 4.2.

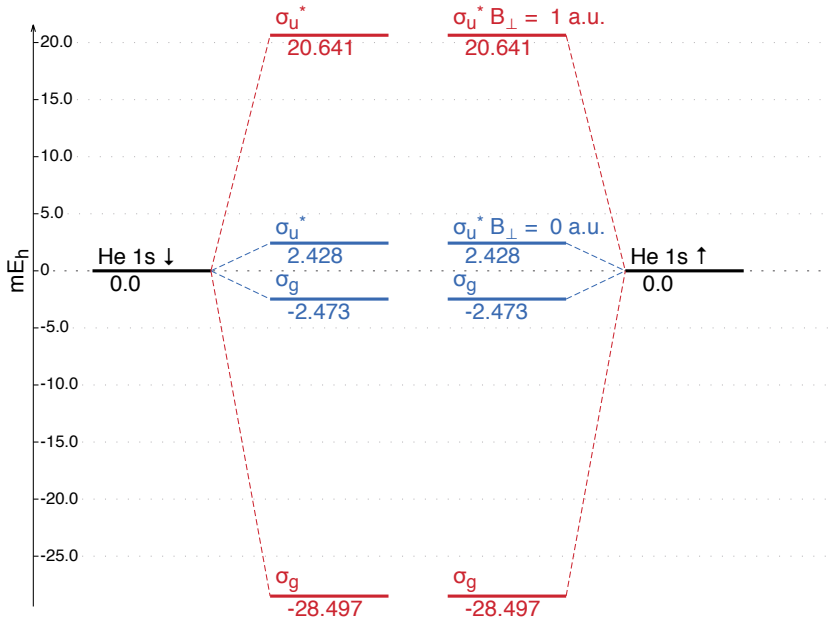


Figure 4.2: Orbital energies for the occupied σ_g and σ_u^* CDFT molecular orbitals for He_2 relative to the atomic 1s orbitals, with (red) and without (blue) a field of 1.0 a.u. perpendicular to the interatomic axis.

In this plot the spin down and spin up orbitals have been separated and their energies defined relative to atomic orbitals of the same spin in the same field. Defined in this way the offset between the orbitals of different spin due to the Zeeman interaction is removed from the plot. Again the energies correspond to the cTPSS He_2 equilibrium internuclear separation $R_e = 2.864$ a.u. in the presence of a perpendicular field. In the absence of a field we see that again the relative stabilisation of σ_g and destabilisation of σ_u^* are approximately compensatory, whilst in the presence of a field the σ_g orbital is more stabilised than the σ_u^* orbital is destabilised. It is also clear that the extra stabilisation of the σ_g orbital of ~ 8 mE_h is considerably less than the ~ 28 mE_h observed for H_2. This is consistent with the strength of binding exhibited for these species in Figure 3.8 and Figure 3.9 as well as in Table 3.9.

Similar orbital energy diagrams may be constructed for the HeNe and Ne_2 systems, however, they become significantly more complex due to large differences between the orbital energies in HeNe and the splitting of the p-orbitals in Ne_2. A complementary visualisation of the bonding effects in these systems based on the charge and (physical) current density presents a considerably simpler analysis of the paramagnetic bonding effects of heavier system.

4.1.2 Interaction electron densities

Calculations of the electronic density and current density in the presence of varying perpendicular magnetic fields ($B_\perp$) were performed for each of the species He_2, HeNe and Ne_2 using the cTPSS functional at the corresponding equilibrium geometries. Here the density change $\Delta\rho_{B_\perp}(\mathbf{r})$ for each system is considered relative to the isolated atoms in the same field,

$$\Delta\rho_{B_\perp}(\mathbf{r}) = \rho^{\text{Dimer}}_{B_\perp}(\mathbf{r}) - \sum_{i=1}^{N_{\text{atoms}}} \rho^{i}_{B_\perp}(\mathbf{r}) \tag{4.2}$$

This difference density allows for a visualisation of the nature of the paramagnetic bonding in the diatomic systems. In a similar manner one can consider the (gauge invariant) *physical* current density difference $\Delta\mathbf{j}$

$$\Delta\mathbf{j}_{B_\perp}(\mathbf{r}) = \mathbf{j}^{\text{Dimer}}_{B_\perp}(\mathbf{r}) - \sum_{i=1}^{N_{\text{atoms}}} \mathbf{j}^{i}_{B_\perp}(\mathbf{r}) \tag{4.3}$$

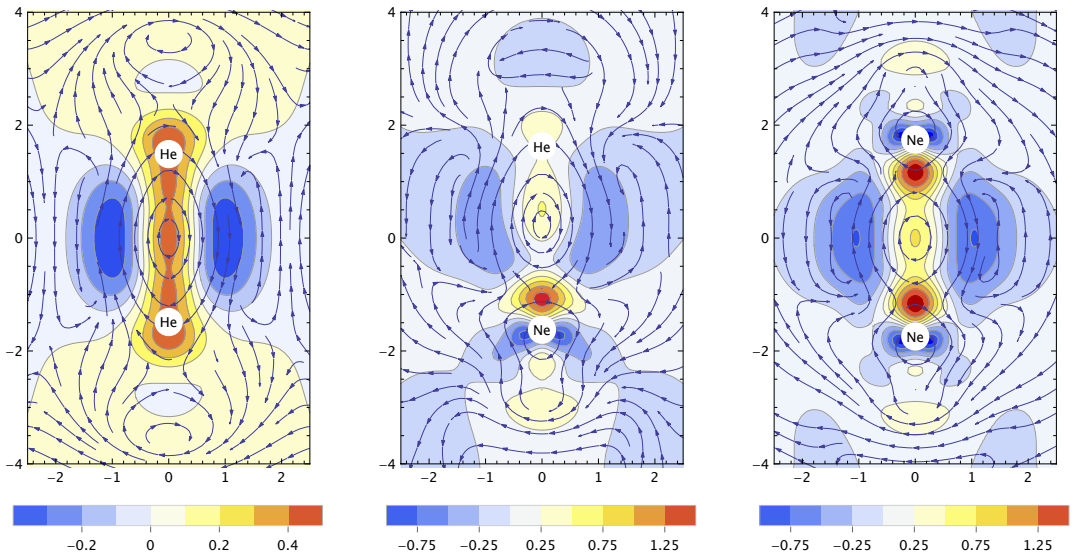


Figure 4.3: $\Delta\rho_{B_\perp}(\mathbf{r})$ (coloured contours) and $\Delta\mathbf{j}_{B_\perp}(\mathbf{r})$ (streamlines) for the rare gas dimers He_2 (left), HeNe (middle) and Ne_2 (right) in a $B_\perp = 1.0$ a.u. magnetic field. The internuclear axis is aligned with the z-axis and the plots are show in the yz-plane intersecting the atomic positions. The number density difference has been multipled by 10^3.

Figure 4.3 presents plots of the density differences in Eq. (4.2) and Eq. (4.3) for each of the species with $B_\perp = 1.0$ a.u. The shading of the contours represents the buildup (red) or depletion (blue) of the charge density, relative to two non-interacting atoms in the same field. In all three cases there is a clear build up of density between the atoms consistent with bonding. The charge density difference is elongated along the field, above and below the plane of the plots. The streamlines show the vector field associated with the current density difference. Paratropic circulations are clearly visible over the centre of the bonds where charge density accumulates, and diatropic circulations are visible in regions where the charge density is depleted. Calculations at higher fields confirm that the alignment between para- / dia-tropic circulations and charge accumulation / depletion becomes more pronounced with stronger magnetic fields.

This picture of the perpendicular paramagnetic bonding suggests that as the charge density is compressed perpendicular to the field, allowing the constituent atoms to approach one another more closely. As they do so they experience a greater nuclear-nuclear repulsion, which may be screened by a rearrangement of the charge density towards the bond centre. This rearrangement is accompanied by consistent para- and dia-tropic current circulations.

4.2 The current modified electron localisation function

The electron localisation function (ELF), introduced for Hartree–Fock theory by Becke and Edgecombe [135] and extended to Kohn–Sham density-functional theory (DFT) via an alternative interpretation due to Savin [136], has enjoyed enormous success as a tool for understanding and visualising chemical bonding. The ELF has been widely applied to understand bonding in atoms [143], molecules [144–149], clusters [150–153], and solid-state structures [153, 154]. A topological analysis of ELF in the spirit of Bader's atoms-in-molecules approach [155] yields further information on the bonding in a given system [136, 143, 156–158], although some caution should be exercised in interpretations based on this analysis [159].

In Section 4.2.1, a generalisation of the ELF for molecules in a magnetic field is proposed. This generalisation is applied to study chemical bonding in Section 4.3, and a topological analysis is performed in Section 4.3.1. Finally, in Section 4.3.2, the physical current density induced by the field is visualised alongside the generalised ELF, illustrating the striking similarity in the topologies

of these quantities.

4.2.1 The field free electron localisation function

The definition of the ELF by Becke and Edgecombe [135] focused on Hartree–Fock theory and the same-spin pair density,

$$P_2^{\sigma\sigma}(\mathbf{r},\mathbf{r}') = \rho_\sigma(\mathbf{r})\rho_\sigma(\mathbf{r}') - |\rho_1^\sigma(\mathbf{r},\mathbf{r}')|^2, \quad \rho_1^\sigma(\mathbf{r},\mathbf{r}') = \sum_{i=1}^{N_\sigma} \varphi_{i\sigma}^*(\mathbf{r}')\varphi_{i\sigma}(\mathbf{r}). \tag{4.4}$$

Expansion of the spherically averaged same-spin conditional pair density,

$$P_{\text{cond}}^{\sigma\sigma}(\mathbf{r},\mathbf{r}') = \rho_\sigma(\mathbf{r}') - \frac{|\rho_1^\sigma(\mathbf{r},\mathbf{r}')|^2}{\rho_\sigma(\mathbf{r})}, \tag{4.5}$$

to leading order gives,

$$P_{\text{cond}}^{\sigma\sigma}(\mathbf{r},s) = \frac{1}{3}\left[\sum_{i=1}^{N_\sigma} |\nabla\varphi_{i\sigma}(\mathbf{r})|^2 - \frac{1}{4}\frac{|\nabla\rho_\sigma(\mathbf{r})|^2}{\rho_\sigma(\mathbf{r})}\right] s^2 + \cdots = \frac{1}{3}D_\sigma(\mathbf{r})s^2\ldots, \tag{4.6}$$

where s is the radius of a spherical shell around $\mathbf{r}$. The term in brackets is related to the Fermi-hole curvature discussed by Dobson [160]. Becke and Edgecombe [135] proposed to use this term as a measure of electron localisation, introducing the relative ELF measure,

$$f_{\text{ELF},\sigma}(\mathbf{r}) = \frac{1}{1 + [D_\sigma(\mathbf{r})/D_\sigma^0(\mathbf{r})]^2}. \tag{4.7}$$

Here $D_\sigma(\mathbf{r})$ is defined in Eq. (4.6), while $D_\sigma^0(\mathbf{r})$ is the corresponding quantity for a homogeneous electron gas,

$$D_\sigma^0(\mathbf{r}) = 2^{5/3}c_{\text{F}}\rho_\sigma(\mathbf{r})^{5/3}, \quad c_{\text{F}} = \frac{3}{10}(3\pi^2)^{2/3}. \tag{4.8}$$

Defined in this manner, the ELF is a dimensionless quantity between 0 and 1. The upper limit, $f_{\text{ELF},\sigma}(\mathbf{r}) = 1$, corresponds to perfect localisation, whereas $f_{\text{ELF},\sigma}(\mathbf{r}) = 0.5$ indicates behaviour close to that of a uniform gas with the same density.

4.2.2 ELF in Kohn–Sham theory

The ELF as proposed for Hartree–Fock theory relies on the definition of the conditional pair-density, $P_{\text{cond}}^{\sigma\sigma}(\mathbf{r},s)$ for the interacting system. This quantity is not accessible in the same manner in Kohn–Sham DFT, since the determinantal wave function is then used to describe a system of *non-interacting* electrons rather than to approximate the physical system. On the other hand, Savin *et al.* [145] noted that the leading term in Eq. (4.6) is accessible in Kohn–Sham theory, being related in a simple manner to the Pauli kinetic-energy density:

$$\tau_\sigma^{\text{Pauli}}(\mathbf{r}) = \tau_\sigma(\mathbf{r}) - \tau_\sigma^{\text{vW}}(\mathbf{r}) = \frac{1}{2}D_\sigma(\mathbf{r}), \tag{4.9}$$

where,

$$\tau_\sigma(\mathbf{r}) = \frac{1}{2}\sum_{i=1}^{N_\sigma} |\nabla\varphi_{i\sigma}(\mathbf{r})|^2, \quad \tau_\sigma^{\text{vW}}(\mathbf{r}) = \frac{1}{8}\frac{|\nabla\rho_\sigma(\mathbf{r})|^2}{\rho_\sigma(\mathbf{r})}, \tag{4.10}$$

The term $\tau_\sigma(\mathbf{r})$ is the σ-spin contribution to the non-interacting kinetic-energy density in the everywhere-positive gauge. Integration of this quantity over all space yields the σ-spin component of the non-interacting kinetic energy T_{s} used in Kohn–Sham theory. This form reflects the fact that, although non-interacting, the Kohn–Sham wave function is a single Slater determinant, preserving the fermionic characteristics of the electrons. The second term in Eq. (4.9), $\tau_\sigma^{\text{vW}}(\mathbf{r})$, is the von Weizsäcker (vW) kinetic-energy density, which can be interpreted as the kinetic-energy density for a system of bosonic particles with orbitals proportional to $\sqrt{\rho_\sigma}$. The difference in Eq. (4.9) can then

be interpreted as the *change in the kinetic-energy density induced by the Pauli principle*. Since the von Weizsäcker kinetic-energy density provides a lower bound on the non-interacting kinetic energy density,

$$\tau_\sigma(\mathbf{r}) \geq \tau_\sigma^{\mathsf{vW}}(\mathbf{r}), \tag{4.11}$$

the Pauli kinetic-energy density is everywhere nonnegative.

Given that $\tau_\sigma^{\mathsf{Pauli}}(\mathbf{r})$ contains the same information as does $D_\sigma(\mathbf{r})$, we may consider whether the ratio $D_\sigma(\mathbf{r})/D_\sigma^0(\mathbf{r})$ required for $f_{\mathsf{ELF},\sigma}(\mathbf{r})$ may be derived from it. Savin *et al.* [145] noted that this can indeed be achieved by using the kinetic-energy density of a uniform electron gas

$$\tau_\sigma^{\mathsf{UEG}}(\mathbf{r}) = 2^{2/3} c_{\mathsf{F}} \rho_\sigma^{5/3} = \frac{1}{2} D_\sigma^0(\mathbf{r}), \tag{4.12}$$

yielding

$$\frac{D_\sigma(\mathbf{r})}{D_\sigma^0(\mathbf{r})} = \frac{\tau_\sigma^{\mathsf{Pauli}}(\mathbf{r})}{\tau_\sigma^{\mathsf{UEG}}(\mathbf{r})}. \tag{4.13}$$

The ELF may then be interpreted as a measure of localisation that reflects changes arising from the fermionic nature of the electrons and the satisfaction of the Pauli principle. This observation goes a long way towards rationalising the practical utility of $f_{\mathsf{ELF},\sigma}(\mathbf{r})$ for chemical interpretation, bearing in mind that the Pauli principle and its consequences govern many aspects of how chemical phenomena may be interpreted. The Pauli principle leads to Fermi-correlation (exchange) effects between electrons of the same spin, which are typically an order of magnitude larger than those between opposite-spin electrons (dynamical correlation). As a result, the interpretation of same-spin interactions, as in ELF, can serve as a useful qualitative tool for interpretation.

The ELF formula discussed above involves two separate functions, one for each spin. Kohout and Savin [143] proposed instead the spin-averaged form

$$f_{\mathsf{ELF}}(\mathbf{r}) = \frac{1}{1 + \left(\frac{\tau_\alpha^{\mathsf{Pauli}}(\mathbf{r}) + \tau_\beta^{\mathsf{Pauli}}(\mathbf{r})}{\tau_\alpha^{\mathsf{UEG}}(\mathbf{r}) + \tau_\beta^{\mathsf{UEG}}(\mathbf{r})} \right)^2}. \tag{4.14}$$

This work considers closed-shell systems, for which the values of $f_{\mathsf{ELF}}(\mathbf{r})$ from Equations (4.7) and (4.14) are identical.

4.2.3 Generalisation to magnetic systems

In a magnetic field, $f_{\mathsf{ELF}}(\mathbf{r})$ becomes gauge dependent.[1] This unphysical dependence can be removed by introducing terms dependent on the paramagnetic current density, such as those that arise in the discussion of the spherical average of the exchange hole by Dobson [160]. This can be accomplished either in the expansion of Eq. (4.6) or by replacing the first term of Eq. (4.9) according to

$$\tau_\sigma \rightarrow \tilde{\tau}_\sigma = \tau_\sigma - \frac{|\mathbf{j}_p(\mathbf{r})|^2}{2\rho(\mathbf{r})} \tag{4.15}$$

where $\mathbf{j}_p(\mathbf{r})$ is the paramagnetic current density.

This generalisation has previously been used to compute time-dependent ELFs [161] and in the generalisation of meta-GGA functionals to calculate response properties perturbatively [93] and magnetic properties non-perturbatively [98] (see Chapter 3). It is also noted that the gauge independent kinetic energy density is not unique, and several other forms have been proposed (see Section 2.4). However, the choice of Eq. (4.15) has the advantage that the kinetic energy density is independent of the external magnetic field, as well as satisfying Eq. (4.11). These issues have previously been examined in the context of meta-GGA functionals in Ref. [94]. Here, the cTPSS functional is used to perform calculations at a finite magnetic field, computing the generalised ELF as a function of field strength. Following the notation cTPSS for the TPSS functional with the substitution in Eq. (4.15), the acronym cELF is used for the similarly modified ELF.

[1] See Section 2.1.3 for a full discussion of gauge transformations.

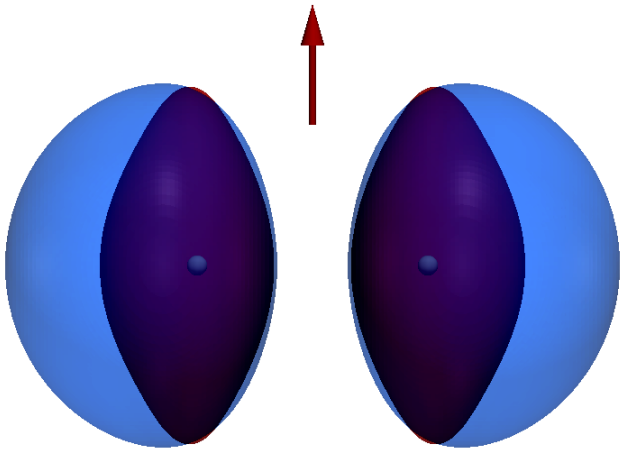


Figure 4.4: Perpendicular paramagnetic bonding in He_2 as calculated using cTPSS / u-aug-cc-pVTZ. The iso-volumes depict the regions of $f_{\mathrm{ELF}} \geq 0.8$ at zero field (blue) and in the presence of a perpendicular magnetic field of strength 1 a.u. (red). The system is considered at the equilibrium geometry of $R = 2.86\ a_0$ as determined in a perpendicular field of $B = 1.0$ a.u.

4.3 Field induced changes in electron localisation

All cELF calculations use the LONDON program [51] with the CDFT implementation of cTPSS described in Chapter 2 to determine the required quantities for ELF at different field strengths. All calculations have been carried out in a u-aug-cc-pCVTZ basis set [20, 162] of London atomic orbitals (Section 2.1.4). Unless otherwise noted, zero-field TPSS geometries are used.

Paramagnetic bonding

Firstly, the recently discovered phenomenon of perpendicular paramagnetic bonding [27] is considered. Figure 4.4 presents iso-volumes for He_2 in the absence of a field (blue) and in a uniform field of strength 1.0 a.u. perpendicular to the internuclear axis (red). The bond distance of $2.864a_0$ has been optimised at the cTPSS/u-aug-cc-pVTZ level in the same field. In Ref. [27], the paramagnetic bonding in He_2 was rationalised in terms of induced electron rotation. The bonding is further analysed at the Kohn–Sham level in Section 4.1, in terms of molecular-orbital energies and density distortions relative to non-bonded atoms in the same field. The electronic confinement induced by the field, shown in red in Figure 4.4, is clearly captured by the cELF. In the field, the iso-surfaces contract around the atoms, becoming much more compact in the perpendicular directions than in the zero field (blue). Relaxation to the equilibrium geometry at zero field (not presented) gives similarly diffuse but near-spherical zero-field ELF iso-surfaces.

Covalent bonding

To illustrate the utility of the cELF in understanding features of covalent bonding in magnetic fields, we consider methane, ethane, ethene, and ethyne as prototypical systems containing single, double, and triple bonds. In Figure 4.5, the methane results are shown. In the absence of a field, the blue iso-surfaces are consistent with those obtained in earlier studies; in the presence of field, the iso-surfaces around the atoms contract. The structure of the cELF is similar for ethane, see Figure 4.6. An additional region of electron localisation is seen at the centre of the C-C bond both at zero field and at $B_\perp = 0.4$ a.u. As the field increases, the localisation becomes less pronounced, eventually splitting into two separate regions.

The zero-field ELF plots for ethene in Figure 4.7 are consistent with those presented elsewhere [136],

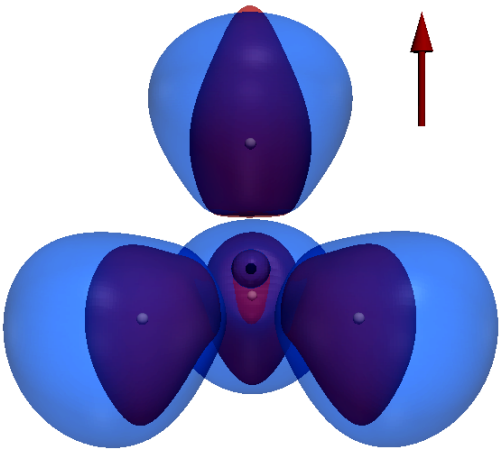


Figure 4.5: The cELF for methane calculated at the cTPSS/u-aug-cc-pCVTZ level at the corresponding zero-field geometry. The blue iso-volumes depict the regions of $f_{\mathrm{ELF}} \geq 0.8$ in the absence of a magnetic field (blue) and in a field of strength 1 a.u. (red). The direction of the field is indicated by the red arrow.

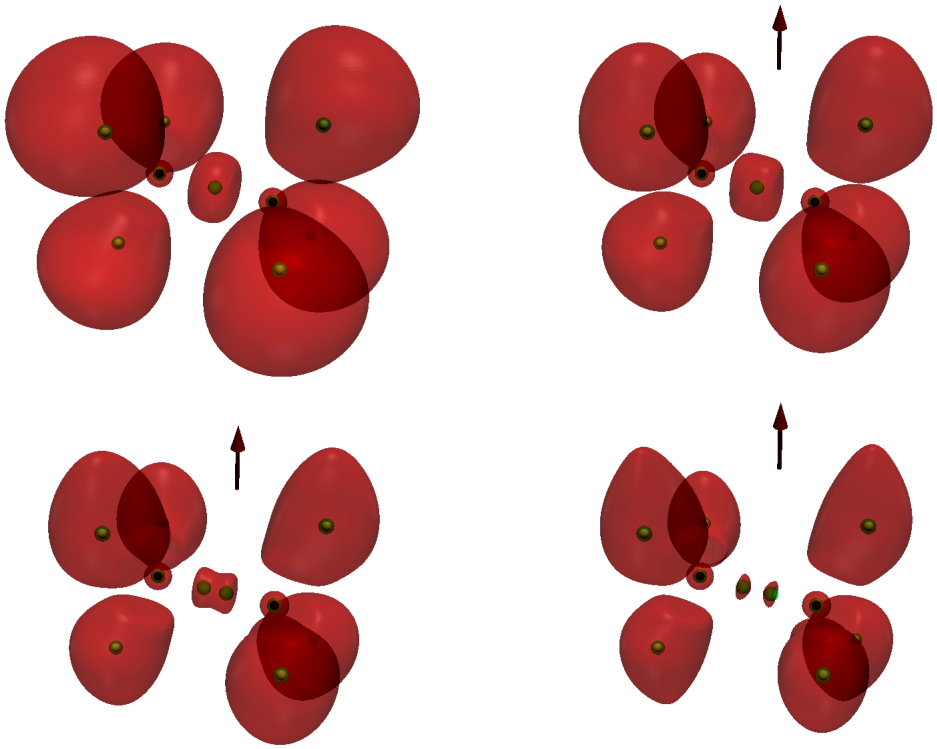


Figure 4.6: The cELF for ethane calculated at the cTPSS/u-aug-cc-pCVTZ at the corresponding zero-field geometry. The red iso-volumes depict the regions of $f_{\mathrm{ELF}} \geq 0.8$ for 0.0 a.u. (upper left), 0.4 a.u. (upper right), 0.7 a.u. (lower left), and 1.0 a.u. (lower right). Field direction is indicated by the red arrow.

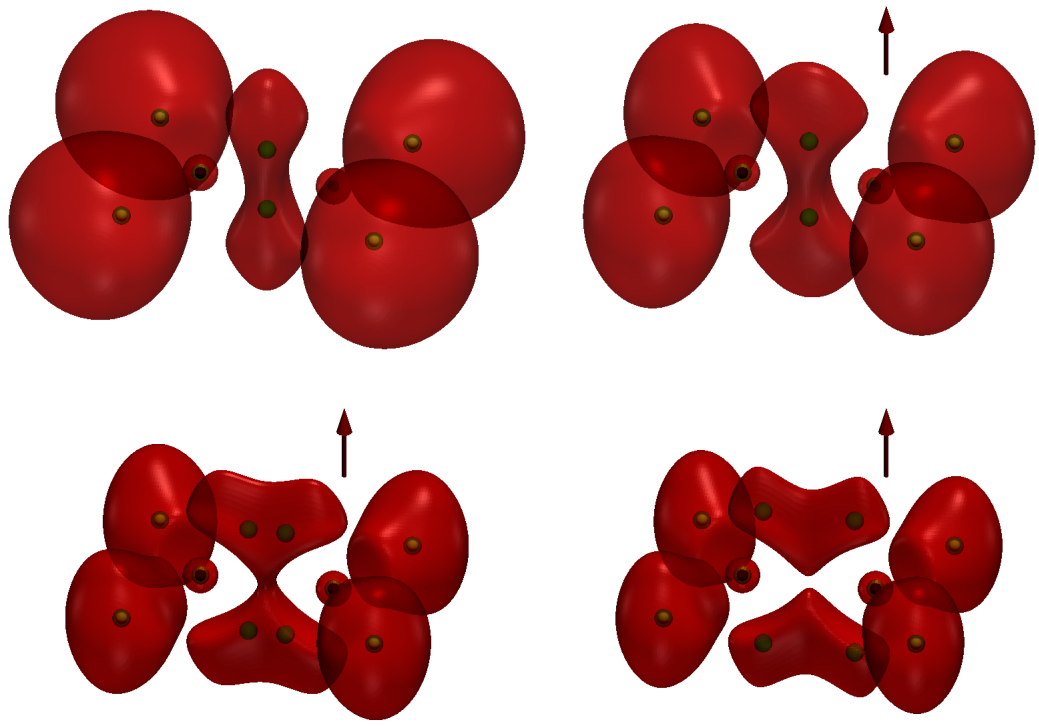


Figure 4.7: The cELF for ethene calculated at the cTPSS/u-aug-cc-pCVTZ at the corresponding zero-field geometry. The red iso-volumes depict the regions of $f_{\mathrm{ELF}} \geq 0.8$ for 0.0 a.u. (upper left), 0.4 a.u. (upper right), 0.7 a.u. (lower left), and 1.0 a.u. (lower right). Field direction is indicated by the red arrow.

with a characteristic dumb-bell shaped structure at the centre of the C=C bond. With increasing field strength, the dumb-bell structure splits into two, developing eventually into two new structures with localisation above and below the C=C bond. Around the hydrogen atoms, the cELF surfaces of ethene contract in a manner similar to that observed for methane and ethane.

Finally, Figure 4.8, presents cELF plots for ethyne. At zero field, the cELF structure is similar to that reported elsewhere [136], with a characteristic ring structure about the triple bond. The ring is distorted at 0.1 a.u., splits into two at 0.5 a.u., and eventually becomes reminiscent of that for ethene at 1.0 a.u., with localisation above and below the bond.

The features of the cELF observed here can help to rationalise the success of the cTPSS meta-GGA functional in strong fields relative to conventional GGA functionals and also the local-density approximation (LDA), see Chapter 2. In the cTPSS functional, the same modification of Eq. (4.15) is employed, entering the functional via

$$\alpha(\mathbf{r}) = \frac{[\tilde{\tau}_\sigma(\mathbf{r}) - \tau_\sigma^{\mathrm{vW}}(\mathbf{r})]}{\tau_\sigma^{\mathrm{UEG}}(\mathbf{r})} \quad \text{and} \quad \frac{\tau_\sigma^{\mathrm{vW}}(\mathbf{r})}{\tilde{\tau}_\sigma(\mathbf{r})}. \tag{4.16}$$

Note that $\alpha(\mathbf{r})$ contains the same information as the cELF, to which it is related as

$$f_{\mathrm{ELF},\sigma}(\mathbf{r}) = 1/(1 + \alpha_\sigma^2(\mathbf{r})). \tag{4.17}$$

Hence $\alpha(\mathbf{r})$ also characterises the nature of different bonding regions, vanishing in one-orbital regions. However, it is not restricted to values between 0 and 1. The ratio $\tau_\sigma^{\mathrm{vW}}(\mathbf{r})/\tilde{\tau}_\sigma(\mathbf{r})$ also serves as a useful indicator of one-orbital regions.

The visualisations presented suggest that, as the field increases, regions of large $f_{\mathrm{ELF},\sigma}(\mathbf{r})$ and low $\alpha(\mathbf{r})$ values distort considerably. Since meta-GGAs are designed to minimise one-electron self-interaction errors in these regions, the good performance of the cTPSS functional in strong magnetic fields

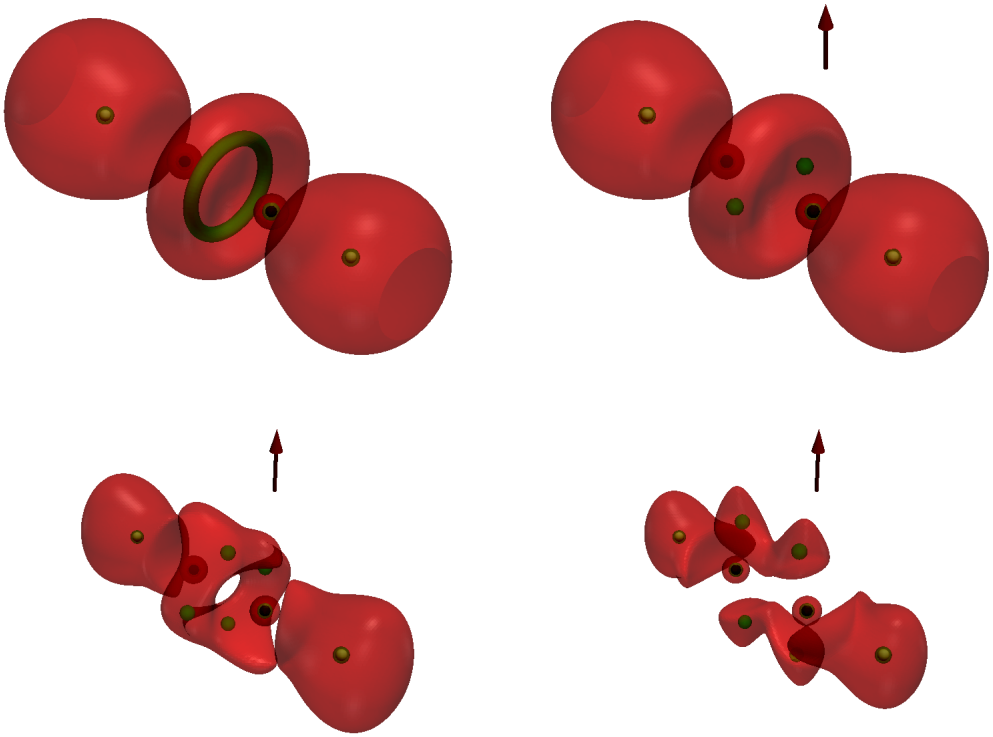


Figure 4.8: The cELF for ethyne calculated at the cTPSS/u-aug-cc-pCVTZ at the corresponding zero-field geometry. The red iso-volumes depict the regions of $f_{\mathrm{ELF}} \geq 0.8$ for 0.0 a.u. (upper left), 0.1 a.u. (upper right), 0.5 a.u. (lower left), and 1.0 a.u. (lower right). Field direction is indicated by the red arrow.

observed in Chapter 2 may reflect an increased importance of these regions, as discussed further in Section 4.3.3.

4.3.1 The topology of cELF

The function f_{ELF} is a continuous scalar field and can therefore be subjected to a topological analysis similar to that used for the electron density by Bader [155]. This approach has been extensively used to highlight features of the ELF related to the chemical bonding in systems at zero field. In particular, the positions of attractors (indicated in Figures 4.6-4.8 as green spheres), which correspond to maxima of f_{ELF}, highlight regions of high localisation and are known to coincide with traditional chemical notions of bonding [136]. Changes in the number and arrangement of attractors in a magnetic field can therefore be indicative of deeper changes in the electronic structure induced by the field.

The attractors for ethane (determined on a uniform grid with spacing 0.05 a_0) are shown in Figure 4.6. At zero field and 0.4 a.u., a single attractor is present at the centre of the C-C bond. As the field increases, two attractors appear along the C-C bond axis, reflecting two separate maxima in the cELF. In Figure 4.7, the central dumb-bell shape of ethene encompasses two attractors. With increasing field strength, new features evolve, with two pairs of attractors appearing above and below the C=C bond.

In Figure 4.8, the attractors for ethyne are shown, the high symmetry of this system leading to a ring attractor about the bond. A magnetic field perpendicular to the bond axis destroys the linear symmetry, breaking the ring attractor into two point attractors. At 0.5 a.u., two further attractors appear above and below the C≡C bond axis. Finally, at 1.0 a.u., the cELF resembles that for ethene in the same field, with attractors above and below the C≡C bond axis.

4.3.2 Structural similarities in cELF and the physical current density

The total physical current density $\mathbf{j}$ is the physically observable electron current induced by the magnetic field. It is related to the total paramagnetic current density that enters $\tilde{\tau} = \tilde{\tau}_\alpha + \tilde{\tau}_\beta$ (Eq. (4.14) and Eq. (4.15)) and hence the cELF by

$$\mathbf{j}(\mathbf{r}) = \mathbf{j}_p(\mathbf{r}) + \rho(\mathbf{r})\mathbf{A}(\mathbf{r}), \tag{4.18}$$

where the second term is the diamagnetic current, dependent on the magnetic vector potential related to the physical field $\mathbf{B}$ as Eq. (2.7).

Visualisation of this quantity can aid with the understanding of the magnetic field's influence on a system. Figure 4.9 shows the physical current vector field superimposed over a cELF contour plot for ethyne at $B_\perp = 1.0$ a.u. in the molecular plane (left) and 1.15 a_0 above it (right). The current streamlines follow the structure of the cELF, circulating around the attractors and following contour regions of high localisation. In this sense, the current plots are complementary to the cELF, highlighting localised and bonding regions in a field. However, unlike the cELF, the current density vanishes (for closed-shell systems) in field-free DFT and is only of interest in a magnetic field.

4.3.3 The importance of self interaction correction within a magnetic field

The magnetic field has a compressive effect on the electron density that is more pronounced in directions perpendicular to the field than parallel, which results in a change in electron localisation. This compression increases the probability of finding an electron close to another electron of the same spin, and consequently a reduction in volume of the regions in which cELF has a value close to one. This effect can be seen in all the systems investigated but is especially apparent in Figures 4.5 and 4.4 which show a direct comparison between the field free and $||\mathbf{B}|| = 1.0$ a.u. cases.

This change in electron localisation has important consequences for mGGA functionals that make use of $\alpha(\mathbf{r})$ (an ingredient of cELF, Eq. (4.16)) as an iso-orbital indicator in order to identify one electron

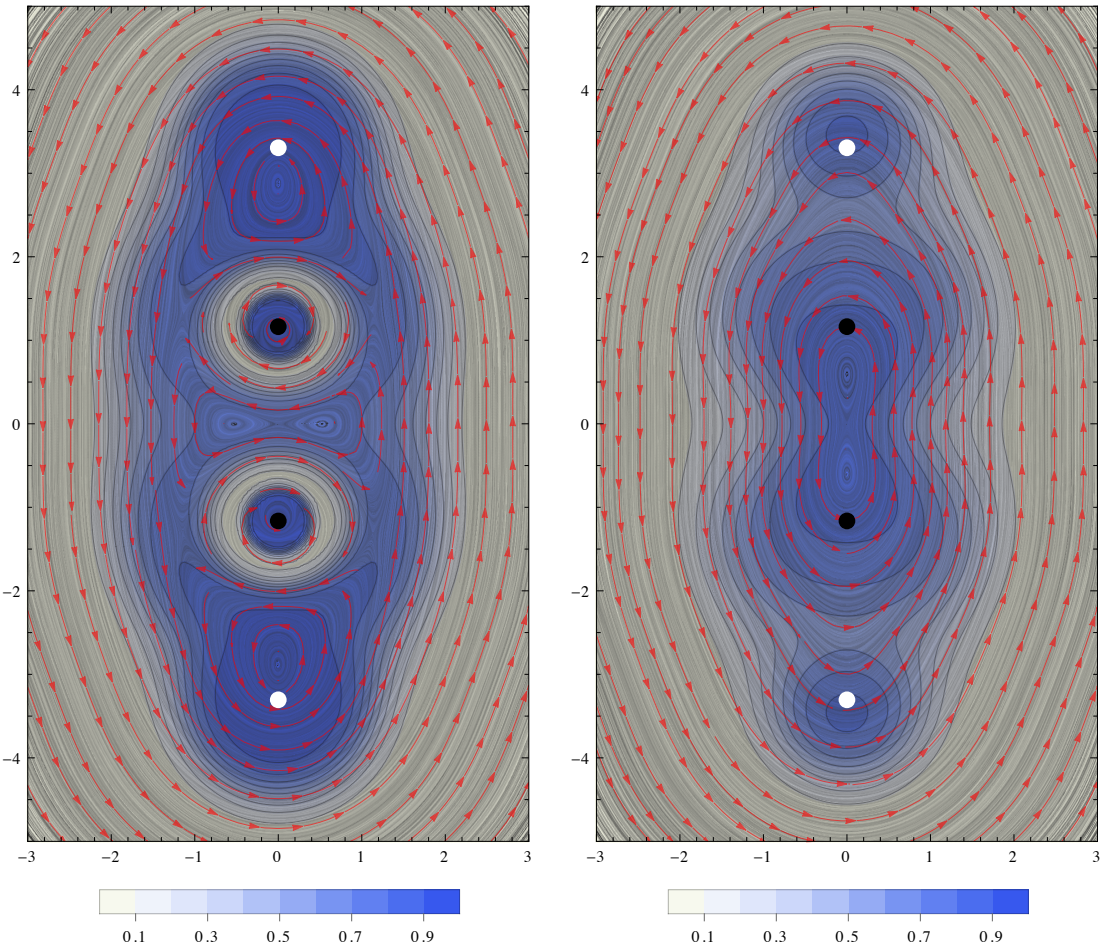


Figure 4.9: The physical current density (red stream lines) and the cELF (blue contours) of ethyne in the molecular plane (left) and $1.15a_0$ above it (right) in a perpendicular magnetic field of strength 1 a.u. The positions of the carbon and hydrogen atoms are labeled with black and white dots respectively.

regions and handle their self interaction error correctly. The visualisations of cELF with increasing field unanimously show areas of high localisation shrinking, corresponding to an increasing importance of one-electron (low localisation) regions. The growing importance of one-electron regions revealed by the cELF analysis, combined with the success of cTPSS in the strong field regime, suggests that self interaction error becomes increasingly important in the presence of strong magnetic fields.

A similar conclusion was reached by Trickey and co-workers in Ref. [83] for atomic systems in extremely strong fields of up to 2000 a.u., strengths made possible by the use of anisotropic basis sets. In agreement with the present analysis they found that electron confinement effects become pronounced in strong fields, giving an increased importance to self interaction error. They note that the exact exchange including TPSS(h) hybrid mGGA functional provides a complete self interaction free functional and find, in agreement with Section 3.5.3, that it is able to accurately reproduce correlated wave function results in strong fields.

In light of the cELF analysis presented here it is clear that further development of CDFT functionals must place great importance on a correct cancellation of self interaction error. A successful approach to CDFT functional development should therefore focus on the mGGA level or extensions to CDFT to more non-local orbital dependent functional forms by means of the optimised effective potential method (see Chapter 6).

4.3.4 Concluding remarks

The accuracy and flexibility of CDFT for modelling strong field effects was established in Chapter 3, allowing CDFT calculations of molecules in strong magnetic fields to be made with some confidence. A wealth of information can be obtained from such CDFT calculations, and a visualisation of the working components can grant a greater qualitative understanding of the challenges posed by a system than is clear from just the total energy. As with all aspects of magnetic field calculations however, care must be taken with regards to the gauge properties of the quantities under investigation.

With this caveat in mind this chapter has sought to utilise the power of density functional methods to give a qualitative understanding of molecules in magnetic fields. Firstly, the electronic densities and energies of the Kohn–Sham orbitals were examined to explain the phenomenon of perpendicular paramagnetic bonding through the stabilisation of correlated anti-bonding orbitals associated with an electron density build-up in paratropic regions. Secondly, the generalised electron localisation function was utilised to visualise the density compression effects of a strong magnetic field and the associated changes in localisation structure. This visualisation reinforces the importance of self-interaction error correction in CDFT functionals and serves as a guide for construction of future CDFT functionals. It is expected that the continued use of such techniques may enhance the descriptive power of CDFT calculations and place it as an invaluable tool for understanding the molecular physics of strong magnetic fields.

Chapter 5

Excited States in Magnetic Fields

So far we have been concerned with finding ground state solutions for molecular systems, and have considered electronic excitations only so far as required for the correlation energy in more sophisticated wave function methods. For some problems restricting attention to ground state configurations is entirely justified, but for many dynamic processes in chemistry an evaluation of the system's excited states is essential. Whilst excited states are accessible by FCI theory the prohibitive computational cost associated with this method prevents its application beyond small systems. Excited states are naturally of interest when considering molecules in the presence of magnetic fields as the field induces a splitting and reorganisation of states (Section 5.2.1) that produce observable changes to the associated spectra. An efficient, correlated description of excited states in a magnetic field through CDFT is therefore desirable and a method to this effect forms the body of this chapter.

The single determinant methods of Hartree–Fock and KS-DFT have proved widely successful in describing ground state electronic systems and it is unsurprising that complementary methods for electronic excited states have been derived as CIS (CI truncated to single excitations only) and time-dependent DFT. Such excited state theories can give reasonable accuracy for lower lying excited states whilst maintaining a tractable computational cost. Both methods however are fundamentally limited as the fixed set of ground state reference orbitals they construct the excited states from are unable to relax in response to the new excited configuration, leading to an overestimation of the energy. This limitation causes CIS and TD-DFT to fail in cases where orbital relaxation is important, and when these cases are found one must return to expensive CI or EOM-CC [163] methods. The necessary improvement is therefore to derive a single determinant scheme that allows the excited state orbitals to relax, without collapsing back to the ground state.

A crude approximation to a singly excited electronic state can be generated from a converged set of ground state HF or KS-DFT orbitals by promoting an electron into a higher lying orbital, adopting the new orbital energy. Clearly this method is deficient, the ground state orbitals are optimal for the ground state configuration only and have not relaxed in response to the change in occupation. One could naively attempt to correct this by restarting the SCF procedure from those occupations, though such an attempt is doomed to failure by an adherence to the aufbau principle at the center of the SCF procedure. As described in Section 1.3.2, the aufbau principle dictates that the lowest N orbitals in each set of MOs should be occupied at each iteration of the SCF cycle. This usually ensures a convergence to the ground state configuration and results in the *variational collapse* of our naively excited MOs back to the original ground state, failing to achieve the desired goal of relaxed excited state orbitals.

The next intuitive protocol for converging the SCF procedure to an excited state is to modify the aufbau principle such that a specified set of orbitals are occupied based upon their energetic ordering, with the set defined such that the desired excitation is maintained and the final set of occupied orbitals are that of the excited state of interest. This scheme is still destined to fail however as the energetic ordering of the MOs at each SCF iteration cannot be expected to be constant as the orbitals relax during the SCF cycles resulting in re-orderings and oscillations as the calculation attempts to converge.

Convergence to the excited state can be successfully achieved using the aufbau principle if the desired

state can be uniquely defined as the lowest energy configuration with some easily evaluated property, most commonly a given electronic spin or symmetry. The aufbau principle can then be extended to occupy the lowest orbitals such that the overall configuration exhibits the prescribed property. This method of excited state calculation is simple to implement and effective in producing fully optimised excited state orbitals with the property requested. It is protected from a variational collapse to the overall ground state by the imposed requirement, but is only useful when the state in question can be uniquely defined. Attempting to produce, for example, the second lowest triplet state is still impossible as the procedure will instead collapse to the lowest triplet, rather than the second lowest as originally intended.

To utilise the SCF procedure for determining a general excited state one must instead abandon the aufbau principle completely and seek an occupation metric beyond a simple energetic ordering. An elegantly pragmatic protocol to this effect was presented in Ref. [12] by Gilbert *et al.* termed the maximum overlap method (MOM). The MOM protocol has been largely successful in facilitating the SCF study of excited states and has been used to investigate problems as diverse as: the Rydberg states and spectroscopies of the helium atom [164] and NO-rare gas clusters [165–167], the exited configurations of weakly bound species [168], the vibrational spectroscopy of small molecules [169] as well as the dynamics and fluorescence spectroscopy of BODIPY[1] molecules [170]. This chapter details an implementation of the MOM method for Hartree–Fock theory and its use for generating excited states in magnetic fields. The excited states are compared against accurate FCI states in order to assess how closely they model the true excited states. This investigation is made with a view to the future implementation of MOM for CDFT to produce a low cost, correlated description of excited states in magnetic fields.

5.1 The maximum overlap method

Instead of following the aufbau principle, the maximum overlap method (MOM) of Gilbert *et al.* [12] determines orbital occupation through the simple rule of 'occupy the orbitals that are most like the last set'. Following this and starting from a guess set of orbitals the occupations of the new MOs at each SCF step can be set as those with the largest projections onto the occupied orbitals of the last iteration. Provided the variation of the orbitals between iterations is sufficiently small then variational collapse is prevented and the excited MOs are optimised, minimising the total electronic energy whilst still allowing for orbital relaxation and reordering as the SCF proceeds.

Following this occupation protocol produces a set of relaxed MOs that minimise the electronic energy whilst remaining true to the configuration of the initial guess set. Whilst the accuracy of the MOM optimised states has been shown to be good [12, 164], the states produced by the MOM method violate the orthogonality condition,

$$\left\langle \Psi_i^{\mathrm{MOM}} \middle| \Psi_j^{\mathrm{MOM}} \right\rangle \neq \delta_{ij}, \tag{5.1}$$

where all the exact excited state wave functions of a given system are orthogonal.

Gilbert *et al.* argue that this is not a significant limitation to the MOM method as, whilst Eq. (5.1) must be true for the exact excited state wave functions, the same expectation should not be made of approximate wave functions. The requirement for strict orthogonality in approximate excited state wave functions has been overstated, the authors argue, and serves only to propagate the limitations of the approximate ground state onto the excited states. The effectiveness of the MOM method stands tribute to this reasoning and a full discussion can be found in the original MOM reference [12].

In order to define the MOM criteria, consider again the linear equations of the SCF cycle,

$$\mathbf{F}\mathbf{C}^{\mathrm{new}} = \mathbf{S}\mathbf{C}^{\mathrm{new}}\boldsymbol{\varepsilon}, \tag{5.2}$$

in which $\mathbf{S}$ the overlap matrix, $\mathbf{C}$ the new matrix of MO coefficients and $\boldsymbol{\varepsilon}$ the orbital energies. A new Fock matrix $\mathbf{F}^{\mathrm{new}}$ must be constructed from $\mathbf{C}^{\mathrm{new}}$ with N orbitals occupied to continue the SCF cycle. As previously stated, this occupation is conventionally set according to the aufbau principle by occupying the N orbitals with the lowest energies.

The MOM protocol however requires the orbital occupations to be set according to the rule:

[1] A class of boron-dipyrromethene based fluorescent dyes.

"The new occupied orbitals should be those that overlap most with the span of the old occupied orbitals."

To define this criteria precisely, an orbital overlap matrix is defined as,

$$\mathbf{O} = (\mathbf{C}^{\text{old}})^{\dagger}\mathbf{S}\mathbf{C}^{\text{new}} \tag{5.3}$$

such that O_{ij} is the overlap of the i^{th} old orbital with the j^{th} new orbital. With the overlap matrix, $\mathbf{O}$, a projection of the j^{th} new orbital onto the occupied space of the old orbitals is defined as,

$$p_j = \sum_{i}^{N} O_{ij} = \sum_{\nu}^{K}[\sum_{\mu}^{K}(\sum_{i}^{N} C_{i\mu}^{\text{old}})S_{\mu\nu}]C_{\nu j}^{\text{new}}, \tag{5.4}$$

orbital occupation is then simply set from the projection vector by occupying the N orbitals with the largest occupied projection scores, p_j. With the MO occupations defined the SCF procedure can continue as normal. No further generalisation is required for the application of the MOM to systems with an external magnetic field, as the possibility of complex orbitals was accounted for in Eq. (5.3).

With the MOM projections defined, all that is required for the practical operation of the MOM scheme is a guess set of excited state orbitals and occupations from which the SCF procedure can begin. Here lies the additional complication of MOM, the initial guess orbitals must lie within the basin of attraction for the relaxed excited state. A common strategy for making such a set of guess MOs is to converge a ground state SCF calculation of the same system and form a crude approximation of the excited state from the promotion of electrons within these orbitals to the state desired. In cases where such a guess is insufficiently close to the true relaxed orbitals a more refined guess must be made to prevent converging to a different solution, Gilbert *et al.* [12] suggest the use of orbitals optimised for the $(N-1)$ cationic system for this approach, termed the cation guess.

5.2 The electronic states of H_2 within a strong magnetic field

The MOM occupation protocol was implemented into a field generalised HF theory program to allow investigation of excited states in strong magnetic fields. The excited states of H_2 were calculated and compared to FCI benchmarks to investigate the effectiveness of MOM at describing states within a magnetic field. In the absence of a magnetic field states can be characterised by their spin degeneracy as being singlet or triplet states. In the presence of a magnetic field however, such terminology becomes misleading as the triply degenerate triplet states are split into 3 distinct states by the spin Zeeman energy, shown in Figure 5.1. As a result of this degeneracy-breaking the states are instead labelled by spin quantum number: s = 0 (singlet at $B = 0$) and s = 1 (triplet at $B = 0$) throughout this Chapter. It is clear from Figure 5.1 that the spin Zeeman splitting complicates the energy surface plots enormously and results in many state crossings, particularly around the equilibrium geometry. As a result of this added complexity the analysis of vertical excitations (Section 5.2.3) and equilibrium distances (Section 5.2.4) considers only the states in which the spin Zeeman contribution is zero. The other states may be obtained by addition or subtraction of the splitting constant.

5.2.1 Potential energy curves

Potential energy curves were constructed for the lowest four s = 0 and s = 1 states of H_2 that were accessible by MOM at internuclear distances (R) from 0.5 to 5 a_0 (in steps of 0.1). The zero field surfaces were characterised and followed through increasing field strength maintaining the field free state labels, as summarised in Table 5.1. Strictly, the zero field state characterisations should not be applied to the same states in a non-zero magnetic field, as the relevant symmetries may have been broken by the field. In the following analysis however states have been given their zero field labels at all field strengths in order to facilitate a simple tracking of changes with field strength. For brevity the full labels have been omitted from plots and discussion in favour of a state number assigned by energetic ordering at equilibrium geometry, a key to these labels is given in Table 5.1, which should be understood in combination with Figures 5.2 and 5.3.

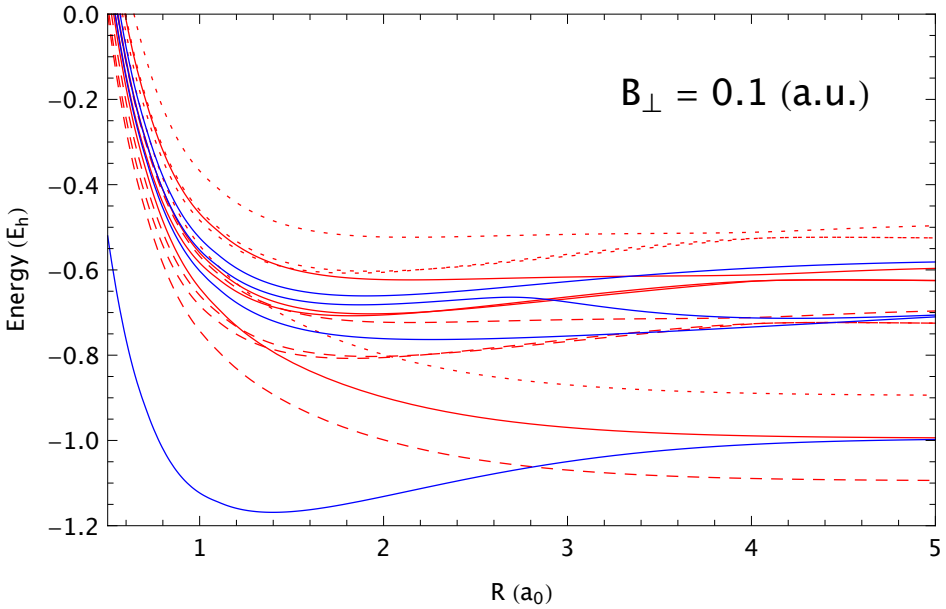


Figure 5.1: The energy surfaces for H_2 in a 0.1 a.u. perpendicular magnetic field calculated using FCI in the aug-cc-pVTZ basis set. The triply degenerate s = 1 states (red) are split by the electron spin Zeeman energy into three components, one where the energy is lowered $(\beta\beta)$ (dashed), one which is raised $(\alpha\alpha)$ (dotted) and one which has zero spin Zeeman contribution (mixed) (solid). For s = 0 states there is no spin Zeeman contribution (blue, solid).

Table 5.1: Characterisation of the zero field states. The attached number label is used when referring to the states throughout the following analysis. See the text for more details.

	s = 0	s = 1
1	$X^1\Sigma_g^+$	$b^3\Sigma_u^+$
2	$B^1\Sigma_u^+$	$a^3\Sigma_g^+$
3	$EF^1\Sigma_u^+$	$c^3\Pi_u^+$
4	$B'^1\Sigma_u^+$	$e^3\Sigma_u^+$

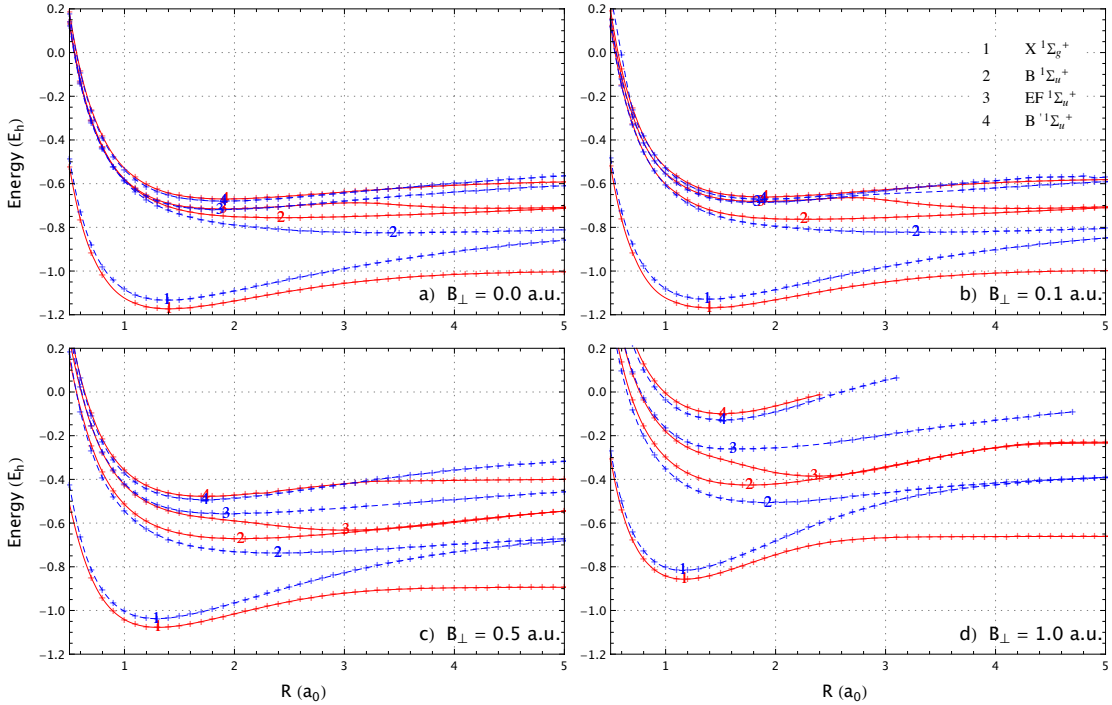


Figure 5.2: The s = 0 potential energy curves of H_2 in an external magnetic field of a) 0.0, b) 0.1, c) 0.5 and d) 1.0 a.u., aligned perpendicular to the internuclear axis. Surfaces were calculated using FCI (red) and MOM (dashed, blue) using the the aug-cc-pVTZ basis set. State labels are placed at the respective equilibrium distances.

Potential energy curves were evaluated using the aug-cc-pVTZ basis set for all states in magnetic field strengths from 0 to 1 a.u. in steps of 0.1 aligned perpendicular to the internuclear axis using Hartree–Fock with the MOM protocol and benchmarked using FCI. The MOM guess MOs were generated for each state from a cationic guess at $r = 0.5\ a_0$ and propagated outwards with each subsequent calculation using the converged orbitals from the last as the initial guess. The FCI calculations were performed pointwise along the curve using the LONDON implementation of Ref. [27] using the same aug-cc-pVTZ basis set. The lowest 20 roots were requested in the Davidson diagonalisation [171] to ensure that the lowest states were well converged and could be tracked accurately as a function of R. The individual states were carefully traced as a function of field from small to large R by assigning the excitation energies carefully, noting that the application of a field can induce a significant re-ordering of the states and induce a large number of crossings.

The s = 0 electronic energy surfaces for a subset of field strengths calculated using MOM are shown in Figure 5.2 along with equivalent FCI benchmarks. Points that did not converge (or collapsed in MOM calculations) have been omitted. These surfaces show that the MOM method is able to give a qualitatively reasonable description of the excited s = 0 states, but is unable to give quantitative accuracy, particularly at large R. For state 1 this error is a well understood failure of HF theory and arises from the fact that both electrons have the same spatial orbital, a source of error that necessarily persists at higher field strengths. A notable feature of the higher lying surfaces is the joining of states 2 and 3 at $\sim$5 a_0, with the coalescence separation shortening at higher field strengths. This feature is absent in the MOM surfaces suggesting this behaviour may be pathological for MOM. It is noteworthy that the MOM criteria was less able to prevent variational collapse around the merging of states 2 and 3, an understandable consequence of the MOs becoming similar. A further difficulty was found in strong fields ($\geq$ 0.8 a.u.) with MOM failing for the higher lying state 4 at large separations, convergence was successful around equilibrium however. This failure can be understood from the FCI data as the result of the many field induced state crossings that exist in this region and because of these state crossings the FCI surface for 4 could not be confidently tracked beyond 2.4 a_0. To do so would require the calculation of many more higher lying states, which was technically infeasible due to computational requirements exceeding available resources.

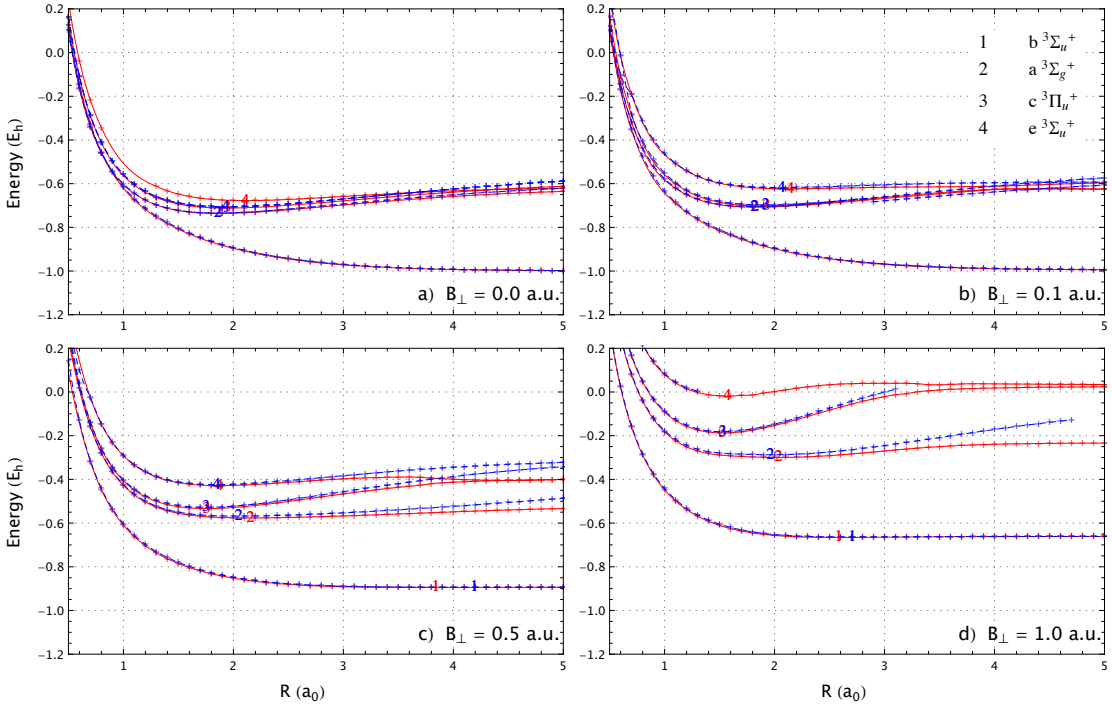


Figure 5.3: The s = 1 energy surfaces with zero spin Zeeman energy for H_2 in an external magnetic field of a) 0.0, b) 0.1, c) 0.5 and d) 1.0 a.u., aligned perpendicular to the internuclear axis. Surfaces were calculated using FCI (red) and MOM (dashed, blue) using the aug-cc-pVTZ basis set. State labels are placed at the respective equilibrium distances.

Equivalent surfaces are shown in Figure 5.3 for the s = 1 states. For these states MOM gives quantitatively accurate results around equilibrium distances and reasonable qualitative agreement at larger separations. The high accuracy of the MOM method for these states can be readily understood from the localisation of the electrons onto separate atoms in these states resulting in small electron-electron interactions and consequently small correlation energies. Despite this quantitative accuracy a number of systemic failures were found, the most obvious being a failure of the MOM protocol in optimising the higher lying states at higher field strengths, seen clearly in Figure 5.3 d) where the equilibrium separation could be reached for state 4. This failure is again attributed to a dense cluster of state crossings blurring the MOM projections making maintaining the desired occupations difficult. A further difficulty was found at $B_\perp = 0$ (sub-fig a) and 0.2 (not shown) for which state 4 collapsed to state 3 during the MOM optimisation. These collapsed surfaces for state 4 at $B_\perp = 0$ and 0.2 a.u. have *not* been omitted from further analysis and are clearly visible in the following plots. As a result of this collapse anomalously large errors are reported in MOM state 4 at field strengths of 0 and 0.2 a.u. This collapse to a lower state highlights some of the potential difficulties encountered when following the MOM protocol.

5.2.2 Spin Zeeman induced state re-ordering

An interesting consequence of the spin Zeeman energy is the resulting change in ground state configuration encountered at higher field strengths, from the lowest s = 0 state, $X^1\Sigma_g^+$, to the lowest s = 1 state, $b^3\Sigma_u^+$. The critical strengths at which each s = 1 state becomes the overall ground state are shown in Figure 5.4, which plots the energy of all the states relative to the lowest s = 0 state, the critical fields are summarised in Table 5.2. There is a quantitative agreement between the FCI and MOM states, though the MOM crossings show a constant shift to lower fields. This constant shift can be understood from the poor MOM description of the s = 0 ground state contrasting with the very good MOM description of the s = 1 states. A constant shift then arises from an absence of error cancellation, lowering the critical field strengths.

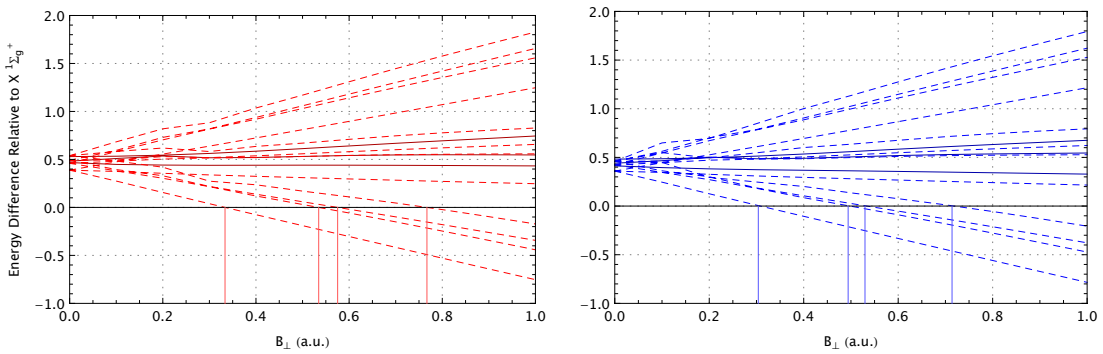


Figure 5.4: The energy difference between the $X^1\Sigma_g^+$ zero field ground state energy and the higher s = 0 (solid) and s = 1 (dashed) states. All calculations are performed at the zero field equilibrium geometry of $R_{\mathrm{FCI}} = 1.405\ a_0$ and $R_{\mathrm{MOM}} = 1.387\ a_0$. Crossings are determined numerically for both the FCI (left, red) and MOM (right, blue) methods. The field strength at which a state becomes lower in energy than the reference state is shown by a vertical line to the horizontal axis.

Table 5.2: Critical perpendicular field strengths at which s = 1 states cross energy with the $X^1\Sigma_g^+$ zero field ground state. All calculations performed at zero field equilibrium geometries shown in the table.

	MOM $R = 1.387\ a_0$	FCI $R = 1.405\ a_0$
$b^3\Sigma_u^+$	0.30	0.33
$a^3\Sigma_g^+$	0.49	0.53
$c^3\Pi_u^+$	0.53	0.58
$e^3\Sigma_u^+$	0.71	0.77

5.2.3 Vertical excitation energies

The vertical excitation energy is defined as the energy required to promote a system from one state to another at a fixed geometry, usually the equilibrium geometry of the initial state. The vertical excitations from the lowest s = 0 state ($X^1\Sigma_g^+$) at the field free equilibrium geometries, $R_{\mathrm{FCI}} = 1.405\ a_0$ and $R_{\mathrm{RHF}} = 1.387\ a_0$ for FCI and MOM respectively, were calculated at increasing perpendicular field strength and are shown in Figure 5.5. As should be expected from the qualitative agreement in energy surfaces, the MOM excited states give qualitatively correct vertical excitation energies across the full range of fields investigated. In general MOM underestimates the vertical excitation energies and becomes less accurate at stronger fields. The systematic underestimation is a result of the relatively poor MOM description of the lowest s = 0 state raising the ground state energy resulting in smaller vertical excitation energies. More complex structure is seen in the vertical excitation plots at lower field strengths of $B_\perp \leq 0.2$, particularly in the excitations to state 3. This structure corresponds to states 3 and 4 becoming close in energy at equilibrium in weaker fields, with the curves becoming more separated at larger fields, see Figure 5.2 a), b) and c). This feature appears to be problematic for MOM and results in the vertical excitations for state 3 and 4 crossing at $B_\perp = 0.2$.

The lowest s = 1 state is unbound at zero field[2] and consequently no equilibrium distance can be identified. The equilibrium distance of lowest s = 0 was used instead for the vertical excitation energies of the s = 1 states. The MOM and FCI vertical excitations for the s = 1 states are shown in Figure 5.6. The MOM method gives a very good description of the s = 1 states and consequently the vertical excitation energy profiles closely match those determined with FCI. A quantitative agreement is found between MOM and FCI for all states and field strengths excepting state 4 for $B_\perp = 0$ and 0.2. The failure of MOM for these excitations is due to the collapse of the MOM protocol at these strengths resulting in the collapse of state 4 into state 3 for these field strengths. Consequently the

[2]Excepting a very weak dispersion induced minimum at 7.85 a_0 with a dissociation energy of 19.6 μE$_\mathrm{h}$ [172]. See Section 5.2.4.

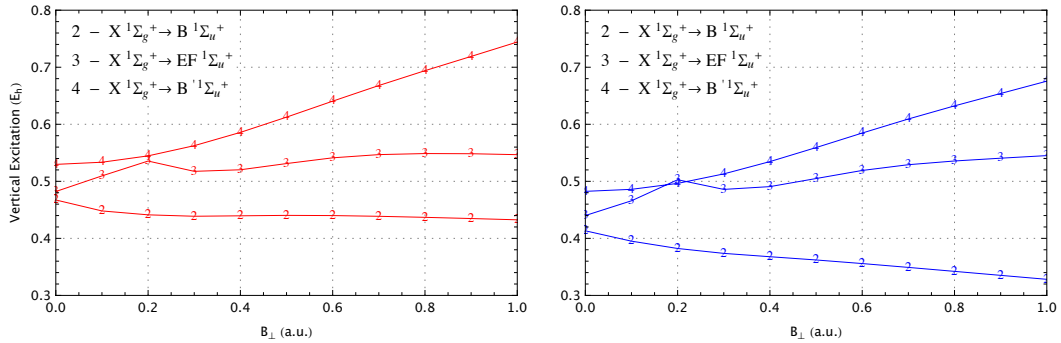


Figure 5.5: Vertical excitation energies from the lowest s = 0 state, $X^1\Sigma_g^+$, calculated with FCI (left, red) and MOM-RHF (right, blue) at zero field equilibrium separation $R_{\mathrm{FCI}} = 1.405\ a_0$ and $R_{\mathrm{RHF}} = 1.387\ a_0$ respectively.

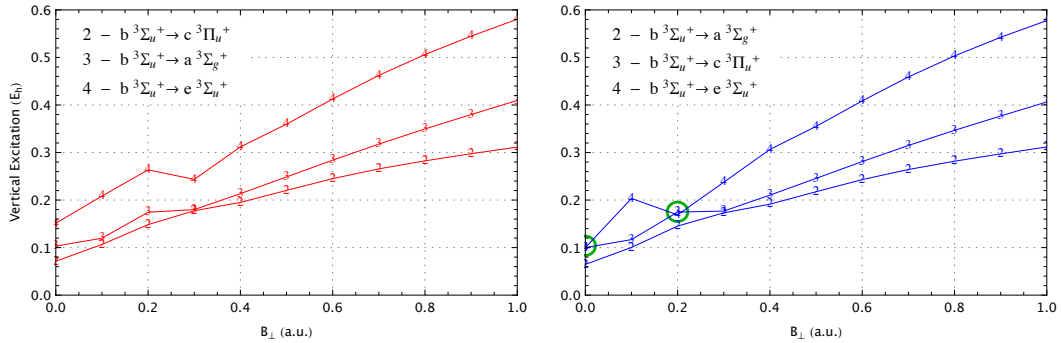


Figure 5.6: Vertical excitation energies from the lowest s = 1 state, $b^3\Sigma_u^+$, calculated with FCI (left, red) and MOM (right, blue) at 0 field equilibrium separation $R_{\mathrm{FCI}} = 1.405\ a_0$ and $R_{\mathrm{RHF}} = 1.387\ a_0$ respectively. Only the spin Zeeman cancelling configuration is considered. Points at which the MOM calculation of state 4 collapsed to state 3 are highlighted with a green ring.

vertical excitations are erroneous, matching those for state 3.

5.2.4 Equilibrium bond distances

A magnetic field compresses the electron density with a greater compression observed in directions perpendicular to the field, visualised in Figure 4.4 by means of the electron localisation function, allowing the nuclei to approach more closely when the magnetic field is aligned perpendicular to the internuclear axis. For some systems this compression allows a bonding interaction to form between normally unbound species, a topic of much discussion in this thesis. The exact effect of the electronic compression is strongly system dependent and does not universally result in stronger bonds. Indeed the s = 0 state 3 shows complicated behaviour with increasing field strength, with its equilibrium internuclear distance becoming first longer then shorter as field strength increases, visible in Figure 5.2. The change in state equilibrium distances with field strength is therefore an interesting property to follow and serves as a sensitive measure for the accuracy of approximate methods.

The equilibrium distances, defined as the local minimum on the energy curves with shortest separation, were determined numerically and are presented for the s = 0 and s = 1 states in Table 5.3 and Table 5.4 respectively. The mean errors in the MOM calculated equilibria relative to FCI are presented at the foot of the tables. The cases for which no energy minimum was identified have been omitted.

The lowest s = 1 state was unbound at zero field for both FCI and MOM. The true state is known to have a small dispersion induced interaction with a minimum at $7.85a_0$ and a dissociation energy of $19.6\mu E_h$ [172]. This binding should be present in a FCI calculation but is absent in the curves presented here. This absence arises from the incompleteness of the aug-cc-pVTZ basis in long range regions, having insufficient diffuse functions to describe the very long-range dispersion interaction. A stronger, though still relatively weak, binding is induced in the lowest s = 1 state through per-

Table 5.3: Equilibrium distances (a_0) for s = 0 states (using $B_\perp = 0$ labels) of H_2 in magnetic fields aligned perpendicular to the internuclear axis (a.u.), calculated using FCI and MOM in the aug-cc-pVTZ basis set. The mean error (ME) for the MOM equilibrium distance relative to the FCI values is presented at the foot of the table.

	1 - $X^1\Sigma_g^+$		2 - $B^1\Sigma_u^+$		3 - $EF^1\Sigma_u^+$		4 - $B'^1\Sigma_u^+$	
$B_\perp$	FCI	MOM	FCI	MOM	FCI	MOM	FCI	MOM
0.0	1.405	1.387	2.425	3.446	1.899	1.871	1.919	1.905
0.1	1.397	1.381	2.259	3.277	1.869	1.836	1.904	1.889
0.2	1.382	1.366	2.224	2.977	3.851	2.003	1.865	1.854
0.3	1.360	1.345	2.172	2.729	3.487	1.989	1.819	1.810
0.4	1.334	1.319	2.120	2.546	3.219	1.960	1.775	1.768
0.5	1.307	1.290	2.058	2.399	3.016	1.929	1.742	1.733
0.6	1.277	1.263	1.992	2.275	2.848	1.867	1.715	1.703
0.7	1.249	1.236	1.927	2.169	2.700	1.738	1.685	1.670
0.8	1.223	1.210	1.866	2.078	2.570	1.647	1.643	1.629
0.9	1.195	1.183	1.812	2.000	2.455	1.609	1.586	1.576
1.0	1.171	1.159	1.761	1.932	2.354	1.618	1.524	1.519
ME	-0.015		0.474		-0.927		-0.011	

Table 5.4: Equilibrium distances (a_0) for s = 1 states (using $B_\perp = 0$ labels) of H_2 in magnetic fields aligned perpendicular to the internuclear axis (a.u.), calculated using FCI and MOM in the aug-cc-pVTZ basis set. The mean error (ME) for the MOM equilibrium distance relative to the FCI values is presented at the foot of the table.

	1 - $b^3\Sigma_u^+$		2 - $a^3\Sigma_g^+$		3 - $c^3\Pi_u^+$		4 - $e^3\Sigma_u^+$	
$B_\perp$	FCI	MOM	FCI	MOM	FCI	MOM	FCI	MOM
0.0	-	-	1.864	1.857	1.945	-	1.945	1.933
0.1	-	-	1.827	1.819	1.930	1.919	2.143	2.064
0.2	6.034	7.229	1.891	1.881	2.135	2.058	1.750	2.062
0.3	5.057	5.760	2.116	2.052	1.845	1.836	1.678	1.672
0.4	4.350	4.839	2.099	2.034	1.798	1.791	1.925	1.899
0.5	3.840	4.193	2.154	2.048	1.758	1.752	1.872	1.848
0.6	3.457	3.730	2.357	2.192	1.722	1.717	1.789	1.766
0.7	3.161	3.377	2.382	2.269	1.683	1.679	1.704	1.681
0.8	2.927	3.105	2.287	2.197	1.638	1.635	1.641	-
0.9	2.738	2.885	2.157	2.077	1.585	1.583	1.601	-
1.0	2.583	2.709	2.035	1.962	1.531	1.529	1.572	-
ME	0.409		-0.071		0.015		0.084	

pendicular paramagnetic bonding in the presence of stronger magnetic fields. MOM was unable to quantitatively reproduce this bonding and gave erroneously long distances for all fields, although some paramagnetic bonding was still observed. This is consistent with the analysis of Section 3.5, particularly Figure 3.8, which showed HF theory to underestimate paramagnetic bonding, and consequently that correlation energy is important for a quantitative description of paramagnetically bound systems.

The s $= 0$ state 3 presents a difficult case for equilibrium distance prediction, giving a complex energy surface with a double minimum structure. At increasing field strengths the longer ranged minimum is stabilised and moves to shorter R, becoming the sole energy minimum at $B_\perp \approx 0.2$. The merging of the two minima corresponds to a sharp increase in equilibrium distance as the two minima coalesce, followed by a shortening in stronger fields. Table 5.3 and Figure 5.2 reveal that this behaviour is not well described by MOM, though in general the correct qualitative increase in equilibrium followed by decrease at > 0.2 a.u. is observed. Excepting the problematic case of the s $= 0$ state 3, MOM gives accurate equilibrium distances with states showing the correct behaviour as field strengths increase with small systematic errors.

5.3 Concluding remarks

The analysis in this chapter provides compelling evidence that, for the H_2 molecule at least, the MOM protocol functions as well in the presence of a magnetic field as it does in the absence of a field [173]. The MOM protocol is able, in most cases, to drive the convergence of the SCF procedure to a singly excited state when a suitably close set of guess MOs are provided. MOM therefore presents a simple method for using single determinant theories for examining the excited states of molecular systems in the presence of a strong magnetic field.

The MOM method is not without limitation however and care must be taken in regions where many electronic states come together. Such problematic regions have a tendency to become more common in the presence of a magnetic field as the field effects cause previously separated states to come together in energy. Where such problematic regions lie is *a priori* unknown and strongly system dependent. To some extent this difficulty can be mitigated by adding a restriction on total electronic spin alongside the MOM criteria. In this way the number of available occupations are reduced and the spin Zeeman shift controlled. One must also be careful with the MOM method that the final converged state truly is the state of interest and that the SCF has not collapsed to a nearby state with similar characteristics. This need for care is highlighted by the collapse of the MOM-RHF protocol from state 4 to state 3 for s $= 1$ $B_\perp = 0$ and 0.2 a.u. It should be noted that these limitations are also present for standard zero field MOM methods, but may be expected to be somewhat more frequently encountered where magnetic field induced state crossings are common.

The preceding investigation has been carried out exclusively with HF theory and as such does not capture any of the correlation energy of the system. The analysis of paramagnetically bound systems with CDFT functionals in Section 3.5 shows that correlated methods are essential for the accurate description of paramagnetic bonding and the electronic structure of larger systems. Combining the analysis of MOM presented here and the ground state CDFT analysis of Chapter 3 suggests that MOM-CDFT could prove a promising route to a correlated description of excited states in strong magnetic fields, without recourse to expensive wave function methods. As the SCF procedure for CDFT is nearly identical to that of HF the implementation of MOM into existing CDFT programs is expected to be trivial. A repeat of the preceding analysis with the cTPSS functional is encouraged as future investigation and is expected to produce greater agreement with FCI benchmark. In particular an improved description of the lowest s $= 0$ state at low field, and the s $= 1$ ground state at strong fields, can be expected as a result of the correlation included in the cTPSS functional.

Chapter 6

Potential Based Density Functional Theory

The remainder of this thesis moves away from the complications of systems under the influence of magnetic fields and considers instead the potentials and orbitals at the heart of field-free Kohn–Sham density-functional theory. A theoretical extension to the standard structure of KS-DFT, the optimised effective potential (OEP) method, can provide a structure for handling fully orbital dependent functionals allowing a greater accuracy for density-functional approximations as well as facilitating greater theoretical understanding of DFT through the Lieb maximisation and Gidopolous variation principle. This Chapter describes the theory and operation of the OEP method and details how the optimised potential can be used to investigate key DFT relations.

6.1 Limitations of the generalised gradient expansion

The impact of standard KS-DFT cannot be understated and the availability of high quality XC functionals has resulted in DFT being by far the most widely used quantum chemical method. Despite these successes there remain a number of systems for which the LDA, GGA and mGGA functional forms can only offer a fundamentally limited description. An exploration of these failings and their origins serves to highlight the limitations of local XC functionals and the potential advantages of orbital dependent XC functionals.

6.1.1 Anions and the lack of Rydberg states

All XC functionals constructed solely around the generalised gradient expansion give a poor description of negative ions. This arises naturally from a failure of local exchange potentials to correctly support the Rydberg series required to bind additional electrons. Negative ions and Rydberg states are a common feature in atmospheric processes and form the building blocks of common salts; a failure in their description presents a stark limitation for DFT methods.

To understand the correct form of the exchange potential, v_{x}, and how this limitation may be corrected consider a simple two electron system, the helium atom. As discussed in Section 1.2, there is no exchange interaction between electrons with opposite spin and the exchange energy for this system only has to cancel the spurious self-interaction included in the Hartree term. To achieve the correct cancellation of Eq. (1.12) the exchange energy must be,

$$E_{\mathrm{x}}^{\mathrm{He}}[\rho] = -\frac{1}{4}\iint \frac{\rho(\mathbf{r})\rho(\mathbf{r}')}{|\mathbf{r}-\mathbf{r}'|}\mathrm{d}\mathbf{r}'\,\mathrm{d}\mathbf{r}. \tag{6.1}$$

The corresponding exchange potential is the trivial functional derivative, giving the non-local exchange potential,

$$v_{\mathrm{x}}^{\mathrm{He}}(\mathbf{r}) = -\frac{1}{2}\int \frac{\rho(\mathbf{r}')}{|\mathbf{r}-\mathbf{r}'|}\mathrm{d}\mathbf{r}', \tag{6.2}$$

with a decay in the asymptotic limit $r \to \infty$ of,

$$v_{\mathrm{x}}^{\mathrm{He}}(\mathbf{r}) \underset{r\to\infty}{\to} -\frac{1}{|\mathbf{r}|}. \tag{6.3}$$

The $-1/r$ decay of the helium exchange potential has a simple physical origin, as an electron is moved far from the core the nucleus and remaining $N-1$ electrons coalesce to a point charge, the potential of which must decay as $-1/r$. The Coulomb potential corresponding to Eq. (1.12) experienced by the remote electron still contains the self repulsion between the distant electron and itself. This self repulsion is clearly non-physical and must be cancelled by an equivalent self exchange interaction. Failing to cancel self interaction raises the energy of an electron far from the nucleus and prevents a Rydberg series forming, seen as the KS virtual orbitals becoming too high lying.

The (semi-)local density dependence in LDA and GGA XC functionals is unable to produce an exchange potential that has both correct near nucleus behaviour and $-1/r$ asymptote, a failure most simply seen for the LDA exchange potential,

$$v_{\mathrm{x}}^{\mathrm{LDA}}(\mathbf{r}) = -\frac{(3\pi^2)^{\frac{1}{3}}}{\pi}\rho(\mathbf{r})^{\frac{1}{3}}, \tag{6.4}$$

which decays asymptotically with the density,

$$\rho(\mathbf{r}) \underset{r\to\infty}{\to} e^{-\alpha r} \;\Rightarrow\; v_{\mathrm{x}}^{\mathrm{LDA}}(\mathbf{r}) \underset{r\to\infty}{\to} e^{-\alpha\frac{r}{3}}. \tag{6.5}$$

The decay of $v_{\mathrm{x}}^{\mathrm{LDA}}(\mathbf{r})$ is tied to the decay of the density, and hence it has exponential like decay, which is faster than $-1/r$, and fails to cancel self interaction. The inclusion of gradient terms into GGA functionals can change the asymptotic behaviour, but the potential remains (semi-)local in nature and unable to properly match the non-local Coulomb interaction.

The correct $-1/r$ asymptote in $v_{\mathrm{x}}(\mathbf{r})$ can be restored if the exchange functional is chosen as the exact Kohn–Sham exchange functional,

$$E_{\mathrm{x}}[\{\varphi\}] \equiv -\frac{1}{2}\sum_{i,j=1}^{\mathrm{occ.}}\iint \frac{\varphi_i^*(\mathbf{r})\varphi_j(\mathbf{r})\varphi_j^*(\mathbf{r}')\varphi_i(\mathbf{r}')}{|\mathbf{r}-\mathbf{r}'|}\mathrm{d}\mathbf{r}\mathrm{d}\mathbf{r}', \tag{6.6}$$

derived as the Fock expression of Eq. (1.13) applied to the Kohn–Sham orbitals. This fully non-local exchange functional ensures that the resulting exchange potential is able to match the asymptotic behaviour of the Coulomb integral and support a Rydberg series.

6.1.2 Dispersion forces

In a model system comprised of two neutral atoms positioned such that there is no overlap of electron densities and no external electrostatic interaction, there can be no classical attractive forces between the two atoms. The real system of separated atoms do, however, experience a weak attractive interaction through the virtual dipole excitations associated with the London dispersion force.[1]

The London dispersion phenomenon cannot be properly described by generalised gradient expansion XC functionals, a failure with a similar origin to the absence of negative ions, though this time the fault lies in the 'short sighted' correlation functional. The lack of a natural description of dispersion in LDA and GGA functionals has led to the creation of many empirical correction schemes to extend GGA functionals to include approximate dispersion forces [174–176].

To understand the absence of dispersion in LDA and GGA functionals, consider again the system of isolated atoms and recall that there is no overlap of electron densities. The LDA and GGA correlation functionals depend only on the density and its derivatives at a point and have the general form,

$$E_{\mathrm{c}}^{\mathrm{GGA}}[\rho,\nabla\rho] = \int \epsilon_{\mathrm{c}}^{\mathrm{GGA}}(\rho(\mathbf{r}),|\nabla\rho(\mathbf{r})|^2)\mathrm{d}\mathbf{r}, \tag{6.7}$$

[1] Discovered by, and named after, the same Prof. Fritz London who derived the gauge including atomic orbitals key to Section 2.1.4. The London dispersion forces are also commonly referred to as *van-der-Waals* forces.

in which ϵ_c is the correlation energy density of the given functional. This correlation energy density can only be sensitive to the electron density at a point and its immediate vicinity. As a result the long range correlations due to instantaneous dipoles that exist between the separated atoms cannot be captured. A non-local form for the correlation functional is required if the long range correlations that produce London dispersion are to be correctly incorporated. Unlike the exact exchange functional, no computationally tractable form for an exact non-local correlation functional is known, though a number of approximate forms have been produced [177–179].

6.2 The optimised effective potential

Kohn–Sham theory (Section 1.6) can be seen as extending the Thomas–Fermi model by using the orbital dependent $T_s[\{\varphi_i\}]$ functional to recover the majority of the electronic kinetic energy exactly. A similar strategy is now adopted for the exchange and correlation energies, reformulating them as functionals of the KS orbitals and eigenvalues.

In order to use an orbital dependent XC functional within the KS scheme the associated multiplicative exchange-correlation potential $v_{xc}(\mathbf{r})$ must be derived in the Kohn-Sham equations,

$$\left[\frac{1}{2}\nabla^2 + v_s(\mathbf{r})\right]\varphi_p = \epsilon_p\varphi_p, \tag{6.8}$$

with $v_{xc}(\mathbf{r})$ entering through the one electron potential,

$$v_s(\mathbf{r}) = v_{ext}(\mathbf{r}) + v_J(\mathbf{r}) + v_{xc}(\mathbf{r}). \tag{6.9}$$

For LDA and GGA type functionals the XC potential is formed as a direct functional derivative with respect to the density,

$$v_{xc}(\mathbf{r}) \equiv \frac{\delta E_{xc}}{\delta\rho(\mathbf{r})}. \tag{6.10}$$

The equivalent potential is not so simply constructed for an orbital dependent XC functional and the chain rule for functional derivatives must be applied instead [177],

$$\frac{\delta E_{xc}[\{\varphi_p,\epsilon_p\}]}{\delta\rho(\mathbf{r})} = \int\frac{\delta v_s(\mathbf{r}')}{\delta\rho(\mathbf{r})}\sum_p\left\{\int\left[\frac{\delta\varphi_p^\dagger(\mathbf{r}'')}{\delta v_s(\mathbf{r}')}\frac{\delta E_{xc}}{\delta\varphi_p^\dagger(\mathbf{r}'')} + \text{c.c.}\right]\mathrm{d}\mathbf{r}'' + \frac{\delta\epsilon_p}{\delta v_s(\mathbf{r}')}\frac{\partial E_{xc}}{\partial\epsilon_p}\right\}\mathrm{d}\mathbf{r}', \tag{6.11}$$

where the summation p runs over both occupied and virtual orbitals. Although initially Eq. (6.11) appears unwieldy it can be written in terms of readily identified familiar quantities.

The functional derivatives $\delta\epsilon_p/\delta v_s$ and $\delta\varphi_p^\dagger/\delta v_s$ are available from first order perturbation theory as

$$\frac{\delta\epsilon_p}{\delta v_s(\mathbf{r})} = \varphi_p^\dagger(\mathbf{r})\varphi_p(\mathbf{r}) \tag{6.12}$$

$$\frac{\delta\varphi_p^\dagger(\mathbf{r})}{\delta v_s(\mathbf{r}')} = -\varphi_p^\dagger(\mathbf{r}')G_p(\mathbf{r}',\mathbf{r}) \tag{6.13}$$

where $G_p(\mathbf{r},\mathbf{r}')$ is the Green's function

$$G_p(\mathbf{r},\mathbf{r}') = \sum_{q\neq p}\frac{\varphi_q(\mathbf{r})\varphi_q^\dagger(\mathbf{r}')}{\epsilon_q-\epsilon_p}. \tag{6.14}$$

The factor $\delta v_s/\delta\rho$ is the inverse of the Kohn–Sham static response function,

$$\frac{\delta\rho(\mathbf{r})}{\delta v_s(\mathbf{r}')} \equiv \chi_s(\mathbf{r},\mathbf{r}') = -\sum_p\varphi_p^\dagger(\mathbf{r})G_p(\mathbf{r},\mathbf{r}')\varphi_p(\mathbf{r}') + \text{c.c.} \tag{6.15}$$

Multiplying Eq. (6.11) by χ_s and integrating over $\mathbf{r}'$ produces the OEP integral equation,

$$\int\chi_s(\mathbf{r},\mathbf{r}')v_{xc}(\mathbf{r}')\mathrm{d}\mathbf{r}' = \Lambda_{xc}(\mathbf{r}), \tag{6.16}$$

in which the remaining terms have been collected into Λ_{xc}, the inhomogeneity function,

$$\Lambda_{\mathrm{xc}}(\mathbf{r}) = \sum_p \left\{ - \int \left[\varphi_p^\dagger(\mathbf{r}) G_p(\mathbf{r}, \mathbf{r}') \frac{\delta E_{\mathrm{xc}}}{\delta \varphi_p^\dagger(\mathbf{r}')} + c.c. \right] \mathrm{d}\mathbf{r}' + |\varphi_p(\mathbf{r})|^2 \frac{\partial E_{\mathrm{xc}}}{\partial \epsilon_p} \right\}. \tag{6.17}$$

The remaining differential terms in Λ_{xc} are determined by the chosen form of the XC functional as the appropriate derivatives.

Eq. (6.16) is recognised in mathematics as a Fredholm integral equation of the first kind. These integral equations are well known for becoming problematic when reduced to a discrete form, giving rise to discrete ill-posed problems. The analytical solution of Eq. (6.16) is unknown and it is necessary to resort to numerical grid or finite basis techniques for its solution. The numerical solution of Eq. (6.16) is only possible for very simple systems and consequently finite basis expansion techniques are more generally applicable. A finite basis expansion results in a discretisation of the continuous Fredholm integral equation and, as expected, suffers severe numerical difficulties. A discussion of these difficulties is delayed to Chapter 7, wherein a comprehensive analysis of the problems and their regularisation is given. The rest of this chapter details an implementation of the Yang–Wu finite basis OEP method and discusses the insights that may be gained from its applications.

6.2.1 The exact exchange functional

The OEP scheme can be applied to any choice of XC functional to produce a multiplicative potential suitable for the Kohn-Sham equations, for LDA and GGA functionals the standard KS potential and the OEP are the same. The mGGA and hybrid functionals discussed in Section 1.7 and Chapter 2 however, have orbital dependent components and should be handled through an OEP scheme to remain strictly within the KS framework. Though, as discussed in Section 1.7.3, the computationally convenient use of orbital specific potentials is often employed instead, as this provides an approximation that is close enough for most applications.

It is instructive for the development of the OEP method and understanding of the surrounding numerical issues to give special attention to the KS exact exchange functional, which is written as the HF exchange operator applied directly to the KS orbitals, shown in Eq. (6.6). Although the orbital dependent KS exact exchange functional is the same as the HF exchange integral the HF exchange energy and OEP exact exchange energy are not the same quantity, a difference that originates in the orbitals that each quantity is constructed from. The exact exchange OEP orbitals are those that solve the KS equations with the multiplicative potential v_{s}, whilst the HF orbitals are those that minimise the HF equations with the non-local exchange potential. By the variational principle, the exact exchange OEP energy must always be above the HF energy, with a difference that is absorbed into E_c.

The exchange only functional is unique in that an accurate solution has been derived using a numerical grid method for atomic systems, detailed in Section 6.2.2, giving the exact exchange potential in the complete basis limit. In addition to having an exact atomic solution, a number exact conditions for the exchange only OEP are known and are discussed in Section 7.9, with four being of special interest in this work. The work of Chapter 7 makes use of these exact features as diagnostic tools for assessing the quality of finite basis OEPs and the effectiveness of regularisation methods.

6.2.2 Numerical solution for the exact exchange potential

The exchange only OEP problem as derived in Section 6.2 was first solved for atomic systems by Talman and Shadwick using a set of self consistent equations evaluated on a numerical grid [180]. The method exploits the spherical symmetry of atomic species to reduce the problem to purely radial equations amenable to solution on a 1D grid. The separation of variables to eliminate angular terms is impossible for species of lower symmetry resulting in more complicated equations, though an implementation for diatomic molecules exploiting cylindrical symmetry is presented in Ref. [181].

An implementation of the Talman–Shadwick numerical procedure for the spherical solution of the exact exchange OEP [180] was available in this work and was used to provide benchmark potentials

in the complete basis limit. The spherical symmetry exhibited by the numerical potentials is correct for all atomic systems though for open shell atoms the symmetry is only observed due to an averaging of multiple degenerate electronic states. As a result, single reference Kohn–Sham OEP calculations are unable to produce comparable potentials for open shell atoms without an explicit averaging of multiple states. Such averaging is not considered in this work, so the numerical benchmark potentials are only available for the lighter closed shell atoms: He, Be, Ne, Mg, Ar and Ca.

6.3 The finite basis OEP problem

For the general case of polyatomic molecules the lack of exploitable symmetry renders a purely numerical solution computationally intractable and the OEP problem must be represented in a finite basis. Within a finite basis representation, the complicated three-dimensional integral equations of Eq. (6.16) are reduced to a set of linear integral equations that can be solved directly to give the optimised potential [177]. Unfortunately the solution of these equations requires the inversion of the discretised response function, χ_{s}, the matrix representation of which is nearly singular. The solution of the resulting matrix equations becomes ill defined and the problem is *ill-posed*. The badly conditioned response matrix poses serious numerical difficulties [182] and it is shown in Ref. [183] that an infinite number of solution potentials $v_{\mathrm{xc}}(\mathbf{r})$ can be formed for any single finite basis OEP problem. In the same work, Hirata *et al.* give a method for projecting out the problematic degrees of freedom to give a regularised OEP problem with a single solution. They note however that the method converges too slowly with orbital basis size to be of use in practical calculations.

In a series of papers [184–186] Yang and Wu (YW) present a finite basis optimisation scheme in which the potential is expanded in a finite basis set of GTO functions weighted by a set of expansion coefficients. The YW scheme improves on other coefficient optimisation based OEP methods [187,188] by providing a computationally tractable optimisation scheme with analytical first and second derivatives, allowing the use of classical optimisation techniques. The core of its success revolves around the use of a fixed reference potential to enforce desired long range characteristics, combined with a linear combination of GTOs, well suited for use in most DFT codes.

6.3.1 The Yang–Wu optimised effective potential scheme

The Yang–Wu finite basis expansion of v_{s} is given as,

$$v_{\mathrm{s}}^{\sigma}(\mathbf{r}) = v_{\mathrm{ext}}(\mathbf{r}) + v_0^{\sigma}(\mathbf{r}) + \sum_t b_t^{\sigma} g_t(\mathbf{r}) \tag{6.18}$$

where $v_{\mathrm{ext}}(\mathbf{r})$ is the external potential, $v_0^{\sigma}(\mathbf{r})$ is the reference potential and $\{g_t\}$ is a basis set of GTO functions (termed the potential basis) weighted by the coefficients $\{b_t^{\sigma}\}$.

The reference potential $v_0^{\sigma}(\mathbf{r})$ is the key component to the YW expansion, accounting for as much of the Coulomb potential as possible in a fixed function and avoiding the non-linear dependence of the v_{J} term on the basis set, thus allowing a simple evaluation of the expansion coefficient derivatives. A popular choice of reference potential is the Fermi–Amaldi potential calculated for a fixed reference density $\rho_0(\mathbf{r})$,

$$v_{\mathrm{FA}}(\mathbf{r}) = \frac{N-1}{N} \int \frac{\rho_0(\mathbf{r}')}{|\mathbf{r}-\mathbf{r}'|} \mathrm{d}\mathbf{r}', \tag{6.19}$$

as it captures much of the Coulomb potential [189]. The same choice is made in this work, using v_{FA} calculated from a core Hamiltonian (Eq. (1.11)) or Hartree–Fock guess density. The exact reference density used was found to have a strong influence over the final quality of $v_{\mathrm{xc}}(\mathbf{r})$ and as such the reference potential was in practice constructed from the more accurate Hartree–Fock density calculated for the same system.

Expanded in this way the OEP can be determined as the one electron potential of Eq. (6.18) with $\{b_t^{\sigma}\}$ chosen such that the orbitals determined through Eq. (6.8) minimise the energy, $E[\{\varphi_i\}]$. All terms are fixed in Eq. (6.18) except $\{b_t^{\sigma}\}$ so the derivative of $v_{\mathrm{s}}^{\sigma}(\mathbf{r})$ with respect to a change in the

coefficients is simply,

$$\frac{\partial v_{\mathrm{s}}^{\sigma}(\mathbf{r})}{\partial b_t^{\sigma}} = g_t(\mathbf{r}). \tag{6.20}$$

The analytical derivatives for the total energy with respect to a change in $\{b_t^{\sigma}\}$ are then determined by perturbation theory with the first derivative given as,

$$\frac{\partial E[\{\varphi_{i\sigma}\}]}{\partial b_t^{\sigma}} = \sum_{i}^{\text{occ.}} \sum_{a}^{\text{virt.}} \int \frac{\delta E[\{\varphi_{i\sigma}\}]}{\delta \varphi_{i\sigma}^{*}(\mathbf{r})} \varphi_{a\sigma}(\mathbf{r}) \frac{\langle \varphi_{a\sigma} | g_t | \varphi_{i\sigma} \rangle}{\epsilon_{i\sigma} - \epsilon_{a\sigma}} \mathrm{d}\mathbf{r} + \text{c.c.} \tag{6.21}$$

where the summations in i and a are over the occupied and virtual orbitals respectively.

The exact analytical form of the second derivative Hessian matrix is known but difficult to compute in practice [190], instead this difficulty is avoided with the use of an approximate Hessian that gives an adequate descent direction. By considering the gradient given in Eq. (6.21) and freezing the KS orbitals (assuming they have only a weak dependence on $\{b_t^{\sigma}\}$) an approximate positive definite Hessian is formed as,

$$\frac{\partial^2 E}{\partial b_u^{\sigma} \partial b_t^{\sigma}} \approx \tilde{H}_{ut}^{\sigma} = -\sum_{i}^{\text{occ.}} \sum_{a}^{\text{virt.}} \frac{\langle \varphi_{a\sigma} | g_u | \varphi_{i\sigma} \rangle \langle \varphi_{a\sigma} | g_t | \varphi_{i\sigma} \rangle}{\epsilon_{i\sigma} - \epsilon_{a\sigma}} + \text{c.c.} \tag{6.22}$$

Given the first and second derivatives of Eq. (6.21) and Eq. (6.22) the coefficients $\{b_t^{\sigma}\}$ can be optimised with a Newton method to produce the minimising OEP in which,

$$\frac{\partial E[\{\varphi_{i\sigma}\}]}{\partial b_t^{\sigma}} = 0, \tag{6.23}$$

for all t, giving the solution to the OEP problem.

The Newton optimisation method minimises the objective function through an iterative procedure constructing each subsequent point as,

$$\mathbf{b}^{*} = \mathbf{b} + \mathbf{p}, \tag{6.24}$$

with the step $\mathbf{p}$,

$$\tilde{\mathbf{H}}(\mathbf{b}) \cdot \mathbf{p} = -\mathbf{g}(\mathbf{b}), \tag{6.25}$$

constructed from $\tilde{\mathbf{H}}(\mathbf{b})$ and $\mathbf{g}(\mathbf{b})$, the approximate Hessian matrix and gradient vector respectively. The coefficient vector is iteratively updated through Eq. (6.24) and Eq. (6.25) until the convergence tolerance on Eq. (6.23) is reached.

6.4 Computational methods

The YW-OEP method has been presented so far in terms of a minimisation of the electronic energy through the variation of the effective potential coefficients. This forms the basis for the the solution of KS-DFT and has clear practical utility for the application of orbital dependent functionals. There are however a number of closely related problems in DFT with very similar forms to this that require the optimisation of an effective potential for their solution. These problems all require the minimisation of an objective function $\Omega(\{b_t\})$, for which the gradient, $\mathbf{g}_{\Omega}(\{b_t\})$, and Hessian matrix, $\mathbf{H}_{\Omega}(\{b_t\})$, are known. Hence they can be optimised using the Newton method by adjusting $\{b_t\}$ to minimise the value returned by $\Omega(\{b_t\})$, the objective function score.

The YW potential expansion optimisation scheme was implemented into our in-house quantum chemistry package QUEST [191]. Structured around a purpose built Newton optimiser, the program was designed as a general framework for solving OEP problems and potential based DFT methods. With this generic construction the QUEST OEP module could be used to implement and optimise arbitrary OEP objective functions with ease. By establishing this common framework, the regularisation techniques developed in Chapter 7 could be applied to all potential based DFT problems (all of which by definition *must* be ill-posed) with little additional programming. Throughout the course of the work

the QUEST OEP module was used to investigate the regularisation of the OEP problem in the context of the exact exchange functional as well as the related problems of solving the Lieb maximisation (Section 6.4.2) and understanding the Gidopolous variational principle (Section 6.4.3).

All the problems considered here require the choice of two basis sets for their solution, a potential basis for the WY expansion, and an orbital basis for expansion of the KS orbitals. The two basis sets are far from independent, with the quality of the potential and orbitals being intimately linked through the objective functions. The QUEST OEP module makes use of standard quantum chemistry GTO basis sets for both the orbital and potential basis and allows the runtime construction of arbitrary even tempered basis sets defined as,

$$\chi(\mathbf{r}) = \beta \cdot \exp[-\alpha^{\{i\ldots j\}}||\mathbf{r}||^2] \tag{6.26}$$

where β is a constant pre-factor and $\alpha^{\{i\ldots j\}}$ is a base α raised to the power of the range of integers between i and j inclusive.

The following sections discuss the form of the objective functions investigated during the course of this work, solved through the QUEST OEP module.

6.4.1 Orbital dependent exchange-correlation functionals

The objective function for solving the KS-DFT equations with an orbital dependent XC functional begins by forming an OEP Fock matrix using the molecular orbitals and the set of potential coefficients $\{b_t\}$,

$$F^{\mathrm{OEP}}_{\nu\mu}[\{b_t\}] = T_{\nu\mu} + V^{\mathrm{nuc.}}_{\nu\mu} + V^{0}_{\nu\mu} + \sum_t b_t \left\langle \chi_\nu | g_t | \chi_\mu \right\rangle , \tag{6.27}$$

where ϕ_ν and ϕ_μ are Gaussian basis functions and $V^0_{\nu\mu}$ is the Fermi–Amaldi matrix (Eq. (6.19)). The OEP Fock matrix is then diagonalised to produce a new set of orbitals that solve Eq. (6.8). These new orbitals are used to construct a standard Kohn–Sham Fock matrix using the orbital dependent exchange-correlation functional. The energy, and hence objective function score, is evaluated from this Fock matrix using standard techniques such that the orbital dependent Kohn–Sham energy expression is evaluated using the orbitals that diagonalise the OEP Fock matrix.

The energy gradient with respect to the expansion coefficients is evaluated through Eq. (6.21), requiring an expression for the functional derivative of the exchange-correlation functional with respect to the orbitals, and partial derivative with respect to the orbital eigenvalues. In the case of exact exchange this is simply the exact exchange potential formed by applying the exchange operator of Eq. (1.20) to the OEP orbitals,

$$\frac{\delta E_{\mathrm{x}}}{\delta \varphi_i^\dagger(\mathbf{r}')} = -\sum_i^{\mathrm{occ.}} \varphi_i(\mathbf{r}') \int \frac{\varphi_j^*(\mathbf{r})\varphi_i(\mathbf{r})}{|\mathbf{r}-\mathbf{r}'|}\mathrm{d}\mathbf{r}', \quad \frac{\partial E_{\mathrm{x}}}{\partial \epsilon_i} = 0. \tag{6.28}$$

The objective Hessian is determined by the frozen orbital approximation for any choice of orbital dependent functional and is constructed from Eq. (6.22).

6.4.2 The Lieb maximisation

The definition of DFT through the Legendre–Fenchel transformation (Section 1.5.6) frames DFT through a pair of dual functionals, the energy functional Eq. (1.122) and the Lieb functional Eq. (1.121). The standard task of a DFT calculation is to evaluate the energy functional and is achieved using the conventional KS SCF cycle (Section 1.6) or with the OEP method discussed above; the electron density is optimised for a given potential. The general framework for the OEP implemented in QUEST allows the solution to the dual problem: the optimisation of the effective potential for a given density, evaluating the Lieb functional.

The wave function methods of Section 1.4 allow systematically increasing accuracy and can, with great computational cost, produce electron densities that are highly accurate. Whilst the cost associated is too great for such methods to be applied to large systems they are invaluable for providing insight

into how the approximations may be improved. Through a maximisation[2] of the Lieb functional, the effective potential that gives the highly accurate input density is obtained.

The most general form of this procedure is the full Lieb maximisation that allows for arbitrary interaction strengths between the electrons of the model system. It is instructive however to first consider the special case of the Lieb maximisation where the input density is reproduced with a model system of non-interacting electrons. This case was derived by Wu and Yang in Ref. [186] and is known as the Wu–Yang (WY) method.

The Wu–Yang method

For a given input density the Kohn–Sham non-interacting kinetic energy can be determined as,

$$T_{\mathrm{S}}[\rho_{\mathrm{in}}] = \min_{\Psi_{\mathrm{SD}} \to \rho_{\mathrm{in}}} T[\Psi_{\mathrm{SD}}] \tag{6.29}$$

where Ψ_{SD} is a Slater determinant of $N/2$ doubly occupied one electron orbitals $\{\varphi_i\}$. The Slater determinant is minimised under the constraint that it yields the input density by means of a Lagrange multiplier function $v(\mathbf{r})$, the potential, giving the objective function,

$$W_{\mathrm{S}}[\Psi_{\mathrm{SD}}, v(\mathbf{r})] = 2\sum_{i}^{N/2} \left\langle \varphi_i \middle| \hat{T} \middle| \varphi_i \right\rangle + \int \{\rho_{\mathrm{SD}}(\mathbf{r}) - \rho_{\mathrm{in}}(\mathbf{r})\} v(\mathbf{r}) \mathrm{d}\mathbf{r}, \tag{6.30}$$

where the orbitals are solutions to a KS-like set of linear eigenvalue equations for a fixed $v(\mathbf{r})$,

$$\left[\hat{T} + v(\mathbf{r})\right] \varphi_p = \epsilon_p \varphi_p. \tag{6.31}$$

The objective functional of Eq. (6.30) may be written in terms of the potential $v(\mathbf{r})$ and hence, through the WY potential expansion, in terms of $\{b_t\}$,

$$\begin{aligned} W_{\mathrm{S}}[\Psi_{\mathrm{SD}}[\{b_t\}], \{b_t\}] = 2\sum_{i}^{N/2} \left\langle \varphi_i \middle| \hat{T} \middle| \varphi_i \right\rangle + \int \{v_{\mathrm{ext}}(\mathbf{r}) + v_0(\mathbf{r})\} \{\rho(\mathbf{r}) - \rho_{\mathrm{in}}(\mathbf{r})\} \mathrm{d}\mathbf{r} \\ + \int \sum_t b_t g_t(\mathbf{r}) \{\rho(\mathbf{r}) - \rho_{\mathrm{in}}(\mathbf{r})\} \mathrm{d}\mathbf{r}. \end{aligned} \tag{6.32}$$

The first derivative of this objective function is given by,

$$\frac{\delta W_{\mathrm{S}}[\Psi_{\mathrm{SD}}[\{b_t\}], \{b_t\}]}{\delta b_t} = \int \{\rho(\mathbf{r}) - \rho_{\mathrm{in}}(\mathbf{r})\} g_t(\mathbf{r}) \mathrm{d}\mathbf{r}, \tag{6.33}$$

showing that T_{S} is optimised when the density constraint is satisfied. The second functional derivative was shown by WY to be,

$$\frac{\delta^2 W_{\mathrm{S}}[\Psi_{\mathrm{SD}}[\{b_t\}], \{b_t\}]}{\delta b_u \delta b_t} = 2\sum_{i}^{\mathrm{occ.}} \sum_{a}^{\mathrm{virt.}} \frac{\langle \varphi_i | g_u(\mathbf{r}) | \varphi_a \rangle \langle \varphi_a | g_t(\mathbf{r}) | \varphi_i \rangle}{\epsilon_i - \epsilon_a} + \mathrm{c.c.} \tag{6.34}$$

As the second functional derivative of the WY functional is necessarily ≤ 0 for any variation in $v(\mathbf{r})$ the WY functional must be concave in $v(\mathbf{r})$. The WY objective functional can be used in an unconstrained maximisation with respect to the potential coefficients,

$$T_{\mathrm{S}}[\rho_{\mathrm{in}}] = \max_{\{b_t\}} W_{\mathrm{S}}[\Psi_{\mathrm{SD}}[\{b_t\}], v(\{b_t\}, \mathbf{r})], \tag{6.35}$$

yielding the non-interacting kinetic energy.

Equations (6.32), (6.33) and (6.34) are the working equations for the implementation in the QUEST OEP module, allowing calculation the set of non-interacting KS orbitals that correspond to the input density ρ_{in}.

[2] Any maximisation can also be performed by a minimisation algorithm using the negative of the objective functions.

The Lieb maximisation

The WY method is a special case of the more general Lieb maximisation that allows for the evaluation of the DFT energy for a given input density. In the Lieb maximisation the electron-electron interaction strength is scaled by the parameter $\lambda \geq 0$,[3] allowing a family of λ-interacting systems to be constructed from a fixed accurate input density [192–195], where the WY method is limited to the $\lambda = 0$ KS system.

The Lieb maximisation is built around a use of the convex Lieb functional (Theorem 1.5.13), constructed from Eq. (1.121) for the general Hamiltonian obeying $\hat{H}\Psi = E\Psi$. If the Hamiltonian is chosen to be the λ-interacting Hamiltonian,

$$\hat{H}_\lambda = \hat{T} + \lambda\hat{W} + \sum_i v_\lambda(\mathbf{r}_i), \tag{6.36}$$

where $\hat{W}$ is the two electron repulsion operator and v_λ is the potential that constrains the density to the real interacting density. A ground state energy $E_\lambda[v_\lambda]$ can then be constructed that is concave in $v_\lambda(\mathbf{r})$ for all interaction strengths $\lambda \geq 0$.

A Lieb functional may then be constructed for a given interaction strength as the Legendre–Fenchel transform of $E_\lambda[v_\lambda]$,

$$F_\lambda[\rho] = \sup_{v_\lambda \in \mathcal{X}^*} \left(E_\lambda[v_\lambda] - \int v_\lambda(\mathbf{r})\rho(\mathbf{r})\mathrm{d}\mathbf{r} \right). \tag{6.37}$$

As discussed in Section 1.5.6 the convex conjugate of F_λ recovers the energy functional if $-E_\lambda[v_\lambda]$ is concave in v_λ. If this is not the case, then the convex envelope to $E_\lambda[v_\lambda]$, denoted $\bar{E}_\lambda[v_\lambda] = -E_\lambda[v_\lambda]^{**}$, is returned instead,

$$\bar{E}_\lambda[v_\lambda] = \inf_{\rho \in \mathcal{X}} \left(F_\lambda[\rho] + \int v_\lambda(\mathbf{r})\rho(\mathbf{r})\mathrm{d}\mathbf{r} \right) \tag{6.38}$$

for which the inequality $\bar{E}_\lambda[v_\lambda] \geq E_\lambda[v_\lambda]$ necessarily holds.

For an arbitrary value of $\lambda \geq 0$ the effective potential $v_\lambda(\mathbf{r})$ is the negative of the functional derivative of $F_\lambda[\rho]$ with respect to $\rho(\mathbf{r})$,

$$\begin{aligned} -v_\lambda(\mathbf{r}) &= \frac{\delta T_\mathrm{S}[\rho]}{\delta\rho(\mathbf{r})} + \lambda\frac{\delta J[\rho]}{\delta\rho(\mathbf{r})} + \lambda\frac{\delta E_\mathrm{x}[\rho]}{\delta\rho(\mathbf{r})} + \frac{\delta E_{\mathrm{c},\lambda}[\rho]}{\delta\rho(\mathbf{r})} \\ &= -v_\mathrm{S}(\mathbf{r}) + \lambda v_\mathrm{J}(\mathbf{r}) + \lambda v_\mathrm{x}(\mathbf{r}) + v_{\mathrm{c},\lambda}(\mathbf{r}) \end{aligned} \tag{6.39}$$

which can be expressed in terms of the WY-OEP expansion as,

$$v_\lambda(\mathbf{r}, \{b_t\}) = v_\mathrm{ext}(\mathbf{r}) + (1-\lambda)v_0(\mathbf{r}) + \sum_t b_t g_t(\mathbf{r}), \tag{6.40}$$

giving the Lieb objective functional as,

$$L_{\lambda,\rho}[\{b_t\}; \rho_\mathrm{in}] = E_\lambda[v_\lambda] - \int v_\lambda(\mathbf{r}, \{b_t\})\rho(\mathbf{r})\mathrm{d}\mathbf{r}. \tag{6.41}$$

Similarly to Eq. (6.30) this is a maximisation, however the same stationary potentials can be obtained by minimising $-L_{\lambda,\rho}[\{b_t\}; \rho_\mathrm{in}]$ instead.

The first derivative of $L_{\lambda,\rho}[\{b_t\}; \rho_\mathrm{in}]$ can be determined by analogy with Eq. (6.33) as,

$$\frac{\delta L_{\lambda,\rho}[\{b_t\}; \rho_\mathrm{in}]}{\delta b_t} = \int [\rho_{v_\lambda}(\mathbf{r}) - \rho_\mathrm{in}(\mathbf{r})] g_t(\mathbf{r})\mathrm{d}\mathbf{r}. \tag{6.42}$$

The Lieb Hessian matrix for an arbitrary interaction strength has the general form,

$$\frac{\delta^2 L_{\lambda,\rho}[\{b_t\}; \rho_\mathrm{in}]}{\delta b_t \delta b_u} = \iint g_t(\mathbf{r}) g_u(\mathbf{r}') \frac{\delta\rho_{v_\lambda}(\mathbf{r})}{\delta v_\lambda(\mathbf{r}')}\mathrm{d}\mathbf{r}\mathrm{d}\mathbf{r}', \tag{6.43}$$

requiring the careful evaluation of the $\frac{\delta\rho_{v_\lambda}(\mathbf{r})}{\delta v_\lambda(\mathbf{r}')}$ term, which can be achieved using the relaxed Lagrangian formulation of Helgaker and Jørgensen [196]. Alternatively, the frozen orbital Hessian of Eq. (6.22) may be used as an approximate Hessian, or supplied as a starting Hessian for first order schemes such as BFGS.

[3] Though normally only the range of $0 \leq \lambda \leq 1$ is considered.

6.4.3 The Gidopolous variational principle

An objective function is presented by Gidopolous in Ref. [13] constructed from an underlying theory which we will refer to as the Gidopolous variational principle. This section will show that the Gidopolous variational principle can be used to obtain the effective potential and Kohn–Sham orbitals corresponding to some input density ρ_{in} by minimising the kinetic correlation energy $T_{\text{c}} = T - T_{\text{s}}$. The Gidopolous functional is then shown to be intimately related to the Lieb functional, having the same derivatives and differing only by a constant, T_{c}, in the final value. This similarity has not been widely recognised and will be explored in the following paragraphs.

Consider the Hamiltonian operator $\hat{H}_0[v]$ that is a functional of some arbitrary multiplicative external potential $v(\mathbf{r})$ with the form,

$$\hat{H}_0[v] = \hat{T} + \hat{V}, \tag{6.44}$$

where $\hat{T}$ is the usual kinetic operator and $\hat{V} = \sum_i v(\mathbf{r}_i)$ is the multiplicative operator corresponding to the potential $v(\mathbf{r})$. The ground state wave function of this Hamiltonian must also be a functional of the potential and, for a system of non-interacting fermions, it is a single Slater determinant of orbitals $\{\varphi\}$ satisfying the one electron equations,

$$\left[\hat{T} + v(\mathbf{r})\right] \varphi_p = \epsilon_p \varphi_p. \tag{6.45}$$

The ground state density is $\rho_0(\mathbf{r}) = \sum_i |\varphi_i(\mathbf{r})|^2$, and the ground state energy is simply $E_0[v] = \sum_i \epsilon_i$, with the subscript 0 signifying a non-interacting system.

Gidopolous suggested a variational principle from this by simple application of the Rayliegh–Ritz variation principle (Theorem 1.5.1),

$$G_0[v; \Psi_{\text{in}}] = \left\langle \Psi_{\text{in}} \middle| \hat{H}_0[v] \middle| \Psi_{\text{in}} \right\rangle - E_0[v] \geq 0, \tag{6.46}$$

and noted that this variation principle was suggested by Davidson in another context [197]. The inequality holds because the physical interacting wave function Ψ_{in} will not in general be the ground state of the non-interacting Hamiltonian $\hat{H}_0$. The inequality of Eq. (6.46) will sharpen to an equality for one electron systems when $v(\mathbf{r})$ is chosen as the exchange only OEP, as in this case the two electron operator $\hat{W}$ then cancels, $\left\langle \Psi_{\text{in}} \middle| \hat{W} \middle| \Psi_{\text{in}} \right\rangle = J[\rho_{\text{in}}] + X[\{\varphi_i\}] = 0$ and Ψ_{in} is indeed a single Slater determinant. For systems with $N > 1$, the inequality becomes strict as Ψ_{in} cannot be a single determinant wave function, so cannot be the ground state of $\hat{H}_0[v]$.

To understand the role of the Gidopolous variational principle and derive a set of objective functions suitable for solution by OEP-DFT, we consider the structure of $G[v; \rho_{\text{in}}]$ in terms of an input density,

$$\begin{aligned} G_0[v; \rho_{\text{in}}] &= \left\langle \Psi_{\text{in}} \middle| \hat{H}_0[v] \middle| \Psi_{\text{in}} \right\rangle - \left\langle \Psi_0 \middle| \hat{H}_0[v] \middle| \Psi_0 \right\rangle \\ &= \left\langle \Psi_{\text{in}} \middle| \hat{T} \middle| \Psi_{\text{in}} \right\rangle + (v|\rho_{\text{in}}) - \left\langle \Psi_0 \middle| \hat{T} \middle| \Psi_0 \right\rangle - (v|\rho_0) \\ &= T[\rho_{\text{in}}] - T[\rho_0] - (v|\rho_{\text{in}} - \rho_0) \\ &\geq 0. \end{aligned} \tag{6.47}$$

Showing,

$$G_0[\{b_t\}; \rho_{\text{in}}] = T[\rho_{\text{in}}] - T[\rho_0] - \sum_t b_t \int [\rho_0(\mathbf{r}) - \rho_{\text{in}}(\mathbf{r})] g_t(\mathbf{r}) \mathrm{d}\mathbf{r} \tag{6.48}$$

as the objective function to be minimised. The first derivative of Eq. (6.48) is,

$$\frac{\partial G_0[\{b_t\}; \rho_{\text{in}}]}{\partial b_t} = \int [\rho_{\text{in}}(\mathbf{r}) - \rho_0(\mathbf{r})] g_t(\mathbf{r}) \mathrm{d}\mathbf{r}, \tag{6.49}$$

with the second derivative being the non-interacting density-density response function,

$$\frac{\partial^2 G_0[\{b_t\}; \rho_{\text{in}}]}{\partial b_t \partial b_u} = \sum_i^{\text{occ.}} \sum_a^{\text{vir.}} \frac{\langle \varphi_i | g_u(\mathbf{r}) | \varphi_a \rangle \langle \varphi_a | g_t(\mathbf{r}) | \varphi_i \rangle}{\epsilon_i - \epsilon_a} + \text{c.c.}. \tag{6.50}$$

This Hessian matrix is positive semi-definite and so $G_0[\{b_t\}; \rho_{\text{in}}]$ is convex in $\{b_t\}$, and can be minimised directly by the QUEST OEP optimiser.

Comparison with the WY functional

Comparison of Eqs. (6.48), (6.49) and (6.50) with Eqs. (6.32), (6.33) and (6.34) shows an immediate similarity between the Gidopolous and WY functionals that is clarified further when the WY functional is expressed as,

$$W_0[v;\rho_{\rm in}] = T[\Psi_0] - (v|\rho_{\Psi_0} - \rho_{\rm in}) \leq T_{\rm s}[\rho_{\rm in}], \tag{6.51}$$

showing that the Gidopolous objective functional can be expressed as,

$$G_0[v;\rho_{\rm in}] = T[\rho_{\rm in}] - W_0[v;\rho_{\rm in}]. \tag{6.52}$$

As the input wave function is fixed through the optimisation the term $T[\rho_{\rm in}]$ is a constant, showing Eq. (6.52) as simply the negative of the WY functional plus a constant, hence the derivatives of both functionals are the same to within a sign.

Extension to arbitrary interaction strengths

The WY functional is the non-interacting case of the Lieb functional and, with the similarity between the WY and Gidopolous functionals established, the same arguments may be followed to derive a Gidopolous functional for arbitrary interaction strengths.

Briefly, consider the Hamiltonian for a system of electrons with interaction strength $\lambda \geq 0$, given in Eq. (6.36), with associated ground state wave function Ψ_λ and energy $E_\lambda[v]$. The case for $\lambda = 0$ has already been established, but for more general values of λ the Gidopolous functional is,

$$\begin{aligned} G_\lambda[v;\rho_{\rm in}] &= \left\langle \Psi_{\rm in} \middle| \hat{H}_\lambda[v] \middle| \Psi_{\rm in} \right\rangle - \left\langle \Psi_\lambda \middle| \hat{H}_\lambda[v] \middle| \Psi_\lambda \right\rangle \\ &= \left\langle \Psi_{\rm in} \middle| \hat{T} + \lambda\hat{W} \middle| \Psi_{\rm in} \right\rangle + (v_\lambda|\rho_{\rm in}) - \left\langle \Psi_\lambda \middle| \hat{T} + \lambda\hat{W} \middle| \Psi_\lambda \right\rangle - (v_\lambda|\rho_\lambda) \\ &= T[\rho_{\rm in}] + \lambda W[\rho_{\rm in}] - T[\rho_\lambda] - \lambda W[\rho_\lambda] - (v_\lambda|\rho_{\rm in} - \rho_\lambda) \geq 0. \end{aligned}$$

The derivatives of the generalised Gidopolous functional are then simply the negative of those for the Lieb functional, Eq. (6.42) and Eq. (6.43).

6.4.4 Numerical equivalence

The Lieb and Gidopolous functionals were evaluated for the H_2 molecule at a range of internuclear distances using the QUEST OEP module and plotted as a function of interaction strength in Figure 6.1. For simplicity, the OEP equations were regularised using truncated singular value decomposition (TSVD) at $\alpha = 10^{-5}$, though the more refined schemes detailed in Section 7 could be used to ensure more physical final potentials.

Both functionals displayed similar behaviour with increasing interaction strength and separation, though this is not immediately obvious. At short separation there is a large interaction between the two electrons that is reflected in the shallow curve of the Gidopolous functional and steeper gradient of the Lieb functional. At large separations the Gidopolous functional quickly approaches the fully interacting limit as there is very little kinetic correlation energy to capture, this is reflected in the Lieb functional by a shallow gradient.

The equivalence of the Lieb and Gidopolous functionals was demonstrated numerically through calculation of $\langle\Psi_\lambda|\,\hat{W}\,|\Psi_\lambda\rangle$, the adiabatic connection integrand, for the stretched hydrogen molecule using both Lieb and Gidopolous functionals, which should be equivalent for both the Lieb and Gidopolous functionals. In Figure 6.2 the Gidololous and Lieb adiabatic connections are shown to superimpose perfectly, numerically confirming their equivalence.

6.5 Concluding remarks

The optimised effective potential presents a promising route towards both higher accuracy XC functionals and insights into the core workings of density functional theory. When suitably implemented

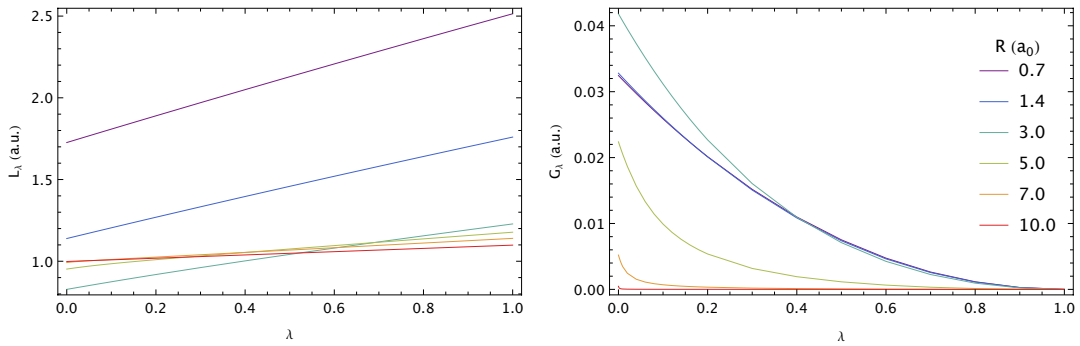


Figure 6.1: Lieb functional (left) and Gidopolis functional (right) evaluated for the H_2 molecule at a range of internuclear separations as a function of interaction strength.

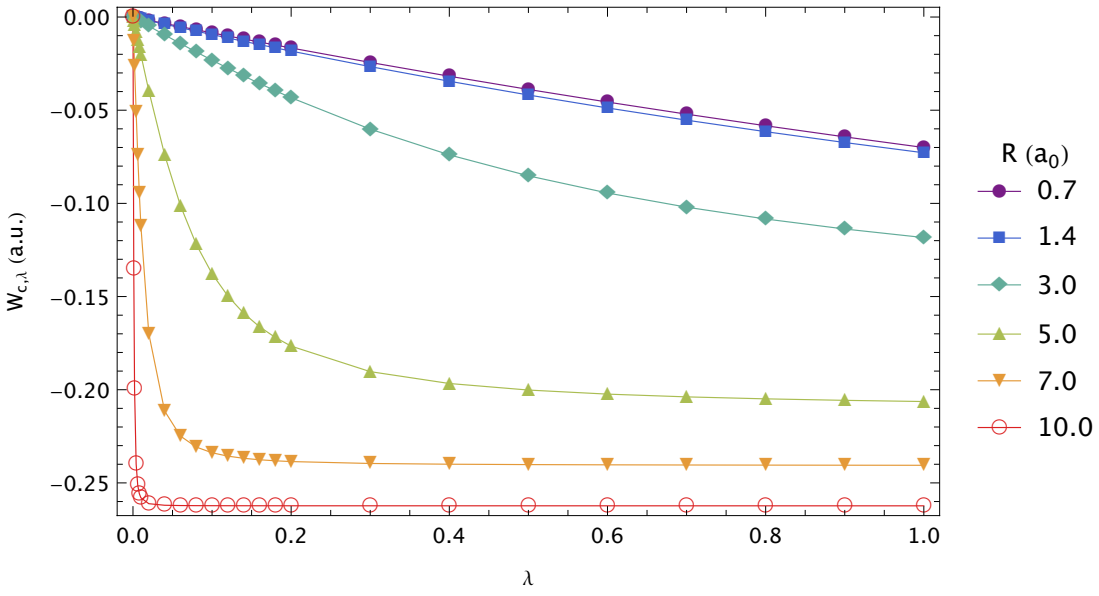


Figure 6.2: The adiabatic connection for the H_2 molecule evaluated using the Lieb (solid lines) and Gidopolous (pointwise markers) functionals at increasing internuclear separation.

the YW potential expansion offers a flexible framework for solving the OEP for a variety of problems and can help to expose the similarities between them.

Unfortunately, as described in Section 6.3, any method for solving the OEP problem in a finite basis will inevitably suffer from the numerical instabilities originating from the discrete Fredholm integral equation, Eq. (6.16). The YW expansion of the OEP does not avoid such instabilities and any useful implementation must at some point apply regularisation to ensure a meaningful solution is obtained. The most appropriate choice of regularisation is complicated and Chapter 7 discusses conventional regularisation methods before describing a scheme for the automatic regularisation for potential expansion based methods in DFT.

Chapter 7

Regularisation of The Optimised Effective Potential

As discussed briefly in Chapter 6, the representation of the OEP equation (Eq. (6.16)) in a finite discrete basis set results in numerically problematic equations, requiring regularisation for their solutions to be physically meaningful. Such *ill-posed* problems are common in the physical sciences and often occur when a solution is calculated from the discretisation of a continuous data source through the inverse matrix problem,

$$\mathbf{A} \cdot \mathbf{x} = \mathbf{b}. \tag{7.1}$$

Many techniques have been constructed for the regularisation of ill posed equations and most require a user to choose the strength of regularisation imposed through the choice of a control parameter. For the OEP problem this choice is difficult to make *a priori* as the regularisation required is system dependent, requiring the user to iteratively correct the regularisation strength until a satisfactory result is obtained. The aim of this chapter is to explore in detail the classical techniques for regularising the OEP before outlining a scheme for automatically adjusting the regularisation strength for the Tikhonov regularisation method [198, 199] to produce a physically meaningful OEP from a single *black box* calculation. The automatic parameter selection scheme is then further developed by incorporating the potential basis kinetic energy integral matrix into the Tikhonov equations to target the regularisation efforts onto problematic regions and further improve the quality of the potentials obtained.

7.1 The ill-posed nature of finite basis OEP

The OEPs constructed by the Yang–Wu optimisation scheme of Section 6.3.1 are formally exact in the limit of complete orbital and potential basis sets. Given this formal completeness, it is disappointing that finite basis YW optimised potentials are often physically absurd, despite being valid solutions to the OEP equations. This is illustrated in Figure 7.1 which shows a comparison between a finite basis YW optimised exchange potential and the equivalent benchmark determined by the Talman–Shadwick numerical grid method described in Section 6.2.2. It should be stressed that the YW constructed potential of Figure 7.1 *is a valid solution* for the OEP problem in the basis sets chosen.

The non-physical oscillations in the finite basis potential of Figure 7.1 are *not* the result of a limitation of the YW scheme and are instead an unavoidable artefact of solving the unregularised OEP equations in an incomplete basis set representation. Similar difficulties are necessarily found for all finite basis OEP schemes [182, 183]. The spurious oscillations in the finite basis potential arise from the incompleteness of the orbital basis and the resulting inability of the KS orbitals to properly respond to all the possible variations in $v_{\mathrm{s}}(\mathbf{r})$ that can be produced by the potential basis. Such inflexibilities are reflected in the discrete KS response function $\chi_s(\mathbf{r}, \mathbf{r}')$, of Eq. (6.16), and result in the solution potential, $v_{\mathrm{s}}(\mathbf{r})$, no longer being unique. The inability of the orbitals to respond to some changes in the potential allows the optimiser freedom to optimise to unphysical solutions and the

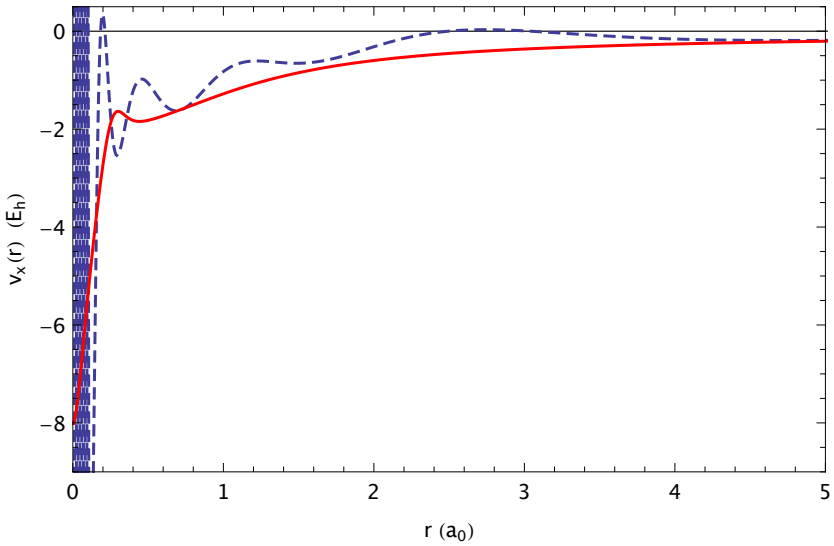


Figure 7.1: Exchange potentials for the neon atom calculated using the Yang–Wu method with u-aug-cc-pVTZ [20] orbital / u-Partridge3 [200] potential basis sets (dashed, blue) and the benchmark Talman–Shadwick numerical solver (red).

oscillatory potential observed in Figure 7.1 is reached. Such instability is not an unexpected result as the numerical difficulties of the discrete Fredholm integral equations are well known. A full formal analysis of the numerical issues associated with finite basis OEP DFT is given in Ref. [183].

The problems arising from the ill-posed nature of the finite basis OEP calculation can be reduced significantly if the orbital and potential basis sets are chosen to have a similar span, termed a balanced choice. Choosing basis sets in this way ensures that most variations in the potential can be properly reflected in the KS orbitals and oscillations resulting from spurious freedoms are minimised. Restricting the basis set choice to only balanced combinations is unsatisfactory however as the increase in computational cost associated with expanding the orbital basis is much greater than that of increasing the potential basis. This is because the potential basis enters the OEP calculation only as the three center overlap integrals of Eq. (6.27)[1] that are much faster to evaluate than the two electron integrals that are required for the orbital basis. Restricting the potential basis to the size of the orbital basis therefore prevents calculations utilising the large potential basis sets that would otherwise be computationally feasible and give a better representation of the true potential. A correctly parametrised regularisation scheme acts to temper the instabilities associated with basis set imbalances and allow calculations to take advantage of the increased flexibility in large potential basis sets whilst producing physically meaningful potentials.

7.2 The regularisation of ill-posed problems

The core mathematical aspects of ill-posed problems will first be explored through the lens of singular value decomposition analysis to set the foundations for how regularisation can be applied to the OEP equations and how more sophisticated schemes may be developed.

The inverse problem is common in the physical sciences and entails the reconstruction of a solution vector, $\mathbf{x}$, from Eq. (7.1) for a given data vector, $\mathbf{b}$ and operator matrix $\mathbf{A}$. The stability of the solution vector with respect to small perturbations in $\mathbf{b}$ or $\mathbf{A}$ can be determined from a singular value decomposition (SVD) of the matrix $\mathbf{A}$,

$$\mathrm{SVD}[\mathbf{A}] = \mathbf{U} \cdot \mathbf{S} \cdot \mathbf{V}^{\mathrm{H}}, \tag{7.2}$$

where $\mathbf{U}$ and $\mathbf{V}$ are unitary matrices. The unitary matrices will be equivalent, $\mathbf{U} = \mathbf{V}$, if $\mathbf{A}$ is a real symmetric matrix, which will always be the case for the YW-OEP Hessian. The matrix $\mathbf{S}$ is a

[1] The three center overlap integrals also enter into the gradient and Hessian equations.

diagonal matrix of singular values $\{\sigma_1 \geq \ldots \geq \sigma_N \geq 0\}$, equivalent to the eigenvalues if $\mathbf{A}$ is a symmetric square matrix.

The condition number of $\mathbf{A}$ is defined from the singular values as

$$\kappa(\mathbf{A}) = \frac{\sigma_1}{\sigma_N}. \tag{7.3}$$

Systems with a small condition number $\kappa(\mathbf{A}) \lesssim 1,000$ are said to be well conditioned and correspond to a well-posed problem, if $\kappa(\mathbf{A}) \gtrsim 10,000$ the matrix is ill conditioned and the system is ill-posed.

Although the condition number is a simple diagnostic measure it has an additional significance as a magnifying factor for the effect of perturbations made in $\mathbf{b}$ or $\mathbf{A}$ on the solution vector $\mathbf{x}$,

$$||\Delta\mathbf{x}||/||\mathbf{x}|| \leq \kappa(\mathbf{A}) \cdot ||\Delta\mathbf{b}||/||\mathbf{b}||, \tag{7.4}$$
$$||\Delta\mathbf{x}||/||\mathbf{x}|| \leq \kappa(\mathbf{A}) \cdot ||\Delta\mathbf{A}||/||\mathbf{A}||, \tag{7.5}$$

such that the solution of an ill-posed system with a large condition number will be highly sensitive to any noise in $\mathbf{b}$ or $\mathbf{A}$.

A large condition number is commonly the result of a number of the singular values of $\mathbf{A}$ becoming very small and it is these small singular values that are responsible for the amplification of perturbations in ill-posed problems. For ill-posed problems it is impossible to obtain a meaningful solution vector as even minor perturbations in $\mathbf{b}$ become amplified and result in large variations in the solution. The origin of this amplification can be seen by solving Eq. (7.1) through multiplication with the Moore–Penrose pseudo-inverse of $\mathbf{A}$ [201],

$$\mathbf{x} = \sum_{i=1}^{N} \mathbf{v}_i \left(\frac{\mathbf{b} \cdot \mathbf{u}_i^{\mathrm{T}}}{\sigma_i} \right), \tag{7.6}$$

where $\mathbf{u}_i^{\mathrm{T}}$ and $\mathbf{v}_i$ the left and right eigenvectors, from $\mathbf{U}$ and $\mathbf{V}$ respectively. In order for the solution of Eq. (7.6) to be physical meaningful we require the *discrete Picard condition*, Theorem 7.2.1, to be satisfied [202],

Theorem 7.2.1 (The discrete Picard condition)**.** *The SVD coefficients* $|\mathbf{b} \cdot \mathbf{u}_i^{\mathrm{T}}|$ *decay faster than* σ_i*.*

If the discrete Picard condition is broken the $\frac{\mathbf{b} \cdot \mathbf{u}_i^{\mathrm{T}}}{\sigma_i}$ term will become large, corresponding to a large $||\mathbf{x}||$ and unphysical solution. Severe problems are encountered in the practical solution of ill-posed problems as the Picard condition necessarily breaks when the singular values approach machine precision, resulting in the amplification of round-off errors into the solution. This problem is compounded by the observation that the number of sign changes in the singular vectors tends to increase as i increases, hence the smaller singular values correspond to more oscillatory singular vectors [202].

In order to obtain a meaningful solution vector from an ill-posed problem, a regularisation must be applied to control the small singular values of $\mathbf{A}$ and instead of solving the ill-posed problem directly we instead solve a related problem constructed such that,

- The solution closely matches the solution of the of the original problem (low *bias*).
- The solution is less sensitive to perturbations in the data vector $\mathbf{b}$ (low *variance*).
- The problem has a parameter α that allows a continuous bias-variance trade-off.

The regularised problem related to the Eq. (7.1) can be solved to give a solution vector that is stable to perturbations in $\mathbf{A}$ and $\mathbf{b}$, allowing a meaningful solution to be obtained from a previously unsolvable problem.

7.3 Classical regularisation techniques for the OEP problem

The ill-conditioned nature of the OEP problem can be seen in the YW Newton optimisation, where the next Newton step is obtained by Eq. (6.25) from an ill-conditioned Hessian matrix, with a condition

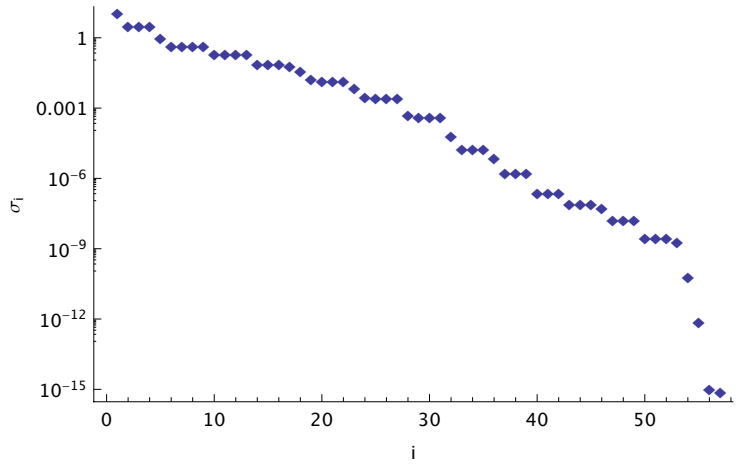


Figure 7.2: The singular values of the Hessian matrix corresponding to the first iteration of the YW-OEP calculation of Figure 7.1.

number that is typically on the order of 10^{16}, though the exact condition is strongly system and basis set dependent. The singular value spectrum for the first iteration Hessian matrix of the YW potential of Figure 7.1 is plotted in Figure 7.2, showing the smooth decay of singular values towards zero that is characteristic of an ill-posed problem. The goal of our regularisation efforts will therefore be to control the influence of the small singular values in the Hessian matrix and construct a regularised form of the Newton equation.

7.3.1 Truncated singular value decomposition

An immediately apparent solution to the amplification of error by the small singular values of the operator matrix is to remove their contribution entirely, forming the Newton step of Eq. (6.25) as a filtered Moore–Penrose pseudo-inverse constructed as Eq. (7.6) with a Heaviside filter function,

$$\mathbf{p} = \sum_{i=1}^{N} f(\sigma_i;\alpha)\cdot \mathbf{v}_i \left(\frac{-\mathbf{g}\cdot\mathbf{u}_i^{\mathrm{T}}}{\sigma_i}\right), \tag{7.7}$$

$$f(\sigma;\alpha) = \begin{cases} 1 & \sigma \geq \alpha \\ 0 & \sigma < \alpha \end{cases}. \tag{7.8}$$

such that the filter function removes singular values smaller than the threshold parameter α. The regularised solution of ill-posed problems by Heaviside filtered Moore–Penrose pseudo inverse is termed the truncated SVD (TSVD) regularisation scheme, with the parameter α acting as the bias-variance control parameter that controls the strength of the regularisation.

Despite its crude appearance TSVD regularisation is effective in controlling the problematic small singular values and solves the numerical instabilities associated with the broken discrete Picard condition in the finite basis OEP method. With a careful choice of the threshold parameter, α, the YW equations that gave the oscillatory potential of Figure 7.1 can be regularised to produce the potential shown in Figure 7.3.

The TSVD regularisation method has a number of undesirable properties however that limit its utility as a practical regularisation for the ill-posed OEP equations. Firstly, the complete SVD of the Hessian matrix must be computed and stored for use in the filtered pseudo-inverse of Eq. (7.6), which becomes expensive for a very large systems[2], though in practice the small pre-factor and relatively small matrices limit the overall cost. More importantly, the strength of regularisation imposed by TSVD is not a continuous function of the regularisation parameter α. As the Heaviside filter simply truncates singular values, only a change in α that crosses a singular value will change regularisation strength and affect the final solution. This stepwise change in regularisation strength means the derivatives

[2]Scaling as $O(N^3)$ operations and requiring significant work space memory for intermediate quantities.

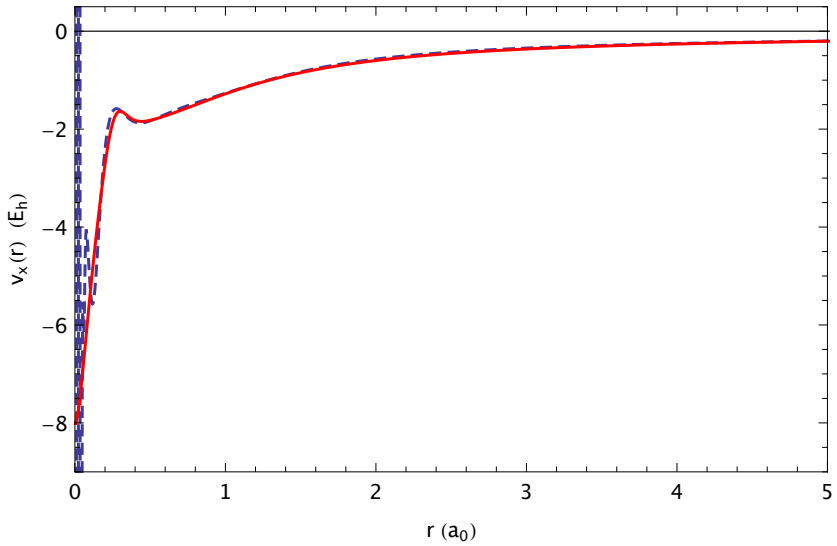


Figure 7.3: The exchange potential of the neon atom calculated using the Yang–Wu method regularised using TSVD with $\alpha = 10^{-5}$ in the u-aug-cc-pVTZ [20] orbital / u-Partridge3 [200] potential basis sets (dashed, blue). The benchmark potential from the Talman–Shadwick numerical solver is included (red).

of regularisation strength with changing α are undefined, preventing the automatic identification of an optimal regularisation strength. As a result of these limitations TSVD is of limited practical use in OEP.

7.3.2 Tikhonov regularisation

Many of the limitations of the TSVD regularisation scheme are addressed by the Tikhonov regularisation technique [198, 199]. In this regularisation method the direct solution of the Newton step is replaced by the minimisation of the related cost functional,

$$\mathbf{p} = \underset{\mathbf{p}}{\operatorname{argmin}}[\,||\mathbf{Hp} - (-\mathbf{g})||^2 + \alpha^2||\mathbf{p}||^2\,], \tag{7.9}$$

where the non-standard notation $-(-\mathbf{g})$ has been adopted for clarity between the general ill-posed problem $\mathbf{Ax} = \mathbf{b}$ and the Newton optimisation, $\mathbf{Hp} = -\mathbf{g}$.

The cost functional of Eq. (7.9) can be interpreted as a bias-variance trade-off, minimising the mean square error in the Newton step residual, $||\mathbf{Hp} - (-\mathbf{g})||^2$ (the bias), whilst penalising the large values in $\mathbf{p}$ (the variance). By reformulating the problem as this minimisation the closest possible solution to the original problem is obtained without allowing the small singular value oscillations to dominate. The structure of Eq. (7.9) implies that $\mathbf{p}$ must be solved as an N dimensional minimisation problem, however a more efficient direct solution is available through the pseudo-inverse equation,

$$(\mathbf{H}^{\mathrm{T}} \cdot \mathbf{H} + \alpha^2\mathbf{I})\mathbf{p} = \mathbf{H}^{\mathrm{T}}(-\mathbf{g}). \tag{7.10}$$

Rewriting the YW Newton step as Eq. (7.10) with an appropriate strength parameter, α, controls the small singular values and produces OEP solutions with physically meaningful potentials, achieving correct regularisation without computing the full SVD of the Hessian. Tikhonov regularisation is not a panacea for the regularisation problem however and a careful selection of α is still required to produce the correct regularisation strength and meaningful solutions. If α is set too high the final potential becomes over-smoothed and important features are missed, whilst an α set too low will not impose sufficient regularisation and the potential remains unphysical. This problem is illustrated by Figure 7.4 which shows the familiar neon exchange potential from Tikhonov regularised YW-OEP with three values of α. The best choice of these is identified as $\alpha = 10^{-4}$, which successfully captures the inter-shell peak at $\sim$0.5 a_0 whilst allowing few spurious oscillations. The potential from $\alpha = 10^{-8}$

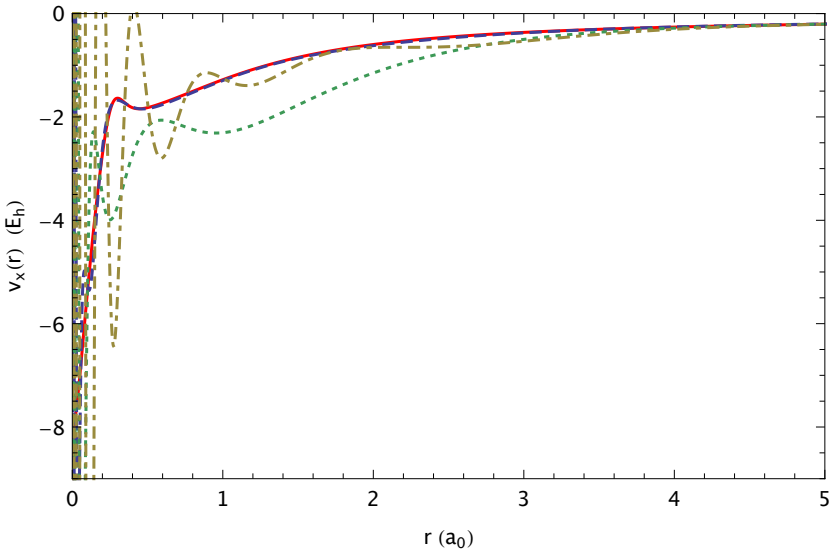


Figure 7.4: The exchange potential of the neon atom calculated using the Yang–Wu method regularised using Tikhonov regularisation with $\alpha = 10^{-8}$ (yellow, dash-dotted), $\alpha = 10^{-4}$ (blue, dashed) and $\alpha = 0.01$ (green, dotted) in the u-aug-cc-pVTZ [20] orbital / u-Partridge3 [200] potential basis sets. The benchmark potential from the Talman–Shadwick numerical solver is included (red).

has been too weakly regularised and remains highly oscillatory, whilst the potential from $\alpha = 10^{-2}$ has been over smoothed.

Although the solution of Eq. (7.10) does not require the computation of the SVD of the Hessian, it can be shown that Tikhonov regularisation is equivalent to applying the filter function,

$$f(\sigma_i, \alpha) = \frac{\sigma_i^2}{\sigma_i^2 + \alpha^2}. \tag{7.11}$$

to Eq. (7.7). The singular value filter functions of TSVD and Tikhonov regularisation are summarised graphically in Figure 7.5, showing that Tikhonov has a smooth sigmoidal filtering effect.

The continuous nature of the Tikhonov regularisation filter function causes the regularisation strength to be a continuous function of α. The continuous regularisation strength of the Tikhonov method combined with further useful properties established from the related trust-region sub-problem in Section 7.4 will form the foundations for an L-Curve analysis in Section 7.5.1 and an automatic parameter selection scheme. The success of the automatic parametrisation scheme highlights further difficulties in the finite basis OEP problem that can be solved using a generalised Tikhonov scheme that targets regularisation onto problematic functions in the potential basis to produce high quality potentials in a single black box calculation.

7.4 Relationship with the trust-region sub-problem

A Newton optimisation is the method of choice for most optimisation problems when the gradient and Hessian are known, though the method can fail in situations where the starting guess $\mathbf{x}_0$ lies in an ill behaved region of the problem space. The trust-region sub-problem (TRS) method of Sorensen [203, 204] addresses this problem by instead seeking a minimum in the objective function through the minimisation of a local quadratic model of the function in a restricted ellipsoidal region, the *trust-region*. The TRS method is closely related to a Tikhonov regularised Newton method, revealing important connections between the solution norm $||\mathbf{x}||$ and the regularisation parameter α, and is explored in the following section.

The TRS solution of Eq. (7.1), $\mathbf{x}$, is constructed by solving the constrained minimisation,

$$\min_{\mathbf{x}\in\mathbb{R}^N} \frac{1}{2}\mathbf{x}^{\mathrm{T}} \cdot \mathbf{A} \cdot \mathbf{x} + \mathbf{b}^{\mathrm{T}} \cdot \mathbf{x} \quad \text{subject to} \quad ||\mathbf{x}|| \leq \Delta, \tag{7.12}$$

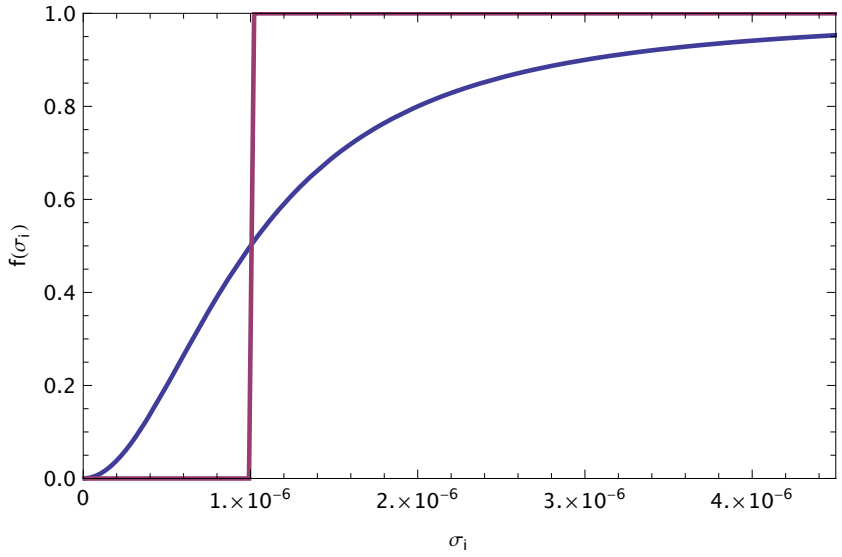


Figure 7.5: The filter function of the truncated singular value decomposition (TSVD, red) and Tikhonov (blue) regularisation techniques for $\alpha = 10^{-6}$.

where $||\cdot||$ denotes an arbitrary norm and Δ is the trust region.

For the solution vector $\mathbf{x}$ to give a global minimum of the TRS there must exist a Lagrange multiplier, $\lambda \in \mathbb{R}$, such that the following conditions are obeyed when the Lagrange multiplier is chosen to be non-positive (≤ 0),

$$(\mathbf{A} - \lambda\mathbf{I}) \cdot \mathbf{x} = -\mathbf{b} \qquad \text{Stationarity} \tag{7.13}$$

$$\lambda \leq 0 \text{ and } \lambda(\Delta - ||\mathbf{x}||) = 0 \qquad \text{Feasibility} \tag{7.14}$$

$$\mathbf{A} - \lambda\mathbf{I} \text{ is positive semi-definite} \qquad \text{Strengthened 2nd Order} \tag{7.15}$$

Furthermore, the optimiser $\mathbf{x}$ is unique if and only if $\mathbf{A} - \lambda\mathbf{I}$ is positive definite, for the full proof see Ref. [203]. The mathematical literature identifies three distinct cases in solving Eq. (7.12).

The easy case

The *easy case* is encountered when the Hessian matrix $\mathbf{A}$ is positive definite and $||\mathbf{A}^{-1} \cdot \mathbf{b}|| < \Delta$, showing that Eq. (7.12) has a solution in the interior of the trust-region ellipsoid found by simple inversion $\mathbf{x} = \mathbf{A}^{-1} \cdot \mathbf{b}$, with the Lagrange multiplier $\lambda = 0$.

The hard case

The so called *hard case* [204], refers to the situation in which the TRS Lagrange multiplier λ is the smallest singular value of the Hessian, σ_N. The hard case occurs in three situations,

- Whenever the Hessian is singular or has negative eigenvalues,

$$\sigma_N \leq 0 \tag{7.16}$$

- The gradient is orthogonal to the right eigenvector of the Hessian associated with its smallest singular value, $\mathbf{v}_N$

$$\mathbf{b} \perp \mathbf{v}_N \tag{7.17}$$

- The norm of the of the shifted Newton step is less than or equal to the trust radius Δ

$$||(\mathbf{A} - \sigma_N\mathbf{I})^{-1}\mathbf{b}|| \leq \Delta \tag{7.18}$$

In practice the hard case is not encountered in the OEP problem, since the approximate Hessians are positive definite by construction. The YW-OEP problem is ill-posed however and has a highly ill-conditioned Hessian matrix $\mathbf{A}$, with small singular values that approach zero with no clear transition. As a result of the small but positive singular values we do not explicitly encounter the hard case, we instead encounter what is known as the *near-hard case* [205], a situation common to all ill-posed problems.

The near-hard case

The near-hard case is defined by the situation in which $\mathbf{b}$ is *nearly* orthogonal to the singular vectors associated with several of the smallest singular values of $\mathbf{A}$. Let σ_k be the k^{th} largest singular value with multiplicity m_k of an ill-conditioned matrix, $\mathbf{A}$, and $\mathbf{u}_j$, $\mathbf{v}_j$, $(k \leq j \leq k + m_k)$ are the left and right singular vectors associated with σ_k. Then,

$$\mathbf{b}^{\mathrm{T}} \cdot \mathbf{v}_j = -\sigma_k \mathbf{u}_j^T \cdot \mathbf{b}, \tag{7.19}$$

as proved in Ref. [205]. In the case that $\mathbf{A}$ is severely ill-conditioned σ_i will be so close to zero that $\mathbf{b}$ and $\mathbf{v}_j$ are necessarily near-orthogonal, defining the near hard case. Since typical ill-conditioned problems have a cluster of small singular values close to zero, $\mathbf{b}$ may also be nearly orthogonal to several singular vectors corresponding to the small singular values.

There are many algorithms proposed for the solution of the TRS in the hard or near-hard cases, with important examples being the Moré and Sorensen robust TRS algorithm for the hard case [204] and its later modification for large scale implementations by Rojas [205, 206]. Two key questions arise from the near-hard case,

1. Are the solutions corresponding to the near-hard case regime meaningful for ill-posed discrete problems?
2. How can a meaningful regularisation be introduced for trust-region and other methods to avoid the near-hard case when little is known about the singular value spectrum of $\mathbf{A}$ *a priori*?

7.4.1 Trust-region sub-problem regularisation

The two questions of the preceding section are of course intimately linked. If one requires for example that the ill-posed problem is modified such that the contributions from the singular vectors that are nearly orthogonal to $\mathbf{b}$ are removed (for example by a TSVD or Tikhonov regularisation) then the near hard case would never be encountered. In this respect a regularised optimisation procedure never attempts to optimise along the directions orthogonal to $\mathbf{b}$ that arise from the right-singular vectors corresponding to the small singular values of the Hessian.

The problem remains to determine how a regularisation may best be applied to achieve this effect, both in Newton optimisation and trust-region approaches. The particular regularisation parametrised trust-region sub-problem method implemented is due to Grodzevich and Wolkowicz, exploring the link between the Rendl-Wolkowicz TRS algorithm and regularisation. In many respects the ideas underlying this approach are similar to the LSTRS algorithm of Rojas, Santos and Sorensen [206]. The TRS of Eq. (7.12) is recast as a parametrised eigenvalue problem, where the optimal parameter is selected by regularisation considerations.

A link will now be made between the problem of the regularised Newton equation, i.e. finding approximate least squares solutions to,

$$\min_{\mathbf{p}} ||\mathbf{H} \cdot \mathbf{p} - (-\mathbf{g})||_2 \tag{7.20}$$

with reasonable solution Euclidean[3] norms, $||\mathbf{p}||_2$, for an ill conditioned $\mathbf{H}$, and the TRS when the near-hard case is encountered.

[3] The Euclidean norm of $\mathbf{x}$ is denoted by $||\mathbf{x}||_2$ and defined as $\sqrt{\mathbf{x} \cdot \mathbf{x}}$.

The regularisation methods considered attempt to find generalised solutions $\mathbf{p}$ that are stable under small changes in $\mathbf{g}$. This amounts to a constrained least-squares problem:

$$r_\varepsilon = \min_{\mathbf{p}}[\ ||\mathbf{H}\cdot\mathbf{p} - (-\mathbf{g})||_2\ ] \quad \text{subject to } ||\mathbf{p}||_2 \leq \varepsilon \tag{7.21}$$

where ε defines a constraint on the size of the solution norm and r_ε is the solution residual. Introducing this restriction increases the residual error $||\mathbf{H}\cdot\mathbf{p} - (-\mathbf{g})||_2$, but reduces the propagated errors and in practice as ε increases, the propagated errors dominate and the solution $\mathbf{p}$ becomes poorly behaved. To regularize the solution an appropriate choice and control mechanism for ε is required.

To obtain a TRS for this constrained least squares problem one simply squares the objective function and constraint. To see this let $\mathbf{A} = \mathbf{H}^{\mathrm{T}}\cdot\mathbf{H}$ and $\mathbf{a} = -\mathbf{H}^{\mathrm{T}}\cdot(-\mathbf{g})$,

$$\begin{aligned}
\mu(\mathbf{A},\mathbf{a},\varepsilon) &= \min_{\mathbf{p}}\left[q(\mathbf{p})\right] \text{ where } q(\mathbf{p}) = \mathbf{p}^{\mathrm{T}}\cdot\mathbf{A}\cdot\mathbf{p} - 2\mathbf{a}^{\mathrm{T}}\cdot\mathbf{p} \qquad \text{subject to } ||\mathbf{p}||_2^2 \leq \varepsilon^2 \qquad (7.22)\\
&= \min_{\mathbf{p}}\left[\mathbf{p}^{\mathrm{T}}\cdot(\mathbf{H}^{\mathrm{T}}\cdot\mathbf{H})\cdot\mathbf{p} + 2\mathbf{H}^{\mathrm{T}}\cdot(-\mathbf{g})\cdot\mathbf{p}\right] \qquad \text{subject to } ||\mathbf{p}||_2^2 \leq \varepsilon^2\\
&= 2\min_{\mathbf{p}}\left[\frac{1}{2}\mathbf{p}^{\mathrm{T}}\cdot(\mathbf{H}^{\mathrm{T}}\cdot\mathbf{H})\cdot\mathbf{p} + \mathbf{H}^{\mathrm{T}}\cdot(-\mathbf{g})\cdot\mathbf{p}\right] \qquad \text{subject to } ||\mathbf{p}||_2 \leq \Delta \qquad (7.23)
\end{aligned}$$

where in the last equality ε is identified as the trust region Δ (with the constraint is written in terms of the solution norm, rather than its square) and the factor of 2 is moved in front of the minimization such that we can identify the quantity in parenthesis with $q(\mathbf{p})$. The optimality conditions for the TRS Eqs. (7.13)—(7.15) may then be re-phrased as

$$\begin{aligned}
(\mathbf{H}^T\cdot\mathbf{H} - \lambda\mathbf{I})\cdot\mathbf{p} &= \mathbf{H}^{\mathrm{T}}\cdot(-\mathbf{g}) && \text{Stationarity} && (7.24)\\
\mathbf{H}^T\cdot\mathbf{H} - \lambda\mathbf{I} &= \text{positive definite}\ \ (\lambda \leq 0) && \text{Dual Feasibility} && (7.25)\\
||\mathbf{p}||_2^2 &\leq \Delta^2 && \text{Primal Feasibility} && (7.26)\\
\lambda(||\mathbf{p}||_2^2 - \Delta) &= 0 && \text{Complementary Slackness} && (7.27)
\end{aligned}$$

and the optimal TRS solution is denoted $\mu(\mathbf{A}, a, \varepsilon)$.

Recall that the Tikhonov regularised Newton step is obtained by solving the equation,

$$(\mathbf{H}^{\mathrm{T}}\cdot\mathbf{H} + \alpha^2\mathbf{I})\cdot\mathbf{p}_\alpha = \mathbf{H}^{\mathrm{T}}\cdot(-\mathbf{g}), \tag{7.28}$$

with α controlling the smoothness of the solution $\mathbf{p}_\alpha$. The TRS optimality conditions imply that the solution of the TRS problem and the Tikhonov regularisation are equivalent in the following manner:

1. Comparing the Eq. (7.28) with the stationarity condition of Eq. (7.24) we see that $\lambda = -\alpha^2$.
2. Using the complementary slackness of Eq. (7.27) and fixing $\lambda = -\alpha^2$ we obtain a solution with $\Delta = ||\mathbf{p}||_2$.

Consequently, for any choice of regularisation parameter α such that $\alpha^2 > 0$ there is a corresponding solution $\mathbf{p}_\alpha$ such that $\Delta = ||\mathbf{p}_\alpha||_2$ and the TRS and Tikhonov regularisation problems coincide.

Since we are only interested in regularised solutions we impose the simple restriction of $\alpha^2 > 0$ and as a consequence $\lambda < 0$, and the optimal TRS solution always lies on the boundary of the trust-region. As the goal is to regularise the solution such that its norm $||\mathbf{p}||_2$ is reasonable and $||\mathbf{p}||_2 = \varepsilon$ for regularized solutions we can seek to vary λ to find the regularised TRS solution and determine the equivalent Tikhonov regularisation.

So far we have established the following relationships between Tikhonov regularised solutions and the TRS:

1. Tikhonov regularised solutions correspond to solutions of the TRS if $\alpha^2 > 0$.
2. The TRS Lagrange multiplier λ is related to the Tikhonov parameter α as,

$$\lambda = -\alpha^2. \tag{7.29}$$

3. For fixed λ, $\varepsilon = \Delta = ||\mathbf{p}||_2$.

4. All regularized solutions are on the boundary of the trust region.

5. Choosing a value for Δ gives λ and a $\mathbf{p}$ consistent with $-\alpha^2$, i.e. a regularised solution.

To obtain a regularised solution one could then solve a sequence of TRS for given values of Δ. This however is clearly not an efficient way to proceed and the problem still remains of what value of α, or equivalently Δ, to choose in order to get an ideally regularised solution offering a low $||\mathbf{H}\cdot\mathbf{p}-(-\mathbf{g})||$ and reasonable $||\mathbf{p}||$ *a priori*.

7.5 Automatic regularisation

If the YW-OEP Newton optimisation is regularised using the Tikhonov or TSVD scheme then a physically reasonable potential can be obtained that has very good agreement with the original OEP problem. Unfortunately, the Tikhonov and TSVD schemes alone do not provide a completely satisfactory solution for practical OEP calculations as the optimal regularisation strength, α, for a given system is *a priori* unknown. To establish the strength of regularisation required for a given system and basis set combination a range of α values must be tested to determine how calculated properties vary with regularisation, such that an optimal α can be established. A procedure for selecting an optimal α in a single black box calculation from quantities intrinsic to the OEP in question is clearly required if OEP calculations are to ever become routine, and is the subject of this section.

As established in Section 7.3.1 the TSVD regularisation scheme is completely unsuitable for automatic parametrisation as the discontinuous dependence of regularisation strength on α prevents a clear analysis. The Tikhonov regularisation scheme however is continuous in α and has been shown (Section 7.4.1) to correspond to the optimal TRS solution for $\Delta = ||\mathbf{p}||_2$. As such we will use the established connection with the TRS and focus efforts on an algorithm for the automatic selection of α in the Tikhonov regularisation scheme.

7.5.1 The L-Curve

To derive an automatic regularisation scheme we begin by considering the trade-off that is sought in the relationship between the problem residual, $||\mathbf{H}\cdot\mathbf{p}_\alpha-(-\mathbf{g})||$, and the solution norm, $||\mathbf{p}_\alpha||$ as controlled by the regularisation parameter α by connection through the TRS to a parametric *L-Curve* plot. In the notation of Section 7.4.1 we let $\mathbf{p}^* = \mathbf{p}_\varepsilon$ denote the optimal solution and $\lambda^* = \lambda_\varepsilon$ the Lagrange multiplier for a given trust region ε respectively.

Theorem 7.5.1 (The L-Curve)**.** *The optimal values for Eq. (7.22) and Eq. (7.21) are related as* $r_\varepsilon = \mu_\varepsilon + (-\mathbf{g})^T\cdot(-\mathbf{g})$ *[207] allowing the definition of the L-curve as a parametric plot in* λ*, and equivalently* α*, through Eq. (7.29),*

$$\mathcal{L}(\mathbf{H},\mathbf{g}) \equiv \left\{(\eta=\log[\varepsilon],\ \rho=\log[||\mathbf{H}\cdot\mathbf{p}_\varepsilon-(-\mathbf{g})||_2]) \;\middle|\; \varepsilon>0,\ \mathbf{p}_\varepsilon \textit{ is optimal for TRS}\right\}, \quad (7.30)$$

such that any point (η,ρ) *on the curve* $(||\mathbf{p}_\alpha||_2,\ ||\mathbf{H}\cdot\mathbf{p}_\alpha-(-\mathbf{g})||_2)$ *is the Tikhonov solution corresponding to the TRS with* $\varepsilon = ||\mathbf{p}_\alpha||_2$*,*

$$\rho = \min||\mathbf{H}\cdot\mathbf{p}-(-\mathbf{g})||_2 \textit{ subject to } ||\mathbf{p}||_2\le\eta, \qquad 0\le\eta\le||\mathbf{p}_0|| \quad (7.31)$$

$$\eta = \min||\mathbf{p}||_2 \textit{ subject to } ||\mathbf{H}\cdot\mathbf{p}-(-\mathbf{g})||_2\le\rho, \qquad \rho_0\le\rho\le\rho_\infty, \quad (7.32)$$

where $\mathbf{p}_0$ *and* ρ_0 *correspond to the unregularised solution.*

First suggested by Lawson and Hansen [208] the L-Curve graphically summarises the relationships between the solution norm and the regularisation error. A typical ill-posed problem has an L-Curve similar to the schematic shown in Figure 7.6. By its construction through the TRS it is impossible to find a solution that lies below the L-Curve, so any regularised solution must lie on or above the L-Curve. The L-Curve boundary can be related to the Tikhonov solution by noting that the

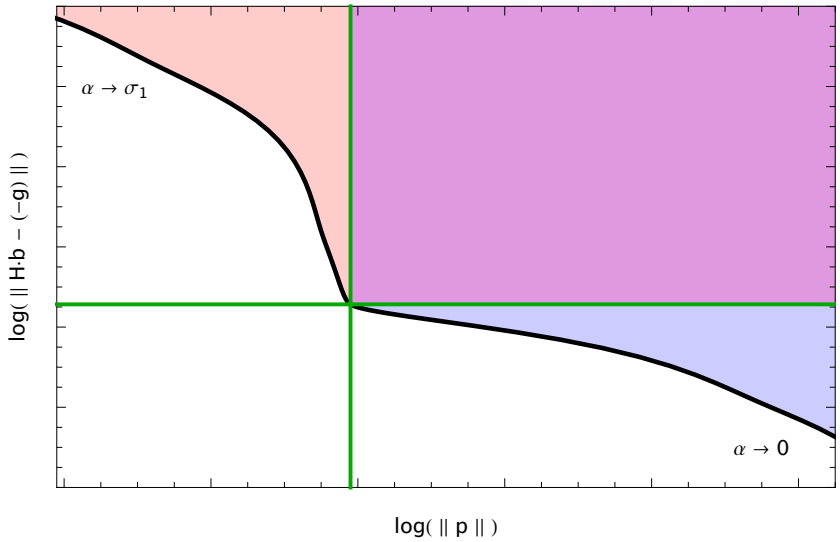


Figure 7.6: Schematic of an L-Curve for a typical ill posed problem. The Tikhonov regularised solutions lie on the L-curve boundary (black line). The regularisation parameter providing optimal trade-off between solution and residual norms is indicated by green lines to the axes. Solutions lying in the blue region have excessive noise, whilst solutions in the red area contain excessive regularisation error (with purple containing both noise and regularisation error).

Tikhonov regularised solution, $\mathbf{p}_\alpha$, is optimal for the TRS and hence for a given η there does not exist a solution with smaller residual norm $||\mathbf{H} \cdot \mathbf{p}_\alpha - (-\mathbf{g})||_2$ (or for a given ρ there is no smaller $||\mathbf{p}||_2$). The Tikhonov regularised solutions are therefore identified as the L-Curve boundary, marked in black on Figure 7.6, showing the L-Curve boundary as a parametric plot in α. A full analysis of the L-Curve and its relationship to Tikhonov regularisation is given in Ref. [209].

Two interesting regions can be seen on the L-Curve plot that identify the optimal regularisation parameter for the ill-posed problem in question. The region in which the L-Curve boundary is horizontal corresponds to under-regularised solutions, where noise is dominating and the solution vector is unphysical (illustrated as the blue region in Figure 7.6). Similarly a vertical region is present in the L-Curve boundary corresponding to the over-regularised region, where the solution has been oversmoothed and no longer aproximates a solution to the original ill-posed problem (illustrated as the red region in Figure 7.6). Intuitively it is clear that an optimum balance in the competing errors lies at L-Curve boundary corner between these regions, giving a solution that is as close as possible to the original ill-posed problem without becoming dominated by small singular value noise. This intuitive optimum is strengthened by Hansen [209,210] with a number of analyses showing that the point of maximum curvature in the L-Curve boundary corresponds to the optimal regularisation parameter.

With the connections between the L-Curve boundary and the optimal Tikhonov parameter established each Newton step in the YW optimisation can be correctly regularised by locating the elbow on the corresponding L-Curve. An algorithm for efficiently locating the elbow of an L-Curve is presented by Grodzevich and Wolkowicz in Ref. [207] as the *regularisation parametrisation by trust-region sub-problem* (RPTRS) algorithm and uses the connection between TRS regularisation and a convex control function to efficiently traverse the L-Curve and identify the point of maximum curvature.

Whilst the RPTRS algorithm is general for all ill-posed problems its application to the YW-OEP problem revealed a number of peculiarities that require consideration for a robust implementation. Section 7.5.2 gives an overview of the algorithm's operation as it applies to general ill-posed problems and the interested reader is referred to Ref. [207] for a complete derivation, description and discussion of the RPTRS algorithm.The modifications to RPTRS required for the YW-OEP problem are detailed in Section 7.6.

7.5.2 The RPTRS algorithm

The RPTRS algorithm first seeks to bracket the elbow region with coarse grain stepping procedure starting from the upper bound of $\alpha = \sigma_1$, a known over regularised solution and hence to the left of the elbow. Coarse grained steps in α are made by exploiting a mapping to a related convex control function. The L-Curve (Eq. (7.30)) is evaluated at each point by solving the TRS with the trust region ε, to obtain the optimal solution $\mathbf{p}_\varepsilon$. The L-Curve curvature, $\kappa(\alpha)$ is evaluated analytically [207, 209, 210], and the coarse grained bracketing is terminated when a maximum in $\kappa(\alpha)$ has been passed; at this point the elbow must lie between the last 3 bracket points. The curvature is approximately concave in the region described by the final three bracket points and a simple bisection search in α is carried out to identify the location of the maximum.

To evaluate each of the P points visited on the L-Curve the algorithm must diagonalise an $N_{\text{pot}} + 1$ dimensioned square matrix related to the TRS, where N_{pot} is the number of potential basis functions. Consequently the RPTRS algorithm formally scales in operations as $O(PN_{\text{pot}}^3)$. In practice P is roughly constant with system size and can be removed from scaling considerations, giving a scaling of $O(N_{\text{pot}}^3)$ with potential basis size. Despite the formal cubic scaling of the diagonalisation step the overall pre-factor is very small and the RPTRS L-Curve search has a negligible impact on the total computational effort of a Newton step.

7.6 RPTRS for the OEP problem

Despite the RPTRS algorithm being general for all ill-posed problems[4] a naive implementation into the YW-OEP problem reveals a number of difficult cases that the original implementation fails to handle. These limitations arise from assumptions made in the construction of RPTRS and are addressed in the following sections.

7.6.1 Regularisation of the full potential

As the Newton optimisation progresses towards a minimum the gradient and corresponding Newton steps become necessarily small. The Tikhonov residual and penalty, ρ^2 and η^2 from Eq. (7.30), correspondingly become very small and approach machine precision. Thus in the final steps of the optimisation the L-Curve disappears amongst noise and the RPTRS parameter selection becomes impossible.

The vanishing of the Newton step and energy gradient are avoided by reformulating the Newton equation to give the next optimisation point $\mathbf{b}^*$ directly, rather than the step $\mathbf{p}$ required to reach it. To reformulate the Newton equation in this way consider that the optimisation step $\mathbf{p}$ can be constructed from next optimisation point $\mathbf{b}^*$ and current point $\mathbf{b}$ as,

$$\mathbf{p} = \mathbf{b}^* - \mathbf{b}. \tag{7.33}$$

Inserting this expression for $\mathbf{p}$ into the Newton equation of 6.25 gives,

$$\begin{aligned} \mathbf{H} \cdot (\mathbf{b}^* - \mathbf{b}) &= -\mathbf{g} \\ \mathbf{H} \cdot \mathbf{b}^* - \mathbf{H} \cdot \mathbf{b} &= -\mathbf{g} \\ \mathbf{H} \cdot \mathbf{b}^* &= -\mathbf{g} + \mathbf{H} \cdot \mathbf{b} \end{aligned} \tag{7.34}$$

let,

$$\mathbf{g}^* = \mathbf{g} - \mathbf{H} \cdot \mathbf{b} \tag{7.35}$$

then,

$$\mathbf{H} \cdot \mathbf{b}^* = -\mathbf{g}^*. \tag{7.36}$$

Which can be regularised and solved for $\mathbf{b}^*$ as in the original formulation of the Newton optimisation. With this construction $\mathbf{b}^*$ will not become small as the optimisation progresses and an L-Curve can

[4] It was applied in Ref. [207] to an image de-blurring problem.

be formed for all points in the optimisation. If the optimal coefficient vector is $\mathbf{b}^* = \mathbf{0}$, a situation that occurs, for example, when the reference potential is exact, then the problem requires no basis set contribution and hence no regularisation. Solving the modified Newton optimisation of Eq. (7.36) is termed *full potential* optimisation whilst the traditional Newton optimisation is termed *stepwise* optimisation. Formulating the Newton optimisation as a regularised form of Eq. (7.36) has the effect of applying the regularisation efforts to the full potential coefficient vector at each iteration, rather than forming the final coefficient vector as the sum of the regularised steps.

Solving the YW-OEP problem as a regularised full potential optimisation has a number of benefits over a stepwise regularisation, the first being a faster convergence for very ill-conditioned systems regularised with Tikhonov regularisation. As described in Section 7.3.2 the Tikhonov filtering restricts the optimiser's ability to explore the directions corresponding to the small singular values. This results in the optimisation stagnating the later stages as the non-singular directions have converged, leaving only the near singular directions unexplored. At each step a small portion of the singular directions pass through the Tikhonov filter, and a small reduction in energy is obtained by exploring them. This incomplete filtering results in many small steps being taken as the optimiser nears the minimum, delaying convergence. When the regularisation is applied in the full potential optimisation however the Tikhonov penalty is the full potential norm $||\mathbf{b}^*||$, rather than the individual step norm $||\mathbf{p}||$ and exploration of the singular directions can only occur until the potential norm penalty has grown sufficiently large giving a more definite convergence. Figure 7.7 shows a comparison between the exchange potentials regularised using Tikhonov regularisation for the neon atom converged to $< 10^{-5}$ $\mathrm{mE_h}$ in $\frac{\partial E}{\partial \mathbf{b}}$. A stepwise optimisation required 1166 iterations whilst a full potential optimisation required only 18.

The second advantage of the full potential optimisation is an overall improvement in the quality of the final potential compared to an equivalent stepwise optimisation. Comparison of the optimised potentials in Figure 7.7 against the numerical benchmark potential shows that whilst both optimisations produce good potentials at longer ranges regions close to the nucleus and around the inter-shell peak show more pronounced oscillations in the stepwise optimisation. This difference can be understood by considering that at each step in the stepwise optimisation a small amount of noise from the singular directions is permitted through the Tikhonov filter. As the final potential in a stepwise optimisation is the summation of all the individual optimisation steps this small noise can accumulate to produce significant oscillations in the final potential. In the full potential optimisation an accumulation of noise cannot occur as the total coefficient vector norm is penalised, not the individual step norm, so the small oscillations are penalised at every iteration.

The benefits of the full potential optimisation become more apparent as the OEP problem becomes more ill-conditioned and in a well conditioned problem, such as the case when the orbital and potential basis sets are equivalent, both optimisation schemes perform similarly. As a result of the benefits described above all OEP calculations in this work are performed using the full potential optimisation scheme of Eq. (7.36), unless otherwise noted.

7.6.2 Optimisation termination criteria

The Tikhonov regularisation scheme restricts the directions the Newton optimisation can explore through the penalty applied to the norm $||\mathbf{b}^*||$. This prevents the optimiser producing extreme oscillations in the elements of $\mathbf{b}$ to completely minimise the energy at the expense of a unphysical potential. Consequently in the regularised optimisation the energy gradient can never become $\mathbf{0}$ resulting in stagnation at a small, but non-zero, gradient around which small steps can be taken to little effect and in the regularised problem a single termination criteria on the gradient norm ceases to be sufficient. Instead it is necessary to include a minimum step size, $\max[\{|b_t^* - b_t|\}]$, and energy change $E_i - E_{i-1}$ between iterations as additional termination criteria. The inability to completely minimise the energy gradient is an unavoidable consequence of solving a regularised approximation of the true ill-conditioned system and indicates that the true energy minimum of the finite basis OEP problem corresponds to an unphysical potential.

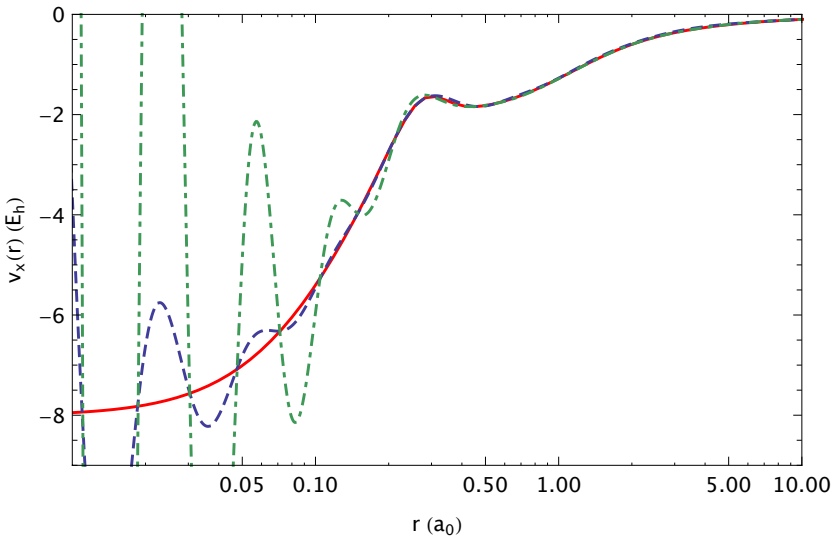


Figure 7.7: The exchange potential for the neon atom calculated using uncontracted Partridge3 orbital basis and an even tempered potential basis set with exponents 2^i, where $i = \{-5, \ldots, 20\}$. The potential was regularised using Tikhonov regularisation with $\alpha = 10^{-6}$. The full potential (dashed, blue) and stepwise (dot-dashed, green) optimisations are compared against the numerical benchmark (solid, red).

7.6.3 Global L-Curve scan

The original definition of the RPTRS algorithm in Ref. [207] does not address the possibility that the L-Curve may contain multiple elbows and simply halts when the first maximum in L-Curve curvature is encountered. This early termination can result in a bisection search of only the first[5] elbow or minor feature encountered, rather than the most pronounced. To correct this limitation the algorithm was modified to perform a more global maximisation of κ by extending the initial coarse grained scan to a minimum value, determined by the machine precision as $\alpha = 10^{-7}$. This restriction may seem overly high, 10^{-7} is of course well above machine precision, instead the restriction is set by the TRS Lagrange multiplier $\lambda = -\alpha^2$ and the precision of the linear algebra relating to it. This does not present a practical limitation to the algorithm as for the vast majority of systems $\alpha < 10^{-7}$ is too weak a regularisation to strongly influence the form of the potential.

A number of methods were implemented into the QUEST OEP optimiser for use in identifying the three adjacent coarse grain points from a full scan in α that bracket the most prominent elbow. The most robust method found was to produce a normalised L-Curve by mapping the the bracketing point η and ρ values to the range [0, 1], such that the smallest value in the coarse grain set is 0 and the largest is 1. The set of three points enveloping the elbow is identified from the normalised L-Curve as the three adjacent points that describe the sharpest clockwise angle. By performing the transformation to a unit L-Curve the ranges of the two measures becomes balanced, and the angles calculated give a better representation of the L-Curve features. A schematic of the global coarse grain bracketing procedure is given in Figure 7.8.

7.6.4 The absence of an elbow

For some systems and basis set choices the OEP equations are well-posed and the YW Hessian is well conditioned with no small singular values, examples being systems for which the potential is completely described by the reference alone and systems where the basis sets are well balanced. This is reflected in the L-Curve plot as the absence of an L shape and with the regularisation error increasing linearly with regularisation strength, and no elbow for the RPTRS algorithm to find. This

[5] i.e. most strongly regularised.

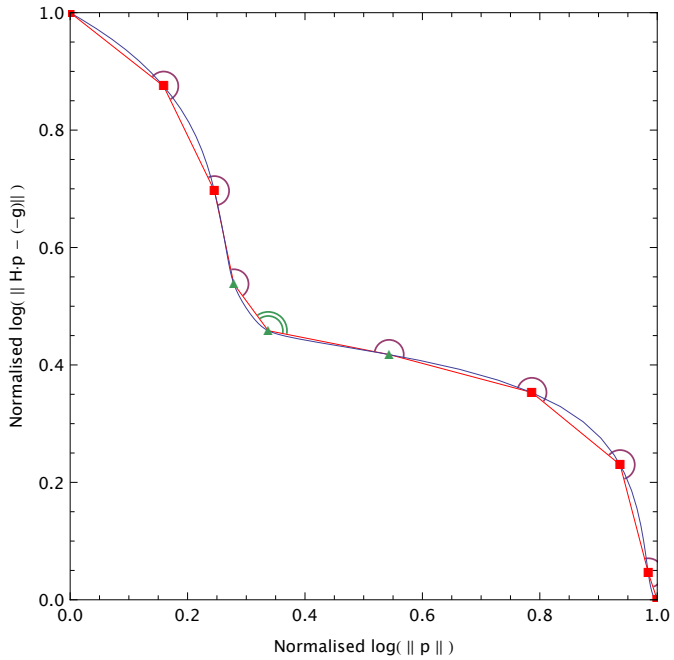


Figure 7.8: Schematic operation of the modified RPTRS L-Curve bracketing routine. The full L-Curve (blue) is approximated by a coarse grained scan (crosses, red). The elbow region (circles, green) is identified as the smallest clockwise angle described by three adjacent bracket points.

situation is detected by the algorithm when all adjacent bracket points describe clockwise angles of $\geq \pi$ radians, and a minimal regularisation of $\alpha = 10^{-7}$ is applied.

7.7 Atomic exchange potentials

The regularisation techniques established throughout this chapter, including the targeted regularisation techniques of Section 7.8, were implemented into the QUEST OEP module to allow their application to general potential based DFT problems. In particular the RPTRS algorithm of Ref. [207] was implemented and the modifications of Section 7.6 were developed during early applications of RPTRS to OEP problems. The regularisation techniques were initially developed for use with the exact exchange OEP problem though the generic construction of the QUEST OEP module allows their application to any potential based DFT problem.

A comparison of the RPTRS regularised YW-OEP exchange potentials with the numerical benchmark potential of Ref. [180] is presented in Figure 7.9 for the six lightest closed shell atoms. The YW-OEP potentials were calculated using the u-Partridge3 [200] orbital and u-UGBS [211] potential basis sets to give a basis set combination with a large orbital basis and a saturated potential basis representing an imbalanced basis combination, leading to ill-conditioned OEP problem. In all cases the RPTRS algorithm identified an appropriate level of regularisation and produced a smooth exchange potential that accurately captures all the essential features of the numerical benchmark.

It is immediately apparent however that the RPTRS regularised potentials remain oscillatory and inaccurate in the near nucleus regions, despite an optimal Tikhonov regularisation parameter being identified. The origin of the near nucleus oscilations is elucidated when the radial potential is compared with the radial electron density, as shown in Figure 7.10 for the neon atom. The small radial electron density $(4\pi r^2 \rho(r))$ near the nucleus prevents the potential in this region from contributing meaningfully to the energy and consequently the high exponent potential basis functions that dominate this region are not effectively targeted by the YW optimiser. As a result of this energetic freedom the near nucleus coefficients remain under-determined and the Tikhonov regularisation acts only to restrict the severity of the oscillations, confining them to the near nucleus region. The appearance of near nucleus oscillations in YW optimised OEPs has be noted elsewhere [183, 212–214] and their

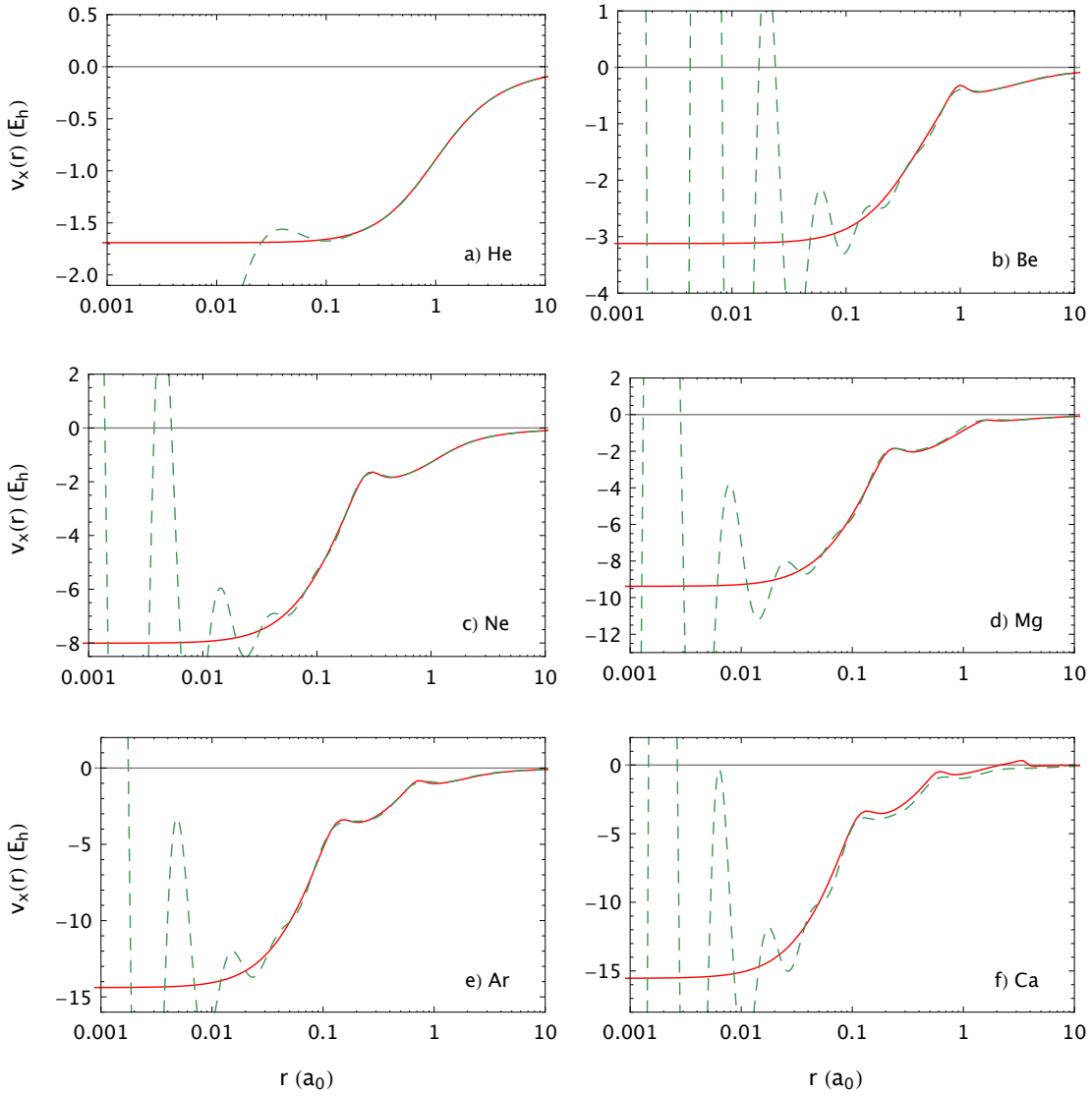


Figure 7.9: Exchange potentials for closed shell atoms (from top left: He, Be, Ne, Mg, Ar, Ca) calculated using the uncontracted u-Partridge3 [200] / u-UGBS [211] basis sets regularised with RPTRS regularisation (dashed, green). Benchmark potentials were calculated using the Talman–Shadwick [180] numerical routine (red).

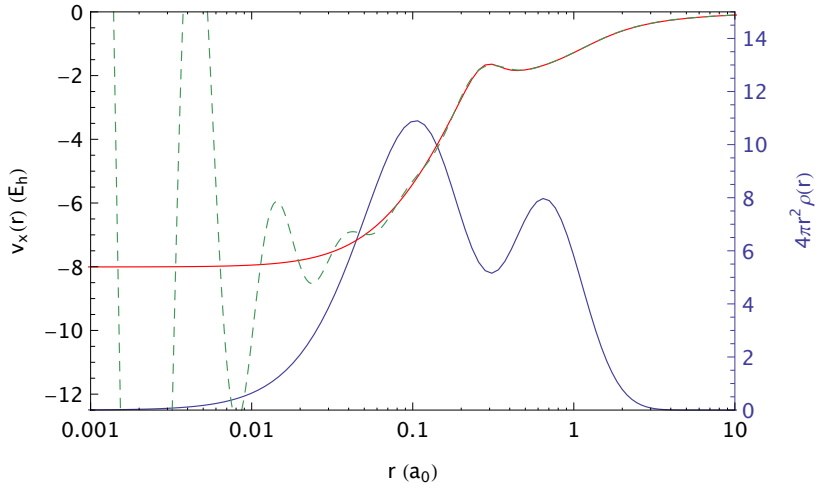


Figure 7.10: Exchange potentials for the neon atom calculated using the u-Partridge3 [200] / u-UGBS basis sets regularised with RPTRS regularisation (dashed, green) and the Talman–Sahdwick numerical benchmark of Ref. [180] (red). The radial electron density is plotted (blue) against the right hand scale.

persistence despite the use of an optimal regularisation parameter reveals a general limitation of standard Tikhonov regularised OEP.

7.8 Targeted regularisation methods

The persistence of noise in the near nucleus regions of Tikhonov regularised calculations implies that the sharper, high exponent potential basis functions are remaining under regularised when α has been set appropriately for the more diffuse functions. This imbalance suggests the high exponent potential basis functions should be targeted with a more aggressive regularisation than the more energetically significant diffuse functions. A complete removal of the high exponent potential basis functions is not practical, as it is hard to know *a priori* which functions should be cut. It is also not desirable to remove the sharp potential basis functions completely as when properly controlled they may contribute beneficially to the OEP.

The following section explores how the problematic high exponent functions may be targeted specifically by equipping the regularisation schemes with additional information from the potential basis kinetic energy integral matrix, allowing additional control to give high quality potentials across all space.

7.8.1 Generalised Tikhonov regularisation

The Tikhonov regularisation technique ensures a smooth potential by imposing the restriction that the norm of the potential coefficients, $||\mathbf{b}^*||$, must be as small as possible for a given residual, $||\mathbf{H}\mathbf{b}^* - (-\mathbf{g})||$. It is clear from the analysis of Section 7.7 that this restriction applies insufficient regularisation in regions close to the nucleus. Whilst the potential in the near nucleus regions does not contribute strongly to the energy, an unphysical near nucleus potential breaks the virial relations discussed in Section 7.9, and can adversely affect the accuracy of response property calculations. The failure of the RPTRS regularisation scheme to prevent these oscillations shows that simply imposing a penalty on the potential coefficient norm is insufficient to prevent noise in this region. We should require instead that the sharp basis functions are weighted more heavily in the Tikhonov penalty functional than the diffuse functions, requiring a *generalised Tikhonov regularisation*.

Rather than simply requiring a small coefficient vector, $||\mathbf{b}||$, we shall wish to impose some other desired property on the potential instead by requiring that the generalised measure $||\mathbf{Bb}||$ remains small, with the penalty matrix $\mathbf{B}$ encoding the desired property. To achieve this regularisation the cost functional is modified to form,

$$||\mathbf{H} \cdot \mathbf{b} - (-\mathbf{g})||^2 + \alpha^2 ||\mathbf{B} \cdot \mathbf{b}||^2. \tag{7.37}$$

Similarly to Section 7.3.2 the cost functional of Eq. (7.37) is minimised by the system of equations,

$$(\mathbf{H}^{\mathrm{T}} \cdot \mathbf{H} + \alpha^2 \mathbf{B}^{\mathrm{T}} \cdot \mathbf{B})\mathbf{b} = \mathbf{H}^{\mathrm{T}} \cdot (-\mathbf{g}), \tag{7.38}$$

which may be solved using standard matrix techniques. Following this construction the residual is minimised subject to the constraint encoded in the penalty matrix $\mathbf{B}$ and the desired property is reflected in the final potential. The standard Tikhonov regularisation of Section 7.3.2 is recovered from the generalised form of Eq. (7.37) if $\mathbf{B} = \mathbf{I}$, such that each function is weighted equally in the penalty norm.

7.8.2 The choice of penalty matrix

It was shown in Section 7.7 that the YW-OEP scheme requires a weighting of regularisation towards the near nucleus functions to prevent oscillations persisting in this region. Many choices of $\mathbf{B}$ that impose this weighting are possible and a convenient choice for the OEP problem is the kinetic energy integral matrix in the potential basis (the KE matrix). This matrix is constructed by applying the kinetic energy operator of Eq. (1.35) to the potential basis functions $\{\phi\}$,

$$T_{\mu\nu} = -\frac{1}{2} \int \phi_\mu^*(\mathbf{r}) \nabla^2 \phi_\nu(\mathbf{r}) \mathrm{d}\mathbf{r}. \tag{7.39}$$

The diagonal elements of the kinetic energy matrix give a measure of the sharpness the basis function ϕ_μ with sharp functions having a large curvature and hence large elements, typically in the millions, whilst diffuse functions have only small curvature with elements on the order of 10^{-2}.

It was observed during the development of a generalised L-Curve analysis that choices of penalty matrix with large off-diagonal elements could produce coupling between elements in the solution vector that broke the L-Curve monotonicity, preventing a proper analysis. To avoid such couplings between elements and ensure the L-Curve analysis was always possible, the choice of penalty matrix was restricted to diagonal matrices. Such a restriction may be lifted if the regularisation problem is reduced to *standard form* [215], though this was not necessary for this work. A diagonal penalty matrix can be viewed as a vector of weights that serve to attenuate or amplify an expansion coefficient's contribution to the penalty norm, thereby allowing it greater or lesser freedom during the optimisation.

The kinetic energy integral matrix is not generally diagonal, though it can be made to be with an appropriate orthogonalisation of the potential basis set. In practice this orthogonalisation was not required and it was sufficient simply to discard the off-diagonal elements, forming a matrix termed the *diagonal KE matrix*. The diagonal elements of the KE matrix are large for sharp basis functions and quickly become small for more diffuse functions, targeting the regularisation onto the problematic near nuclear functions when used as the penalty matrix. In practice the raw diagonal KE matrix imposed too weak a penalty on the diffuse functions and resulted in an under-regularisation of the valence and asymptotic regions. This was corrected by adding the identity matrix to the diagonal KE matrix to impose a minimum regularisation weight of 1 upon all functions. The final diagonal KE penalty matrix, denoted as $\tilde{\mathbf{T}}$, was formed from Eq. (7.39) as,

$$\tilde{\mathbf{T}} = \mathrm{diag}[\mathbf{T}] + \mathbf{I}. \tag{7.40}$$

7.8.3 The generalised Tikhonov L-Curve

The near nucleus region that is problematic for identity based Tikhonov regularisation can be penalised more heavily using a generalised Tikhonov scheme but an automatic parametrisation method

is required for its use in a black box calculation. Inspired by the RPRTS automatic parametrisation scheme the generalised Tikhonov regularisation scheme was combined with the maximum L-Curve curvature criterion to form such a scheme, termed the generalised Tikhonov L-Curve scheme (TLC). The L-Curve formulation of Theorem 7.5.1 is modified to account for the penalty matrix by reformulating the solution norm measure, η, as the generalised semi-norm $||\mathbf{B}\mathbf{b}^*||$. The generalised L-Curve formulated in this way has the same properties as the identity matrix Tikhonov L-Curve, as shown by Hansen in Ref. [209] through relation to the TRS in standard form. The derivatives of the generalised L-Curve required for the corner finding algorithm could be cheaply estimated by finite difference without significantly increasing calculation time, removing the practical need for analytical derivatives from a reduction to standard form. Following this approach a simplified L-Curve search scheme was formulated for identifying the point of maximum curvature on the generalised L-Curve.

A coarse grained bracketing scan of the L-Curve was achieved by evaluating $\log[\eta]$ and $\log[\rho]$ for a set of points $\{\alpha_i\}$ linearly spaced on a log scale between the same upper and lower bounds of Section 7.6.3,

$$\alpha_{i+1} = 0.25\alpha_i, \tag{7.41}$$

where 0.25 controls the coarse grain step length. The choice of step length was chosen empirically to strike a balance between stepping completely over the elbow and evaluating an excessive number of points.[6] Once the bracketed region had been identified the exact elbow position was again determined by a simple bisection maximisation of the curvature. The TLC procedure was checked for consistency against RPTRS by choosing the identity matrix as the penalty matrix, and showed good agreement. Whilst lacking some of the refinements of the later RPTRS algorithm TLC is similar to the early L-Curve search algorithms of Ref. [210].

Throughout the following text the TLC regularisation scheme with the $\tilde{\mathbf{T}}$ penalty matrix of Section 7.8.2 is denoted TLC(T), whilst identity matrix based regularisation is denoted TLC(I).

7.8.4 The Yang smoothing norm

An alternative regularisation scheme for the finite basis OEP problem termed the *smoothing norm* was suggested by Yang *et al.* in Ref. [216] as a direct modification of the energy function in the OEP optimisation to include a quadratic penalty term. In the smoothing norm procedure the energy function is directly regularised becoming,

$$\Omega_\alpha(\mathbf{b}) = E^{\mathrm{YW}}(\mathbf{b}) + \alpha||\nabla v_{\mathbf{b}}(\mathbf{r})||^2, \tag{7.42}$$

where $||\nabla v_{\mathbf{b}}(\mathbf{r})||^2$ is the *smoothing norm* $||\nabla v_{\mathbf{b}}(\mathbf{r})||^2 = 2\mathbf{b}^{\mathrm{T}}\mathbf{T}\mathbf{b}$ and $\mathbf{T}$ is the full kinetic energy integral matrix of the potential basis. The parameter α has the same function as the α parameter in Tikhonov regularisation, allowing a bias-variance trade-off. The first derivative of the modified energy expression is then,

$$\nabla_{\mathbf{b}}\Omega_\alpha = \nabla_{\mathbf{b}}E^{\mathrm{YW}} + 4\alpha\mathbf{T}\mathbf{b}, \tag{7.43}$$

with the Hessian matrix,

$$\nabla^2_{\mathbf{b}}\Omega_\alpha = \nabla^2_{\mathbf{b}}E^{\mathrm{YW}} + 4\alpha\mathbf{T}. \tag{7.44}$$

The Yang smoothing norm technique is remarkably effective in producing a smooth, physically reasonable potential with the near nucleus oscillations controlled, a success that is readily understood from the inclusion of $\mathbf{T}$ into the penalty expression. The scheme is also able to converge efficiently as quadratic dependence of the objective function on the smoothing norm ensures a global minimum in the overall objective function for any strength of regularisation.

Despite the many benefits present in the Yang smoothing norm the scheme fails to provide a black box regularisation solution, with the choice of α remaining unknown. Within Ref. [216] Yang *et al.* make use of an L-Curve type analysis to inform the choice of α, though they do not attempt this in a black box manner. The L-Curve like analysis of the smoothing norm in Ref. [216] is defined as a parametric log-log plot between the variance measure $||\nabla v_{\mathbf{b}}||^2$ and the bias measure $E^{\mathrm{YW}} - E^{\mathrm{exact}}$. Whilst an optimal α can be identified from the elbow of this plot it remains an unsatisfactory method

[6] Bracketing that is too fine may also result in minor features of the L-Curve being incorrectly identified as the elbow. In practice the method was not overly sensitive to choice of step length.

for runtime parameter selection and the authors of Ref. [216] note that it cannot provide the *a priori* judgement of regularisation strength required for routine applications. The limitation of this L-Curve like analysis lies in the bias measure of $E^{\mathrm{YW}} - E^{\mathrm{exact}}$, requiring not only a full OEP calculation per point evaluated but also the knowledge of an unregularised solution for the problem to construct the bias measure. For the finite basis OEP problem the unregularised solution is ill-defined but is taken in Ref. [216] as the Hartree–Fock energy in the same orbital basis as a reasonable estimate. In the absence of a suitable bias measure that is available *a priori* the runtime determination of smoothing norm regularisation strength by this L-Curve like analysis remains impossible.

7.8.5 Improvement of the near nucleus region

A comparison between numerical benchmark exchange potentials and finite basis YW-OEP exchange potentials regularised with the TLC(T) scheme is given in Figure 7.11 for the light closed shell atoms. When compared with the equivalent RPTRS regularised potentials of Figure 7.9 the improved regularisation of the TLC(T) scheme is strikingly apparent. The use of $\tilde{\mathbf{T}}$ in a generalised Tikhonov scheme has successfully weighted regularisation towards the tight potential functions and prevented the near nucleus oscillations observed with identity matrix based regularisation whilst maintaining accuracy in the valence regions. It should be stressed that beyond choosing $\tilde{\mathbf{T}}$ as the penalty matrix no user input was required to identify the correct regularisation strength.

7.9 Exact constraints for multiplicative potentials

Numerical benchmark potentials are not generally available for polyatomic molecular systems as the absence of exploitable symmetry makes their calculation problematic, internal measures of potential quality are required instead. Such internal measures can be formed by considering conditions that must be satisfied by the exact OEP as a true functional derivative, but that cannot be perfectly satisfied when the OEP is expressed in a finite basis. A more physically reasonable finite basis potential will agree closely with more exact conditions than a less well regularised unphysical potential.

The following sections discuss some conditions related to the exact exchange functional in OEP-DFT that can only be properly obeyed by a potential that has the form of a functional derivative. With these internal measures established a quantitative analysis of regularisation performance can be carried out for general molecular species without requiring a benchmark potential for comparison.

7.9.1 Hartree–Fock energy bound

The HF method is a variational search for the Slater determinant that minimises the expectation value of the Fock operator of Eq. (1.17) with the non-local potential $v_{\mathrm{HF}}(\mathbf{r})$ of Eq. (1.18). The exact exchange OEP method can be seen as a related problem: the variational search for the Slater determinant that minimises Eq. (1.17) with $v_{\mathrm{OEP}}(\mathbf{r})$, a local effective potential. The solutions must therefore be different, as the OEP orbitals minimise a local multiplicative exchange potential, where the Hartree–Fock orbitals minimise the fully non-local exchange potential. By the variation principle the exact exchange OEP solution must be higher in energy than the Hartree–Fock solution in a complete basis. In the a finite basis however it is always possible to recover the Hartree–Fock energy from the OEP equations, though the corresponding potential will be highly unphysical [217].

The regularisation schemes detailed throughout this chapter restrict the form of the final effective potential by filtering information from the OEP equations, consequently they have the effect of raising the final electronic energy away from the Hartree–Fock bound. Performing only a very weak regularisation allows OEP solution to approach the Hartree–Fock energy at the expense of a poor quality potential, whilst an excessive regularisation will cause the energy to become too high. The goal of a successful regularisation is therefore to find the minimum OEP energy whilst maintaining a physically meaningful potential. From this relationship the deviation of the OEP energy above the equivalent basis Hartree–Fock energy roughly indicates regularisation quality, exposing over or under regularisation through energy differences that are too large or small respectively. Unfortunately due

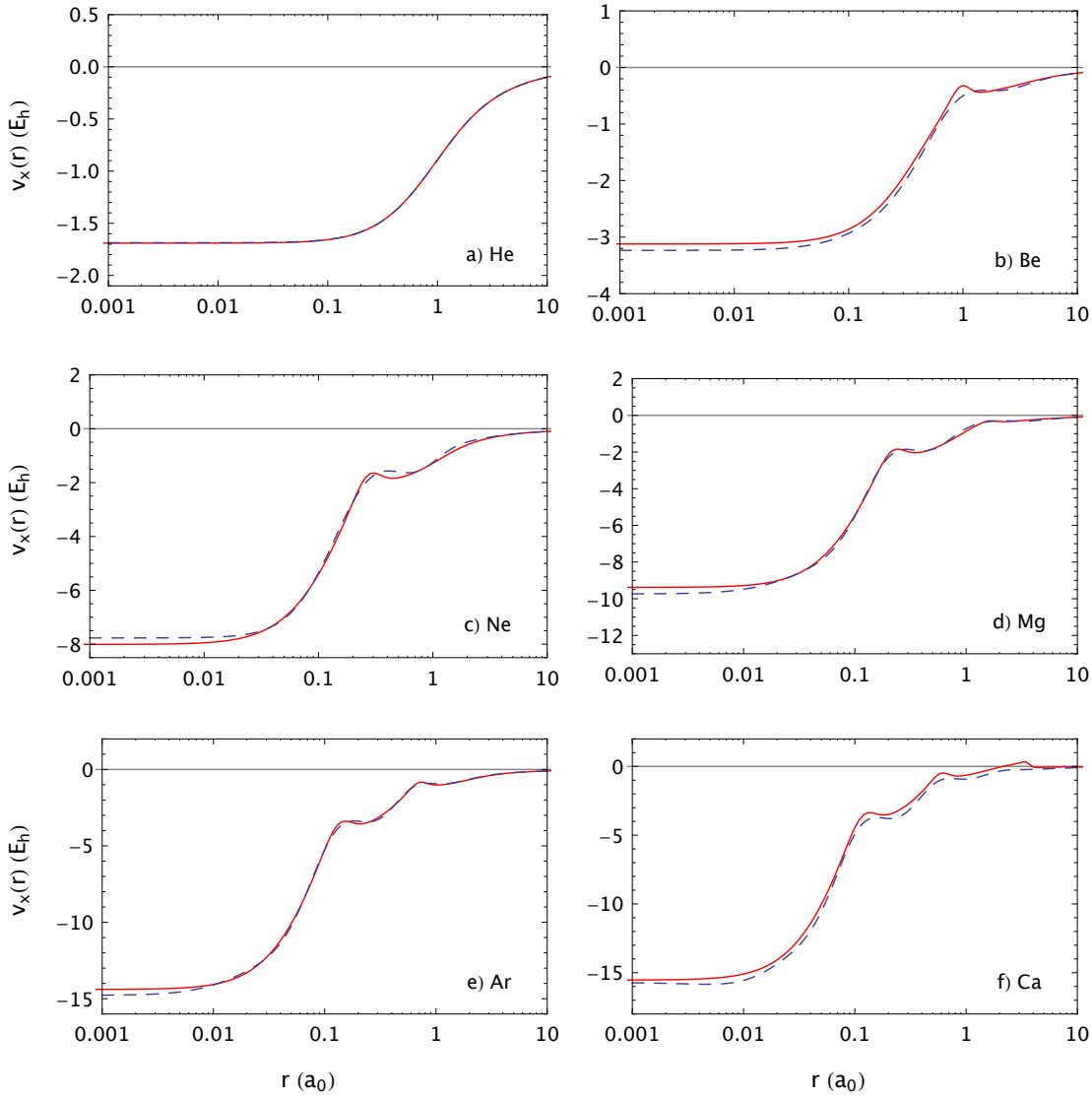


Figure 7.11: Comparison of exchange potentials for closed shell atoms calculated using the u-Partridge3 [200] / u-UGBS [211] basis sets regularised with and TLC(T) (dashed, blue) against benchmark potentials are calculated using the Talman–Shadwick [180] numerical routine (red). Equivalent potentials regularised with the RPTRS scheme are presented in Figure 7.9.

to the ill-posed nature of the finite basis OEP problem the exact OEP energy is ill defined and cannot be directly compared against.

7.9.2 The HOMO condition

The Hartree–Fock Hamiltonian and the OEP Hamiltonian have the same form and differ only through the definition of the potential, which is a fully non-local operator in HF theory and a local multiplicative operator for the OEP. From this it is shown by Refs. [218] and [219] that,

$$\left\langle \varphi^{\mathrm{OEP}}_{\mathrm{HOMO}} \right| v_{\mathrm{x}}(\mathbf{r}) \left| \varphi^{\mathrm{OEP}}_{\mathrm{HOMO}} \right\rangle - \left\langle \varphi^{\mathrm{OEP}}_{\mathrm{HOMO}} \right| v^{\mathrm{HF}}_{\mathrm{x}}(\mathbf{r}) \left| \varphi^{\mathrm{OEP}}_{\mathrm{HOMO}} \right\rangle = 0 \tag{7.45}$$

the energy of the highest occupied OEP MO (HOMO) must be the same for both the HF and OEP exchange potentials, in the case of the exact OEP. Note that this relationship only holds for the HOMO and will in general not be true for the lower lying orbitals. In a finite basis representation the OEP will not be exact and the two orbital energies will differ, with the difference becoming more pronounced for less accurate OEPs.

The HOMO condition is particularly sensitive to the quality of the OEP in the valence region, where the HOMO orbital density is greatest, and to constant shifts to all potential coefficients that raise or lower the OEP, which act to raise or lower the OEP orbital energy. It is possible to directly constrain the OEP optimisation to force adherence to the HOMO condition through addition of a penalty function formed from Eq. (7.45), thereby preventing constant shifts in the potential [220]. Enforcing the HOMO constraint is not considered further in this work, but is suggested in Section 7.10.2 as a means to further improve the TLC(T) regularised potentials.

7.9.3 The virial conditions

Through considerations of the exact scaling relations required of the potential Ghosh and Levy [221, 222] derived virial conditions for the OEP exchange and kinetic energy terms,

$$E_{\mathrm{x}}\left[\{\varphi\}\right] - \int v_{\mathrm{x}}(\mathbf{r})(3\rho(\mathbf{r}) + \mathbf{r}\cdot\nabla\rho(\mathbf{r}))d\mathbf{r} = 0, \tag{7.46}$$

$$T_{\mathrm{s}}\left[\{\varphi\}\right] + \frac{1}{2}\int v_{\mathrm{s}}(\mathbf{r})(3\rho(\mathbf{r}) + \mathbf{r}\cdot\nabla\rho(\mathbf{r}))d\mathbf{r} = 0. \tag{7.47}$$

A full proof of the virial relations can be found in Ref. [221] with a simplified derivation given in Ref. [223].

If the optimised exchange potential is not the functional derivative of $E_{\mathrm{x}}\left[\{\phi\}\right]$ then the virial conditions of Eqs. (7.46) and (7.47) cannot be simultaneously obeyed, and will deviate from zero. As the properly regularised OEP will approximate a true functional derivative, and a poorly regularised potential will not, the virial conditions can be a sensitive measure of potential quality, reflecting both under and over regularisation in its deviation from zero.

Care must be taken however not to over-emphasise the importance of the virial relations as a measure of potential regularisation quality for two reasons. Firstly the virial measures are only truly obeyed in the orbital basis limit and are strongly sensitive to orbital basis quality, thus in smaller orbital basis sets even an optimally regularised potential may give large deviations in the virial relations. Secondly, neither virial relation is more important than the other and both should be taken in combination to properly assess potential quality. As the relations are sensitive to different qualities in the potential it is possible to tune the regularisation parameter such that one of the two relations is obeyed exactly, and in general this will result in a large deviation of the other. A full examination of this effect is given in Section 7.12. Despite these limitations, the virial conditions remain a valuable tool as an internal measure of potential quality.

7.10 Evaluation using exact constraints

The following section examines the quality and flexibility of the newly formulated automatic parametrisation methods as applied to the exact exchange OEP problem for small molecules. The quality of

the calculated potentials is examined through their adherence to the exact conditions described in Section 7.9. Initially, in Section 7.10.1, analysis is focussed on the N_2 molecule and the automatic regularisation schemes are compared against the full range of smoothing norm regularisation strength. Following this a systematic expansion of the N_2 potential basis is made in order to test the ability of the automatic parametrisation schemes to correctly adjust regularisation as the basis sets become more imbalanced. A general assessment of regularisation flexibility and performance is then established by investigating the quality of the potentials for a set of small molecules using the exact conditions of Section 7.9.

7.10.1 The orbital and potential basis limit

The exact exchange OEP was calculated for the N_2 molecule with the basis set combination of u-aug-cc-pVQZ / u-aug-cc-pV6Z to produce a system with a pronounced imbalance between potential and orbital sets. In Figure 7.12 the RPTRS and TLC(T) regularised solutions (dotted and dashed lines respectively) are compared with potentials regularised using the smoothing norm set at a range of parameters (solid line). Adherence to the exchange (blue) and kinetic (red) virial conditions is shown alongside energy deviation from the HF limit (green). The manual scan in the smoothing norm parameter reveals that an optimal trade-off between measures is found at $\sim 5\times10^{-5}$ for this system, with both exchange and kinetic virial conditions having small values. The RPTRS regularised potentials performed poorly in this case, producing a large deviation in virial conditions. This failure arises from the under-regularised core functions producing oscillatory potentials in regions where $|\nabla\rho|$ is large, breaking the virial relations of Eqs. (7.46) and (7.47), a failure that is consistent with the atomic potential plots of Figure 7.9. The TLC(T) scheme produces potentials that do not suffer near nucleus noise and and therefore are roughly equivalent to the optimum conditions manually identified from the manual smoothing norm regularisation scan.

The analysis of Figure 7.12 further serves to highlight the danger inherent in minimising one measure in isolation. Following the blue solid line that plots the exchange virial condition as a function of smoothing norm strength one can identify that the virial exchange measure becomes 0 at $\alpha \approx 2\times10^{-5}$. Regularisation with this parameter value however produces a worse kinetic virial condition than could be obtained with stronger regularisation. Both virial conditions should be satisfied, though in a finite basis this is impossible and a balance must be found instead. Deciding regularisation strength to simply minimise any one condition is consequently ill advised, and an appropriate regularisation should be considered as a trade-off between the competing factors.

An automatic regularisation scheme should adjust the regularisation to become stronger as the basis sets become more imbalanced, allowing the potential basis to be systematically expanded to the basis set limit without the potential becoming unphysical. Such a systematic expansion is difficult using a manually set regularisation as it is not clear how the strength parameter should be increased to match the increasingly ill-posed OEP problem. To test the ability of the automatic regularisation schemes to correctly make this adjustment the exact exchange OEP was calculated for N_2 using the u-aug-cc-pVQZ orbital and a series of augmented Dunning basis sets with increasing cardinal number u-aug-cc-pVXZ (X = D, T, Q, 5 and 6) for the potential basis. The calculations were regularised with the RPTRS and TLC(T) regularisation schemes as well as the smoothing norm scheme with $\alpha = 10^{-6}$.

In Figure 7.13 it is seen that the increasing potential basis size initially improved virial relations, showing that the smaller sets were insufficient to properly represent the potential. As the potential basis increased in size the TLC(T) regularisation maintained consistent virial conditions and deviation from the HF energy showing a consistent level of regularisation and potential quality. The smoothing norm scheme initially gave good regularisation, but this became insufficient as the basis sets became more imbalanced. The onset of an under-regularised potential can be seen in the deterioration of the virial conditions and is accompanied by a drop in the deviation from the HF energy, showing a stronger regularisation was required. The RPTRS scheme gave poor virial conditions in larger potential basis sets whilst maintaining a consistent deviation from the HF energy. This contrast is explained by the increasing number of high exponent functions in the larger basis sets exaggerating the oscillations in near nucleus regions. Such oscillations break the virial conditions but do not affect the overall energy, so the deviation from the HF energy remains consistent, but virial conditions deteriorate significantly as the cardinal number increases.

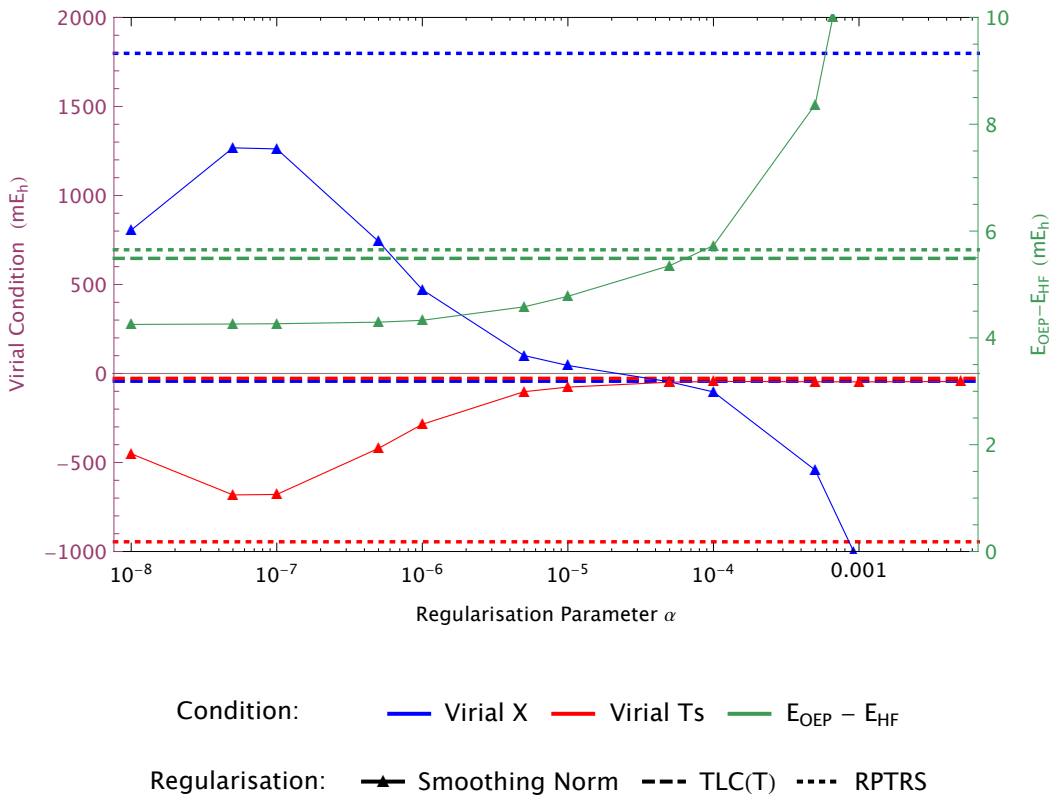


Figure 7.12: Comparison between potentials calculated with smoothing norm (triangles) regularisation with regularisation strengths shown on the horizontal axis, RPTRS automatic regularisation (dotted lines) and TLC(T) automatic regularisation(dashed lines) are plotted as horizontal lines. For each regularisation the virial exchange condition is plotted in blue and the virial kinetic condition is plotted in red, both against the left hand (purple) axis. The energy difference between the exact exchange OEP solution and Hartree–Fock solution is plotted in green against the right hand (green) axis. All calculations used the u-aug-cc-pVQZ / u-aug-cc-pV6Z basis set combination.

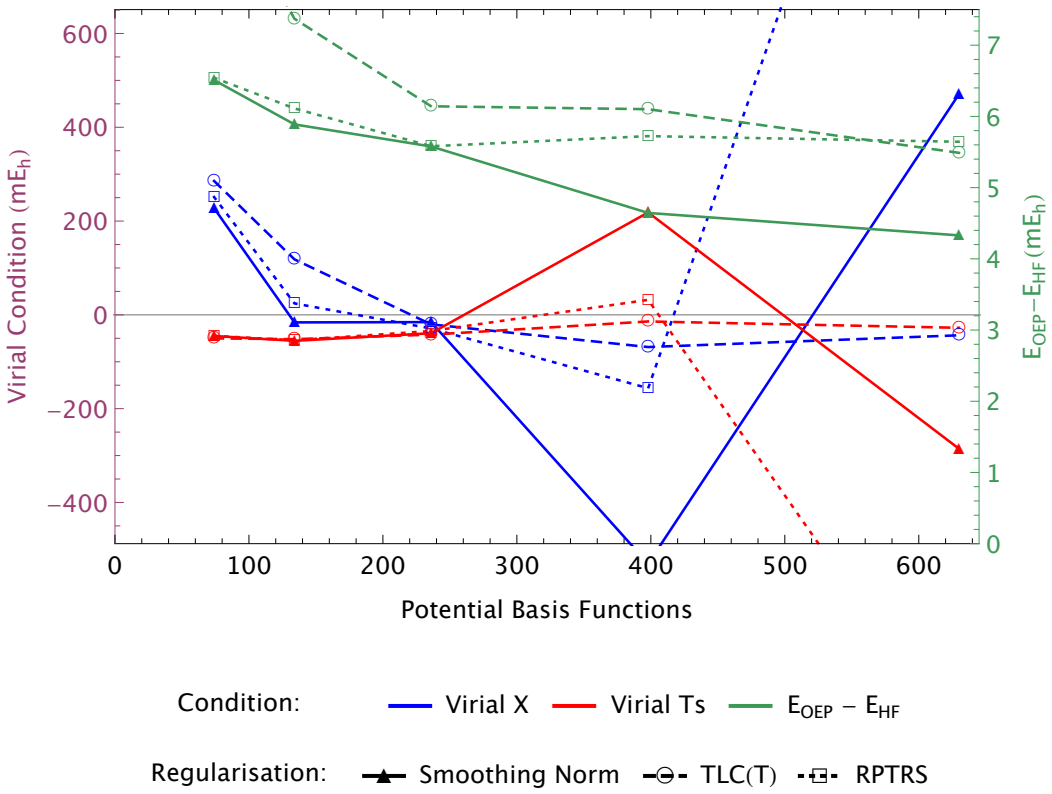


Figure 7.13: Comparison between potentials regularised with smoothing norm (solid, triangle), RPTRS automatic regularisation (dotted, square) and TLC(T) automatic regularisation (dashed, circle). For each regularisation the virial exchange condition is plotted in blue and the virial kinetic condition is plotted in red, against the left hand purple axis. The energy difference between the exact exchange OEP solution and Hartree–Fock solution is plotted in green against the right hand green axis. All calculations used the u-aug-cc-pVQZ orbital basis with a systematic increase of potential basis u-aug-cc-pVXZ (X = D, T, Q, 5, 6), the number of potential basis functions are shown on the horizontal axis.

The consistent regularisation maintained by the TLC(T) scheme as the basis set was expanded clearly shows the utility of an automatic parameter selection scheme, and that the TLC(T) scheme successfully in identified an optimal regularisation as the basis sets become more imbalanced. The ability to perform a consistently regularised calculation in the basis set limit without requiring a manually defined α stands as a stark improvement over previous schemes for which black box calculations are not possible. It is hoped that the increased confidence of a rigorous regularisation technique will open the way for finite basis OEP techniques to be more widely adopted.

7.10.2 Analysis through exact relations

Exact exchange OEP calculations were performed for a small set of test molecules (Ne, Ar, N_2, CO, H_2O, HCN and NH_3) with the u-aug-cc-pVQZ / u-aug-cc-pV6Z basis sets. The calculations were regularised using the RPTRS and TLC(T) automatic regularisation schemes as well as the TSVD, Tikhonov and smoothing norm methods for comparison. For the manually set techniques, the regularisation parameter was set as $\alpha = 10^{-6}$ for all molecules, as a commonly cited value [185,213, 216]. The exact conditions detailed in Section 7.9 were calculated for each potential and tabulated in Table 7.1. As described in Section 7.9 and Section 7.10.1, care must be taken when interpreting the results of Table 7.1 as one cannot say that satisfying any one condition is any more important than

satisfying any other and a good regularisation should strike an optimal balance between all.

It is notable that in all cases the virial conditions are higher than commonly reported in other studies of the optimised effective potential [214, 223], with values more commonly reported as $<$10 mE_h elsewhere. The worse adherence to virial conditions observed here arises from the deliberate choice to imbalance the orbital and potential basis sets by saturating the potential basis, creating a more ill-conditioned problem. Whilst the regularisation schemes are able to control the influence of this imbalance the ill-posed problem is still more difficult than the balanced case. Due to the small size of the molecules in the current set it would be feasible to balance orbital and potential basis sets by increasing the orbital size. In larger molecules however this balance may not be feasible and utilising a larger potential basis than the orbital may be necessary to afford sufficient flexibility in the potential. In such cases a consistent regularisation scheme with an imbalanced choice is preferable. It has been reported by others [214, 224, 225] that using balanced orbital and potential basis sets can still fail to produce produce satisfactory potentials when both basis sets are small.

The identity matrix based RPTRS regularisation is unable to consistently produce low virial condition values, frequently producing potentials with very poor virial conditions. This failure can be understood by comparison with the standard Tikhonov regularised potentials, noting that the RPTRS scheme is simply an automatic parametrisation of standard Tikhonov regularisation. In all cases (excepting Ar for which RPTRS gave a poor exchange virial condition) RPTRS regularisation is an improvement on the simple $\alpha = 10^{-6}$ regularisation and the varying quality of results for Tikhonov and RPTRS regularisation can be understood as a systemic failure of identity matrix based regularisation. The poor virial conditions are attributed to the failure to properly regularise oscillations in the near nucleus regions, as seen in Figure 7.9. The poor virial conditions are in contrast to the relatively good HOMO conditions reported for the RPTRS and Tikhonov regularised potentials. As discussed in Section 7.9.2 the HOMO condition is largely insensitive to the near nucleus regions as the condition predominantly measures the quality of the valence regions. The good HOMO conditions with bad virial conditions implies that the valence regions were correctly regularised, whilst the near nuclear regions were not. As a result of this imbalance the identity matrix based regularisation schemes cannot be recommended for molecular applications.

The KE matrix (Section 7.8.2) based regularisation schemes (smoothing norm and TLC(T)) produce potentials with far closer adherence to the exact constraints, having eliminated spurious noise from the near nucleus regions. In all cases (excepting Ne) the TLC(T) regularised potentials were higher quality than the smoothing norm regularised potentials, giving smaller values for nearly all exact conditions, failing only for the HOMO condition (a failure discussed further in the following paragraph). In the case of neon, noise was identified in the valence region for TLC(T), suggesting an over-emphasis of near nucleus regularisation in this case and seen visually in Figure 7.11c. For some systems the smoothing norm gave potentials with similar condition values as the TLC(T) regularised potentials (Ne, Ar, H_2O and NH_3), though for other systems (N_2, CO and HCN) $\alpha = 10^{-6}$ proved to be insufficient regularisation. Such failures do not show a systemic inadequacy of the smoothing norm technique but instead highlight the difficulty in selecting an appropriate regularisation strength *a priori* for a general ill conditioned problem. In contrast to this TLC(T) regularisation is able to adjust regularisation strength to fit the system in question, and consequently gives a much smaller variation in potential quality.

The most apparent weakness of the TLC(T) regularisation scheme lies in the poor HOMO condition values. This can be understood from two systemic errors observed in molecular potentials regularised with the TLC(T) scheme. The first of these errors is the slight increase in noise in the valence region that can occur when the $\tilde{\mathbf{T}}$ penalty matrix weights the regularisation too heavily towards the sharp near nuclear functions, allowing excessive freedom in the diffuse functions. The addition of the identity matrix into $\tilde{\mathbf{T}}$ detailed in Section 7.8.2 corrects much of this error, though in some cases the weighting in the penalty functional appears to remain too focused on the tight functions. This analysis is supported by the observation that the identity based regularisation methods which penalise each function equally give much better HOMO conditions, suggesting that further improvements can be made in the choice of penalty matrix. The second systemic fault in TLC(T) is the possibility for constant shifts in the potential coefficients that may offset the OEP HOMO energy, breaking the HOMO condition. As discussed in Section 7.9.2 such shifts may be prevented by enforcing the HOMO condition during potential optimisation and the poor TLC(T) HOMO condition scores suggest this may be beneficial.

Table 7.1: Deviations from exact condition for exchange only OEP-DFT for a set of small molecules using the u-aug-cc-pVQZ / u-aug-cc-pV6Z basis set combination, all values are in units of mE_h. The TSVD, Tikhonov and smoothing norm (S. Norm) regularisation techniques require a manually set parameter, in all cases this parameter was set to $\alpha = 10^{-6}$ (denoted with *).

a)	Virial Exchange Condition				
	TSVD*	Tikhonov*	RPTRS	S. Norm*	TLC(T)
Ne	3.001	1.921	3.716	3.222	-18.664
Ar	0.120	2.390	147.009	-5.967	5.746
N_2	4187.000	4095.282	1742.107	470.568	-40.017
CO	3372.860	2971.388	2189.936	309.995	41.871
H_2O	25.395	15.464	2.082	-5.792	-1.585
HCN	-1713.851	-1828.126	-809.132	263.857	-102.558
NH_3	0.459	-11.343	1.547	-12.236	-3.855

b)	Virial Kinetic Condition				
	TSVD*	Tikhonov*	RPTRS	S. Norm*	TLC(T)
Ne	-6.002	-5.836	-4.997	-6.384	-4.916
Ar	-0.952	-0.579	-0.252	-0.872	0.457
N_2	-2141.730	-2096.271	-916.481	-285.424	-27.376
CO	-1738.182	-1537.540	-1145.287	-208.054	-71.575
H_2O	-20.700	-15.792	-8.566	-5.394	-9.355
HCN	830.764	887.690	378.312	-158.983	24.459
NH_3	-10.684	-4.737	-11.135	-4.613	-6.806

c)	E_{OEP} - E_{HF}				
	TSVD*	Tikhonov*	RPTRS	S. Norm*	TLC(T)
Ne	0.897	0.901	1.523	0.907	1.505
Ar	4.585	4.567	4.695	4.519	5.968
N_2	4.355	4.361	5.644	4.329	5.489
CO	4.323	4.336	5.468	4.282	5.355
H_2O	1.700	1.698	2.286	1.712	2.594
HCN	3.710	3.727	4.807	3.712	4.564
NH_3	2.187	2.187	2.691	2.200	2.527

d)	HOMO Condition				
	TSVD*	Tikhonov*	RPTRS	S. Norm*	TLC(T)
Ne	-28.253	25.206	-22.621	-161.925	447.219
Ar	74.929	80.531	77.791	-212.843	-112.879
N_2	8.193	32.598	6.888	-42.423	203.980
CO	-20.648	-14.705	19.350	14.709	98.758
H_2O	-50.138	-38.715	6.135	13.686	15.384
HCN	13.384	21.671	35.584	42.375	67.640
NH_3	-2.133	-12.142	-0.315	-3.569	-186.314

In summary, the analysis of Table 7.1 points to the general success of including the KE matrix in regularisation construction, with such methods giving potentials that better satisfy the virial conditions. The automatic parameter selection schemes of TLC(T) and RPTRS were able to produce high quality potentials for the entire range of species whilst the manual schemes were more variable and unable to produce consistent results without manual adjustment. The poor HOMO condition value of the TLC(T) regularised potentials suggests that the choice of the $\tilde{\mathbf{T}}$ as penalty matrix may over emphasise the tight functions in some cases leading to under-regularised valence regions, though some of this failure may be attributed to constant shifts in the potential coefficients. Such shortcomings are minor concerns however and the TLC(T) scheme represents a powerful means to an efficient black box regularisation scheme able to ensure high quality potentials from highly imbalanced basis sets without resorting to user defined parameters.

7.10.3 Future developments

The analyses presented show the TLC(T) scheme can give a pronounced improvement over manual methods, especially in cases where the basis set imbalance is large. This is achieved by providing an adaptive regularisation strength tailored to fit the system in question. The TLC(T) scheme is not without limitation however and constant shifts in the potential may still be degrading the HOMO and virial conditions. Enforcing the HOMO condition during optimisation [220] to prevent such shifts is therefore expected to improve TLC(T) potential quality, further reducing HOMO and virial condition deviations.

It is also noted that for some systems (see for example neon in Figure 7.11) the $\tilde{\mathbf{T}}$ penalty matrix appears to skew regularisation too far towards the high exponent functions, allowing noise into the valence regions. Whilst some improvement may still be possible in penalty matrix choice, generating an improved *a priori* measure of regularisation balance is expected to be a challenging task.

7.11 The regularisation of spin polarised systems

Discussion of the OEP regularisation has so far been limited to closed shell systems in which $N_\uparrow = N_\downarrow$ with an effective potential that is the same for both spins. If an unrestricted formalism is adopted then separate potential coefficients are required for each spin, requiring two coefficient vectors, $\mathbf{b}_\uparrow$ and $\mathbf{b}_\downarrow$.

The YW Newton optimisation for an unrestricted system can be performed in two ways: the step for each spin can be calculated separately requiring two matrix equations, $\mathbf{H}_\sigma \cdot \mathbf{b}^*_\sigma = -\mathbf{g}^*_\sigma$, denoted the *independent spin* method; or the step can be calculated for both spins in a single combined equation,

$$\begin{pmatrix} \mathbf{H}_\uparrow & \mathbf{0} \\ \mathbf{0} & \mathbf{H}_\downarrow \end{pmatrix} \begin{pmatrix} \mathbf{b}^*_\uparrow \\ \mathbf{b}^*_\downarrow \end{pmatrix} = - \begin{pmatrix} \mathbf{g}^*_\uparrow \\ \mathbf{g}^*_\downarrow \end{pmatrix}, \tag{7.48}$$

termed the *combined spin* method.

Whilst both methods give equivalent step vectors the independent spin method is preferable, offering greater flexibility in Hessian regularisation. In the independent spin method a separate regularisation parameter may be chosen for each spin, though it has been difficult to make use of the increased flexibility in the absence of an automatic parametrisation scheme. A manual search to determine the single α for the restricted case was undesirable, and in the spin independent case two parameters are required. Manual selection of spin independent parameters is further complicated by the coupling of $\alpha_\uparrow$ and $\alpha_\downarrow$ through the Coulomb operator, requiring a two dimensional search. The automatic parametrisation schemes of RPTRS and TLC however, are able to utilise the flexibility of a spin independent regularisation, as an optimal regularisation parameter can be determined from the L-Curve for each spin at each optimisation step.

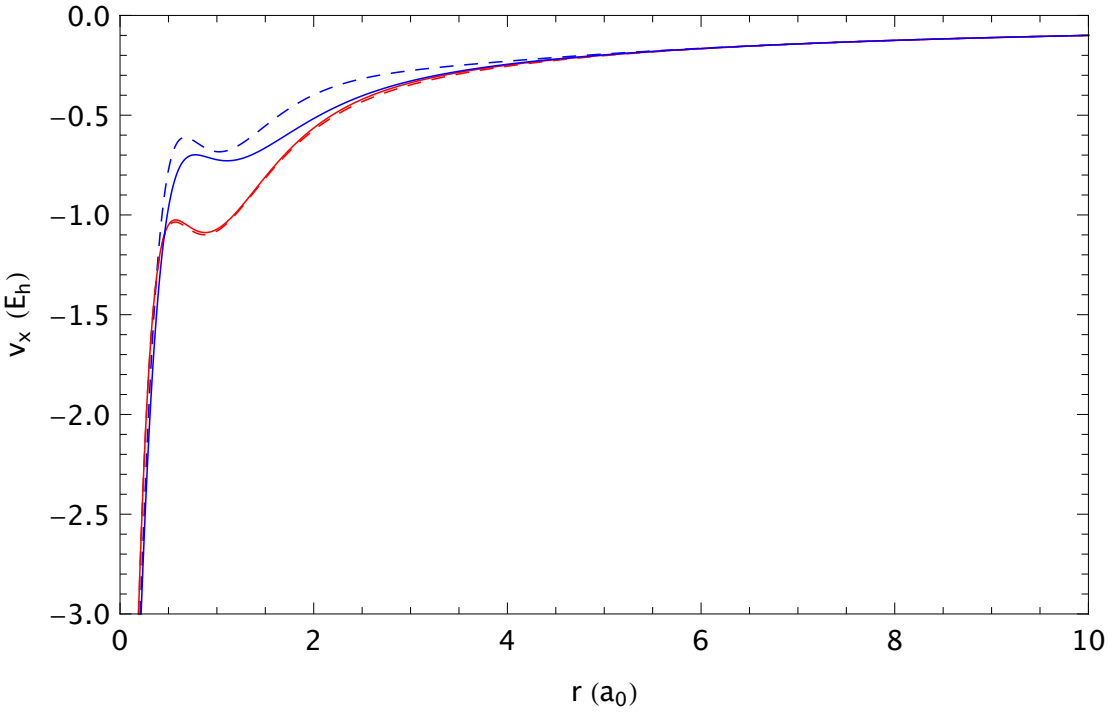


Figure 7.14: Exchange potentials for the lithium atom with the u-Partridge3 / u-Partridge3 [200] basis set combination. The spin excess exchange potential is shown in red, and the spin deficit exchange potential is shown in blue. The potential was regularised with a combined spin TLC(T) regularisation (solid line), and with independent spin TLC(T) regularisation (dashed line).

7.11.1 Independent spin potential regularisation

The TLC(T) and RPTRS schemes present a method for performing a spin independent unrestricted OEP calculation, and a comparison between the spin independent and combined TLC(T) regularisation of the lithium atom is made in Figure 7.14. Allowing TLC(T) to regularise each spin separately produces a significant change in the form of the spin deficient exchange potential but little change in the spin excess potential. In the combined spin regularisation case a final regularisation parameter of 1.53×10^{-4} was selected for each spin whilst in the spin independent case the spin excess potential was regularised at 1.31×10^{-4} whilst the spin deficient potential was regularised more weakly at 1.28×10^{-5}. The increased flexibility in regularisation has allowed for more freedom in the spin deficient potential and a more pronounced inter shell peak to form.

Figure 7.14 shows that for the case of the lithium atom independent spin regularisation can significantly change the form of the exchange potential. The increased flexibility afforded by independent spin regularisation in unrestricted OEP calculations is expected to be beneficial and as such spin independent regularisation is recommended for use in all unrestricted OEP calculations.

7.12 Concluding remarks

By their very nature ill-posed problems will always be fraught with compromise and a careful need to balance competing factors. To this end the L-Curve offers an appealing method of visualising and understanding the essential relationships at the core of an ill-posed problem and, when properly applied, it can offer a systematic route towards the desired solution. It is also instructive to carefully consider the properties desired in the regularised solution and whether information to enforce them can be included into the regularisation to enhance the result. The relations described in the opening sections of this chapter are general to all ill-posed problems and it is hoped that the lessons learned here for the case of OEP-DFT may be applied more generally to better handle other ill-posed systems found in quantum chemistry.

For the case of the finite basis OEP such considerations have resulted in the TLC(T) scheme and opened the way for black box OEP calculations that give physically meaningful potentials. The automatic determination of regularisation strength by TLC(T) allows the potential basis limit to be taken with confidence, ensuring the regularisation is adjusted to correctly account for the basis set imbalance. As was also shown in Section 7.11, removing the burden of regularisation strength choice also allows for increased flexibility to be included into the regularisation scheme, with different strengths of regularisation being imposed on the potentials for different spin electrons.

Such flexibility in regularisation is likely to be critical if the OEP is to be extended to optimise the vector potentials required by CDFT, as each direction of the vector potential must be optimised alongside the scalar potential that is normally considered in OEP. It is expected that an extension of the OEP method to CDFT could yield increased accuracy in low field response property calculation as the application of orbital dependent functionals may prove beneficial for the treatment of the inherently orbital dependent paramagnetic current density.

Chapter 8

Concluding Remarks

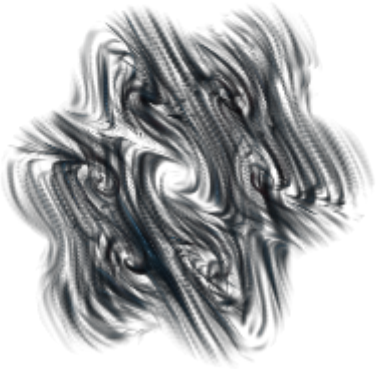
The weak field regime and the prediction of magnetic response properties remain something of a challenge for CDFT, though current dependent mGGA functionals are able to slightly improve on the accuracy of standard DFT functionals without resorting to empirical fitting. Molecular bonding in the strong field regime, however, is captured much more successfully, with the cTPSS functional giving quantitative agreement with high accuracy wave function calculations. This success at high field suggests that electron currents are effectively included by modified mGGA functional construction and presents a working set of CDFT functionals for strong field applications.

The analysis of the current modified electron localisation function revealed the increasing importance of dealing with self interaction errors in strong fields as the density compression induced by the field makes one electron regions increasingly prominent. This observation of the increased importance of self interaction error in the presence of magnetic fields rationalises the success of the cTPSS functional, and highlights the insight that can be gained from the visualisation of current dependent quantities in fields of increasing strength.

The success of the modified mGGA functionals in CDFT is perhaps less surprising when one considers the indirect dependence of these functionals on the KS orbitals through the kinetic energy density, an orbital dependence that is shared by the paramagnetic, and hence physical, current density. The increased non-locality orbital dependency affords can therefore be expected to be beneficial, reflecting the intrinsically non-local nature of the induced orbital currents in the functional. This interpretation is supported by the similarities in structure between the cELF and orbital currents shown in Figure 4.9 and makes this choice of $\tilde{\tau}$ dependent functionals compelling. With these considerations in mind, fully orbital dependent functionals present a promising route to further increasing accuracy through a fully non-local exchange-correlation energy description, and complete cancellation of self interaction errors. The inherent gauge-origin dependence of the KS orbitals however mandates care in how such functionals are constructed and the manner in which the orbitals enter XC functionals.

The OEP method is essential for the development of orbital dependent functionals, and a generalised OEP will be essential for orbital dependent CDFT functionals. The work of Chapter 7 in addressing the numerical difficulties inherent in finite basis OEP is expected to be critical for making OEP-CDFT a reality, allowing all three components of the effective vector potential to be regularised independently, alongside the scalar potential normally considered. The requirement for a flexible regularisation is well handled by L-Curve analysis techniques and, in particular, the independent spin regularisation of Section 7.11 shows the power of automatic regularisation in solving the analogous problem of spin resolved OEP.

It is hoped that the work contained in this thesis will aid in further developing the exciting field of CDFT and facilitate a greater understanding of the chemistries of highly magnetic systems.



A visualisation of the field induced physical current-density in the σ bonding system of a benzene molecule.

Acknowledgements

First and foremost I whole heartedly thank Dr. Andy Teale for his invaluable supervision and unwavering support throughout this project. I could not have asked for a better mentor for my personal development as a scientist, or for a better introduction to the scientific world. I hope that one one day I can inspire and guide students as he has me.

Similarly, I thank Dr. June McCombie MBE for helping me find my feet as an undergraduate, for providing me with opportunities to develop my teaching as a postgrad, and for taking an extended interest in my progress throughout.

I must also thank Jack Turner (I'll meet you after training for a pint), Sam Quinn (who one day I will beat at a board game) and Joe Jones (who will also be beaten one day) for sharing the PhD journey with me.

Importantly, I thank my parents, for showing me that I could, and supporting me whilst I did.

I am especially grateful to my colleagues in the Teale group: Tom Irons, Matt Riley and Dr. Jan Zeman for their discussions, support and development efforts in the work presented here. I am also indebted to them for their tireless proof reading and editing efforts during the writing of this thesis.

I am grateful to my colleagues and friends throughout the theoretical chemistry department of the University of Nottingham for insightful discussions and the interesting questions they have raised throughout, as well as for the pleasant company and camaraderie that have made the PhD experience a pleasure. Special mention must go to Dr. Ho-kei Chan for his grounded input when I had lost sight of the wood for the trees during the work of Chapter 7, and to Fouad Husseini for the long evenings shared writing our respective theses.

I thank Dr. Erik Tellgren, Dr. Ulf Ekström, Dr. Stella Stopkowicz, Prof. Trygve Helgaker and Sarah Reimann for the fruitful collaborations shared, and the late Prof. J. Talman for providing the numerical OEP code used in Chapter 7.

I'm thankful to Guy and Mary Harris, and Chris and Brian Furness, who's patronage has made the experience more comfortable and enabled the purchasing of materials and books.

I'd like to express thanks to the many friends with whom I've enjoyed (and will continue to enjoy) many happy hours with and special thanks are given to Chris Roberts, for the long discussions on the running track that were the genesis of a number of ideas.

Finally, I am grateful to the EPSRC and the University of Nottingham School of Chemistry for the funding that made this work possible.

Bibliography

[1] P. Hohenberg and W. Kohn, "Inhomogeneous electron gas," *Phys. Rev.*, vol. 136, no. 3B, pp. 864–870, 1964.

[2] G. Vignale and M. Rasolt, "Current- and spin-density-functional theory for inhomogeneous electronic systems in strong magnetic fields," *Phys. Rev. B*, vol. 37, no. 18, pp. 10685–10696, 1988.

[3] D. S. Finley, D. Koester, and B. Gibor, "The Temperature Scale and Mass Distribution of Hot DA White Dwarfs," *Astrophys. J.*, vol. 488, pp. 375–396, 1997.

[4] D. Reimers, S. Jordan, V. Beckmann, N. Christlieb, and L. Wisotzki, "Four magnetic DB white dwarfs discovered by the Hamburg/ESO survey," *Astron. Astrophys.*, vol. 8, pp. 1–5, 1998.

[5] K. M. Vanlandingham, G. D. Schmidt, D. J. Eisenstein, H. C. Harris, S. F. Anderson, P. B. Hall, J. Liebert, D. P. Schneider, N. M. Silvestri, G. S. Stinson, and M. a. Wolfe, "Magnetic White Dwarfs from the SDSS. II. The Second and Third Data Releases," *Astron. J.*, vol. 130, pp. 734–741, 2005.

[6] S. Jordan, P. Schmelcher, W. Becken, and W. Schweizer, "Evidence for helium in the magnetic white dwarf GD229," *Astron. Astrophys.*, vol. 8, pp. 8–11, 1998.

[7] D. T. Wickramasinghe and L. Ferrario, "Magnetism in Isolated and Binary White Dwarfs," *Publ. Astron. Soc. Pacific*, vol. 112, pp. 873–924, 2000.

[8] B. N. Murdin, J. Li, M. L. Y. Pang, E. T. Bowyer, K. L. Litvinenko, S. K. Clowes, H. Engelkamp, C. R. Pidgeon, I. Galbraith, N. V. Abrosimov, H. Riemann, S. G. Pavlov, H.-W. Hübers, and P. G. Murdin, "Si:P as a laboratory analogue for hydrogen on high magnetic field white dwarf stars.," *Nat. Commun.*, vol. 4, pp. 1469–1477, 2013.

[9] K. L. Litvinenko, M. Pang, J. Li, E. Bowyer, H. Engelkamp, V. B. Shuman, L. M. Portsel, A. N. Lodygin, Y. A. Astrov, S. G. Pavlov, H.-W. Hübers, C. R. Pidgeon, and B. N. Murdin, "High-field impurity magneto-optics of Si:Se," *Phys. Rev. B*, vol. 90, no. 11, p. 115204, 2014.

[10] E. I. Tellgren, A. M. Teale, J. W. Furness, K. K. Lange, U. Ekström, and T. Helgaker, "Non-perturbative calculation of molecular magnetic properties within current-density functional theory," *J. Chem. Phys.*, vol. 140, no. 3, p. 034101, 2014.

[11] E. I. Tellgren, T. Helgaker, A. Soncini, K. K. Lange, A. M. Teale, S. Stopkowicz, J. H. Austad, and J. W. Furness, "LONDON, a quantum-chemistry program for plane-wave/GTO hybrid basis sets and finite magnetic field calculations."

[12] A. T. B. Gilbert, N. A. Besley, and P. M. W. Gill, "Self-Consistent Field Calculations of Excited States Using the Maximum Overlap Method (MOM)," *J. Phys. Chem.*, vol. 112, pp. 13164–13171, 2008.

[13] N. I. Gidopoulos, "Progress at the interface of wave-function and density-functional theories," *Phys. Rev. A - At. Mol. Opt. Phys.*, vol. 83, no. 4, pp. 1–4, 2011.

[14] E. H. Lieb, "Density functionals for coulomb systems," *Int. J. Quantum Chem.*, vol. 24, no. 3, pp. 243–277, 1983.

[15] C. C. J. Roothaan, "Self-Consistent field theory for open shells of electronic systems," *Rev. Mod. Phys.*, vol. 32, no. 2, pp. 179–185, 1960.

[16] C. A. Coulson and I. Fischer, "XXXIV. Notes on the molecular orbital treatment of the hydrogen molecule.," *London, Edinburgh Dublin Philos. Mag. J. Sci.*, vol. 40, no. 303, pp. 386–393, 1949.

[17] L. Laaksonen, P. Pyykkö, and D. Sundholm, "Fully numerical Hartree-Fock methods for molecules," *Comput. Phys. Reports*, vol. 4, no. 5, pp. 313–344, 1986.

[18] A. D. Becke and R. M. Dickson, "Numerical solution of Schrödinger's equation in polyatomic molecules," *J. Chem. Phys.*, vol. 92, no. 6, pp. 3610–3612, 1990.

[19] R. Ditchfield, W. J. Hehre, and J. A. Pople, "Self-Consistent Molecular-Orbital Methods. IX. An Extended Gaussian-Type Basis for Molecular-Orbital Studies of Organic Molecules," *J. Chem. Phys.*, vol. 54, no. 2, pp. 724–728, 1971.

[20] T. H. Dunning, "Gaussian basis sets for use in correlated molecular calculations. I. The atoms boron through neon and hydrogen," *J. Chem. Phys.*, vol. 90, no. 2, pp. 1007–1023, 1989.

[21] A. Szabo and N. S. Ostlund, *Modern Quantum Chemistry*. Macmillan Publishing Co. Inc., revised ed., 1982.

[22] H. Weinstein and R. Pauncz, "Molecular orbital set determined by a localization procedure," *Symp. Faraday Soc.*, vol. 2, pp. 23–31, 1968.

[23] M. Wolfsberg and L. Helmholz, "The Spectra and Electronic Structure of the Tetrahedral Ions MnO4-, CrO4–, and ClO4-," *J. Chem. Phys.*, vol. 20, no. 5, pp. 837–843, 1952.

[24] P. Pulay, "Convergence acceleration of iterative sequences. The case of SCF iteration," *Chem. Phys. Lett.*, vol. 73, no. 2, pp. 393–398, 1980.

[25] P. Pulay, "Improved SCF Convergence Acceleration," *J. Comput. Chem.*, vol. 3, no. 4, pp. 556–560, 1982.

[26] P. O. Löwdin, "Quantum theory of many-particle systems. III. Extension of the Hartree–Fock scheme to include degenerate systems and correlation effects," *Phys. Rev.*, vol. 97, no. 6, pp. 1509–1520, 1955.

[27] K. K. Lange, E. I. Tellgren, M. R. Hoffmann, and T. Helgaker, "A paramagnetic bonding mechanism for diatomics in strong magnetic fields.," *Science (80-.).*, vol. 337, no. 327, pp. 327–331, 2012.

[28] R. J. Bartlett, "Many-body perturbation theory and coupled cluster theory for electron correlation in molecules," *Annu. Rev. Phys. Chem.*, vol. 32, pp. 359–401, 1981.

[29] W. Kohn and L. Sham, "Self-consistent equations including exchange and correlation effects," *Phys. Rev.*, vol. 140, no. 4A, pp. 1133–1139, 1965.

[30] M. Levy, "Electron densities in search of Hamiltonians," *Phys. Rev. A*, vol. 26, no. 3, pp. 1200–1208, 1982.

[31] T. Helgaker, P. Jørgensen, and J. Olsen, *Principles of Density-Functional Theory*. Pending Publication, 2017.

[32] L. H. Thomas, "The calculation of atomic fields," *Math. Proc. Cambridge Philos. Soc.*, vol. 23, no. 05, pp. 542–548, 1927.

[33] E. Fermi, "Un metodo statistico per la determinazione di alcune priorieta dell'atome.," *Rend. Accad. Naz. Lincei*, vol. 6, no. 32, pp. 602–607, 1927.

[34] P. A. M. Dirac, "Note on Exchange Phenomena in the Thomas Atom," *Math. Proc. Cambridge Philos. Soc.*, vol. 26, no. 03, pp. 376–385, 1930.

[35] D. M. Ceperley and B. J. Alder, "Ground state of the electron gas by a stochastic model," *Phys. Rev. Lett.*, vol. 45, no. 7, pp. 566–569, 1980.

[36] S. H. Vosko, L. Wilk, and M. Nusair, "Accurate spin-dependent electron liquid correlation energies for local spin density calculations: a critical analysis," *Can. J. Phys.*, vol. 58, no. 8, pp. 1200–1211, 1980.

[37] J. P. Perdew, "Accurate density functional for the energy: Real-space cutoff of the gradient expansion for the exchange hole," *Phys. Rev. Lett.*, vol. 55, no. 16, pp. 1665–1668, 1985.

[38] J. P. Perdew and Y. Wang, "Accurate and simple density functional for the electronic exchange energy: Generalised gradient approximation," *Phys. Rev. B*, vol. 33, no. 12, pp. 8800–8802, 1986.

[39] C. Adamo, M. Ernzerhof, and G. E. Scuseria, "The meta-GGA functional: Thermochemistry with a kinetic energy density dependent exchange-correlation functional," *J. Chem. Phys.*, vol. 112, no. 6, pp. 2643–2649, 2000.

[40] R. Neumann, R. H. Nobes, and N. C. Handy, "Exchange functionals and potentials," *Mol. Phys.*, vol. 87, no. 1, pp. 1–36, 1996.

[41] S. Kümmel and J. P. Perdew, "Optimized effective potential made simple: Orbital functionals, orbital shifts, and the exact Kohn-Sham exchange potential," *Phys. Rev. B*, vol. 68, no. 3, p. 035103, 2003.

[42] S. Kümmel and L. Kronik, "Orbital-dependent density functionals: Theory and applications," *Rev. Mod. Phys.*, vol. 80, no. 1, pp. 3–60, 2008.

[43] A. Görling, "New KS Method for Molecules Based on an Exchange Charge Density Generating the Exact Local KS Exchange Potential," *Phys. Rev. Lett.*, vol. 83, no. 26, pp. 5459–5462, 1999.

[44] A. D. Becke, "A new mixing of Hartree-Fock and local density-functional theories," *J. Chem. Phys.*, vol. 98, no. 2, pp. 1372–1377, 1993.

[45] A. D. Becke, "Density-functional exchange-energy approximation with correct asymptotic behavior," *Phys. Rev. A*, vol. 38, no. 6, pp. 3098–3100, 1988.

[46] J. P. Perdew, M. Ernzerhof, and K. Burke, "Rationale for mixing exact exchange with density functional approximations," *J. Chem. Phys.*, vol. 105, no. 22, pp. 9982–9985, 1996.

[47] K. Burke, M. Ernzerhof, and J. P. Perdew, "The adiabatic connection method: a non-empirical hybrid," *Chem. Phys. Lett.*, vol. 265, pp. 115–120, 1997.

[48] C. Adamo and V. Barone, "Toward reliable density functional methods without adjustable parameters: The PBE0 model," *J. Chem. Phys.*, vol. 110, no. 13, pp. 6158–6170, 1999.

[49] H. R. Romero and G. A. Aucar, "QED approach to the nuclear spin-spin coupling tensor," *Phys. Rev. A*, vol. 65, no. 3400, p. 053411, 2002.

[50] S. P. A. Sauer, *Molecular Electromagnetism*. Oxford University Press, 2011.

[51] E. I. Tellgren, A. Soncini, and T. Helgaker, "Nonperturbative ab initio calculations in strong magnetic fields using London orbitals.," *J. Chem. Phys.*, vol. 129, no. 15, p. 154114, 2008.

[52] U. Kappes and P. Schmelcher, "Atomic orbital basis set optimization for ab initio calculations of molecules with hydrogen atoms in strong magnetic fields," *J. Chem. Phys.*, vol. 100, no. 4, pp. 2878–2887, 1994.

[53] P. Schmelcher, T. Detmer, and L. S. Cederbaum, "Excited states of the hydrogen molecule in magnetic fields: The triplet Sigma states of the parallel configuration," *Phys. Rev. A*, vol. 61, no. 4, p. 043411, 2000.

[54] Y. P. Kravchenko and M. A. Liberman, "Application of Gaussian-Type Basis Sets to Ab Initio Calculations in Strong Magnetic Fields," *Int. J. Quantum Chem.*, vol. 64, no. 5, pp. 513–522, 1997.

[55] A. Kubo, "The hydrogen molecule in strong magnetic fields: optimizations of anisotropic Gaussian basis sets.," *J. Phys. Chem. A*, vol. 111, no. 25, pp. 5572–5581, 2007.

[56] C. J. Ballhausen and A. E. Hansen, "Electronic Spectra," *Annu. Rev. Phys. Chem.*, vol. 23, pp. 15–38, 1972.

[57] P. Schmelcher, L. S. Cederbaum, and H.-D. Meyer, "On the validity of the Born-Oppenheimer approximation in magnetic fields," *J. Phys. B*, vol. 21, no. 15, pp. L445–L450, 1988.

[58] P. Schmelcher, L. S. Cederbaum, and H. D. Meyer, "Electronic and nuclear motion and their couplings in the presence of a magnetic field," *Phys. Rev. A*, vol. 38, no. 12, pp. 6066–6079, 1988.

[59] E. I. Tellgren, S. Kvaal, E. Sagvolden, U. Ekström, A. M. Teale, and T. Helgaker, "Choice of basic variables in current-density-functional theory," *Phys. Rev. A*, vol. 86, no. 6, p. 062506, 2012.

[60] K. Capelle and G. Vignale, "Nonuniqueness and derivative discontinuities in density-functional theories for current-carrying and superconducting systems," *Phys. Rev. B*, vol. 65, no. 11, p. 113106, 2002.

[61] X.-Y. Pan and V. Sahni, "Density and physical current density functional theory," *Int. J. Quantum Chem.*, vol. 110, pp. 2833–2843, 2010.

[62] X.-Y. Pan and V. Sahni, "Generalization of the Hohenberg-Kohn theorem to the presence of a magnetostatic field," *J. Phys. Chem. Solids*, vol. 73, no. 5, pp. 630–634, 2012.

[63] G. Diener, "Current-density-functional theory for a nonrelativistic electron gas in a strong magnetic field," *J. Phys. Condens. Matter*, vol. 9417, pp. 9417–9428, 1991.

[64] G. Vignale, C. A. Ullrich, and K. Capelle, "Comment on "Density and physical current density functional theory" by Xiao-Yin Pan and Viraht Sahni," *Int. J. Quantum Chem.*, vol. 113, no. 9, pp. 1422–1423, 2013.

[65] G. Vignale and M. Rasolt, "Densty-Functional Theory in Strong Magnetic Fields," *Phys. Rev. Lett.*, vol. 59, no. 20, pp. 2360–2363, 1987.

[66] K. Capelle and E. K. U. Gross, "Spin-density functionals from current-density functional theory and vice versa: A road towards new approximations," *Phys. Rev. Lett.*, vol. 78, no. 10, pp. 1872–1875, 1997.

[67] M. Taut, P. MacHon, and H. Eschrig, "Violation of noninteracting v-representability of the exact solutions of the Schrodinger equation for a two-electron quantum dot in a homogeneous magnetic field," *Phys. Rev. A*, vol. 80, no. 2, p. 0225171, 2009.

[68] E. H. Lieb and R. Schrader, "Current densities in density-functional theory," *Phys. Rev. A*, vol. 88, no. 3, p. 032516, 2013.

[69] E. Cances, "Self-consistent field algorithms for Kohn-Sham models with fractional occupation numbers," *J. Chem. Phys.*, vol. 114, no. 24, pp. 10616–10622, 2001.

[70] E. Cances, K. N. Kudin, G. E. Scuseria, and G. Turinici, "Quadratically convergent algorithm for fractional occupation numbers in density functional theory," *J. Chem. Phys.*, vol. 118, no. 12, pp. 5364–5368, 2003.

[71] E. Kraisler, G. Makov, N. Argaman, and I. Kelson, "Fractional occupation in Kohn-Sham density-functional theory and the treatment of non-pure-state v-representable densities," *Phys. Rev. A*, vol. 80, no. 3, pp. 1–8, 2009.

[72] C. R. Nygaard and J. Olsen, "A second-order unconstrained optimization method for canonical-ensemble density-functional methods," *J. Chem. Phys.*, vol. 138, no. 9, p. 094109, 2013.

[73] E. I. Tellgren, S. Kvaal, and T. Helgaker, "Fermion N-representability for prescribed density and paramagnetic current density," *Phys. Rev. A*, vol. 89, no. 1, p. 012515, 2014.

[74] G. Vignale, M. Rasolt, and D. J. W. Geldart, "Diamagnetic susceptibility of a dense electron gas," *Phys. Rev. B*, vol. 37, no. 5, pp. 2502–2507, 1988.

[75] A. M. Lee, S. M. Colwell, and N. C. Handy, "The calculation of magnetizabilities using current density functional theory," *Chem. Phys. Lett.*, vol. 229, pp. 225–232, 1994.

[76] A. M. Lee, N. C. Handy, and S. M. Colwell, "The density functional calculation of nuclear shielding constants using London atomic orbitals," *J. Chem. Phys.*, vol. 103, no. 23, pp. 10095–10109, 1995.

[77] E. Orestes, T. Marcasso, and K. Capelle, "Density-functional calculation of ionization energies of current-carrying atomic states," *Phys. Rev. A*, vol. 68, no. 2, p. 022105, 2003.

[78] J. Tao and J. P. Perdew, "Nonempirical Construction of Current-Density Functionals from Conventional Density-Functional Approximations," *Phys. Rev. Lett.*, vol. 95, no. 19, p. 196403, 2005.

[79] J. Tao and G. Vignale, "Analytic expression for the diamagnetic susceptibility of a uniform electron gas," *Phys. Rev. B*, vol. 74, no. 19, p. 193108, 2006.

[80] K. Higuchi and M. Higuchi, "Vorticity expansion approximation of the exchange-correlation energy functional in current density functional theory," *Phys. Rev. B*, vol. 74, no. 19, p. 195122, 2006.

[81] M. Higuchi and K. Higuchi, "Evaluation of vorticity expansion approximation of current-density functional theory by means of Levy's asymptotic bound," *Phys. Rev. B*, vol. 75, no. 19, p. 195114, 2007.

[82] W. Zhu and S. B. Trickey, "Analytical solutions for two electrons in an oscillator potential and a magnetic field," *Phys. Rev. A*, vol. 72, no. 2, p. 022501, 2005.

[83] W. Zhu, L. Zhang, and S. B. Trickey, "Comparative studies of density-functional approximations for light atoms in strong magnetic fields," *Phys. Rev. A*, vol. 90, no. 2, p. 022504, 2014.

[84] A. D. Becke, "Current-density dependent exchange-correlation functionals," *Can. J. Chem.*, vol. 74, no. 6, pp. 995–997, 1996.

[85] S. Pittalis, S. Kurth, S. Sharma, and E. K. U. Gross, "Orbital currents in the Colle-Salvetti correlation energy functional and the degeneracy problem," *J. Chem. Phys.*, vol. 127, no. 12, p. 124103, 2007.

[86] J. F. Dobson, "Spin-density functionals for the electron correlation energy with automatic freedom from orbital self-interaction," *J. Phys. Condens. Matter*, vol. 4, pp. 7877–7890, 1992.

[87] J. F. Dobson, "Alternative expressions for the Fermi hole curvature," *J. Chem. Phys.*, vol. 98, no. 11, pp. 8870–8872, 1993.

[88] A. D. Becke, "Hartree-Fock exchange energy of an inhomogeneous electron gas," *Int. J. Quantum Chem.*, vol. 23, no. 6, pp. 1915–1922, 1983.

[89] A. D. Becke and M. R. Roussel, "Exchange holes in inhomogeneous systems: A coordinate-space model," *Phys. Rev. A*, vol. 39, no. 8, pp. 3761–3767, 1989.

[90] A. D. Becke, "A new inhomogeneity parameter in density-functional theory," *J. Chem. Phys.*, vol. 109, no. 6, pp. 2092–2098, 1998.

[91] J. Tao, J. P. Perdew, V. N. Staroverov, and G. E. Scuseria, "Climbing the Density Functional Ladder: Nonempirical Meta-Generalized Gradient Approximation Designed for Molecules and Solids," *Phys. Rev. Lett.*, vol. 91, no. 14, p. 146401, 2003.

[92] J. Tao, "Explicit inclusion of paramagnetic current density in the exchange-correlation functionals of current-density functional theory," *Phys. Rev. B*, vol. 71, no. 20, pp. 205107–205112, 2005.

[93] J. E. Bates and F. Furche, "Harnessing the meta-generalized gradient approximation for time-dependent density functional theory.," *J. Chem. Phys.*, vol. 137, no. 16, p. 164105, 2012.

[94] E. Sagvolden, U. Ekström, and E. I. Tellgren, "Isoorbital indicators for current density functional theory," *Mol. Phys.*, vol. 111, no. 9-11, pp. 1295–1302, 2013.

[95] S. N. Maximoff and G. E. Scuseria, "Nuclear magnetic resonance shielding tensors calculated with kinetic energy density-dependent exchange-correlation functionals," *Chem. Phys. Lett.*, vol. 390, no. 4-6, pp. 408–412, 2004.

[96] A. D. Becke, "Density-functional thermochemistry. V. Systematic optimization of exchange-correlation functionals," *J. Chem. Phys.*, vol. 107, no. 20, pp. 8554–8560, 1997.

[97] U. Ekström, L. Visscher, R. Bast, and A. J. Thorvaldsen, "Arbitrary-Order Density Functional Response Theory," *J. Chem. Theory Comput.*, vol. 6, pp. 1971–1980, 2010.

[98] J. W. Furness, J. Verbeke, E. I. Tellgren, S. Stopkowicz, U. Ekström, T. Helgaker, and A. M. Teale, "Current Density Functional Theory Using Meta-Generalized Gradient Exchange-Correlation Functionals," *J. Chem. Theory Comput.*, vol. 11, no. 9, pp. 4169–4181, 2015.

[99] J. W. Furness, U. Ekström, T. Helgaker, and A. M. Teale, "Electron localisation function in current-density-functional theory," *Mol. Phys.*, vol. 114, no. 7-8, pp. 1415–1422, 2016.

[100] A. D. Becke, "A multicenter numerical integration scheme for polyatomic molecules," *J. Chem. Phys.*, vol. 88, no. 4, pp. 2547–2553, 1988.

[101] C. W. Murray, N. C. Handy, and G. J. Laming, "Quadrature schemes for integrals of density functional theory," *Mol. Phys.*, vol. 78, no. 4, pp. 997–1014, 1993.

[102] R. Lindh, P.-A. Malmqvist, and L. Gagliardi, "Molecular integrals by numerical quadrature. I. Radial integration," *Theor. Chem. Acc.*, vol. 106, pp. 178–187, 2001.

[103] V. I. Lebedev, "Values of the nodes and weights of ninth to seventeenth order gauss-markov quadrature formulae invariant under the octahedron group with inversion," *USSR Comput. Math. Math. Phys.*, vol. 15, pp. 44–51, 1975.

[104] V. I. Lebedev, "Quadratures on a sphere," *USSR Comput. Math. Math. Phys.*, vol. 16, no. 2, pp. 293–306, 1976.

[105] V. I. Lebedev, "Spherical quadrature formulas exact to orders 25-29," *Sib. Mathamtical J.*, vol. 18, no. 1, pp. 99–107, 1977.

[106] V. I. Lebedev and A. L. Skorokhodov, "Quadrature formulas of orders 41, 47 and 53 for the sphere," *Russ. Acad. Sci. Dokl. Math.*, vol. 45, p. 587, 1992.

[107] V. I. Lebedev, "A quadrature formula for the sphere of 59th algebraic order of accuracy," *Russ. Acad. Sci. Dokl. Math.*, vol. 50, p. 283, 1995.

[108] V. I. Lebedev and D. N. Laikov, "A quadrature formula for the sphere of the 131st algebraic order of accuracy," *Russ. Acad. Sci. Dokl. Math.*, vol. 59, no. 3, p. 477, 1999.

[109] "The Dalton quantum chemistry program system," *Wiley Interdiscip. Rev. Comput. Mol. Sci.*, vol. 4, no. 3, pp. 269–284, 2014.

[110] W. Zhu and S. B. Trickey, "Exact density functionals for two-electron systems in an external magnetic field," *J. Chem. Phys.*, vol. 125, no. 9, p. 094317, 2006.

[111] E. I. Tellgren, S. S. Reine, and T. Helgaker, "Analytical GIAO and hybrid-basis integral derivatives: application to geometry optimization of molecules in strong magnetic fields," *Phys. Chem. Chem. Phys.*, vol. 14, no. 26, pp. 9492–9499, 2012.

[112] E. I. Tellgren, T. Helgaker, and A. Soncini, "Non-perturbative magnetic phenomena in closed-shell paramagnetic molecules.," *Phys. Chem. Chem. Phys.*, vol. 11, no. 26, pp. 5489–5498, 2009.

[113] O. B. Lutnæs, A. M. Teale, T. Helgaker, D. J. Tozer, K. Ruud, and J. Gauss, "Benchmarking density-functional-theory calculations of rotational g tensors and magnetizabilities using accurate coupled-cluster calculations.," *J. Chem. Phys.*, vol. 131, no. 14, p. 144104, 2009.

[114] A. M. Teale, O. B. Lutnæs, T. Helgaker, D. J. Tozer, and J. Gauss, "Benchmarking density-functional theory calculations of NMR shielding constants and spin-rotation constants using accurate coupled-cluster calculations.," *J. Chem. Phys.*, vol. 138, no. 2, p. 024111, 2013.

[115] S. Stopkowicz, K. K. Lange, E. I. Tellgren, and T. Helgaker, "Coupled-cluster theory for atoms and molecules in strong magnetic fields," *J. Chem. Phys.*, vol. 143, p. 074110, 2015.

[116] T. Helgaker, M. Jaszuński, and K. Ruud, "Ab Initio Methods for the Calculation of NMR Shielding and Indirect Spin-Spin Coupling Constants," *Chem. Rev.*, vol. 99, no. 1, pp. 293–352, 1999.

[117] A. Halkier, T. Helgaker, P. Jorgensen, W. Klopper, H. Koch, J. Olsen, and A. K. Wilson, "Basis-set convergence in correlated calculations on Ne, N2, and H2O," *Chem. Phys. Lett.*, vol. 286, no. 3-4, pp. 243–252, 1998.

[118] S. Vennes, G. D. Schmidt, L. Ferrario, D. J. Christian, D. T. Wickramasinghe, and A. Kawka, "A multiwavelength study of the high-field magnetic white dwarf EUVE J0317-85.5 (=RE J0317-853)," *Astrophys. J.*, vol. 593, pp. 1040–1048, 2003.

[119] S. Reimann, U. Ekström, S. Stopkowicz, A. M. Teale, A. Borgoo, and T. Helgaker, "The importance of current contributions to shielding constants in density-functional theory.," *Phys. Chem. Chem. Phys.*, vol. 17, no. 28, pp. 18834–18842, 2015.

[120] G. I. Pagola, M. C. Caputo, M. B. Ferraro, and P. Lazzeretti, "Calculation of the fourth-rank molecular hypermagnetizability of some small molecules," *J. Chem. Phys.*, vol. 74, no. 2, p. 022509, 2006.

[121] G. I. Pagola, S. Pelloni, M. C. Caputo, M. B. Ferraro, and P. Lazzeretti, "Fourth-rank hypermagnetizability of medium-size planar conjugated molecules and fullerene," *Phys. Rev. A*, vol. 72, no. 3, p. 033401, 2005.

[122] D. Lai, "Matter in strong magnetic fields," *Rev. Mod. Phys.*, vol. 73, no. 3, pp. 629–661, 2001.

[123] T. Detmer, P. Schmelcher, and L. S. Cederbaum, "Hydrogen molecule in a magnetic field: The lowest states of the Π manifold and the global ground state of the parallel configuration," *Phys. Rev. A*, vol. 57, no. 3, pp. 1767–1777, 1998.

[124] P. Schmelcher, M. V. Ivanov, and W. Becken, "Exchange and correlation energies of ground states of atoms and molecules in strong magnetic fields," *Phys. Rev. A*, vol. 59, no. 5, pp. 3424–3431, 1999.

[125] W. Becken and P. Schmelcher, "Electromagnetic transitions of the helium atom in a strong magnetic field," *Phys. Rev. A*, vol. 65, no. 3, p. 033416, 2002.

[126] O.-A. Al-Hujaj and P. Schmelcher, "Beryllium in strong magnetic fields," *Phys. Rev. A*, vol. 70, no. 2, p. 023411, 2004.

[127] A. Lühr, O.-A. Al-Hujaj, and P. Schmelcher, "Resonances of the helium atom in a strong magnetic field," *Phys. Rev. A*, vol. 75, no. 1, p. 013403, 2007.

[128] A. Ishikawa, H. Nakashima, and H. Nakatsuji, "Accurate solutions of the Schrödinger and Dirac equations of H2+, HD+, and HT+: With and without Born-Oppenheimer approximation and under magnetic field," *Chem. Phys.*, vol. 401, pp. 62–72, 2012.

[129] Z. Medin and D. Lai, "Density-functional-theory calculations of matter in strong magnetic fields. I. Atoms and molecules," *Phys. Rev. A*, vol. 74, no. 6, p. 062507, 2006.

[130] Z. Medin and D. Lai, "Density-functional-theory calculations of matter in strong magnetic fields. II. Infinite chains and condensed matter," *Phys. Rev. A*, vol. 74, no. 6, p. 062508, 2006.

[131] J. Sun, A. Ruzsinszky, and J. P. Perdew, "Strongly Constrained and Appropriately Normed Semilocal Density Functional," *Phys. Rev. Lett.*, vol. 115, no. 3, p. 036402, 2015.

[132] K. Higuchi, M. Miyasita, M. Kodera, and M. Higuchi, "New practicable forms for exchange and correlation energy functionals of the CDFT," *J. Magn. Magn. Mater.*, vol. 310, no. 2, pp. 1065–1066, 2007.

[133] E. Goll, M. Ernst, F. Moegle-Hofacker, and H. Stoll, "Development and assessment of a short-range meta-GGA functional," *J. Chem. Phys.*, vol. 130, no. 23, p. 234112, 2009.

[134] R. Peverati and D. G. Truhlar, "Improving the accuracy of hybrid meta-GGA density functionals by range separation," *J. Phys. Chem. Lett.*, vol. 2, no. 21, pp. 2810–2817, 2011.

[135] A. D. Becke and K. E. Edgecombe, "A simple measure of electron localization in atomic and molecular systems," *J. Chem. Phys.*, vol. 92, no. 9, pp. 5397–5403, 1990.

[136] B. Silvi and A. Savin, "Classification of chemical bonds based on topological analysis of electron localization functions," *Nature*, vol. 371, no. 6499, pp. 683–686, 1994.

[137] J. P. Perdew, R. G. Parr, M. Levy, and J. L. Balduz, "Density-functional theory for fractional particle number: Derivative discontinuities of the energy," *Phys. Rev. Lett.*, vol. 49, no. 23, pp. 1691–1694, 1982.

[138] C. O. Almbladh and U. Von Barth, "Exact results for the charge and spin densities, exchange-correlation potentials, and density-functional eigenvalues," *Phys. Rev. B*, vol. 31, no. 6, pp. 3231–3244, 1985.

[139] R. J. Bartlett, I. Grabowski, S. Hirata, and S. Ivanov, "The exchange-correlation potential in ab initio density functional theory," *J. Chem. Phys.*, vol. 122, no. 3, p. 034104, 2005.

[140] E. J. Baerends and O. V. Gritsenko, "A quantum chemical view of density functional theory," *J. Phys. Chem. A*, vol. 101, no. 30, pp. 5383–5403, 1997.

[141] R. Stowasser and R. Hoffmann, "What do the Kohn-Sham orbitals and eigenvalues mean?," *J. Am. Chem. Soc.*, vol. 121, no. 14, pp. 3414–3420, 1999.

[142] R. van Meer, O. V. Gritsenko, and E. J. Baerends, "Physical Meaning of Virtual Kohn-Sham Orbitals and Orbital Energies : An Ideal Basis for the Description of Molecular Excitations," *J. Chem. Theory Comput.*, vol. 10, pp. 4432–4441, 2014.

[143] A. Savin, B. Silvi, and F. Colonna, "Topological analysis of the electron localization function applied to delocalized bonds," *Can. J. Chem.*, vol. 74, pp. 1088–1096, 1996.

[144] A. Savin, A. D. Becke, J. Flad, R. Nesper, H. Preuss, and H. G. von Schnering, "A new look at electron localization," *Angew. Chemie Int. Ed. English*, vol. 30, no. 4, pp. 409–412, 1991.

[145] A. Savin, O. Jepsen, J. Flad, O. K. Andersen, H. Preuss, and H. G. von Schnering, "Electron Localization in Solid-State Structures of the Elements: the Diamond Structure," *Angew. Chemie Int. Ed. English*, vol. 31, no. 2, pp. 187–188, 1992.

[146] H. Binder, I. Duttlinger, H. Loos, K. Locke, A. Pfitzner, J. Flad, A. Savin, and M. Kohout, "Synthesis and Vibrational Spectroscopic Investigation of [H3B-Se-Se-BH3]2- and [H3B-{μ2}-Se(B2H5)]- Crystal Structure and Theoretical Investigation of the Molecular Structure of [H3B-{μ2}-Se(B2H5)]-," vol. 621, pp. 400–404, 1995.

[147] X. Krokidis, V. Goncalves, A. Savin, and B. Silvi, "How Malonaldehyde Bonds Change during Proton Transfer," *J. Phys. Chem. A*, vol. 102, no. 97, pp. 5065–5073, 1998.

[148] D. B. Chesnut and A. Savin, "The Electron Localization Function (ELF) Description of the PO Bond in Phosphine Oxide," *J. Am. Chem. Soc.*, vol. 121, pp. 2335–2336, 1999.

[149] P. Fuentealba and A. Savin, "Electronic structure and bonding of the ground state of alkaline-earth-metal monoxides and carbides," *J. Phys. Chem. A*, vol. 104, no. 46, pp. 10882–10886, 2000.

[150] A. Burkhardt, U. Wedig, H. G. von Schnering, and A. Savin, "The electron localisation function in closo boron clusters," *Zeitschrift fur Anorg. und allgerneine Chemie*, vol. 619, pp. 437–441, 1993.

[151] R. Llusar, A. Beltran, J. Andres, B. Silvi, and A. Savin, "Pseudopotential Periodic Hartree-Fock Study of K8In11 and Rb8In11 Systems," *J. Phys. Chem.*, vol. 99, no. 33, pp. 12483–12487, 1995.

[152] H. J. Flad, Schautz, Y. Wang, M. Dolg, and A. Savin, "On the bonding of small group 12 clusters," *Eur. Phys. J. D*, vol. 6, no. 2, pp. 243–254, 1999.

[153] P. Fuentealba and A. Savin, "Bonding analysis of hydrogenated lithium clusters using the electron localization function," *J. Phys. Chem. A*, vol. 105, no. 51, pp. 11531–11533, 2001.

[154] Y. Grin, U. Wedig, F. Wagner, G. H. Von Schnering, and A. Savin, "The analysis of "empty space" in the PdGa5, structure," *J. Alloys Compd.*, vol. 255, pp. 203–208, 1997.

[155] R. F. W. Bader, S. Johnson, T.-H. Tang, and P. L. a. Popelier, "The Electron Pair," *J. Phys. Chem.*, vol. 100, no. 38, pp. 15398–15415, 1996.

[156] A. Savin, R. Nesper, S. Wengert, and T. F. Fässler, "ELF: The Electron Localization Function," *Angew. Chemie Int. Ed. English*, vol. 36, no. 17, pp. 1808–1832, 1997.

[157] D. Marx and A. Savin, "Topological Bifurcation Analysis : Electronic Structure of CH5+," *Angew. Chemie Int. Ed. English*, vol. 36, no. 19, pp. 2077–2080, 1997.

[158] S. Noury, F. Colonna, A. Savin, and B. Silvi, "Analysis of the delocalization in the topological theory of chemical bond," *J. Mol. Struct.*, vol. 450, pp. 59–68, 1998.

[159] A. Savin, "The electron localization function (ELF) and its relatives: Interpretations and difficulties," *J. Mol. Struct. THEOCHEM*, vol. 727, no. 1-3 SPEC. ISS., pp. 127–131, 2005.

[160] J. Dobson, "Interpretation of the Fermi hole curvature," *J. Chem. Phys.*, vol. 94, no. 6, pp. 4328–4333, 1991.

[161] T. Burnus, M. a. L. Marques, and E. K. U. Gross, "Time-dependent electron localization function," *Phys. Rev. A*, vol. 71, no. 1, pp. 1–4, 2005.

[162] R. A. Kendall, T. H. Dunning Jr., and R. J. Harrison, "Electron affinities of the first-row atoms revisited. Systematic basis sets and wave functions," *J. Chem. Phys.*, vol. 96, no. 9, pp. 6796–6806, 1992.

[163] J. F. Stanton and R. J. Bartlett, "The equation of motion coupled-cluster method. A systematic biorthogonal approach to molecular excitation energies, transition probabilities, and excited state properties," *J. Chem. Phys.*, vol. 98, no. 9, pp. 7029–7039, 1993.

[164] J. Deng, A. T. B. Gilbert, and P. M. W. Gill, "Rydberg states of the helium atom," *Int. J. Quantum Chem.*, vol. 109, pp. 1915–1919, 2009.

[165] O. V. Ershova, J. Klos, N. A. Besley, and T. G. Wright, "Interaction of the NO 3pπ (C 2Π) Rydberg state with RG (RG = Ne, Kr, and Xe): Potential energy surfaces and spectroscopy," *J. Chem. Phys.*, vol. 142, p. 034311, 2015.

[166] O. V. Ershova, J. Klos, J. P. Harris, A. M. Gardner, V. M. Tame-Reyes, A. Andrejeva, M. H. Alexander, N. A. Besley, and T. G. Wright, "Interaction of the NO 3pπ Rydberg state with Ar: Potential energy surfaces and spectroscopy," *J. Chem. Phys.*, vol. 138, p. 214313, 2013.

[167] O. V. Ershova and N. A. Besley, "Theoretical calculations of the excited state potential energy surfaces of nitric oxide," *Chem. Phys. Lett.*, vol. 513, pp. 179–183, 2011.

[168] E. A. Briggs and N. A. Besley, "Modelling excited states of weakly bound complexes with density functional theory.," *Phys. Chem. Chem. Phys.*, vol. 16, no. 28, pp. 14455–14462, 2014.

[169] M. W. D. Hanson-Heine, M. W. George, and N. A. Besley, "Calculating excited state properties using Kohn-Sham density functional theory," *J. Chem. Phys.*, vol. 138, no. 6, pp. 064101–8, 2013.

[170] E. A. Briggs, N. A. Besley, and D. Robinson, "QM/MM excited state molecular dynamics and fluorescence spectroscopy of BODIPY," *J. Phys. Chem. A*, vol. 117, no. 12, pp. 2644–2650, 2013.

[171] E. R. Davidson, "The iterative calculation of a few of the lowest eigenvalues and corresponding eigenvectors of large real-symmetric matrices," *J. Comput. Phys.*, vol. 17, no. 1, pp. 87–94, 1975.

[172] W. Kolos and L. Wolniewicz, "Potential-Energy Curves for the X 1Σ g + , b 3Σ u + , and C 1Π u States of the Hydrogen Molecule," *J. Chem. Phys.*, vol. 43, no. 7, pp. 2429–2441, 1965.

[173] G. M. J. Barca, A. T. B. Gilbert, and P. M. W. Gill, "Communication: Hartree-Fock description of excited states of H2," *J. Chem. Phys.*, vol. 141, no. 11, p. 111104, 2014.

[174] S. Grimme, "Accurate description of van der Waals complexes by density functional theory including empirical corrections," *J. Comput. Chem.*, vol. 25, no. 12, pp. 1463–1473, 2004.

[175] S. Grimme, "Semiempirical GGA-type density functional constructed with a long-range dispersion correction," *J. Comput. Chem.*, vol. 27, no. 15, pp. 1787–1799, 2006.

[176] Q. Wu and W. Yang, "Empirical correction to density functional theory for van der Waals interactions," *J. Chem. Phys.*, vol. 116, no. 2, pp. 515–524, 2002.

[177] A. Görling and M. Levy, "Exact Kohn-Sham scheme based on perturbation theory," *Phys. Rev. A*, vol. 50, no. 1, pp. 196–204, 1994.

[178] E. J. Baerends, "Exact Exchange-Correlation Treatment of Dissociated H2 in Density Functional Theory," *Phys. Rev. Lett.*, vol. 87, no. 13, p. 133004, 2001.

[179] M. Lein, J. F. Dobson, and E. K. U. Gross, "Toward the description of van der Waals interactions within density functional theory," *J. Comput. Chem.*, vol. 20, no. 1, pp. 12–22, 1999.

[180] J. Talman and W. Shadwick, "Optimized effective atomic central potential," *Phys. Rev. A*, vol. 14, no. 1, pp. 36–40, 1976.

[181] A. Makmal, S. Kümmel, and L. Kronik, "Fully numerical all-electron solutions of the optimized effective potential equation for diatomic molecules," *J. Chem. Theory Comput.*, vol. 5, no. 7, pp. 1731–1740, 2009.

[182] F. Della Sala and A. Görling, "Efficient localized Hartree-Fock methods as effective exact-exchange Kohn-Sham methods for molecules," *J. Chem. Phys.*, vol. 115, no. 13, pp. 5718–5732, 2001.

[183] S. Hirata, S. Ivanov, I. Grabowski, R. J. Bartlett, K. Burke, and J. D. Talman, "Can optimized effective potentials be determined uniquely?," *J. Chem. Phys.*, vol. 115, no. 4, pp. 1635–1649, 2001.

[184] W. Yang and Q. Wu, "Direct Method for Optimized Effective Potentials in Density-Functional Theory," *Phys. Rev. Lett.*, vol. 89, no. 14, p. 143002, 2002.

[185] Q. Wu and W. Yang, "Algebraic Equation and Iterative Optimization for the Optimized Effective Potential in Density Functional Theory," *J. Theor. Comput. Chem.*, vol. 02, no. 04, pp. 627–638, 2003.

[186] Q. Wu and W. Yang, "A direct optimization method for calculating density functionals and exchange-correlation potentials from electron densities," *J. Chem. Phys.*, vol. 118, no. 2003, pp. 2498–2509, 2003.

[187] L. Fritsche and J. Yuan, "Alternative approach to the optimized effective potential method," *Phys. Rev. A*, vol. 57, no. 5, pp. 3425–3432, 1998.

[188] R. Colle, R. K. Nesbet, and C. Applicata, "Optimized effective potential in finite-basis-set treatment," *J. Phys. B*, vol. 34, pp. 2475–2480, 2001.

[189] Q. Zhao, C. Morrison, and R. G. Parr, "From electron densities to Kohn-Sham kinetic energies, orbital energies, exchange-correlation potentials, and exchangre-correlation energies," *Phys. Rev. A*, vol. 50, no. 3, pp. 2138–2142, 1994.

[190] W. Yang, P. W. Ayers, and Q. Wu, "Potential functionals: Dual to density functional and solution to the v-representability problem," *Phys. Rev. Lett.*, vol. 92, no. 14, p. 146404, 2004.

[191] A. M. Teale, T. Irons, J. W. Furness, M. Ryley, and J. Zeman, "QUEST: QUantum Electronic Structure Techniques. A rapid development quantum chemistry platform," 2016.

[192] D. C. Langreth and J. P. Perdew, "The exchange-correlation energy of a metallic surface," *Solid State Commun.*, vol. 17, no. 11, pp. 1425–1429, 1975.

[193] O. Gunnarsson and B. I. Lundqvist, "Exchange and correlation in atoms,molecules, and solids by the spin-density-functional formalism," *Phys. Rev. B*, vol. 13, no. 10, pp. 4274–4298, 1976.

[194] O. Gunnarsson and B. I. Lundqvist, "Erratum: "Exchange and correlation in atoms, molecules, and solids by the spin-density- functional formalism" [Phys. Rev. B (13), 4274 (1976)]," *Phys. Rev. B*, vol. 15, no. 12, p. 6006(E), 1977.

[195] D. C. Langreth and J. P. Perdew, "Exchange-correlation energy of a metallic surface: Wave-vector analysis," *Phys. Rev. B*, vol. 15, no. 6, pp. 2884–2901, 1977.

[196] T. Helgaker and P. Jorgensen, "Configuration-interaction energy derivatives in a fully variational formulation," *Theor. Chim. Acta*, vol. 75, no. 2, pp. 111–127, 1989.

[197] E. R. Davidson, *No Title*. Academic Press, 1979.

[198] A. N. Tikhonov, "Solution of incorrectly formulated problems and regualrization method.," *Dokl. Akad. Nauk SSSR*, vol. 151, no. 3, p. 501, 1963.

[199] A. N. Tikhonov and V. Arsenin, *Solution of Ill-Posed Problems*. New York: Wiley, 1977.

[200] H. Partridge, "Near Hartree-Fock quality GTO basis sets for the first and third-row atoms," *J. Chem. Phys.*, vol. 90, no. 2, pp. 1043–1047, 1989.

[201] R. Penrose and J. A. Todd, "A generalized inverse for matrices," *Math. Proc. Cambridge Philos. Soc.*, vol. 51, no. 3, pp. 406–413, 1955.

[202] P. C. Hansen, "The L-curve and its use in the numerical treatment of inverse problems," *Tech. Rep. to Tech. Univ. Denmark*, vol. 2, pp. 1–24, 1999.

[203] D. C. Sorensen, "Newton's Method with a Model Trust Region Modification," *SIAM J. Numer. Anal.*, vol. 19, no. 2, pp. 409–426, 1982.

[204] J. J. Moré and D. C. Sorensen, "Computing A Trust Region Step," *Sci. Stat. Comput.*, vol. 4, no. 3, pp. 553–572, 1983.

[205] M. Rojas and D. C. Sorensen, "A trust-region approach to the regularisation of large-scale discrete forms of ill-posed problems," *SIAM J. Sci. Comput.*, vol. 23, no. 6, pp. 1842–1860, 2002.

[206] M. Rojas, S. A. Santos, and D. C. Sorensen, "LSRTS," *ACM Trans. Math. Softw.*, vol. 34, no. 2, pp. 1–28, 2008.

[207] O. Grodzevich and H. Wolkowicz, "Regularization using a parameterized trust region subproblem," *Math. Program.*, vol. 116, no. 1-2, pp. 193–220, 2007.

[208] C. L. Lawson and R. J. Hanson, *Solving least squares problems*. Philadelphia: Siam, 1995.

[209] P. C. Hansen, "Analysis of discrete ill-posed problems by means of the L-curve," *Soc. Ind. Appl. Math. Rev.*, vol. 34, no. 4, pp. 561–580, 1992.

[210] P. C. Hansen and D. P. O'Leary, "The use of the L-Curve in the regularization of discrete ill-posed problems," *Soc. Ind. Appl. Math.*, vol. 14, no. 6, pp. 1487–1503, 1993.

[211] E. V. R. de Castro and F. E. Jorge, "Accurate universal Gaussian basis set for all atoms of the Periodic Table," *J. Chem. Phys.*, vol. 5225, pp. 5225–5229, 1998.

[212] F. A. Bulat, T. Heaton-Burgess, A. J. Cohen, and W. Yang, "Optimized effective potentials from electron densities in finite basis sets.," *J. Chem. Phys.*, vol. 127, no. 17, p. 174101, 2007.

[213] T. Heaton-Burgess and W. Yang, "Optimized effective potentials from arbitrary basis sets.," *J. Chem. Phys.*, vol. 129, no. 19, p. 19410212, 2008.

[214] I. G. Ryabinkin, A. A. Kananenka, and V. N. Staroverov, "Accurate and efficient approximation to the optimized effective potential for exchange," *Phys. Rev. Lett.*, vol. 111, no. 1, pp. 1–5, 2013.

[215] A. K. Cline, C. B. Moler, G. W. Stewart, and J. H. Wilkinson, "An estimate for the condition number of a matrix," *SIAM J. Numer. Anal.*, vol. 16, no. 2, pp. 368–375, 1979.

[216] T. Heaton-Burgess, F. Bulat, and W. Yang, "Optimized Effective Potentials in Finite Basis Sets," *Phys. Rev. Lett.*, vol. 98, no. 25, p. 256401, 2007.

[217] V. N. Staroverov, G. E. Scuseria, and E. R. Davidson, "Optimized effective potentials yielding Hartree-Fock energies and densities.," *J. Chem. Phys.*, vol. 124, p. 141103, apr 2006.

[218] J. B. Krieger, Y. Li, and G. J. Iafrate, "Exact relations in the optimized effective potential method employing an arbitrary Exc[$\{\Psi$i$\}$]," *Phys. Lett. A*, vol. 148, no. 8-9, pp. 470–474, 1990.

[219] Y. Li, J. B. Krieger, J. A. Chevary, and S. H. Vosko, "Self-consistency test for the exchange-only Kohn-Sham potential," *Phys. Rev. A*, vol. 43, no. 9, pp. 5121–5123, 1991.

[220] D. R. Rohr, O. V. Gritsenko, and E. J. Baerends, "Precision of total energy and orbital energies with the expansion method for the optimized effective Kohn-Sham potential," *J. Mol. Struct. THEOCHEM*, vol. 762, no. 1-3, pp. 193–199, 2006.

[221] S. K. Ghosh and R. G. Parr, "Density-determined orthonormal orbital approach to atomic energy functionals," *J. Chem. Phys.*, vol. 82, no. 1985, pp. 3307–3315, 1985.

[222] M. Levy and J. P. Perdew, "Hellmann-Feynman, virial, and scaling requisites for the exact universal density functionals. Shape of the correlation potential and diamagnetic susceptibility for atoms," *Phys. Rev. A*, vol. 32, no. 4, pp. 2010–2021, 1985.

[223] A. P. Gaiduk and V. N. Staroverov, "Virial exchange energies from model exact-exchange," *J. Chem. Phys.*, vol. 128, no. 20, p. 204101, 2008.

[224] A. Heßelmann, A. W. Götz, F. Della Sala, and A. Görling, "Numerically stable optimized effective potential method with balanced Gaussian basis sets," *J. Chem. Phys.*, vol. 127, no. 5, p. 054102, 2007.

[225] A. Görling, A. Heßelmann, M. Jones, and M. Levy, "Relation between exchange-only optimized potential and Kohn-Sham methods with finite basis sets, and effect of linearly dependent products of orbital basis functions," *J. Chem. Phys.*, vol. 128, no. 10, p. 104104, 2008.